Metamaterial-Inspired Structures and Their Applications in Microwave, Millimeter-wave and Terahertz Planar Circuits

by

Ali Karami Horestani

B. Eng. (Electrical and Electronic),
Shiraz University, Iran, 2003
M. Eng. (Electrical and Electronic),
Shahid Beheshti University, Iran, 2006

Thesis submitted for the degree of

Doctor of Philosophy

in

Electrical and Electronic Engineering,
Faculty of Engineering, Computer and Mathematical Sciences
The University of Adelaide, Australia

2014

Supervisors:

Prof Derek Abbott, School of Electrical & Electronic Engineering

Dr Said Al-Sarawi, School of Electrical & Electronic Engineering

Prof Christophe Fumeaux, School of Electrical & Electronic Engineering

THE UNIVERSITY *of* ADELAIDE

To my Mom and Dad
and also to my wife, Zahra
with all my love.

Contents

Abstract

Metamaterials are generally defined as periodic composite structures that are engineered to modify the electromagnetic properties of materials, especially in order to achieve new physically realizable responses that may not be readily available in nature. The key to the application of metamaterial resonators for the synthesis of such effective media is their small electrical size. This feature can be also exploited for the miniaturization of planar circuits.

Motivated by the need for miniaturized planar structures in mobile wireless systems, metamaterial-inspired structures are proposed throughout this thesis for the design of compact microwave, millimeter-wave and terahertz planar structures with improved performance. The thesis firstly proposes slow-wave and SRR-loaded coplanar strips resonators for the design of compact high quality factor balanced resonators for 60 GHz VCOs in CMOS technology. Next, the thesis is focused on the miniaturization of microwave filters either by proposing resonators with dual-band functionality or through modifying the shape of metamaterial resonators. Shape modifications of metamaterial resonators are also used for the design of high-dynamic-range one- and two-dimensional displacement sensors as well as of a rotation sensor with improved dynamic range. It is further shown that high level of miniaturization can be achieved in a single-layer S-shaped SRR (S-SRR), if the loops of the S-SRR are excited by contra-directional magnetic fluxes, which makes the S-SRR very well suited for application in coplanar waveguide (CPW) technology. The thesis also proposes the dual counterpart of the S-shaped SRR, i.e., S-shaped complementary split ring resonator (S-CSRR) for application in the design of compact differential bandpass filters with inherent common-mode suppression. Finally, the application of SRRs to the design of compact bandpass filters for terahertz surface waves on single wire waveguides—the so-called planar Goubau lines (PGLs)—is studied numerically and experimentally. The results of this research show the versatility and potential of metamaterial-inspired resonators for the realization of miniaturized structures in planar technologies in different frequency bands.

Statement of Originality

I certify that this work contains no material, which has been accepted for the award of any other degree or diploma in my name, in any university or other tertiary institution and, to the best of my knowledge and belief, contains no material previously published or written by another person, except where due reference has been made in the text. In addition, I certify that no part of this work will, in the future, be used in a submission in my name, for any other degree or diploma in any university or other tertiary institution without the prior approval of the University of Adelaide and where applicable, any partner institution responsible for the joint-award of this degree.

I give consent to this copy of my thesis when deposited in the University Library, being made available for loan and photocopying, subject to the provisions of the Copyright Act 1968.

The author acknowledges that copyright of published works contained within this thesis resides with the copyright holder(s) of those works.

I also give permission for the digital version of my thesis to be made available on the web, via the University's digital research repository, the Library Search and also through web search engines, unless permission has been granted by the University to restrict access for a period of time.

	2014/05/05
Signed	Date

Acknowledgment

First and foremost, I would like to take this opportunity and glorify this Thesis to the name of God, the beneficent, the merciful. "Every inhalation of the breath prolongs life and every expiration of it gladdens our nature; wherefore every breath confers two benefits and for every benefit gratitude is due" as Saadi said in his *Rose Garden*. Thus, our hands and tongues are not capable to fulfill the obligation of thanks to Him.

I would also like to take the opportunity to express my gratitude to all those people whose support, skills and encouragement has helped me to complete this journey successfully. First, I would like to express my deep gratitude to my principal supervisor, Prof Derek Abbott for accepting me as a PhD candidate in 2009 and introducing to me the amazing world of metamaterials. His unwavering optimism, ever-so encouraging attitude, constructive suggestions, linguistic finesse, and generous travel financial assistance have been helpful in propelling my research forward. I also wish to express my appreciation to my co-supervisor, Dr Said Al-Sarawi. His critical suggestions and constructive advice in various areas, especially in the field of millimeter-wave CMOS circuits, have been of great importance towards my research. From the second year of my PhD, I have had the pleasure to work with another great scientist, my co-supervisor, Prof Christophe Fumeaux. His theoretical understanding and experimental experience in the field of electromagnetic and microwave engineering have been of great importance towards my research. He has always welcomed scientific discussions and has given me critical feedback. I would like to gratefully acknowledge his enthusiastic supervision, encouraging attitude, and generously sharing his knowledge and experience. He provided me with direction and technical support, and taught me the alphabet of ethics in science. Dear Christophe, you became more of a mentor and friend, than a supervisor. I am also indebted to all my supervisors for tirelessly reviewing all our publications including this thesis. I appreciate all their contributions, time, ideas, strict requirements, funding, and answering quickly all questions I had about topics of their expertise to make my PhD experience productive and stimulating.

Another key person whom I am strongly indebted to is Prof Ferran Martín. He has been a great mentor to my research during my visit at GEMMA/CIMITEC, Departament d'Enginyeria Electronica, Universitat Autónoma de Barcelona, Bellaterra, Spain.

His deep theoretical knowledge and long experimental experience with metamaterial-inspired microwave structures have been of great importance towards my research. I would also like to include my gratitude to Dr Miguel Durán-Sindreu, and Jordi Naqui, who have enabled part of this research work together with Prof Ferran Martín. I would also thank Anna Cedenilla for her administrative assistance, and Dr Gerard Sisò, Dr Ferran Paredes, Paris Vélez, Gerard Zamora and other members of GEMMA/CIMITEC, for making such a friendly research environment during my stay in the Universitat Autonoma de Barcelona.

I wish to express my warm thanks to Dr Tahsin Akalin, Abdallah Chahadih, Abbas Ghaddar, and Mokhtar Zehar at the Institut d'Electronique de Microelectronique et de Nanotechnologie IEMN, France for their fabrication and measurement support for part of this work.

I am indebted to Dr Withawat Withayachumnankul and Dr Thomas Kaufmann, outstanding scholars at the University of Adelaide, for being supportive colleagues and friends, and for their kindness, passion, and patience in discussing long hours around different research issues and also for their critical suggestions. I would also express my appreciation to my friends and colleagues in the Applied Electromagnetics Group at the University of Adelaide, Dr Akhilesh Verma, Dr Longfang Zou, Dr Shifu Zhao, Pouria Yaghmaee, Tiaoming (Echo) Niu, Amir Ebrahimi, Shengjian (Jammy) Chen, Chengjun (Charles) Zou, Nghia Nguyen, and Sree Pinapati, and to the people at the Adelaide T-ray Group, Mr Henry Ho, Dr Shaghik Atakaramians, Dr Gretel M. Png, Dr Mayank Kaushik, Dr Benjamin Ung, Dr Jega Balakrishnan, Dr Hungyen Lin, Mr Shaoming Zhu, and Mr Andrew Li. It was great to work with you all.

I would like to express my appreciation for all the fellow researchers at the University of Adelaide for creating a conductive and friendly environment. Special thanks to Dr Omid Kavehi, Ms Taraneh Arianfar, Mr Mostafa Rahimi, Ms Maryam Ebrahimpour, Dr Muammar Kabir, Mr Arash Mehdizadeh, Mr Sam Darvishi, Mr Mehdi Kasaee, Mr Mohammad Asraful Hasan, Ms Sarah Anita Immanuel. Also, to all my friends and their family in Adelaide, specially Mr Yadollah Bahrami, Mr Mehregan Ebrahimi and Mr Azim Kalantari. I also like to thank the office & support staff of The School of Electrical & Electronic Engineering at The University of Adelaide, Mr Ian Linke, and Mr Pavel Simick for their practical suggestions and fabrication of samples in the midst of tight time frames. Mr Danny Di Giacomo for his friendliness and logistical supply of

parts. To IT officers, David Bowler, Mark J. Innes, and Ryan King, and the administrative staff, Mr Stephen Guest, Ms Ivana Rebellato, Ms Rose-Marie Descalzi, Ms Deborah Koch, Ms Lenka Hill, Ms Jodie Schluter for their kindness and assistance.

I am also indebted to all my good teachers for planting love of knowledge in my heart, Mr Reza Dada, Mr Shirovi, Mr Parishani, Mr Zarei, Mr Khorami, Mr Asgari, Mr Ahmad Dibaj, Mr Mani, Mr Tabrizi among others. Special thanks to Mr Mohsen Tavasoli for his kindness and support. I learned electromagnetics and microwave engineering from three masters: A/Prof Farzad Mohajeri (Shiraz University), A/Prof Esfandiar Mehrshahi (Shahid Beheshti University), and Prof Christophe Fumeaux (The University of Adelaide), and it is appropriate to express my gratitude to them here.

This thesis was made possible by an Iranian Government Overseas Scholarship. I am grateful to the Iran Ministry of Sciences, Research and Technology for the scholarship, which enabled me to undertake a PhD program at the University of Adelaide. Also, to travel grants and awards from the School of Electrical & Electronic Engineering (the University of Adelaide), IEEE SA Section through student travel award, and the Australia's Defence Science and Technology Organisation (DSTO) through the Simon Rockliff Supplementary Scholarship.

My endless appreciation goes to my father and mother who always endow me with infinite support, wishes, continuous love, encouragement, and patience. I also thank them for being my first teachers together with my older brother. I would like to thank my sisters and younger brother for being my first students. It was amazing how much I learned through teaching them. I wish to express my warm and sincere thanks to my father- and mother-in-law for their kindness, guidance, and heartfelt wishes.

Last but not least, the warmest thanks to my dear wife, my most ardent supporter, research partner, and dearest friend, Zahra, who stood by me in the ups and downs, when I was right and when I was wrong, and never doubted my abilities. Dear, I love you.

Thesis Conventions

The following conventions have been adopted in this Thesis:

Typesetting

This document was compiled using LaTeX2e. Texmaker and TeXstudio were used as text editor interfaced to LaTeX2e. Inkscape was used to produce schematic diagrams and other drawings.

Referencing

The Harvard style has been adopted for referencing.

System of units

The units comply with the international system of units recommended in an Australian Standard: AS ISO 1000–1998 (Standards Australia Committee ME/71, Quantities, Units and Conversions 1998).

Spelling

American English spelling is adopted in this thesis.

Publications

Journal Articles

Horestani-A. K., Fumeaux-C., Al-Sarawi-S., and Abbott-D. (2012b). Split ring resonators with tapered strip width for wider bandwidth and enhanced resonance, *IEEE Microwave and Wireless Components Letters*, **22**(9), pp. 450–452.

Horestani-A. K., Fumeaux-C., Al-Sarawi-S., and Abbott-D. (2013a). Displacement sensor based on diamond-shaped tapered split ring resonator, *IEEE Sensors Journal*, **13**(4), pp. 1153–1160.

Horestani-A. K., Abbott-D., and Fumeaux-C. (2013b). Rotation sensor based on horn-shaped split ring resonator, *IEEE Sensors Journal*, **13**(8), pp. 3014–3015.

Horestani-A. K., Withayachumnankul-W., Chahadih-A., Ghaddar-A., Zehar-M., Abbott-D., Fumeaux-C., and Akalin-T. (2013c). Metamaterial-inspired bandpass filters for terahertz surface waves on Goubau lines, *IEEE Transactions on Terahertz Science and Technology*, **3**(6), pp. 851–858 (**Invited**).

Horestani-A. K., Naqui-J., Shaterian-Z., Abbott-D., Fumeaux-C., and Martín-F. (2014). Two-dimensional alignment and displacement sensor based on movable broadside-coupled split ring resonators, *Journal of Sensors and Actuators A: Physical*, **210**, pp. 18–24.

Horestani-A. K., Durán-Sindreu-M., Naqui-J., Fumeaux-C., and Martín-F. (2014). S-shaped complementary split ring resonators and their application to compact differential bandpass filters with common-mode suppression, *IEEE Microwave and Wireless Components Letters*, **24**(3), pp. 150–152.

Horestani-A. K., Naqui-J., Abbott-D., Fumeaux-C., and Martín-F. (2014). Two-dimensional displacement and alignment sensor based on reflection coefficients of open microstrip lines loaded with split ring resonators, *Electronics Letters*, **50**(8), pp. 620–622.

Horestani-A. K., Durán-Sindreu-M., Naqui-J., Fumeaux-C., and Martín-F. (n.d.a). Coplanar Waveguides Loaded with S-Shaped Split Ring Resonators:

Modeling and Application to Compact Microwave Filters, *IEEE Antennas Wireless Propagation Letters,* submitted.

Conference Articles

Horestani-A. K., Al-Sarawi-S., and Abbott-D. (2010). Designing of high-Q slow-wave coplanar strips for CMOS MMICs, *Proc. 35th International Conference on Infrared, Millimeter, and Terahertz Waves*, Rome, Italy, DOI: 10.1109/ICIMW.2010.5612952.

Horestani-A. K., Shaterian-Z., Withayachumnankul-W., Fumeaux-C., Al-Sarawi-S., and Abbott-D. (2011c). Compact wideband filter element based on complementary split-ring resonators, *Proc. SPIE Smart Nano-Micro Materials and Devices*, Melbourne, Australia, art. no. 820431.

Horestani-A. K., Shaterian-Z., Al-Sarawi-S., and Abbott-D. (2011b). High quality factor mm-wave coplanar strip resonator based on split ring resonators, *Proc. 36th International Conference on Infrared, Millimeter and Terahertz Waves, (IRMMW-THz)*, Houston, TX, DOI: 10.1109/irmmw-THz.2011.6105225.

Horestani-A. K., Mehdizadeh-A., Al-Sarawi-S., Fumeaux-C., and Abbott-D. (2011a). Quality factor optimization process of a tapered slow-wave coplanar strips resonator in CMOS technology, *Proc. Asia-Pacific Microwave Conference (APMC)*, Melbourne, Australia, pp. 45–48.

Mehdizadeh-A., **Horestani-A. K.**, Al-Sarawi-S., and Abbott-D. (2011). An efficient 60 GHz resonator using Harmony Search, *2011 IEEE Recent Advances in Intelligent Computational Systems,*Trivandrum, India, pp. 369–372.

Horestani-A. K., Fumeaux-C., Al-Sarawi-S., and Abbott-D. (2012a). Characterization of the complex permittivity of thin films using a slow-wave coplanar strips resonator, *Proc. 37th International Conference on Infrared, Millimeter, and Terahertz Waves*, DOI: 10.1109/IRMMW-THz.2012.6379510.

Horestani-A. K., Shaterian-Z., Al-Sarawi-S., Abbott-D., and Fumeaux-C. (2012c). Miniaturized bandpass filter with wide stopband using complementary spiral resonator, *Proc. Asia-Pacific Microwave Conference (APMC)*, Kaohsiung, Taiwan, pp. 550–552.

YAGHMAEE-P., **HORESTANI-A. K.**, BATES-B., AND FUMEAUX-C. (2012). A multi-layered tunable stepped-impedance resonator for liquid crystal characterization, *Asia-Pacific Microwave Conference Proceedings (APMC)*, Kaohsiung, Taiwan, pp. 776–778.

SHATERIAN-Z., **HORESTANI-A. K.**, AND FUMEAUX-C. (2013). Metamaterial-Inspired Displacement Sensor with High Dynamic Range, *Proc. 4th International Conference on Metamaterials, Photonic Crystals and Plasmonics, META'13*, Vol. 1, Sharjah, United Arab Emirates, pp. 9–11.

YAGHMAEE-P., WITHAYACHUMNANKUL-W., **HORESTANI-A. K.**, AMIR EBRAHIMI, BATES-B., AND FUMEAUX-C. (2013). Tunable electric-LC resonators using liquid crystal, *IEEE Antennas and Propagation Society International Symposium (APSURSI)*, pp. 382–383.

HORESTANI-A. K., WITHAYACHUMNANKUL-W., FUMEAUX-C., ABBOTT-D., AND AKALIN-T. (2013c). Metamaterial-inspired bandpass filter for the terahertz Goubau line, *Proc. 4th International Conference on Metamaterials, Photonic Crystals and Plasmonics, META'13*, Sharjah, United Arab Emirates, pp. 117–118.

List of Figures

List of Tables

Chapter 1

Introduction

THIS introductory chapter presents a short historical overview on metamaterials and highlight their attractive features for the miniaturization of planar circuits. This is followed by an overview of the objectives of the thesis and its original contributions. The outline of this work is sketched out and the contents of each chapter are overviewed at the end of this chapter.

1.1 Introduction

1.1.1 Historical Overview

The history of artificial materials, for manipulating electromagnetic radiation, can be dated back to the late nineteenth century when Jagadish Chandra Bose studied in 1898 the rotation of the plane of polarization of electromagnetic waves by man-made twisted structures (Bose 1898). Later in the early 20th century Karl Ferdinand Lindman published his work on artificial chiral media formed by a collection of randomly-oriented small wire helices (Lindman 1920, Elezzabi and Sederberg 2009). These studies were followed by several other research programs on artificial man-made materials, such as artificial dielectrics for light-weight antenna lenses and artificial chiral materials, as reviewed by Ziolkowski and Engheta (2003). Although none of the pioneering investigations explicitly used the terms 'artificial materials' or 'metamaterials', many of the studied structures can be categorized as metamaterials by today's definition (Ziolkowski and Engheta 2003).

The research on the electrodynamics of double negative (DNG) metamaterials started with Veselago's theoretical studies on hypothetical media with simultaneously negative values of permittivity and permeability at the end of the 1960s (Veselago 1968). However, there was little research carried out on this topic for more than 30 years, until the concept was revived by the work of Pendry's group (Pendry *et al.* 1996, Pendry *et al.* 1999), followed by the first practical realization of DNG metamaterials in the microwave regime by Smith *et al.* (2000). Following publication of these papers in the late 1990s, left-handed metamaterials have received a significant attention for a wide variety of applications from the microwave regime to optical frequencies. As a consequence, in many academic circles the word *metamaterials* was usually used to refer to double-negative artificial materials. However, at present, the term metamaterial is broadly used to refer to any engineered discrete media for manipulating electromagnetic properties and includes artificial materials with negative permittivity (Pendry *et al.* 1996), negative permeability (Pendry *et al.* 1999), and so-called left-handed media with simultaneously negative permittivity and permeability (Smith *et al.* 2000).

1.1.2 Objectives of the Thesis

A general definition is that metamaterials are denoted as periodic composite structures that are engineered to modify the electromagnetic properties of materials. This concept is especially useful in order to achieve new physically realizable electromagnetic responses that may not be readily available in nature. With this broad definition, the concept of metamaterials can cover any engineered material including double negative (DNG) materials, electromagnetic bandgap (EBG) structures, materials with negative index of refraction (NIR), and complex surfaces such as high-impedance ground planes (Ziolkowski and Engheta 2003).

Beyond the initial goals of creating different types of bulk metamaterials with engineered electromagnetic properties, metamaterial resonators such as split ring resonators (SRRs) and complementary split ring resonators (CSRRs) have opened new perspectives for other novel applications in planar circuits. The key in the application of these resonators to the synthesis of metamaterial-inspired planar circuits is their small electrical size compared to the operating wavelength. As a consequence, these resonators can be considered as quasi-lumped elements which makes them especially interesting for the miniaturization of planar microwave structures and circuits such as filters (Martel *et al.* 2004, García-García *et al.* 2006, Bonache *et al.* 2006a, Gil *et al.* 2007, Velez *et al.* 2009, Horestani *et al.* 2012c), couplers (Jarauta *et al.* 2006), and antennas (Herraiz-Martínez *et al.* 2011, Herraiz-Martínez *et al.* 2012, Paredes *et al.* 2012), or to improve the performance of these components (García-García *et al.* 2005b, Shi *et al.* 2012).

Miniaturization of electronic components and devices is of great importance, especially in order to develop light-weight portable devices, or in the areas such as aerospace, where every gram sent into the outer space contributes to the costs. This is assisted by the dramatic increase in application of portable devices such as smart phones, tablets and laptops to access to wireless networked services such as cellular telephony WiFi, Bluetooth, Global Positioning system (GPS), satellite communications, and so on. Utilizing metamaterial-inspired planar circuits proves to be an efficient approach towards the miniaturization of planar microwave circuits. Moreover, the electromagnetic properties of these lines can be engineered to achieve enhanced functionalities such as wideband or dual-band operation. It is worth to mention that, while the small electrical size of metamaterial-inspired resonators is the key in the application of these resonators for

the synthesis of compact planar microwave circuits, this is almost always at the cost of a narrow bandwidth.

The high quality factor resonance, subwavelength dimensions, and the sensitivity of the metamaterial-inspired resonators to their constituent materials and physical dimensions also make them ideal structures for sensory applications, or to improve the sensitivity of conventional sensors (Naqui *et al.* 2011, Schueler *et al.* 2012, Naqui *et al.* 2012a, Withayachumnankul *et al.* 2012, Withayachumnankul *et al.* 2013, Horestani *et al.* 2013b).

In this context, the application of metamaterial-inspired resonators in planar circuits and in sensory applications will be investigated in this thesis. In the first part of this thesis, including Chapter 3 and 4 the focus is on the miniaturization of microwave and millimeter-wave metamaterial components with enhanced functionalities. Chapter 5 proposes several compact metamaterial-inspired sensors with improved dynamic range and linearity. Finally, in the last part of the thesis, including Chapters 6 and 7, applications of metamaterial-inspired resonator for the design of miniaturized filters in the microwave and terahertz regimes are studied.

1.2 Statement of Original Contribution

This thesis includes several original contributions in the field of metamaterial-inspired planar structures. The original contributions can be described in three major parts. The first part of the thesis is focused on the miniaturization of metamaterial components. The second part of the thesis investigates the application of metamaterial-inspired resonators for the design of displacement and rotation sensors. And finally, the third part of the thesis is devoted to miniaturized metamaterial-inspired filters in microwave and terahertz planar circuits.

1.2.1 Miniaturization of Metamaterial Components

This section lists the original contributions of the first major part of the thesis, which is focused on the miniaturization of metamaterial components.

- A parametric study on the geometrical dimensions of a slow-wave CPS structure in a standard 90 nm CMOS process is conducted based on 3D electromagnetic simulations. The study leads to the derivation of guidelines for the design of slow-wave CPS resonators with high quality factor and small on-chip area. On the basis of the extracted guidelines, a high quality factor slow-wave CPS resonator is designed to operate in the millimeter-wave band at 60 GHz. The results of the study were presented at the *35th International Conference on Infrared, Millimeter, and Terahertz Waves,* 2010 and are published in the proceedings under the title "Designing of high-Q slow-wave coplanar strips for CMOS MMICs" (Horestani *et al.* 2010).

- As an alternative application, resonance properties of an optimized slow-wave CPS resonator are proposed for characterization of the complex permittivity of thin films of dielectrics in millimeter-wave band. It is shown that while the resonance frequency of the resonator can be used to determine the permittivity of an unknown thin film of dielectric, the loss tangent of the unknown layer can be accurately determined from the quality factor of the resonance. The characterization method was presented at the *37th International Conference on Infrared, Millimeter, and Terahertz Waves,* 2012 and is published in the proceedings under the title "Characterization of the complex permittivity of thin films using a slow-wave coplanar strips resonator" (Horestani *et al.* 2012a).

- An alternative approach for the design of high quality factor balanced resonator is proposed based on a quarter-wavelength short-ended CPS loaded with split ring resonators (SRRs). Based on the SRR's rejection and phase shift properties in the vicinity of their resonance, a quarter-wavelength composite right/left handed (CRLH) CPS resonator is designed to operate in mm-wave regime at 60 GHz with a substantially higher quality factor compared to comparable conventional resonators. The proposed design was presented at the *36th International Conference on Infrared, Millimeter and Terahertz Waves,* 2011 and is published in the proceedings under the title "High quality factor mm-wave coplanar strip resonator based on split ring resonators" (Horestani *et al.* 2011b).

- Motivated by the promising results of the slow-wave CPS resonator, the study is further extended to improve the quality factor of the quarter-wavelength slow-wave CPS resonator through the optimization of the layout of the structure based on the standing wave profile of the current and voltage along the resonator. It

is shown that the optimized tapered slow-wave CPS resonator, benefits from a high quality factor of around 28. The optimization method was presented at the *Asia-Pacific Microwave Conference (APMC)*, 2011 and is published in the proceedings under the title "Quality factor optimization process of a tapered slow-wave coplanar strips resonator in CMOS technology" (Horestani *et al.* 2011a).

- Miniaturization of metamaterial-inspired structures can be performed either by directly miniaturizing the resonators or through providing resonators with dual-band functionality. To this end, a compact dual-mode defected ground resonator is proposed. The resonator has a compact size since it is composed of a pair of complementary split ring resonators (CSRRs) embedded in a dumbbell shape defected ground structure (DGS). It is demonstrated through parametric study that the two resonances of the structure can be independently adjusted by manipulating the physical dimensions of the CSRR and DGS. Thus, the structure can be used as the building block for compact microwave circuits such as dual-mode wideband filters. The proposed dual-mode resonator was presented at the *SPIE Smart Nano-Micro Materials and Devices*, 2011, conference and is published in the proceedings under the title "Compact wideband filter element based on complementary split-ring resonators" (Horestani *et al.* 2011c).

- While bandpass filters with wide stopband are required in many applications, conventional bandpass filters suffer from unwanted harmonic passbands. It is shown that by loading a quarter-wavelength resonator with inductive loads the ratio of the spurious resonance frequency to the fundamental resonance frequency can be increased. On this basis, a bandpass filter with wide upper stopband is designed by using complementary spiral resonators. The proposed filter was presented at the *Asia-Pacific Microwave Conference (APMC)*, 2012 and is published in the proceedings under the title "Miniaturized bandpass filter with wide stopband using complementary spiral resonator" (Horestani *et al.* 2011c).

- A modified edge-coupled SRR with tapered strip width is proposed. The tapered shape, which has been developed based on the current and voltage distribution in the SRR structure, enables us to reduce the SRR electrical area by 33%. More importantly, it is shown that the proposed structure with the same electrical size as a uniform SRR has a stronger resonance with 84% wider fractional bandwidth. This strong and wideband resonance is required in many applications such as a wideband filter design. The proposed tapered SRR is experimentally validated

and published in *IEEE Microwave and Wireless Components Letters* under the title "Split ring resonators with tapered strip width for wider bandwidth and enhanced resonance" (Horestani *et al.* 2012b).

1.2.2 Metamaterial-Inspired Sensors

The high quality factor resonance, subwavelength dimensions, and the sensitivity of the metamaterial resonators to the constituent materials and physical dimensions can be exploited in the design of sensors. To this end, the second major part of this thesis is focused on metamaterial-inspired sensors. Original contributions of the thesis in this part are described in the following.

- A one-dimensional displacement sensor based on a diamond-shaped tapered SRR coupled to a coplanar waveguide (CPW) is proposed. It is shown that, compared to previous designs, the proposed sensor benefits from superior linearity and higher dynamic range. More importantly, it is shown that in contrast to a previous design, where the displacement changed both the resonant frequency and depth of the resonance notch, the proposed tapered diamond-shaped sensor have a fixed resonance frequency. This is an important improvement since the sensor does not require a frequency sweeping microwave source such as an expensive network analyzer, but can be operated at a single frequency. It is also demonstrated that, while retaining a compact size, the proposed sensor benefits from a lower operating frequency. The proposed one-dimensional displacement sensor was published in *IEEE Sensors Journal* under the title "Displacement sensor based on diamond-shaped tapered split ring resonator" (Horestani *et al.* 2012b). The paper has attracted considerable attention and was listed as one of the journal's top downloaded papers in April 2013.

- Metamaterial-inspired displacement sensors proposed by Naqui *et al.* (2011) and Horestani *et al.* (2013b) have a fundamental dynamic range limit dictated by the CPW lateral dimension. To address this issue, a one-dimensional displacement sensor based on a microstrip line loaded with broadside-coupled split-ring resonators (BC-SRRs) is proposed, with virtually no dynamic range limit. It is also shown that with modifications in the geometry of the BC-SRRs, the proposed

one-dimensional sensor can be modified and extended by adding a second element to create a high-dynamic range two-dimensional displacement sensor. Furthermore, since the operation principle of the sensors is based on the shift in the resonance frequency, rather than variation in the depth of notch, the sensors are generally immune to the environmental noise. Moreover, because the proposed sensors operate based on the breaking of symmetry, they are also robust to ambient conditions such as changes in the temperature, and can be also used as one- or two-dimensional alignment sensors. The concept and simulation results are validated experimentally. The proposed one-dimensional displacement sensor was presented at the *4th International Conference on Metamaterials, Photonic Crystals and Plasmonics, META'13,* 2013 and is published in the proceedings under the title "Metamaterial-inspired displacement sensor with high dynamic range" (Shaterian *et al.* 2013), and the extension of the sensor to a two-dimensional sensor has been submitted for publication in *Journal of Sensors and Actuators A: Physical* under the title "Metamaterial-inspired two-dimensional displacement sensor with high dynamic range".

- It has been shown by Naqui *et al.* (2011) that further to application in displacement sensors, the symmetry properties of an SRR-loaded CPW can be used for rotation sensing. However, one limitation of the sensor is that a change in rotation not only changes the depth of resonance, but also causes a shift in the resonance frequency. To address this issue, a rotation sensor based on a horn-shaped SRR is proposed. It is shown that the shape modification suppresses the frequency shift, allowing the sensor to be operated as an inexpensive single frequency system. The concept and simulation results are validated through experiment. The proposed rotation sensor was published in *IEEE Sensors Journal* under the title "Rotation sensor based on horn-shaped split ring resonator" (Horestani *et al.* 2013a).

1.2.3 Miniaturized Metamaterial-Inspired Filters

The Original contributions of the third major part of the thesis, which is focused on compact metamaterial-inspired microwave and terahertz filters, are as follows:

- Toward the miniaturization of metamaterial inspired microwave planar structures, it is shown that, rather than by a uniform time-varying magnetic field, the

resonant currents in an S-shaped SRR (S-SRR) are excited by contra-directional magnetic fields, axially applied to each loop of the resonator. Therefore, a high level of miniaturization can be achieved when the S-SRR is excited by the contra-directional magnetic fields of a CPW transmission line. To highlight the potential of S-SRR-loaded CPWs for compact filter design, two narrowband bandpass filters are designed and fabricated: one of them based on S-SRR/gap-loaded CPW resonators coupled through admittance inverters; the other one based on coupled S-SRRs, externally driven by open ended CPWs. Filters performance and size have been found to be competitive. The proposed method of miniaturization is ready to be submitted for publication in a journal.

- The dual counterpart of the S-shaped split ring resonator, i.e., the S-shaped complementary split ring resonator (S-CSRR) is proposed for application in the design of differential filters. It is shown that compared to the conventional configuration of CSRRs in differential microstrip technology, the proposed resonator benefits from a high level of miniaturization when excited by the contra-directional electric fields of a differential microstrip line. More importantly, it is shown that S-CSRRs can be used in the design of bandpass filters that suppress the common-mode noise inherently. The study has been accepted for publication in *IEEE Microwave and Wireless Components Letters* under the title "S-shaped complementary split ring resonators and their application to compact differential bandpass filters with common-mode suppression."

- Considering the need to have functional components for terahertz single wire transmission lines, the application of SRRs for the design of compact bandpass filters for terahertz surface waves on planar Goubau lines (PGL) is investigated. It is shown that while a pair of SRRs coupled to a PGL inhibits the propagation of surface waves along the line, introducing a capacitive gap to the PGL switches the bandstop behavior to a bandpass behavior. In order to highlight the potential application of the proposed structure to the design of compact filters for surface waves on PGL, two types of bandpass filters, one based on SRR/gap-loaded PGL, and the second one based on coupled SRRs, are designed. More importantly, it is shown that the filters bandwidth can be conveniently controlled over a large range by altering the geometrical dimensions of the SRRs. The methodology and simulation results have been validated through measurement of the filters' fabricated prototypes. The proposed bandpass filters can be used for controlling

the propagation of terahertz surface waves on planar Goubau lines in real applications, particularly for future broadband terahertz communications. The preliminary results of the study was presented at the *4th International Conference on Metamaterials, Photonic Crystals and Plasmonics, META'13,* 2013 and is published in the proceedings under the title "Metamaterial-inspired bandpass filter for the terahertz Goubau line" (Horestani *et al.* 2013d), whereas the more comprehensive study on the application of SRRs for the design of higher order bandpass filters and controlling their bandwidth is publication as an invited paper in *IEEE Transactions on Terahertz Science and Technology* under the title "Metamaterial-inspired bandpass filters for terahertz surface waves on Goubau lines."

1.3 Overview of the Thesis

As outlined in Fig. 1.1 the thesis encompasses five parts, including background, three major parts that describe the original contributions of the study and the conclusion. The detailed description for each part of the thesis is as follows.

Background (Chapters 1 & 2) includes the current introductory chapter as well as Chapter 2 that provides the context and background information required for the rest of the thesis. This includes the definition of 'metamaterial' from the cell size point of view, electrodynamics of right-handed and left-handed effective media, and some of the exotic characteristics of so-called left-handed metamaterials. The chapter also discusses artificial transmission lines (TLs), as one-dimensional metamaterial media from two different perspectives, namely, using the homogeneous TL theory and the theory of periodic structures. Finally, different methods of implementation of composite right/left-handed (CRLH) TLs as well as some of the most well-known metamaterial resonators are presented in the chapter.

Metamaterial Components (Chapters 3 & 4) is focused on various types of metamaterial resonators and their miniaturization. In Chapter 3 a high quality factor quarter-wavelength slow-wave coplanar strips (CPS) resonators is designed for application in millimeter-wave CMOS VCOs at 60 GHz. As an alternative application, the proposed slow-wave CPS is also used for the characterization of complex permittivity of thin films of dielectric materials. The chapter also proposes two other high quality factor balanced resonators for application in low

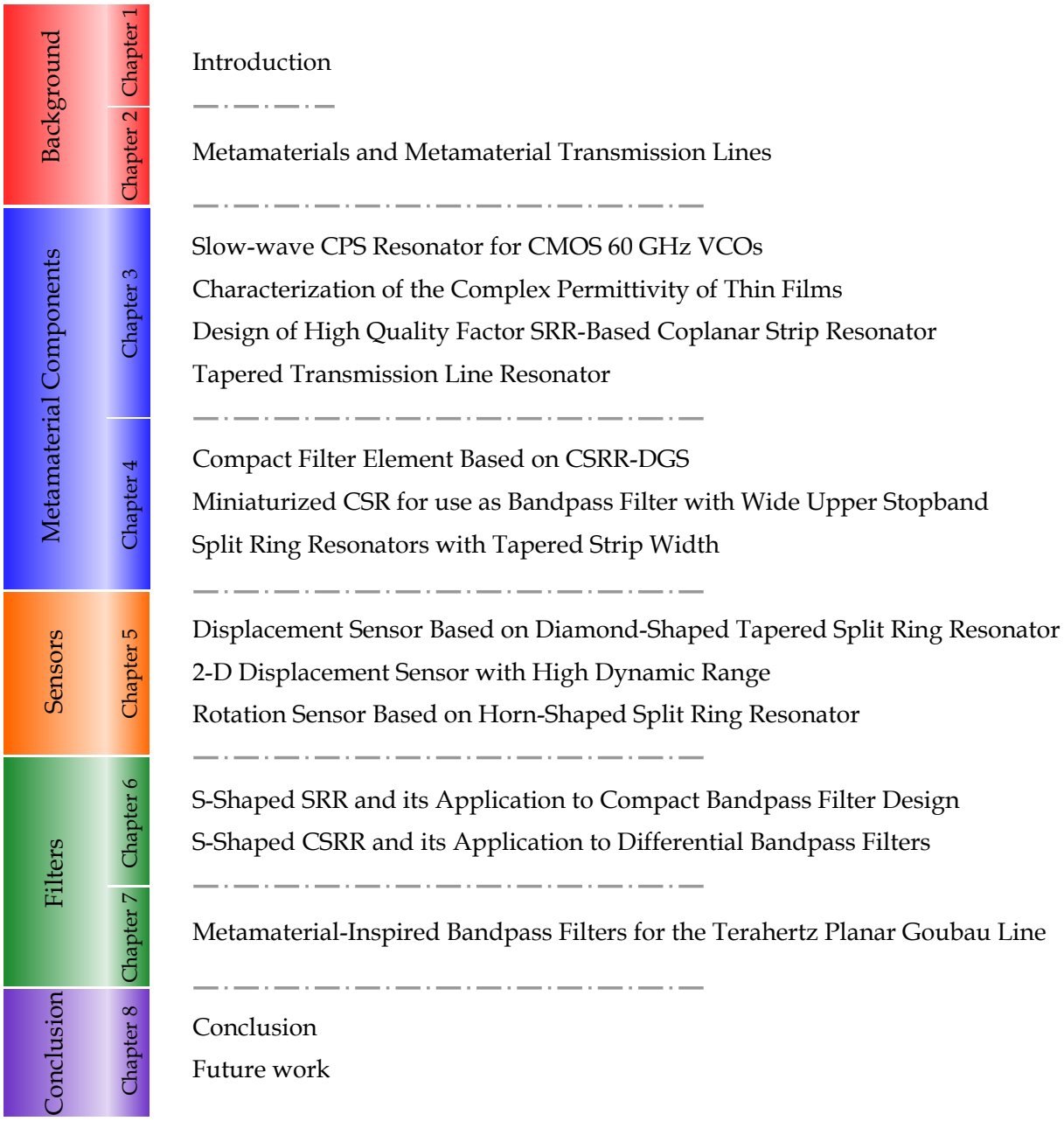

Figure 1.1. Thesis outline. The thesis is composed of 8 chapters including background and conclusion. The original contributions are distributed in three parts: Metamaterial components, sensors, and filters. All chapters are virtually self-contained.

phase noise 60 GHz VCOs in CMOS technology: The improvement in the quality factor of the first resonators in achieved by loading a quarter-wavelength CPS with SRRs, while the improvement in the second resonator is achieved by optimizing the TL layout of a quarter-wavelength resonator. Chapter 4 is focused on the miniaturization of microwave structures either by miniaturizing metamaterial resonators and/or by creating resonators with enhanced functionalities. In particular in this chapter, it is shown theoretically and experimentally that geometrical modifications of the metamaterial-inspired resonators can be used to achieve miniaturized structures with enhanced performance.

Sensors (Chapter 5) introduces three different metamaterial-inspired sensors. In Chapter 5 the high quality factor, subwavelength dimensions and sensitivity of metamaterial resonators are exploited for the design of compact high dynamic range one- and two-dimensional displacement sensors. The chapter also proposes a horn-shaped rotation sensor with improved linearity and dynamic range. All proposed sensors are validated numerically and experimentally.

Filters (Chapters 6 & 7) involves design, fabrication and measurement of three compact bandpass filters. Chapter 6 shows that a high level of miniaturization can be achieved if the fundamental resonance of an S-shape resonator is excited by contra-directional magnetic fluxes, which are readily available in CPW technology. The chapter also shows that the complementary counterpart of the particle, i.e., the S-shaped complementary split ring resonator (S-CSRR) can act as a compact resonator in differential microstrip technology. More importantly, it is shown that S-CSRRs can be used in the design of differential bandpass filters that suppress the common-mode noise inherently. Chapter 7 is focused on the application of split ring resonators (SRRs) to the design of compact bandpass filters for terahertz surface waves on single wire waveguides, the so-called planar Goubau lines (PGLs). The effects of geometric parameter variations on the frequency response of the proposed filters is studied. Using the guidelines extracted from the parametric study, two different types of bandpass filters for terahertz surface waves on PGL are designed. All the designed filters in this part are validated through experiments.

Conclusion (Chapter 8) summarizes the results of this thesis and recommends possible directions for future work.

Chapter 2

Metamaterials and Metamaterial Transmission Lines

METAMATERIALS are composite structures that are engineered to modify the electromagnetic properties of materials. The concept of metamaterials is especially useful in order to achieve new physically realizable electromagnetic responses that may not be readily available in nature. This chapter briefly reviews the concept and the fundamental theory of metamaterials as basic knowledge for the other chapters of this thesis. Using the equivalence between the parameters of transmission lines and effective media, the chapter also shows that the concept of metamaterials can be used to implement one-dimensional artificial TLs. Finally, the main methods of implementation of composite right/left-handed (CRLH) TLs, with emphasis on the resonator-based method, are reviewed.

2.1 Introduction

From the unit cell point of view, metamaterials can be classified in two categories: The first category corresponds to structures whose period is in the order of the guided wavelength, including the structures known as electromagnetic bandgaps (EBGs). The electromagnetic properties of these structures mainly arise from interference effects between scattered fields from the unit cells, which give rise to frequency bandgaps. In contrast, metamaterials whose unit cells are much smaller than the guided wavelength appear as homogeneous media for incident electromagnetic waves. The electromagnetic properties of this category is mainly obtained from a homogenization procedure, and they show effective electromagnetic properties, therefore the name *effective media* (Alù *et al.* 2006). It is worth mentioning that this is the fact that enables metamaterials to mimic the electromagnetic properties of a known material or desired electromagnetic properties that are not readily available in nature. Thus, we simply use the word *metamaterials* in the rest of this thesis to refer to composite structures in the effective media regime. Note that in many metamaterial-inspired planar circuits effective media theory is not applicable, because the planar circuit is loaded with only a few resonators. Nevertheless, the key in the application of these resonators to the synthesis of metamaterial-inspired planar circuits is their small electrical size compared to the operating wavelength. As a consequence, these resonators can be considered as quasi-lumped elements that gives rise to their potential for the miniaturization of planar microwave structures and circuits.

2.1.1 Chapter Objective and Framework

This chapter briefly reviews the concept and the fundamental theory of metamaterials as basic knowledge for the other chapters of this thesis. Categorization of materials with effective electromagnetic parameters, based on the sign of the effective permittivity and effective permeability will be presented in Section 2.2. Based on this classification we will briefly in Section 2.3 review the electrodynamics of left-handed metamaterials, and review some of the exotic behaviors of these artificial materials. Required formulations for the analysis of artificial transmission lines (TLs) are discussed in Section 2.4 considering both the classical TL perspective as well as the periodic structure perspective. Based on these formulations, specifically by using the theory of dispersion

relation and Bloch impedance, the behavior of left-handed and composite right/left-handed (CRLH) artificial TLs are studied in Section 2.5. Finally, the main methods of implementation of CRLH TLs, with emphasis on the resonator-based method, are reviewed in Sections 2.6 and 2.7.

2.2 Metamaterials with Effective Parameters

As mentioned in the previous section, since the dimensions of the unit cells of an effective media are much smaller than the guided wavelength, the propagating electromagnetic wave experiences the composite structure as a homogeneous medium with effective permittivity and permeability. These effective material parameters arise from the geometry and can be different from those of the constituent materials. This is the most prominent characteristic of effective media that enables us to engineer artificial materials with exotic electromagnetic properties not readily available in nature.

The frequency dependence for the propagation of a monochromatic wave in a substance is governed by the dispersion equation. In the case of an isotropic material or an isotropic effective medium, the dispersion equation is expressed as:

$$k^2 = \frac{\omega^2}{c^2} n^2, \tag{2.1}$$

where k denotes the propagation constant, ω is the angular frequency, c is the velocity of light in vacuum, and n is the refractive index of the medium defined as

$$n^2 = \epsilon_r \mu_r, \tag{2.2}$$

where ϵ_r and μ_r are the relative permittivity and relative permeability of the medium, respectively. The equations show that if we consider a lossless medium and regard n, ϵ_r and μ_r as real numbers, a simultaneous change in the sign of the relative permittivity and relative permeability does not affect these relations (Veselago 1968). The equations also show that for a single negative (SNG) medium, i.e. a medium with ϵ_r and μ_r having different signs, the propagation constant k and refractive index n are imaginary values. Thus, SNG media are opaque, i.e., the propagation of electromagnetic waves are inhibited in such media. On the contrary, a medium with ϵ_r and μ_r having the same sign, no matter whether positive or negative, the propagation

constant and refractive index both are real values. Thus, double positive (DPS) materials and double negative (DNG) materials are both transparent to electromagnetic waves (Veselago 1968, Marqués *et al.* 2008).

Fig. 2.1 shows that considering these relations, depending on the sign of the permittivity and permeability, substances and effective media can be categorized in four different groups: The first quadrant includes materials whose both parameters are positive, such as dielectrics at microwave frequencies. Materials with negative permittivity—or epsilon-negative (ENG) materials—are in the second quadrant. Plasmas below their cutoff frequency and metals at optical frequencies, which are opaque to electromagnetic waves are examples of ENG materials. Materials with negative permeability—or mu-negative (MNG) materials—i.e. materials in the fourth quadrant, are also opaque to electromagnetic waves. Ferromagnetic materials lie in this category. Finally, the third quadrant contains DNG materials. As mentioned earlier, this later category is not naturally available, however, synthesis of the first artificial DNG media (Smith *et al.* 2000) proved Veselago's prediction about the feasibility and behavior of artificial materials with double negative properties (Veselago 1968).

2.3 Electrodynamics of Left-Handed Metamaterials

As mentioned earlier, the history of artificial materials dates back to nineteenth century, however the electrodynamics of artificial materials with double-negative parameters was first theoretically studied by Veselago (1968). He showed that a simultaneous change in the sign of the permittivity and permeability does not affect the dispersion equations (2.1) and (2.2), which has important implications. Furthermore, he showed that in order to investigate the electromagnetic laws related to the sign of ϵ_r and μ_r, Maxwell equations in which ϵ_r and μ_r appear separately, and not in the form of their product as in (2.1) and (2.2), must be used, i.e. assuming linear isotropic media

$$\nabla \times \mathbf{E} = -\frac{\partial \mathbf{B}}{\partial t}, \tag{2.3}$$

$$\nabla \times \mathbf{H} = \frac{\partial \mathbf{D}}{\partial t}, \tag{2.4}$$

$$\mathbf{B} = \mu \mathbf{H}, \tag{2.5}$$

$$\mathbf{D} = \epsilon \mathbf{E}. \tag{2.6}$$

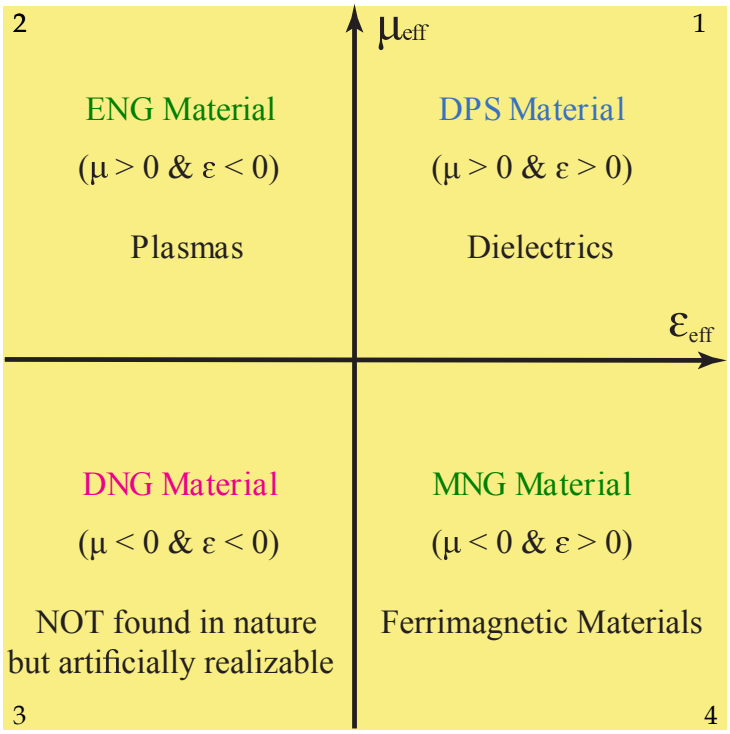

Figure 2.1. Categorization of materials based on the sign of their permittivity and permeability. Substances and effective media can be categorized in four different groups: Double positive materials, epsilon negative materials, mu negative materials, and double negative materials.

For a monochromatic plane wave, the first two equations can be reduced to

$$\mathbf{k} \times \mathbf{E} = \omega\mu\mathbf{H}, \tag{2.7}$$

$$\mathbf{k} \times \mathbf{H} = -\omega\epsilon\mathbf{E}. \tag{2.8}$$

It can be deduced from these equations that if $\epsilon > 0$ and $\mu > 0$, the wave vector $\mathbf{k}$, and the vectors of the electric field $\mathbf{E}$ and the magnetic field $\mathbf{H}$ form a right-handed triplet. On the contrary, when ϵ and μ are simultaneously negative, the three vectors $\mathbf{k}$, $\mathbf{E}$, and $\mathbf{H}$ are a left-handed set. That is why DNG materials are also called left-handed (LH) materials.

Now let us focus on the energy flux carried by electromagnetic waves. The Poynting vector $\mathbf{S}$, that characterizes the surface power density of the electromagnetic wave is given by

$$\mathbf{S} = \mathbf{E} \times \mathbf{H}. \tag{2.9}$$

This relation clearly shows that the vectors **S**, **E**, and **H** always form a right-handed triplet. Thus, as shown Fig. 2.2, for a right-handed material **S** and **k** are in the same direction, whereas in the left-handed materials they are in the opposite directions. Since the wave vector **k** is in the direction of the phase velocity, in a left-handed medium the group velocity v_g and the phase velocity v_p are in opposite directions (Veselago 1968). Veselago theoretically showed that this type of propagation in left-handed media, called "*backward propagation*" gives rise to several remarkable consequences such as the inverse Doppler effect and reverse Vavilov-Cerenkov effect (Veselago 1968).

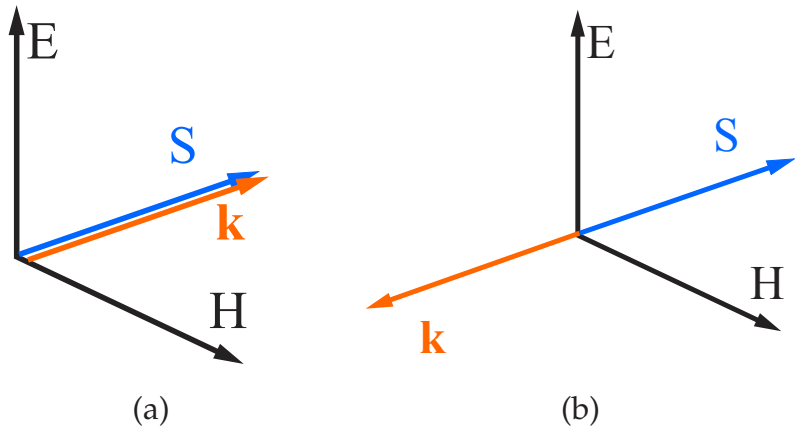

Figure 2.2. Wave vector and Poynting vector. Representation of the electric and magnetic fiels and wave vector **k** and Poynting vector **S** in (a) right-handed media and (b) left-handed media. Note that for a left-handed medium the three vectors **k**, **E**, and **H** form a left-handed triplet. Thus, while **S** and **k** in a right-handed media are in the same direction, in the left-handed materials they are in the opposite directions.

Similarly, (2.2) shows ambiguity in the sign of the refractive index in regard to the simultaneous change in the sign of ϵ_r and μ_r. However, the ambiguity can be avoided by expressing ϵ_r and μ_r in polar coordinates:

$$n = \sqrt{\epsilon_r \mu_r} = \sqrt{\epsilon_r}\sqrt{\mu_r} = \sqrt{|\epsilon_r \mu_r|}\exp(j\frac{\angle \epsilon_r}{2})\exp(j\frac{\angle \mu_r}{2}). \tag{2.10}$$

The relation now, clearly shows that for a left-handed media, where $\epsilon_r = |\epsilon_r|\exp(j\pi)$, and $\mu_r = |\mu_r|\exp(j\pi)$, the refractive index is;

$$n = \sqrt{|\epsilon_r \mu_r|}\exp(j\frac{\pi}{2})\exp(j\frac{\pi}{2}) = -\sqrt{|\epsilon_r \mu_r|}. \tag{2.11}$$

Thus, the refractive index of a left-handed medium relative to vacuum is negative (Veselago 1968, Smith *et al.* 2004, Pendry and Smith 2004). As shown in Fig. 2.3(a)

the immediate consequence of this fact is that, a negative refractive index medium bends an incident electromagnetic wave (e.g. light) to a negative angle with the surface normal. Thus, as shown in Figs. 2.3(b) and (c), in left-handed media, concave and convex lenses swap their function, that is a convex lens has a diverging effect while the concave lens will become converging. As a further instance of a seemingly anomalous effect, a diverging beam of light can be made to converge to a point using a flat slab of negative refractive index material. This phenomenon can be used in the implementation of so-called superlenses to overcome the fundamental focusing limitation of the traditional lenses, and achieving superresolution (Pendry 2000, Marqués *et al.* 2005, Fang *et al.* 2005, Liu *et al.* 2007b, Smolyaninov *et al.* 2007, Zhang and Liu 2008).

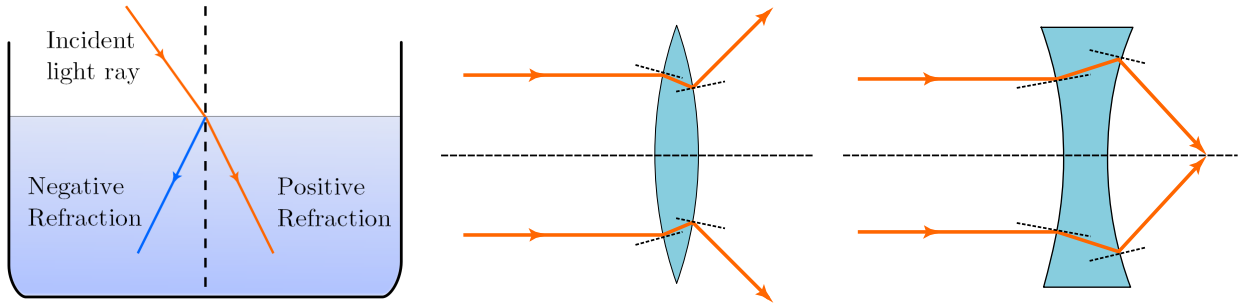

Figure 2.3. Refractive index of left-handed media. (a) Comparison between the refraction of electromagnetic waves in right-handed and left-handed media. In contrast to the right-handed media, a left-handed medium bends an incident electromagnetic wave (e.g. light) to a negative angle with respect to the surface normal. In left-handed media, concave and convex lenses swap their effect, that is a convex lens becomes diverging (b) and conversely a concave lens becomes converging (c).

All these remarkable phenomena were first studied theoretically only, and there was no empirical study conducted on practical realizations until it was shown by Pendry *et al.* that an array of split ring resonators (SRRs) can behave as a medium with negative effective permeability in a narrow band (Pendry *et al.* 1999). The introduction of this realization by Pendry *et al.*, opened the door for Smith *et al.* to synthesize the first composite medium with simultaneously negative permittivity and permeability (Smith *et al.* 2000). As shown in Fig. 2.4(a) the medium was composed of a periodic array of interlaced conducting SRRs and continuous conducting wires. In order to achieve the desired left-handed behavior, the structure needs to be illuminated with a properly polarized wave, that is, the polarization of the electric field must be parallel to the

conducting wires and the magnetic field must be normal to the SRRs plane. In their experiment, Smith *et al.* first showed that if the structure is only composed of the parallel wires, a transmission bandgap from zero frequency up to the structure's cutoff frequency $\omega_p = 13$ GHz is observed. This bandgap can be interpreted as due to the negative effective permittivity of the medium. As shown in Fig. 2.4(b) (solid line), repeating the experiment with SRRs alone, a bandgap extending from 4.2 GHz to 4.6 GHz in the transmission spectrum of the structure is observed, which is due the negative effective permeability of the structure. Finally, as depicted by dashed lines in Fig. 2.4(b), a periodic array of interlaced SRRs and wires demonstrates a passband in the transmitted power. The fact that this passband occurs within the previously forbidden band of the SRRs indicates that the negative effective permittivity of the conducting wires has combined with the negative effective permeability of the SRR array to form a left-handed effective medium that allows the propagation of the electromagnetic waves in the corresponding frequency band.

After this first experimental demonstration of a left-handed medium, a significant interest to exploit the exotic properties of metamaterials in various applications emerged. One of the most famous applications of metamaterials (although not based on left-handedness) is the use of cloaking metamaterials in order to achieve invisibility. The first practical realization of such cloak was demonstrated by Schurig *et al.* (2006) to operate over a narrow band at microwave frequencies. As shown in Fig. 2.5 in their study a they used cylinder composed of several layers of SRRs designed to hide a metallic object inside the cylinder. The SRRs dimensions are tuned to provide a spatially varying permeability, and consequently spatially varying refractive index, to bend the electromagnetic waves around the object inside the cylinder. In this configuration, the cloak decreases the scattering from the hidden object. Thus, the radiation that reaches the observer behind the shield does not contain information about the hidden object, i.e the object's shadow is removed (Schurig *et al.* 2006, Pendry *et al.* 2006).

Fig. 2.6 shows a snapshot of the simulated steady-state electric field pattern of the structure, where the black lines indicate the direction of the electromagnetic power flow, that clearly shows the radiation is not reflected by the object, and the propagation behind the object is nearly identical as when there is no obstacle. It is worth mentioning that so far cloaking has been achieved only for relatively narrow bands at microwave frequencies, and great efforts have been invested for the realization of

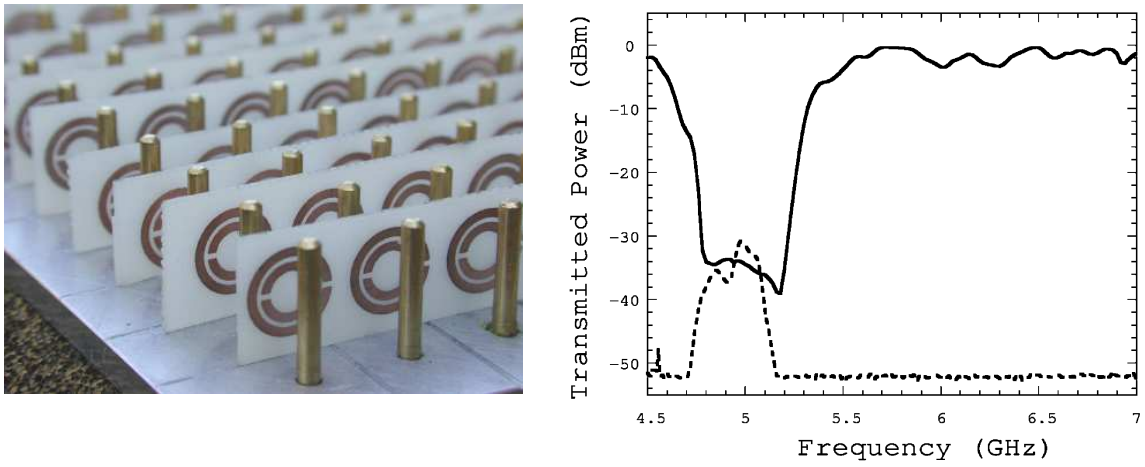

(a) (b)

Figure 2.4. First realization of left-handed media. (a) First realization of composite medium with simultaneously negative permittivity and permeability. The medium was composed of a periodic array of interlaced conducting SRRs and continuous conducting wires. After Smith *et al.* (2000). (b) Transmission power of the SRR array only (solid line) has a notch that corresponds to the frequency region where the SRR array act as an effective media with negative effective permeability. In contrast, the transmission power of the composition of the interlaced conducting SRRs and continuous conducting wires (dashed curve) has a passband that can be interpreted as due to the double negative behavior of the structure in this frequency region. After Smith *et al.* (2000).

wideband invisibility cloaking, especially at optical frequencies (Cai *et al.* 2007, Valentine *et al.* 2008, Alitalo and Tretyakov 2009, Dubinov and Mytareva 2010, Zheng *et al.* 2010, Monti *et al.* 2011).

2.4 Analysis of Artificial Transmission Lines

Soon after the first realization of left-handed media, the concept of metamaterials was applied to the implementation of left-handed transmission lines (TLs) in planar and multilayer technologies (Caloz and Itoh 2002, Iyer and Eleftheriades 2002, Oliner 2003, Martín *et al.* 2003a). In contrast to conventional TLs, artificial TLs benefit from higher level of miniaturization, and more importantly more flexibility in tailoring the phase constant and characteristic impedance to suit the requirements of each design.

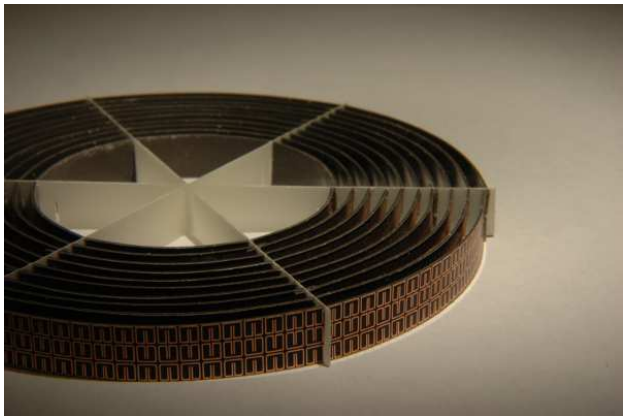

Figure 2.5. The first practical realization of cloaking metamaterials. The first practical realization of cloaking metamaterials in order to achieve invisibility over a band of microwave frequencies was demonstrated by Schurig et al. After Schurig *et al.* (2006).

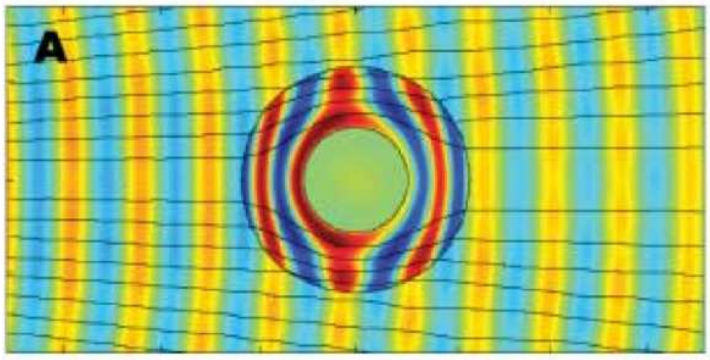

Figure 2.6. Simulated metamaterial cloak. A snapshot of the simulated instantaneous electric field pattern of the structure in steady-state. The black lines indicate the direction of the electromagnetic power flow, clearly showing that the radiation is not reflected by the object, and the propagation behind the object is nearly identical as to when there is no obstacle. After Schurig *et al.* (2006).

This section provides the formulation for analysis of the artificial TLs from two different perspectives: TL perspective and periodic structures perspective.

2.4.1 Transmission Line Perspective

When it comes to the study of metamaterial TLs, it is instructive to make an analogy between the electromagnetic parameters of an effective medium, i.e., effective permittivity ϵ_{eff} and effective permeability μ_{eff}, with the impedance per unit length $Z' = Z/\Delta x$ and admittance per unit length $Y' = Y/\Delta x$ of a TL. Fig. 2.7(a) depicts the general incremental circuit model of a TL, where $Z' = Z/\Delta x$ represents the impedance per unit length of the line, while the line's admittance per unit length is shown by $Y' = Y/\Delta x$. From an analogy between telegraphers' equations for this TL with Maxwell's equations for an effective medium it can be concluded that it is possible to make an equivalence between the effective permeability and permittivity of the medium with the equivalent impedance per unit length and admittance per unit length of the TL, respectively (Iyer and Eleftheriades 2002)

$$Z'_s = j\omega\mu_{\text{eff}}, \tag{2.12}$$

$$Y'_p = j\omega\epsilon_{\text{eff}}. \tag{2.13}$$

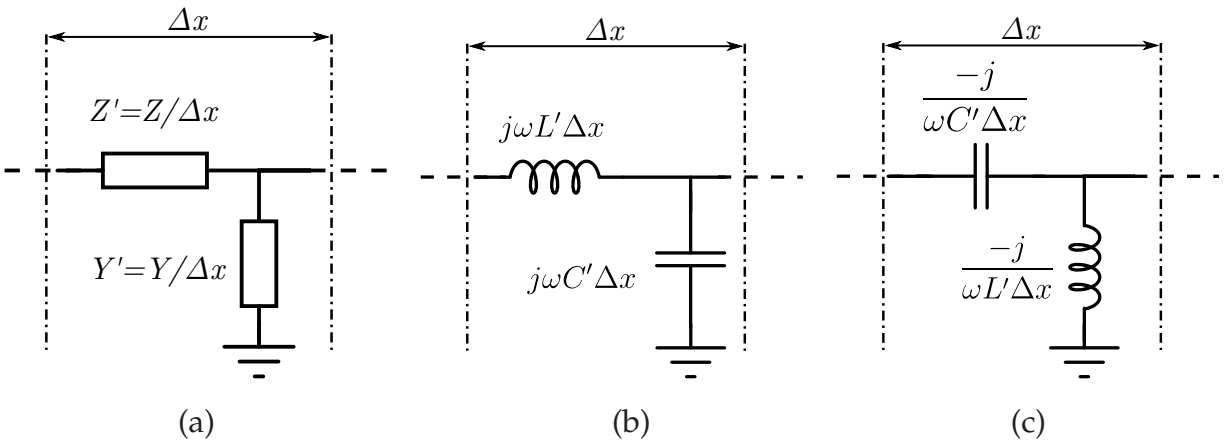

Figure 2.7. TLs circuit model. (a) General incremental circuit model of a TL, where $Z' = Z/\Delta x$ represents the impedance per unit length of the line, while the line's admittance per unit length is shown by $Y' = Y/\Delta x$. (b) Circuit model of a conventional TL, and (c) circuit model of a dual TL.

Note that, since there is no assumption regarding the nature of the immittances of the model, the TL immittances generally could be either positive or negative. Considering the incremental circuit model of a conventional TL of Fig. 2.7(b) we have

$$j\omega L' = j\omega\mu_{\text{eff}} \implies \mu_{\text{eff}} = L', \tag{2.14}$$

$$j\omega C' = j\omega\epsilon_{\text{eff}} \implies \epsilon_{\text{eff}} = C'. \tag{2.15}$$

Thus, the analogy shows that for a conventional TL effective parameters are both positive, resulting in the forward propagation of electromagnetic waves in this medium.

In contrast, effective parameters of the dual TL of Fig. 2.7(c) are both negative:

$$\frac{1}{j\omega C'} = j\omega\mu_{\text{eff}} \implies \mu_{\text{eff}} = \frac{-1}{\omega^2 C'}, \tag{2.16}$$

$$\frac{1}{j\omega C'} = j\omega\epsilon_{\text{eff}} \implies \epsilon_{\text{eff}} = \frac{-1}{\omega^2 L'}. \tag{2.17}$$

As expected from this analogy to double negative effective media, electromagnetic waves can propagate (although backward) in such TL with double negative parameters, i.e. with both negative Z' and Y'.

Finally, based on the same analysis it can be concluded that in TLs described by the incremental circuit models of Fig. 2.8 where Z' and Y' have opposite signs, i.e. in single negative TLs, the propagation of electromagnetic waves is inhibited.

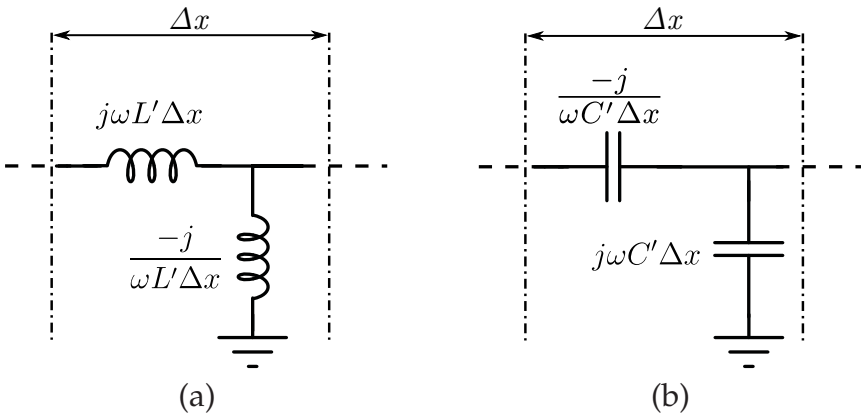

Figure 2.8. Circuit models of artificial single negative TLs. (a) Circuit model of an artificial TL with negative Y', and (b) circuit model of an artificial TL with negative Z'. From the analogy to the single negative effective media in can be concluded that propagation of electromagnetic waves in these TLs is inhibited.

In summary, as listed in Table. 2.1, similarly as discussed in Section. 2.2 and represented in Fig 2.1, four types of TLs can exist depending on the sign of Z' and Y'. Forward and backward wave propagations are allowed in right-handed (RH) and left-handed (LH)

Table 2.1. Four possible types of TLs. Depending on the sign of impedance per unit length Z' and admittance per unit length Y', four types of TLs can exist. Forward and backward wave propagations are allowed in right-handed (RH) and left-handed (LH) TLs, respectively, whereas the propagation of electromagnetic waves in single negative TLs is inhibited.

Immittances		Medium	Propagation
$Z'(\sim \mu_{\text{eff}})$	$Y'(\sim \epsilon_{\text{eff}})$		
> 0	> 0	Conventional TL (DPS)	Forward
> 0	< 0	SNG	None
< 0	> 0	SNG	None
< 0	< 0	Dual TL (DNS)	Backward

TLs, respectively, whereas the propagation of electromagnetic waves in single negative TLs is inhibited.

2.4.2 Periodic Structures Perspective

The analysis of the previous section was based on the assumption of homogeneity of the artificial TLs. However, in many of the metamaterial-inspired designs proposed in microwave, the condition of homogeneity does not necessarily hold in a satisfactory approximation. Thus, the concept of effective electromagnetic parameters cannot be used to analyze such a media, and similarly the telegraphers' equations might not be appropriate for describing artificial TLs. Thus in many cases, the theory of periodic structures is more appropriate to analyze the characteristics of this type of artificial TLs, either considering infinite periodicity or perfect matching to ports. From this theory, the dispersion characteristic of a periodic artificial TL can be inferred as (Collin 2000, Pozar 2009)

$$\cos(\beta l) = \frac{A+D}{2}, \tag{2.18}$$

where A and D are the diagonal parameters of the $ABCD$ matrix of the structure's unit cell. This relation is valid for any periodic structure of arbitrary cell size, and can be used for the analysis of an artificial TL with general T- or π-circuit models of Fig. 2.9 as

$$\cos(\beta l) = 1 + \frac{Z_s(\omega)}{Z_p(\omega)} \tag{2.19}$$

where $Z_s(\omega)$ and $Z_p(\omega)$ are series and shunt impedances of the unit cell circuit model.

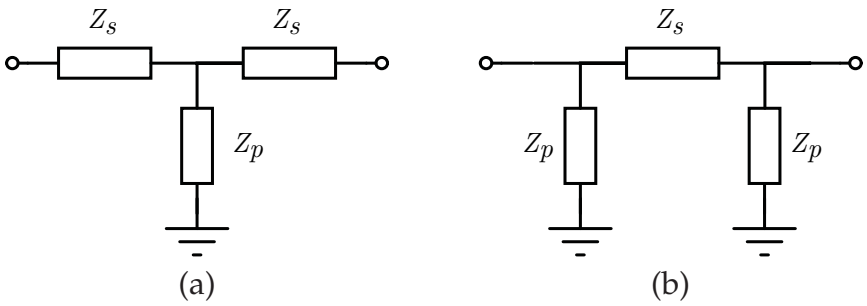

Figure 2.9. T and π unit cell circuit model. General (a) T-, and (b) π-circuit model of a unit cell of a periodic structure.

The dispersion relation of (2.19) can be expressed in terms of the scattering parameters simply by considering the relation between the $ABCD$ and S parameters:

$$\cos(\beta l) = \frac{1 - S_{11}S_{22} + S_{21}S_{12}}{2S_{21}}. \tag{2.20}$$

For the case of a lossless, reciprocal, symmetric and passive periodic structure this last equation can be further reduced to

$$\cos(\beta l) = \frac{\cos(\Phi_{21})}{|S_{21}|}, \tag{2.21}$$

where Φ_{21} is the phase of S_{21}.

Beside the propagation constant, the characteristic impedance is one of the most relevant parameters for the characterization of TLs. However, since the infinitesimally small unit cell condition is not satisfied for non-homogeneous TLs, the classical concept of TL characteristic impedance cannot be used. Therefore, we consider the so-called Bloch impedance Z_B, which is a characteristic impedance defined at the unit cell terminals of a periodic structure (Pozar 2009). Note that the concept of Bloch impedance in periodic structures relates the voltage and currents at unit cell terminals and plays the same role as the characteristic impedance in homogeneous TLs. That is why sometimes it is even called characteristic impedance (Marqués *et al.* 2008). The Bloch impedance can be obtained from the $ABCD$ matrix of the periodic structure's unit cell by

$$Z_B^{\pm} = \frac{-2\,B\,Z_0}{A - D \mp \sqrt{(A+D)^2 - 4}}, \tag{2.22}$$

where A, B and C are parameters of the $ABCD$ matrix and Z_0 is the reference characteristic impedance. In the case of symmetric unit cells, this relation can be reduced to

$$Z_B^{\pm} = \frac{\pm B\, Z_0}{\sqrt{(A)^2 - 1}}, \tag{2.23}$$

where $\pm$ corresponds to the Bloch impedance for positively and negatively traveling waves, respectively. Taking this into account, the Bloch impedance of a periodic structure is related to the structure's general T- or π-models of Fig. 2.9 by

$$Z_{B_T} = \sqrt{Z_s(\omega)\left[Z_s(\omega) + 2Z_p(\omega)\right]}, \tag{2.24}$$

$$Z_{B_\pi} = \sqrt{\frac{Z_p^2(\omega)\, Z_s(\omega)}{2Z_p(\omega) + Z_s(\omega)}}, \tag{2.25}$$

where Z_{B_T} and Z_{B_π} are the Bloch impedances of the structure using T- and π-model, respectively.

It is very important to note that while both T- and π-models of a periodic structure result in the same propagation constant, we have two different equations (2.24) and (2.25) for evaluating the Bloch impedance of an identical structure. The reason is that, according to the definition, Bloch impedance relates the voltages and currents at the unit cell terminals, thus, it will vary when changing the location of the cutting plane defining the unit cells (Collin 2000, Pozar 2009, Caloz and Itoh 2005). This is in contrast to the case of the characteristic impedance for a homogeneous TL, which is identical at any cutting plane along the TL.

Another important point is that for a lossless passive structure, which is only composed of reactive components, the equations (2.24) and (2.25) result in a purely real or purely imaginary Bloch impedance. The frequency band in which the Bloch impedance is purely real corresponds to the passband of the periodic structure, whereas the region with a purely imaginary Bloch impedance corresponds to the frequency band where wave propagation is inhibited (Caloz and Itoh 2005). Thus, for any kind of lossless periodic structure, which can be modeled with reactive components, propagation constant and Bloch impedance can be used to control and/or analyze the behavior of the structure to achieve a desired frequency response.

2.5 Metamaterial Transmission Lines

In the previous section we discussed artificial TLs from two different perspectives, namely using homogeneous TL theory or considering the theory of periodic structures. It can be emphasized that the theory of periodic structures is a more general method, which converges to the theory of TLs when dealing with infinitesimally small unit cells. Thus, in this section the described theory of periodic structures is used to analyze lossless right- and left-handed TLs, as well as composite right/left-handed (CRLH) TLs.

2.5.1 Purely Right- or Left-Handed Transmission Lines

First, lets us focus on a right-handed TL. The unit cell of such TL can be modeled with the T-network of Fig. 2.10(a). Thus, the series impedance Z_s and shunt impedance Z_p of the equivalent T-network are

$$Z_s = j\omega\frac{L_R}{2}\,, \tag{2.26}$$

$$Z_p = \frac{1}{j\omega C_R}\,, \tag{2.27}$$

where L_R and C_R are the series inductance and shunt capacitance of the unit cell, and subscript R refers to the right-handedness of the line. Therefore, using equations (2.19)

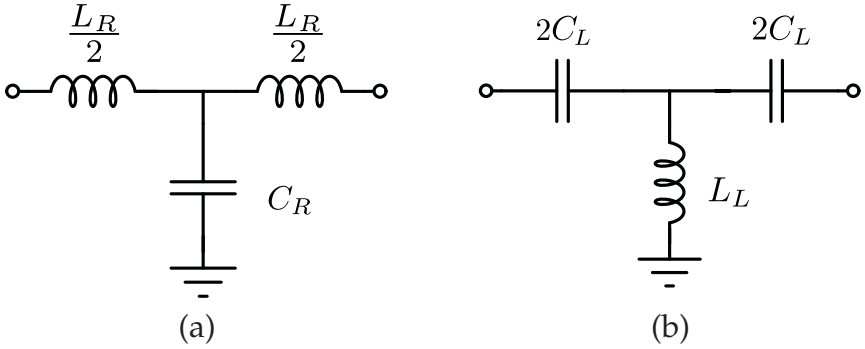

Figure 2.10. Unit cells of purely right-handed and purely left-handed TLs. The T-network of a unit cell of (a) a right-handed TL, and (b) a left-handed TL.

and (2.24) the propagation constant and Bloch impedance of the line can be obtained

from:

$$\cos(\beta_R l) = 1 - \frac{L_R C_R}{2}\omega^2, \tag{2.28}$$

and

$$Z_{BR} = \sqrt{\frac{L_R}{C_R}\left(1 - \frac{\omega^2}{\omega_{cR}^2}\right)}, \tag{2.29}$$

where l is the length of the unit cell, and $\omega_{cR} = 2/\sqrt{L_R C_R}$ is the angular cutoff frequency of the transmission line.

On the other hand, the series and shunt impedances of T-circuit model of the left-handed TL of Fig. 2.10(b) are

$$Z_s = \frac{1}{j\omega 2C_L}, \tag{2.30}$$

$$Z_p = \frac{1}{j\omega L_L}, \tag{2.31}$$

where C_L and L_L are the series capacitance and shunt inductance of the unit cell, respectively, and the subscript L refers to the left-handedness of the line. Therefore, by substituting (2.30) and (2.31) into equations (2.19) and (2.24), the propagation constant and Bloch impedance of the line can be obtained as:

$$\cos(\beta_L l) = 1 - \frac{1}{2L_L C_L \omega^2}, \tag{2.32}$$

and

$$Z_{BR} = \sqrt{\frac{L_L}{C_L}\left(1 - \frac{\omega_{cL}^2}{\omega^2}\right)}, \tag{2.33}$$

where $\omega_{cL} = 1/2\sqrt{L_L C_L}$ is the angular cutoff frequency of the left-handed transmission line (Marqués *et al.* 2008).

As an example, the dispersion diagram and Bloch impedance of a right-handed TL with $L_R = 4$ nH and $C_R = 1$ pF, and those of a left-handed TL with $L_L = 1$ nH and $C_L = 0.25$ pF are depicted in Figs. 2.11 and 2.12. Note that transmission is allowed in the frequency band where propagation constant and Bloch impedance are real. Thus, as shown in the figures, the right-handed medium behaves as a lowpass structure, whereas the left-handed medium has a highpass nature.

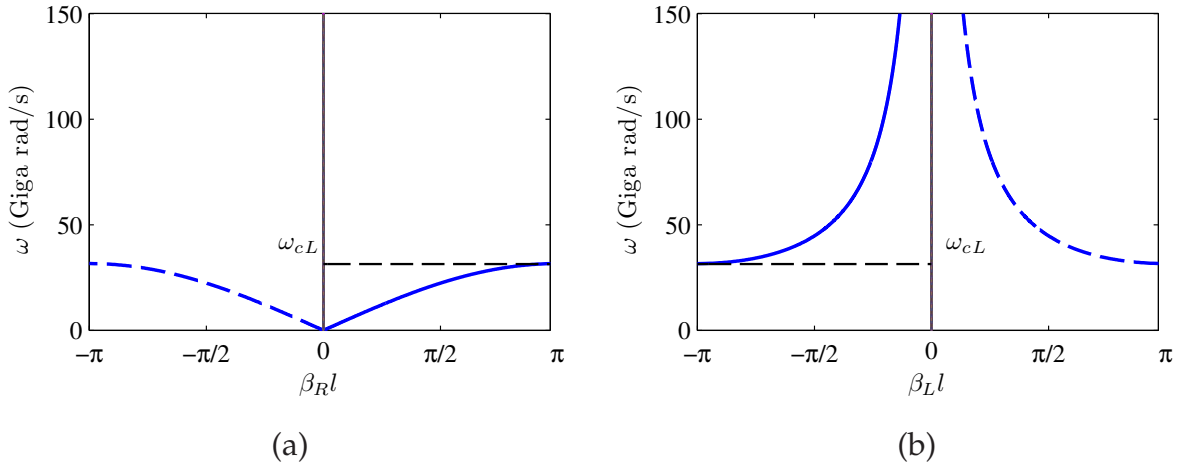

Figure 2.11. Dispersion diagram of right- and left-handed TLs. Dispersion diagram of (a) a right-handed TL with $L_R = 4$ nH, $C_R = 1$ pF, and (b) a left-handed TL with $L_L = 1$ nH, and $C_L = 0.25$ pF.

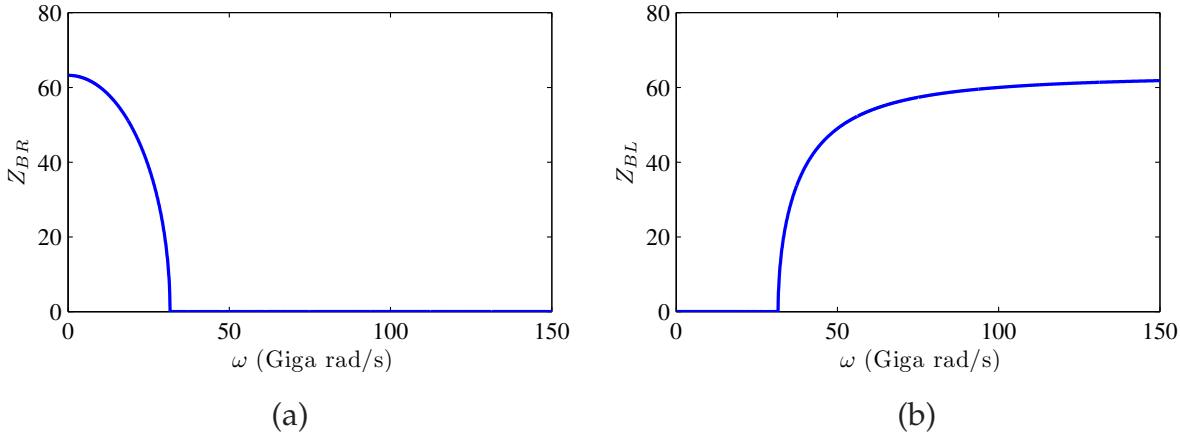

Figure 2.12. Bloch impedance of right- and left-handed TLs. Bloch impedance of (a) a right-handed TL with $L_R = 4$ nH, $C_R = 1$ pF, and (b) a left-handed TL with $L_L = 1$ nH, and $C_L = 0.25$ pF.

Figure 2.11 also shows that both structure are dispersive. It is worth recalling that in the long wavelength limit, i.e. at those frequencies that condition $\lambda_g \gg l$ is satisfied, these models converge to the homogeneous TL line models. In other words to correctly model a homogeneous TL at higher frequencies we need to reduce the unit cell size to have a valid long wavelength approximation. Under this approximation propagation

constant and Bloch impedance of a right-handed TL, i.e. expressions (2.28) and (2.29) are reduced to the following well known expressions:

$$\beta_R l = \omega\sqrt{L_R C_R}, \tag{2.34}$$

and

$$Z_{BR} = \sqrt{\frac{L_L}{C_L}}. \tag{2.35}$$

From (2.34), the phase velocity v_{pR} and the group velocity v_{gR} of the right-handed medium are given as:

$$v_{\mathrm{pR}} = \frac{\omega}{\beta_R} = \frac{l}{\sqrt{L_R C_R}}, \tag{2.36}$$

$$v_{\mathrm{gR}} = \left(\frac{\partial\beta_R}{\partial\omega}\right)^{-1} = v_{\mathrm{pR}}. \tag{2.37}$$

Note that for a homogeneous right-handed medium, both phase and group velocities are positive and constant.

In a similar manner, under the long wavelength approximation the propagation constant and Bloch impedance of a left-handed medium can be reduced to:

$$\beta_L l = -\frac{1}{\omega\sqrt{L_L C_L}}, \tag{2.38}$$

and

$$Z_{BL} = \sqrt{\frac{L_L}{C_L}}. \tag{2.39}$$

Thus, the phase velocity v_{pL} and the group velocity v_{gL} of the left-handed medium can be obtained from (2.38) as:

$$v_{\mathrm{pL}} = \frac{\omega}{\beta_L} = -\omega^2 l\sqrt{L_L C_L}, \tag{2.40}$$

and

$$v_{\mathrm{gL}} = \left(\frac{\partial\beta_L}{\partial\omega}\right)^{-1} = +\omega^2 l\sqrt{L_L C_L}. \tag{2.41}$$

It is important to note that the phase and group velocities of a left-handed medium have opposite signs. As shown in the dispersion diagrams of Figs. 2.11(a) and (b),

equations (2.28) and (2.32) show an ambiguity in the sign of propagation constant, that is, β can be either positive or negative. This ambiguity comes from the two possible propagating waves, i.e., positively and negatively traveling waves. However, if we focus on one of the waves, for instance the wave traveling from left to right, and adopt an appropriate coordinate system, the group velocity must be positive in order to satisfy causality. Thus, in Figs. 2.11(a) and (b) the portions of the curves with positive group velocity (shown by solid lines) correspond to a positively traveling wave. Accordingly, the figures show that for a right-handed medium both β and v_p are positive, while these parameters are negative for a left-handed medium.

2.5.2 Composite Right/Left-Handed Transmission Lines

So far, we analyzed ideal artificial TLs that support either purely right-handed or purely left-handed wave propagation. However, it is also possible to design artificial TLs that behave as a right-handed TL in certain frequency band, while their behavior in another part of the spectrum is left-handed (Eleftheriades 2002, Caloz and Itoh 2002, Grbic and Eleftheriades 2002, Oliner 2003). In fact, unlike the purely right-handed TLs, the practical realization of pure left-handed transmission lines is not possible. This is because in order to implement the required negative series impedance and negative shunt admittance, a host conventional transmission line is required to be loaded with series capacitive and shunt inductive elements. Thus, as will be shown in the next section, the resulting TL has both right- and left-handed behaviors depending on the frequency region. Such artificial lines are known as composite right/left-handed (CRLH) transmission lines (Caloz and Itoh 2005, Marqués *et al.* 2008). Figs. 2.13(a) and (b) depict the T- and π-circuit model of the first implementation of a CRLH line (Caloz and Itoh 2002, Eleftheriades 2002, Grbic and Eleftheriades 2002, Oliner 2003). Note that, depending on the frequency region, series and/or shunt branch could be capacitive or inductive.

Fig. 2.14(a) depicts the typical dispersion diagram of a CRLH TL with unit cell of Fig. 2.13(a) with $L_R = 1$ nH, $C_R = 1$ pF, $L_L = 2$ nH, and $C_L = 1$ pF. Notice that the dispersion diagram shows two passbands that are separated with a band gap. The lower passband corresponds to the frequency region where reactances of the inductance L_L and the capacitance C_L are dominant. Thus, the line has a left-handed behavior in this frequency band. Conversely, in the upper passband the line acts as a right-handed medium, because the capacitance C_R and the inductance L_R are the dominant

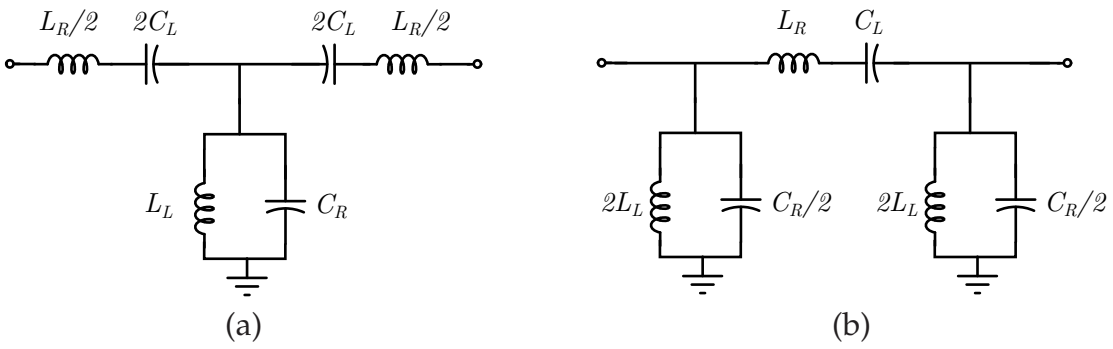

Figure 2.13. Circuit models of CRLH TLs. Composite right/left-handed TL (a) T-model (b) π-model.

reactances. The band gap between the both bands corresponds to the region where the TL acts as a single negative medium, and thus, the propagation of electromagnetic waves is inhibited in this frequency band. The lower and upper frequency limits of the band gap, i.e., f_{G1} and f_{G2} are

$$f_{G1} = \min(f_s, f_p), \tag{2.42}$$

$$f_{G2} = \max(f_s, f_p), \tag{2.43}$$

where f_s and f_p are the resonance frequency of the series and shunt branches, respectively (Marqués *et al.* 2008):

$$f_s = \frac{1}{2\pi\sqrt{L_R C_L}}, \tag{2.44}$$

$$f_p = \frac{1}{2\pi\sqrt{L_L C_R}}. \tag{2.45}$$

Thus, the lower and upper frequency limits of the bandgap are determined by the resonance frequency of the series and shunt branches, depending on which one resonates at a lower frequency.

In the special case when both series and shunt impedances of the T-circuit model of the unit cell resonate at the same frequency, i.e., $f_s = f_p = f_0$, the bandgap is suppressed and a continuous transition between the right- and left-handed passbands appears, as shown in Fig. 2.15(a). This CRLH TL is known as balanced TL, whereas a CRLH TL with non-continuous transition from left-handed to right-handed band is denoted as an unbalanced line.

The Bloch impedance of the unbalanced and balanced CRLH TLs are also depicted in Figs. 2.14(b) and 2.15(b), respectively. Fig. 2.14(b) shows that the Bloch impedance of an

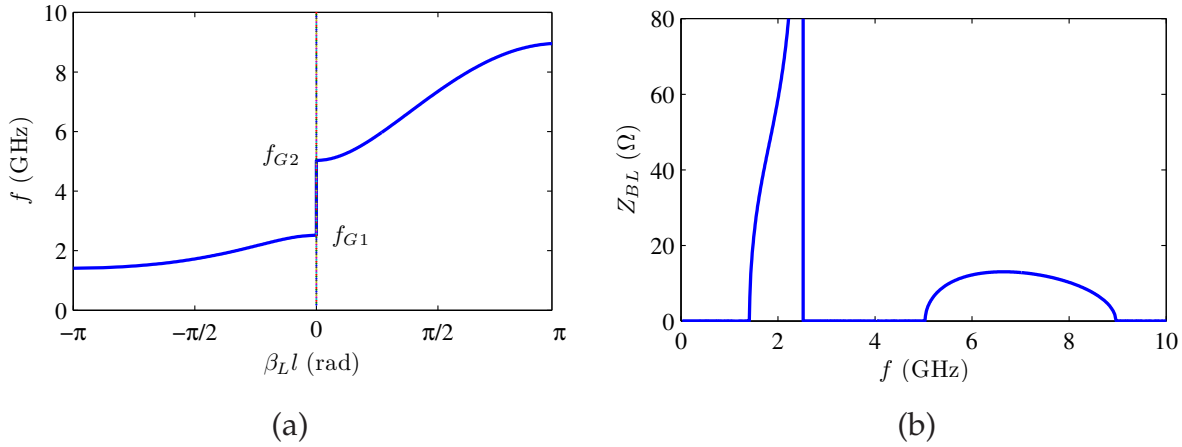

Figure 2.14. Propagation constant β and Bloch impedance Z_B of a lossless CRLH line. (a) Dispersion diagram and (b) real part of the Bloch impedance of an unbalanced CRLH TL with $L_R = 1$ nH, $C_R = 1$ pF, $L_L = 2$ nH, and $C_L = 1$ pF. The dispersion diagram shows two passbands that are separated with a band gap. The lower passband corresponds to the frequency region where the line has a left-handed behavior, whereas the upper passband relates to the frequency region where the line acts as a right-handed medium. The band gap between the both bands corresponds to the region where the TL acts as a single negative medium, thus, the propagation of electromagnetic waves is inhibited in this frequency band.

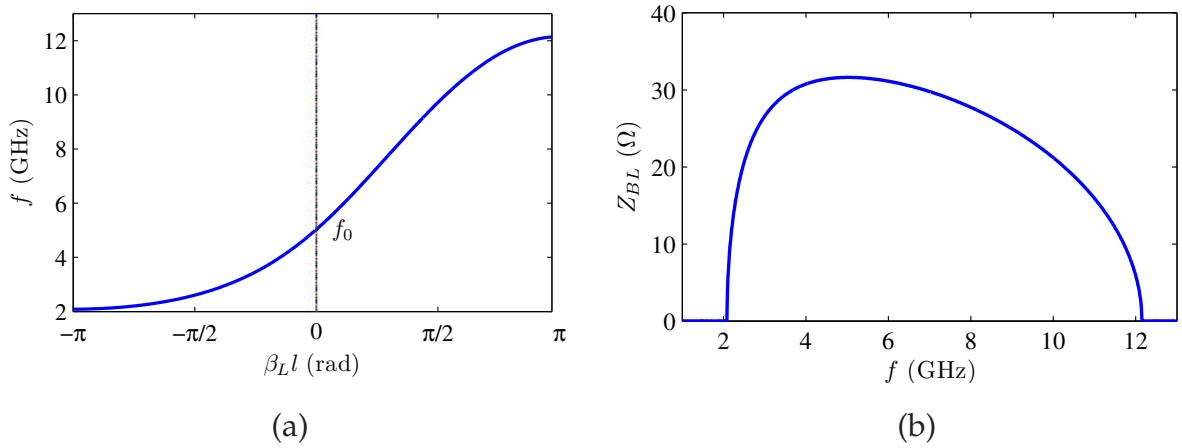

Figure 2.15. Propagation constant β and the Bloch impedance Z_B of a balanced CRLH line. (a) Dispersion diagram and (b) real part of the Bloch impedance of a balanced CRLH TL with $L_R = 1$ nH, $C_R = 1$ pF, $L_L = 1$ nH, and $C_L = 1$ pF

unbalanced line is real in the same frequency bands as the passbands in the dispersion diagram of the line. In the bandgap region, the Bloch impedance of the line is purely

imaginary. It was shown that in this frequency region an unbalanced line can be used for the impedance matching for complex impedances (Damm *et al.* 2007). One the other hand, Fig. 2.14(b) shows that the Bloch impedance of the balanced TL presents a continuous transition from left-handed to right-handed region, having its maximum value at transition frequency f_0. In summary, it can be concluded that while the unbalanced TLs can be used to the design of dual-band structures, the balanced CRLH TLs are suitable to achieve broad-band responses (Gil and Bonache 2007, Bonache *et al.* 2008).

Figure 2.16 depicts the unit cell and typical dispersion diagram of the so-called dual composite right/left-handed (dual-CRLH) line (Caloz 2006). Note that in contrast to the conventional CRLH lines, in the dual-CRLH line the elements of the series branch are in parallel and those of the shunt branch are in series. The duality in the structure gives rise to a duality in the dispersion diagram of the structure, i.e. having a right-handed behavior in the lower passband and a left-handed behavior in the higher passband. However, even when the resonance frequency of the series branch coincides with that of the shunt branch a bandgap exists between the two passbands (Caloz 2006).

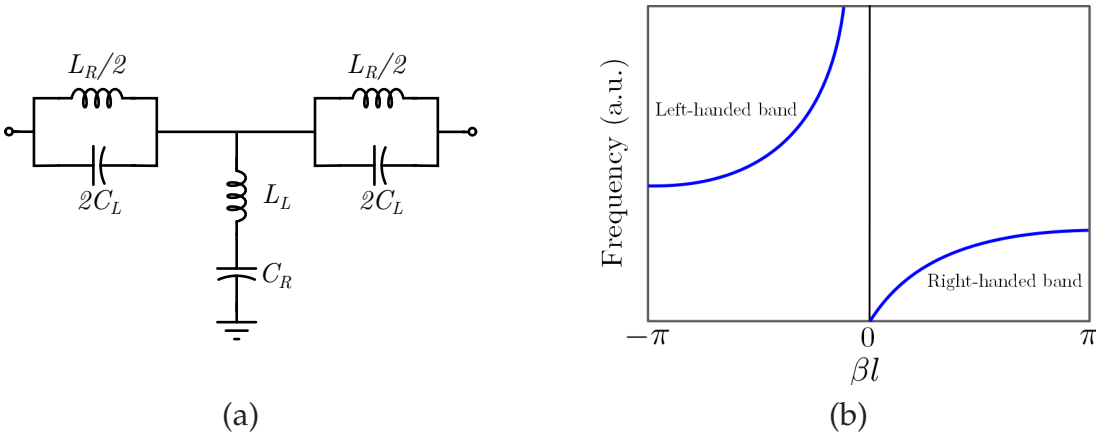

Figure 2.16. Dual composite right/left-handed. Unit cell (a) and typical dispersion diagram (b) of a dual composite right/left-handed (dual-CRLH) line.

2.6 Implementation of CRLH TLs: CL-Loaded Lines

The CRLH TLs of the previous section can be implemented with different approaches. A simple method of implementation, which directly can be inferred from the unit cell circuit models of the CRLH TLs, is by means of loading a host conventional line with

lumped or semi-lumped capacitors and inductors (Grbic and Eleftheriades 2002, Caloz and Itoh 2004b). Fig. 2.17(a) depicts the layout of a CL-loaded artificial TL in coplanar waveguide (CPW) technology, where the required series capacitances are realized with capacitive gaps in the CPW's signal strip line, and the narrow metallic connections from the signal strip line to the CPW grounds are used for the implementation of the required shunt inductances (Grbic and Eleftheriades 2002). Two different CRLH TLs implemented in microstrip technology are also shown in Figs. 2.17(b) and (c) (Caloz and Itoh 2002, Caloz and Itoh 2004b, Aznar *et al.* 2008a). In the first implementation capacitive gaps and vias to ground are used for the realization of the required series and shunt impedances, while in the second implementation interdigital capacitors and short-circuited stubs are used to achieve higher values of series capacitance and shunt inductance.

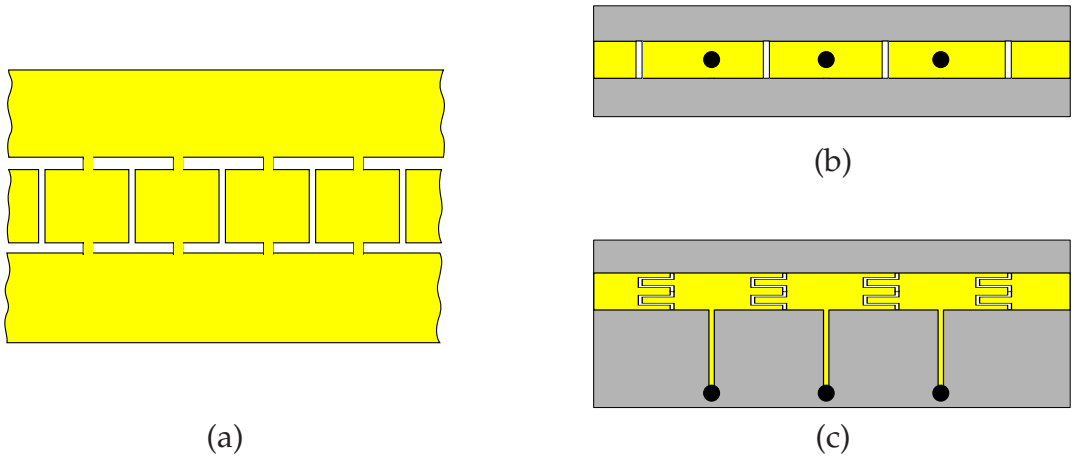

Figure 2.17. CL-loaded artificial TLs. A simple method for implementing CRLH TL is by loading a host conventional line with lumped or semi-lumped capacitors and inductors. (a) Layout of a CL-loaded artificial TL in CPW technology, and (b) and (c) two different layouts for implementation of CRLH lines in microstrip technology. After Aznar *et al.* (2008a)

Note that, as mentioned earlier, this method initially was used to realize pure left-handed TLs, i.e. TLs with series capacitances and shunt inductances. However, since the implementation method requires a conventional right-handed host TL, which has distributed series inductance and shunt capacitance, the resulted line is a CRLH line.

2.7 Implementation of CRLH TLs: Resonator-Loaded Lines

Soon after implementation of CRLH TLs based on CL-loaded lines, a second approach for the implementation of CRLH TLs was presented. In this approach, a host TL is loaded with different types of electrically small resonators to obtain the CRLH behavior, thus the method is known as resonant-type approach. Different types of resonators can be used to obtain CRLH or dual-CRLH TLs. Since the focus of this thesis is mostly on the resonant-type metamaterial TLs, it is useful to review the structures and equivalent circuit models of some of the major types of metamaterial resonators. Split ring resonators (SRRs) and complementary split ring resonators (CSRR), which are the most well-known metamaterial particles, can be used for the implementation of conventional CRLH TLs, while open split ring resonators (OSRRs) and open complementary split ring resonators (OCSRRs), which have been recently introduced, are generally used for the implementation of dual-CRLH TLs.

2.7.1 Split Ring Resonator (SRR)

Fig. 2.18(a) depicts an illustration of a split ring resonator (SRR), which consists of two concentric metallic rings with two slits etched in opposite sides of the rings. This metamaterial particle was first introduced by Pendry *et al.* (1999) for the synthesis of bulk artificial media with negative effective permeability. An axial time-varying magnetic field (parallel to z axis in the figure) can induce electric currents to flow in the split rings. Since the rings have slits in opposite sides, the induced currents are forced to transform to displacement currents and flow across the inter-ring slots from one ring to another. Thus, as shown in Fig. 2.18(b), the SRR can be modeled near resonance with an LC resonator composed of an equivalent inductor L_s, which models the inductive behavior of the SRR's metallic rings, and an equivalent capacitor C_s, which represents the distributed capacitances between the two split rings (Marqués *et al.* 2002). The equivalent inductance can be calculated from the inductance of a ring of radius r_0 and width c, where r_0 is the mean radius of the SRR's rings and c is the width of the metallic rings (Marqués *et al.* 2002). The SRR's total equivalent capacitance is the series connection of the equivalent capacitances of both halves of the SRR. Thus, $C_s = C_0/2 \parallel C_0/2 = C_0/4$, where C_0 is the total capacitance between the two rings, which can be approximated from the per-unit-length capacitance C_{pul} of two parallel strips of width c and space d as $C_0 = 2\pi r C_{\text{pul}}$. There are some other methods of calculating the

values of the SRR's equivalent inductance and capacitance (Marqués *et al.* 2003, Shamonin *et al.* 2005, Baena *et al.* 2005), however, they all lead to the similar results.

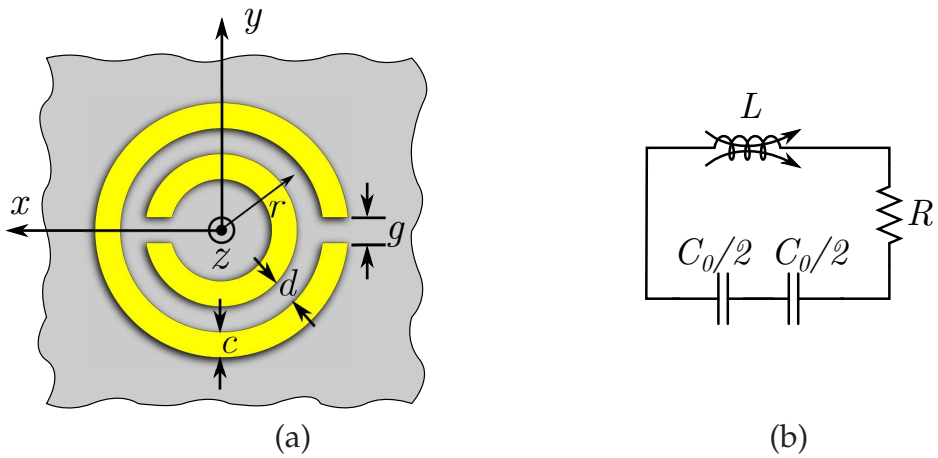

Figure 2.18. SRR structure and circuit model. (a) The structure of a split ring resonator (SRR), which consists of two concentric metallic rings with two slits etched in opposite sides of the rings, and (b) the SRR's equivalent circuit model.

Based on the SRR's equivalent circuit model the resonance frequency ω_0 of an SRR can be obtained from

$$\omega_0 = \frac{1}{\sqrt{L_s C_s}}. \tag{2.46}$$

Note that due to the relatively large value of the equivalent capacitance, the SRRs generally have a very small electrical size. It was shown by Pendry *et al.* (1999) that effective permeability of a medium loaded with an array of SRRs is given by:

$$\mu = 1 - \frac{F\omega^2}{\omega^2 - \omega_0^2}, \tag{2.47}$$

where F is the fractional area of the unit cell occupied by the SRR, and ω_0 is the resonance frequency of the SRR. The equation shows that the effective permeability of such media is frequency dependent and for a certain frequency range becomes negative. These two characteristics of the SRR, i.e., small electrical size and negative effective permeability, are the important features of this particle that opened doors to the realization of first double negative medium (Smith *et al.* 2000).

Beside the application of SRRs in the synthesis of different types of bulk metamaterials with engineered electromagnetic properties, these resonators have been also used in the design of one- and two- dimensional metamaterial TLs. Fig. 2.19(a) illustrates

the layout of a typical configuration of an SRR-based metamaterial TL in CPW technology. The structure consists of a CPW that is loaded with pairs of SRRs etched on the back side of the CPWs substrate, with the center of the rings symmetrically located underneath the two slots of the CPW. In this configuration, the CPWs axial magnetic field is induced in the inner region of the SRRs and excite the SRRs. Thus, as shown in Fig. 2.19(b) electromagnetic wave propagation along the CPW is inhibited in a narrow band in the vicinity of the SRRs resonance frequency (Martín *et al.* 2003b, Martín *et al.* 2003a).

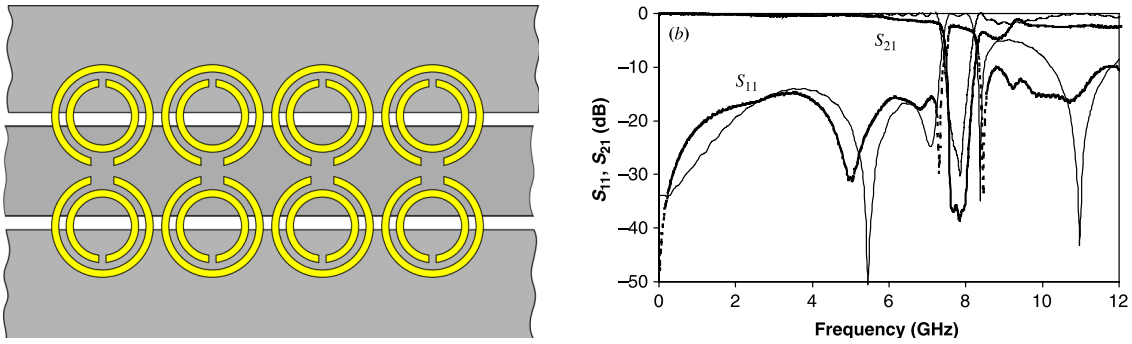

(a) (b)

Figure 2.19. SRR-based metamaterial TL in CPW technology. (a) The layout of a typical configuration of an SRR-based metamaterial TL in CPW technology. The structure consists of a CPW that is loaded with pairs of SRRs etched on the back side of the CPWs substrate, with the center of the rings symmetrically located underneath the two slots of the CPW. (b) Simulated and measured transmission and reflection coefficints of the structure. Electromagnetic wave propagation along the CPW is inhibited in a narrow band in the vicinity of the SRRs resonance frequency. After Martín *et al.* (2003b).

Metamaterial TLs with negative effective permeability can also be synthesized in microstrip technology by loading a microstrip line with pairs of SRRs that are etched on the same layer as the microstrip line. Fig. 2.20(a) shows an illustration of a typical configuration of SRR-loaded microstrip line in which square-shaped SRRs are used to achieve a high magnetic coupling between the line and the SRRs (García-García *et al.* 2005a, Gil *et al.* 2005). Fig. 2.20(b) depicts a bandgap in the measured transmission coefficient of the structure in the vicinity of the SRRs resonance frequency.

The stopband in the transmission coefficient of the SRR-loaded lines, in both CPW and microstrip technologies, can be interpreted as the spectrum where the SRR-loaded

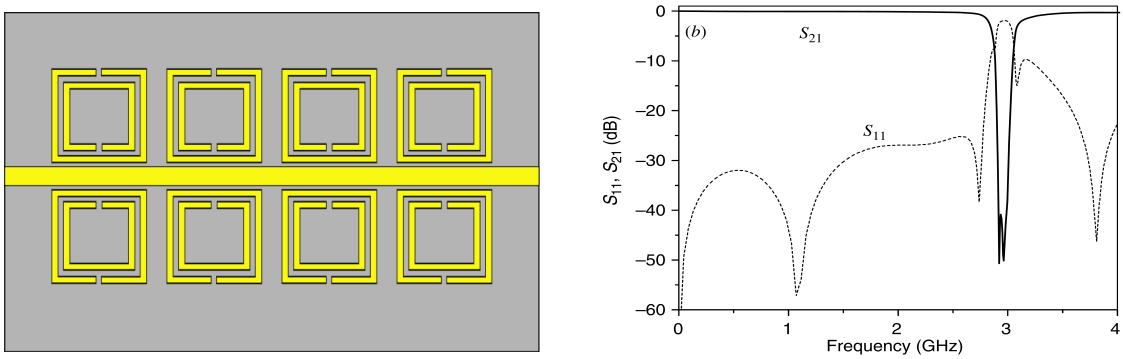

(a) (b)

Figure 2.20. SRR-based metamaterial TL in microstrip technology. (a) Layout of an SRR-loaded microstrip line, and (b) measured transmission and reflection coefficients of the structure. After Marqués *et al.* (2008).

transmission line behaves as a single-negative one-dimensional medium, i.e. with negative effective permeability. It has been shown in (Martín *et al.* 2003a, Falcone *et al.* 2004c, Bonache *et al.* 2004) that this bandstop behavior can be switched to a bandpass behavior simply by introducing inductive shunt elements to the TL structure. Fig. 2.21(a) shows the layout of such TL in CPW technology. The structure is identical to the single negative TL of Fig. 2.19(a) where a CPW is loaded with SRRs that are etched on the back side of the CPW's substrate, except that signal-to-ground inductive strips are located above the SRRs. These shunt-connected inductive strips cause the medium to act as a negative-permittivity medium up to a frequency, namely a cutoff frequency f_c known as plasma frequency. Thus, if this cutoff frequency is set to occur above the resonance frequency of the SRRs, a frequency region (above the resonance of the SRRs) exist where both effective permeability and effective permittivity are negative. Thus, as shown by the simulated and measured frequency response of the structure in Fig. 2.21(b) a backward electromagnetic wave propagation is allowed in this band. As shown in Fig. 2.22 a similar left-handed bandpass behavior can be achieved in microstrip technology by introducing shunt-connected inductive metallic vias to the structure of the SRR-loaded microstrip line of Fig. 2.20.

2.7.2 Complementary Split Ring Resonator (CSRR)

Based on the concept of duality (Booker 1946), the complementary counterparts of a planar metallic structure is obtained by replacing the metallic parts of the structure

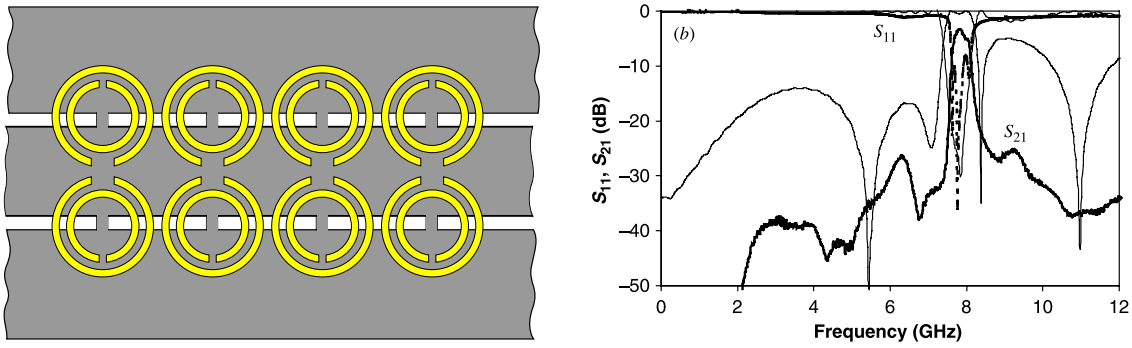

(a) (b)

Figure 2.21. CRLH TL in CPW technology. (a) Layout of an SRR/strip-loaded CPW. The structure is identical to the single negative TL of Fig. 2.19(a) where CPW is loaded with SRRs that are etched on the back side of the CPW's substrate, except that signal-to-ground inductive strips are located above the SRRs. (b) Frequency response of the structure. After Martín *et al.* (2003a).

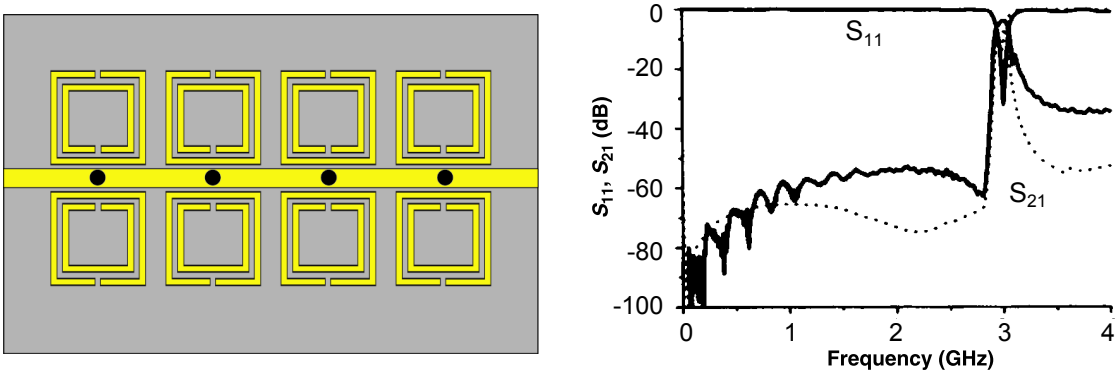

(a) (b)

Figure 2.22. CRLH TL in microstrip technology. (a) Layout of an SRR/via-loaded microstrip line, and (b) the structure's frequency response. The passband in the transmission coefficient of the structure corresponds to the frequency region where both effective permittivity and effective permeability of the structure are negative.

with slots, and vice versa (Booker 1946, Deschamps 1959, Getsinger 1983). Thus, as illustrated in Fig. 2.23(a), a complementary split ring resonator (CSRR) can be considered as a negative image of an SRR in a metallic plane (Falcone *et al.* 2004a). While the SRRs can be essentially (although not exclusively) excited by an axial magnetic field to achieve negative effective permeability in a frequency band close to their resonance frequency, the CSRRs can essentially be driven by time varying axial electric fields, as expected from duality, to obtain negative values of effective permittivity. Fig. 2.23(b)

depicts the equivalent circuit model of a CSRR, which is the dual of the SRR's equivalent circuit model. In this model, the SRR's inductance L_s is substituted with CSRR's equivalent capacitance C_c, and the series connected capacitors $C_0/2$ of the SRR's circuit model are replaced with parallel combination of two inductors $L_0/2$. Considering the average radius of the CSRR's slot rings r_0 and the slots' width c, the value of the CSRR's equivalent capacitance C_c can be obtained from the capacitance of a metallic disk of radius $r_0 - c/2$ that is separated with a slot of width c from the surrounding ground plane. Also, the inductance $L_0/2$ of each of the two strips that connect the inner disk to the ground plane can be obtained from $L_0 = 2\pi r_0 L_{\text{pul}}$, where L_{pul} is the per-unit-length inductance of a CPW line with same dimensions as the connecting strips (Marqués *et al.* 2002, Baena *et al.* 2005). Thus, the CSRR's resonance frequency is given by $\omega_0 = 1/\sqrt{L_c C_c}$, where $L_c = L_0/4$.

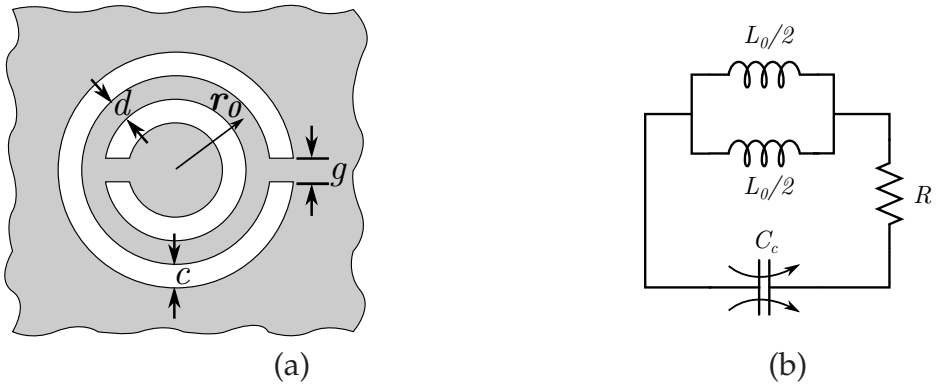

Figure 2.23. CSRR structure and circuit model. (a) The structure of a CSRR, which is the complementary counterpart of an SRR, and (b) the CSRR's equivalent circuit model.

Similarly to the SRRs, beyond applications in the implementation of bulk metamaterials with negative effective permittivity, CSRRs can be also used for the synthesis of planar one- and two-dimensional TLs with engineered properties. Since CSRRs need to be etched in a metallic plane and excited by an axial electric field, the natural (although not exclusive) host TL for the CSRRs is in microstrip technology, where a metallic ground plane and normal electric field are readily available. Fig. 2.24(a) depicts an illustration of a microstrip line which is loaded with four CSRRs that are etched in the microstrip ground plane. As expected from the duality theorem, and shown in Fig. 2.24(b), due to the negative effective permittivity of the structure, propagation of electromagnetic waves is inhibited in a frequency region in the vicinity of the CSRR's resonance frequency.

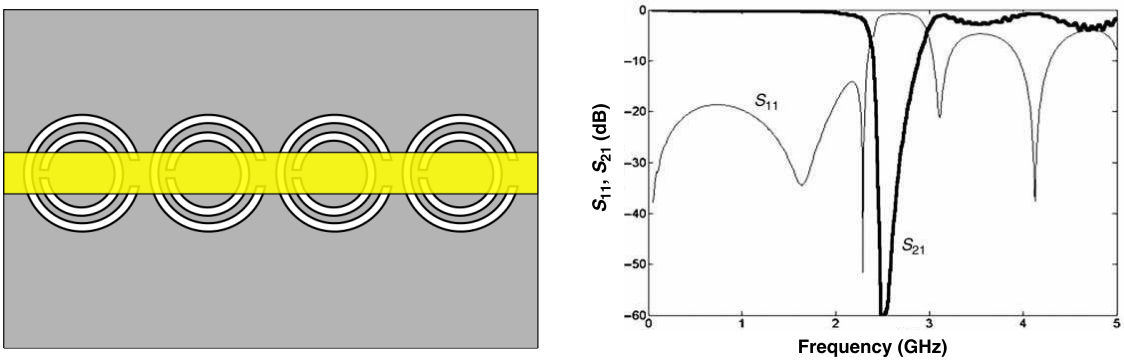

(a) (b)

Figure 2.24. CSRR-loaded microstrip line. (a) Layout of a microstrip line which is loaded with four CSRRs that are etched in the ground plane, and (b) typical frequency response of the structure; from (Falcone *et al.* 2004a). The stopband corresponds to the frequency region where the structure acts as a one-dimensional medium with negative effective permittivity.

This bandstop behavior can be switched to a bandpass behavior by introducing a series capacitive element to the host TL, as shown in Fig. 2.25(a). This series capacitive element provides a negative effective permeability up to a cutoff frequency f_c, which is known as magnetic plasma frequency. This cutoff frequency depends on the resonator formed by the series capacitive element and series inductance of the host TL, and as long as it is above the resonance frequency of the CSRRs, a narrow frequency region exists where both effective permeability and effective permittivity are simultaneously negative. Thus, as depicted in Fig. 2.25(b) the structure acts as a left-handed medium that allows a backward propagation of electromagnetic waves.

2.7.3 Open Split Ring Resonator (OSRR)

Open split ring resonator (OSRR), which is an open version of SRR was first proposed by Martel *et al.* (2004). As shown in the illustration of Fig. 2.26(a), unlike SRR that need to be magnetically (or electrically) coupled to a TL, the OSRR has two terminals for excitation by a voltage or a current source. Thus, as depicted in Fig. 2.26(b), the resonator can be modeled with a series LC resonant tank, where the equivalent inductance L_s is equal to that of an SRR with the same dimensions, and the OSRR's equivalent capacitance C_0 is the distributed capacitance between the two metallic hooks (Martel *et al.* 2004). Note that the equivalent capacitance of the OSRR is four times larger than that

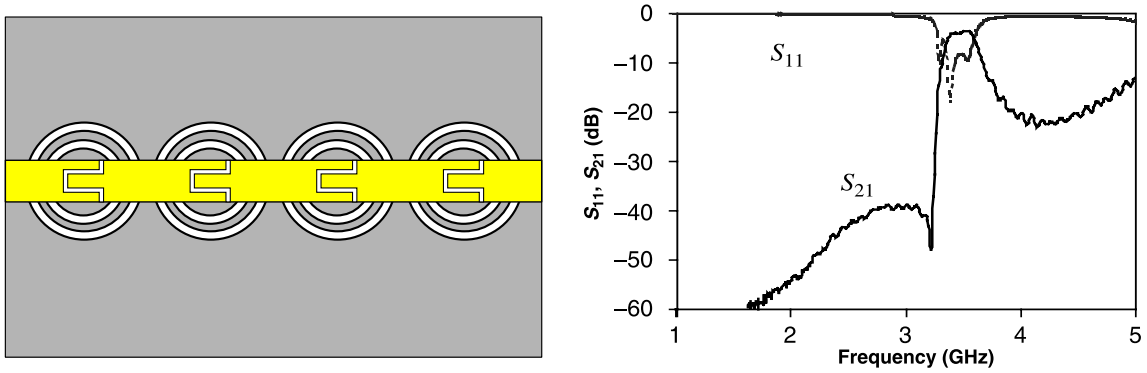

(a) (b)

Figure 2.25. CSRR/gap-loaded microstrip line. (a) Layout of a CSRR/gap-loaded microstrip line, and (b) typical frequency response of the structure. After Gil *et al.* (2006).

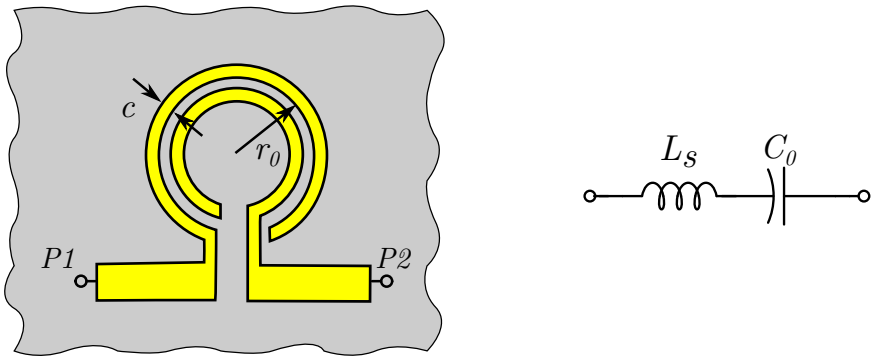

(a) (b)

Figure 2.26. OSRR structure and its circuit model. (a) The structure of an OSRR, which is the open version of an SRR, and (b) the OSRR's equivalent circuit model.

of an SRR with the same dimensions. Thus, the resonance frequency and consequently the electrical size of an OSRR is half of those of an SRR with the same physical dimensions.

2.7.4 Open Complementary Split Ring Resonator (OCSRR)

In the same way that the CSRR is the complementary counterpart of the SRR, the duality principle can be used to derive the dual counterpart of the OSRR, i.e., the open complementary split ring resonator (OCSRR) (Velez *et al.* 2009, Duran-Sindreu *et al.* 2009). Fig. 2.27(a) illustrates the typical layout of the OCSRR. As indicated in the figure, the

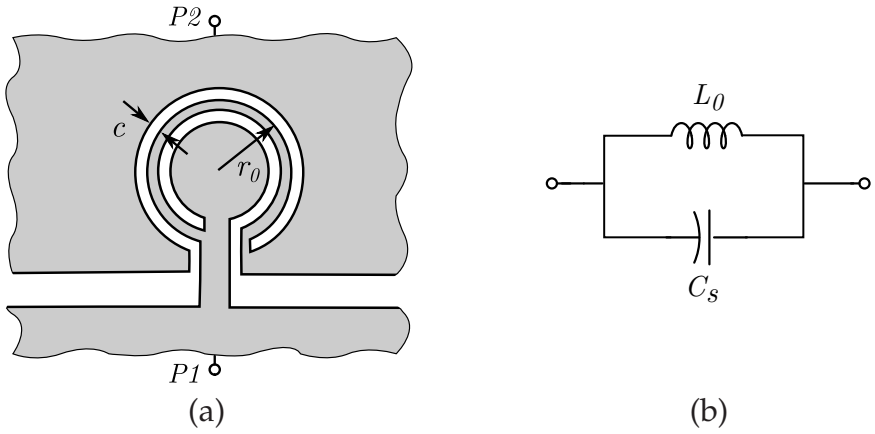

Figure 2.27. OCSRR structure and its circuit model. (a) The structure of an OCSRR, which is the complementary counterparts of an OSRR, and (b) the OCSRR's equivalent circuit model.

structure has two terminals that are connected with a metallic strip that can be modeled with its equivalent inductance L_0. The two terminals are also coupled through the capacitance of the metallic disk of radius $r_0 - c/2$ (r_0 being the average radius of the OCSRR slot rings) which is separated by a slot of width c from the surrounding ground plane. Thus, the resonator can be modeled with the parallel LC tank of Figs. 2.27(b). Note that the equivalent inductance of an OCSRR is L_0, while that of a CSRR is four times smaller, i.e. $L_0/4$. Thus, the resonance frequency and consequently the electrical size of an OCSRR is half of a CSRR with the same physical dimensions.

2.8 Summary

From the unit cell point of view, metamaterials can be classified in two general categories: Electromagnetic bandgap (EBG) structures, and effective media. Since all the structures proposed in this thesis fall into the category of effective media, this chapter has predominantly reviewed this category, which consists of metamaterials whose unit cells dimensions are much smaller that the operating wavelength. In order to achieve a general intuition for the concept of metamaterials, electrodynamics of effective media have been discussed, with focus on the left-handed metamaterials.

Using the equivalence between the parameters of transmission lines and effective media, it has been shown that the concept of metamaterials can be used to implement one-dimensional artificial TLs. As two important tools, the dispersion diagram and

Bloch impedance have been used to analyze the behavior of the artificial TLs. Finally different methods of implementation of artificial TLs have been discussed: Since this thesis is mostly focused on the application of metamaterial resonators in planar technologies, the most important types of metamaterial resonators and their equivalent circuit models have been reviewed.

The chapter has provided the required fundamental knowledge for the following chapters of the thesis. Based on this fundamental understanding of the electrodynamics of metamaterials and their implementation methods in planar technologies, several metamaterial-inspired structures are presented in the following chapters of the thesis.

Chapter 3

High Quality Factor Coplanar Strips Resonators for CMOS MMICs

IN recent times, continuing technological improvement has started enabling low-cost silicon technology to operate at millimeter-wave frequencies. High carrier frequencies allow higher bandwidths to be realized for increased throughput or for an increased number of users sharing the spectrum. Voltage controlled oscillators (VCOs) are one of the main building blocks of any communication system for upconversion of data from baseband to the transmitter RF band and downconversion from RF to the receiver baseband. Design of CMOS millimeter-wave VCOs, however involves a complex set of tradeoffs between DC power consumption, on-chip area, tuning range, phase noise, and output power. Among these factors, reducing the VCO phase noise and on-chip area are of great importance for most applications. It is well known that increasing the quality factor of the VCO's resonator is the most efficient method of decreasing the phase noise in a VCO. Therefore, this chapter is focused on the application of metamaterial transmission lines to the design of high quality factor quarter-wavelength balanced resonators for 60 GHz CMOS VCOs. We also show that the proposed resonators benefit from a high level of miniaturization, which is a favorable feature for on-chip MMICs.

3.1 Millimeter-Wave Silicon CMOS Technology

Our world is becoming more and more dependent on the digital multimedia devices such as high-definition video systems, digital cameras, portable audio/video players and compact devices for data and multimedia storage. As the number of such high-quality multimedia devices and the volume of data to be transfered are increasing there is a stronger demand for multi-gigabit/second data rate links. High speed cables are today's reliable and moderate-cost industry standard for such high speed data transfers. Compared to the wired data transfer systems, wireless systems are generally preferred due to the ease of setup, lower cost and possibility of application in mobile systems. However, it can be shown that the bandwidth of today's commercially available wireless systems operating at low GHz frequencies has a theoretical upper bound on the information rate that cannot provide such a multi-gigabit/sec transfer rate. Based on the Shannon's theorem, the capacity of a channel C (in bits/s) with additive white Gaussian noise can be obtained from (Shannon 1949)

$$C = B \log_2 \left(1 + \frac{S}{N}\right), \tag{3.1}$$

where B is the channel bandwidth in Hertz and S and N are the average power of the received signal and noise over the bandwidth in Watts, respectively. The theorem clearly shows that a large bandwidth and a large signal power is required for a channel to provide the desired multi-gigabit/sec information rates.

3.1.1 60 GHz Unlicensed Band

In December 1995, Federal Communication Commission (FCC) allocated a 5 GHz band for unlicensed applications in the millimeter-wave regime at around 60 GHz. Later on, this unlicensed band was extended to 7 GHz (57 – 64 GHz) (Van Tuyl 1996). As depicted in Fig. 3.1 in many other countries, including Australia, similar frequency bands have been allocated for high data rate unlicensed communications at millimeter-wave frequencies.

Because of a strong attenuation caused by the resonance of oxygen molecules close to 60 GHz, this band is in principle not suitable for long-range wireless communication (order of a few kilometers). However, a positive aspect of this range limitation is that the spectrum can be reused by multiple systems within close proximity of one

Table 3.1. License-free wireless communication bands. A comparison between different features of some of the license-free wireless communication bands, currently in use, and those of 60 GHz band.

	802.11b	Bluetooth	802.11a	UWB	60 GHz
Cell radius (m)	100	10	50	10	10
Information rate per channel (Mbps)	11	1	54	50	500
Number of channels	3	10	12	6	10
Capacity (Mbps/m^2)	0.001	0.03	0.1	1	16

another. Furthermore, in addition to the larger available bandwidth at higher frequencies that results in higher capacity in data communication, one other advantage of using millimeter-wave frequencies is the small required antenna size and spacing in multiple-antenna systems, which contribute to making the systems more compact and potentially affordable (Niknejad and Hashemi 2008).

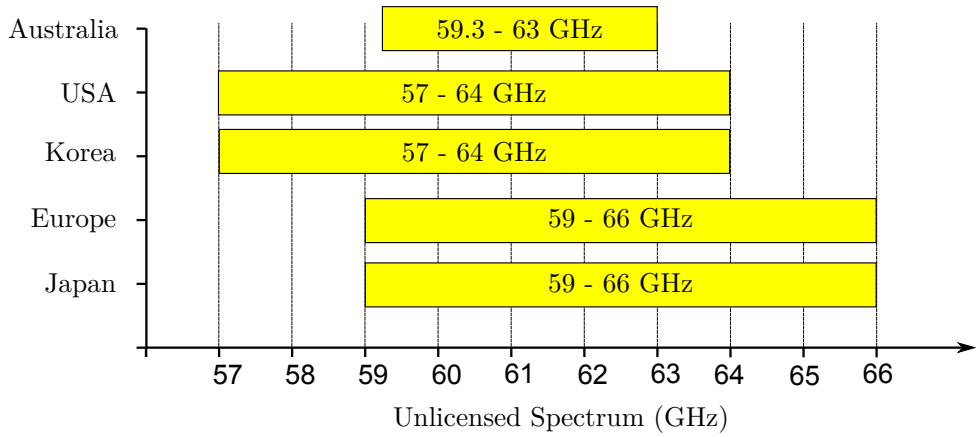

Figure 3.1. Unlicensed 60 GHz bandwidth regulation in different countries. In many countries including Australia an ultrawide band has been allocated for high data rate unlicensed communications at millimeter-wave frequencies around 60 GHz.

The allocation of 7 GHz (54 – 60 GHz) bandwidth for the next generation of license-free communication devices provides an unprecedented information transfer rate. Such a high data rate is far beyond the capacity of previously used bands at low GHz frequencies (Howarth *et al.* 2005, Smulders 2003). Table 3.1 provides a comparison between different features for some of the currently in use license-free wireless communication bands versus those in the 60 GHz band.

3.1.2 Voltage Controlled Oscillators in Silicon CMOS Technology

Monolithic microwave integrated circuits (MMICs) are usually designed using III-V semiconductor technologies, such as GaAs, due to their higher electron mobility, higher breakdown voltage, and the availability of high quality factor passive components on chip. In contrast, silicon technology suffers from a standard low-resistivity substrate ($\sim 10-20\ \Omega\cdot$cm), compared to the typical GaAs substrate resistivity ($\sim 10^7-10^9\ \Omega\cdot$cm). Despite the drawbacks associated with the use of low-resistivity silicon substrates, silicon CMOS technology, offers high level of integration at low cost. Furthermore, a direct benefit of using this technology is the exploitation of rapid technology scaling (Doan *et al.* 2005). Moreover, with the scaling of the CMOS transistors to sub-100 nm dimensions, the intrinsic frequency has increased dramatically, making this technology very attractive for the design of circuits operating at microwave and millimeter-wave frequencies. This has assisted with increased market demand for low-cost electronics that operate in the license-free band at 60 GHz (Doan *et al.* 2004, Lai *et al.* 2006).

One of the essential building blocks of almost any wireless communication system, including millimeter-wave communication systems, are VCOs. As shown in the generic communication system block diagram of Fig. 3.2, a high frequency local signal is needed for up-conversion of data signals on the transmitter side. Correspondingly, at least one local oscillator is necessary on the receiver side for down-conversion of the RF received signal (two local signals in heterodyne receivers). Note that VCOs are also the core component of phase locked loop systems and generally have great influence on the performance of PLLs and transceivers.

3.1.3 Chapter Objective and Framework

Despite significant improvements of VCOs in silicon RF technologies in the last two decades, high performance oscillator design in millimeter-wave frequencies is still a challenge even in today's nanometer silicon technologies (Niknejad and Hashemi 2008). As will be shown in the next section, this is mainly due to the conductive loss in the silicon substrate, which in turn results in the poor quality factor of the VCO's resonator in this technology.

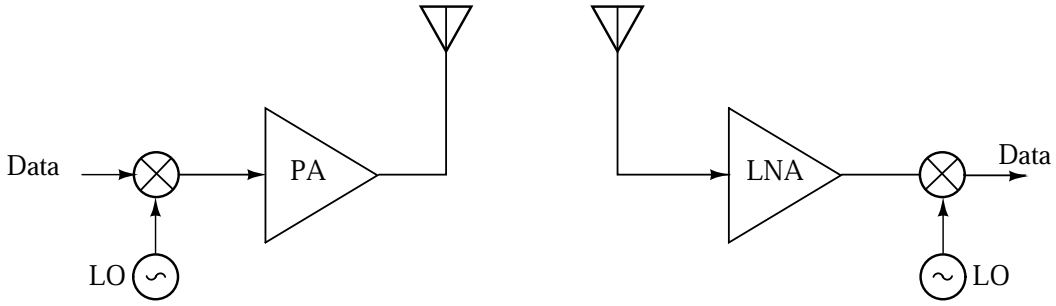

(a) Transmitter (b) Receiver

Figure 3.2. Oscillator in transmitter and receiver. Note that VCOs are one of the essential building blocks of almost any wireless communication systems. For the transmitter, a high frequency local oscillator signal is needed for up-conversion of data signals, while for the receiver at least one local oscillator is necessary for down-conversion of the RF received signal.

To address this issue, this chapter provides a study on the design of balanced metamaterial transmission lines as high-quality-factor resonators for the realization of low-phase-noise VCOs in CMOS technology. To this end, a short introduction to the concept of phase noise is first provided in Section 3.2, with emphasis on its importance and the most effective methods of reducing it. Application of TL resonators, instead of *LC* tanks, is then discussed in Section 3.3. In Section 3.4, a comprehensive parametric study, on the geometrical dimensions of a slow-wave CPS structure in a standard 90 nm CMOS process is conducted based on 3D electromagnetic simulations. This leads to the derivation of guidelines for the design of slow-wave CPS resonators with high quality factor, small on-chip area and a desired characteristic impedance. Then, using the extracted guidelines, a high quality factor slow-wave CPS resonator is designed. Since this work aimed to the design of slow-wave CPS for MMICs, all the simulations are conducted in the millimeter-wave band at 60 GHz.

As an alternative application to the implementation of low phase noise VCOs, Section 3.5 is focused on the characterization of the complex permittivity of thin films of dielectrics, based on the resonance properties of the previously proposed slow-wave CPS resonator. It is shown in Section 3.5 that permittivity and loss tangent of an unknown thin film at millimeter-wave frequencies can be accurately determined using the resonant frequency and the quality factor of the resonator. The method is validated by characterizing a silicon dioxide layer in a standard CMOS process as the thin film under test.

In order to address the need for balanced resonators with higher quality factors, this chapter proposes two other metamaterial-inspired quarter-wavelength resonators for operation at 60 GHz. In Section 3.6, based on the split ring resonator's (SRR) rejection and phase shift properties in the vicinity of its resonance, a high quality factor $\lambda/4$ composite right/left handed (CRLH) CPS resonator is designed. Seeking even a higher quality factor, Section 3.7 is focused on the improvement of the quality factor of the quarter-wavelength slow-wave CPS resonator through the optimization of the structure's layout based on the standing wave profile of the current and voltage along the resonator. Section 3.7 presents an optimization process for a quarter wavelength slow-wave CPS resonator with a maximum quality factor at 60 GHz. Finally, the conclusions of the research are highlighted in Section 3.8.

3.2 Phase Noise of Voltage Controlled Oscillators

The output signal of a VCO can be ideally described as:

$$V_{\text{out}}(t) = V_0 \cos(2\pi f_c t + \phi), \tag{3.2}$$

where ϕ is a fixed phase. As shown in Fig. 3.3, this signal is represented in the frequency domain by a delta function located at f_c.

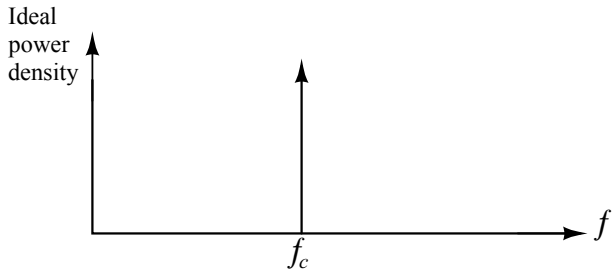

Figure 3.3. Output voltage of an ideal VCO. In the frequency domain, the output voltage of an ideal VCO is represented by a delta function located at f_c.

Any practical oscillator, however, has fluctuations in its amplitude and frequency due to noise and interference sources such as shot and flicker noise or substrate and supply noise (Hajimiri and Lee 1999). Since variation in the oscillation frequency is the most relevant in VCOs, let us assume that the amplitude of oscillation is constant. Thus, the output voltage can be represented as:

$$V_{\text{out}}(t) = V_0 \cos(2\pi f_c t + \phi(t)), \tag{3.3}$$

where $\phi(t)$ is a small random excess phase representing variation in the frequency, or period in time domain (Razavi 1998). In the time domain, thus, this fluctuation can be seen as a random perturbation of zero crossing of the periodic signal, which is called "jitter" (see Fig.3.4(a)). In the frequency domain, however, these fluctuations create side bands close to the frequency of oscillation, f_c, as illustrated in Fig. 3.4(b). These side bands are called phase noise side bands. They are usually characterized by the single side band noise spectral density normalized to the carrier signal power. This can be expressed at a certain offset from the central frequency $\Delta\omega$ as (Kinget 1999)

$$\mathcal{L}(\Delta\omega) = \frac{\text{noise power in 1 Hz BW at } (\omega_0 + \Delta\omega)}{\text{total carrier power}} \tag{3.4}$$

or in the units of decibels below the carrier per Hertz (dBc/Hz) as

$$\mathcal{L}(\Delta\omega) = 10\log\left[\frac{P_{\text{sideband}}(\omega_0 + \Delta\omega)}{P_{\text{carrier}}}\right]. \tag{3.5}$$

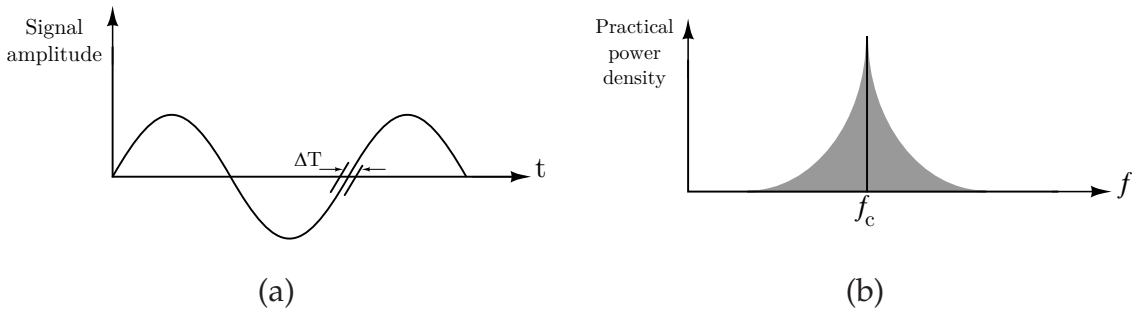

Figure 3.4. Jitter and phase noise of an oscillator. Representation of variations in the frequency of oscillation in (a) time domain, and (b) frequency domain.

3.2.1 Importance of Phase Noise

To understand the importance of the phase noise, let us consider Fig. 3.5 that depicts the effect of phase noise in the local oscillator signal used for downconversion in a receiver. We further assume the presence of an undesirable signal with large power in an adjacent channel to the desired signal. After mixing with the local oscillator output, the down-converted spectrum consists of two overlapping spectra. As illustrated in the figure, the desired signal can be overlapped and corrupted by the down-converted adjacent signal due to the side bands of the local oscillator output (Hajimiri and Lee

1999, Tiebout *et al.* 2006). The same problem exists in the upconversion process in the transmitter.

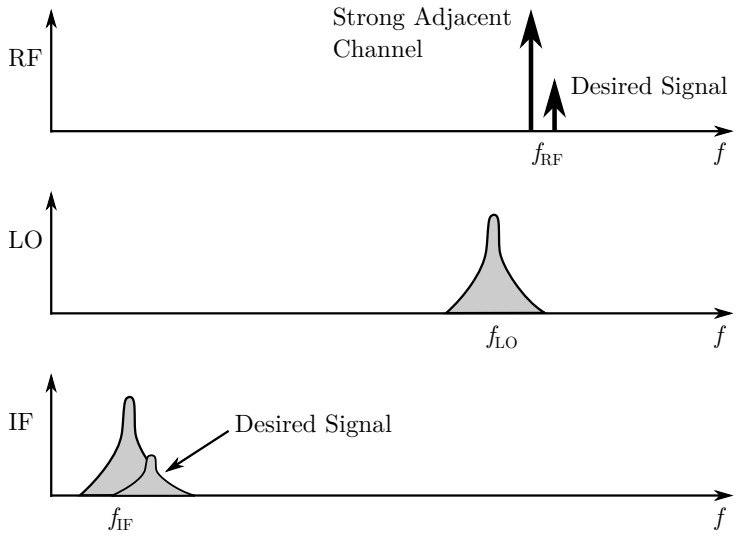

Figure 3.5. Effect of phase noise in a reciever. The presence of phase noise sidebands in the local oscillator signal in a receiver results in sidebands in the downconverted signals. Thus, a desired signal can suffer from the sidebands of the down-converted adjacent signals. After Hajimiri and Lee (1999).

3.2.2 Effect of Resonator Quality Factor on the Phase Noise

The performance of various VCOs is difficult to compare for different central frequency, output power, power consumption and phase noise. Therefor, to compare VCOs, a figure of merit (FOM) definition is required. A widely accepted FOM for VCOs has been introduced by Kinget (1999) as

$$\text{FOM} = \mathcal{L}(\omega_0 + \Delta\omega) + 10\log\left[\left(\frac{\omega_0}{\Delta\omega}\right)^2 \frac{P_{\text{supply}}}{[\text{mW}]}\right]. \tag{3.6}$$

The first term in the right hand side of the equation is the phase noise of the VCO at the offset frequency Δf from the carrier frequency. A better VCO has a negative FOM with a higher absolute value. Thus, to have a VCO with a high (negative) FOM, the VCO phase noise need to be minimized.

Based on Leeson's (1966) mathematical model the phase noise of a VCO is a function of the known or expected noise, signal level, and resonator characteristics according to

$$\mathcal{L}(\Delta\omega) = 10\,\log\left[\frac{2FKT}{P_s}[1 + (\frac{\omega_0}{2Q_L\Delta\omega})^2](1 + \frac{\omega_{1/f^3}}{|\Delta\omega|})\right], \tag{3.7}$$

where Q_L is the loaded quality factor of the resonator, $\Delta\omega$ is the offset frequency and F is an empirical parameter. This expression can be rewritten after some approximation for $\Delta\omega \ll \omega_0$ as

$$\mathcal{L} = 10 \log \left[\frac{2FKT}{P_{\text{sig}}} \cdot \left(\frac{\omega_0}{2Q_L \Delta\omega} \right)^2 \right]. \tag{3.8}$$

From this expression, it can be seen that increasing the output power P_{sig} or using a resonator with a higher quality factor reduces the phase noise. However, increasing the output power results in a higher power consumption. Thus, using a high quality factor resonator is the most efficient method of reducing the VCO's phase noise.

3.3 TL Resonators at Millimeter-Wave Frequencies

The most common resonators in VCOs are LC tanks, and accordingly different methods for improving their quality factor have been proposed in literature (Razavi 1997, Razavi 1998, Niknejad and Meyer 1998, Niknejad and Meyer 2000, Tiebout *et al.* 2002, Tiebout *et al.* 2006). However, at high frequencies in the millimeter-wave band, the size of these lumped elements becomes an appreciable fraction of wavelength. Thus, for these high frequencies, their distributed behavior needs to be considered. Alternatively, TL resonators can be used at these high frequencies, because they explicitly take into account distributed behavior. Furthermore, due to the relatively small wavelength, significantly long structures like quarter-wavelength TLs have reasonable size for on chip realization (Niknejad and Hashemi 2008). Another advantage of the quarter-wavelength resonators is that they are inherently scalable in length, allowing for the realization of precise values of small reactances (Niknejad and Hashemi 2008). Among the various commonly used TLs, coplanar strips (CPS) are amenable to a high level of integration and as a balanced structure, they provide a favorable basis for the realization of VCOs (Arif and Peroulis 2009). Furthermore, CPS have both their signal and ground paths on the same layer (Gupta *et al.* 1996). Consequently, the physical gap between signal and ground paths is not dictated by the thickness of the inter-metal dielectrics of the CMOS process. Thus, in contrast to the microstrip lines, implementation of a desired characteristic impedance with moderate resistive loss is possible even on thin and high-permittivity substrates such as those common in silicon technology by keeping both signal and ground strips relatively wide (Yang *et al.* 2009). As shown in Fig. 3.6, a short ended $\lambda/4$ CPS can be used as a balanced resonator, instead of a classical LC tank, for the realization of a cross-coupled VCO.

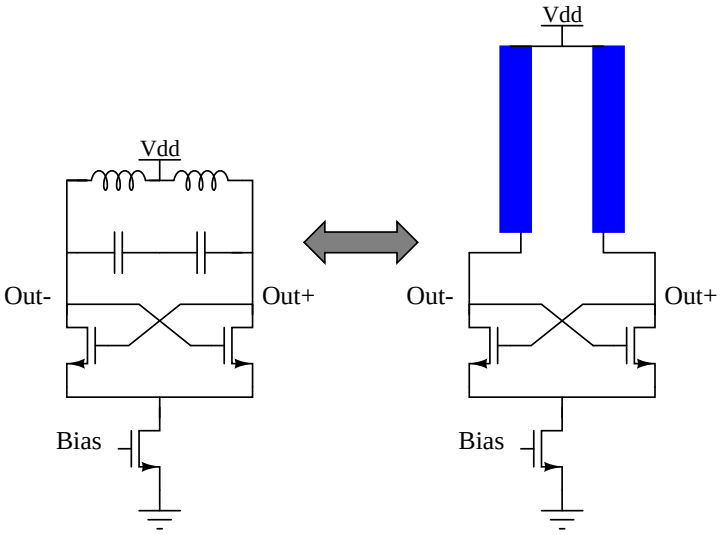

Figure 3.6. LC- versus TL-based Oscillator. Due to relatively small wavelength at millimeter-wave frequencies, quarter-wavelength TLs can be realized on chip. Thus, a quarter-wavelength short-circuited CPS can be used, instead of an LC tank, in the monolithic integrated VCOs in the millimeter-wave regime.

3.3.1 Slow-Wave Coplanar Strips

Although coplanar TLs such as CPS have the advantage of low resistive losses, they typically suffer from substrate conductive loss. More specifically this conductive loss is mainly due to the penetration of the electric field of the CPS into the low resistivity silicon substrate (Reyes *et al.* 1994). One solution to reduce the penetration of the electric field into the lossy substrate, is to place a solid metal shield under the CPS (Kleveland *et al.* 2001). However, this approach is not a suitable solution because the solid metal shield removes the substrate losses by preventing the electric field from penetrating into the lossy substrate, but it adds another type of loss due to the eddy currents flowing in the solid metal shield (Kleveland *et al.* 2001, Kaddour *et al.* 2009).

An effective solution to this problem is to shield the CPS with an array of closely spaced narrow floating metallic strips. Figure 3.7 shows an illustration of such structure, which is composed of a CPS and an array of floating metallic strips that are separated with a thin dielectric layer. In contrast to the solid metal shield, if the floating strips are narrow enough, eddy current loss is negligible. Therefore, the shield efficiently reduces the substrate losses and it does not add a considerable eddy current loss (Cheung and Long 2006). This is known as a slow-wave structure because the TL loaded with the array of floating strips can be considered as a one-dimensional metamaterial medium

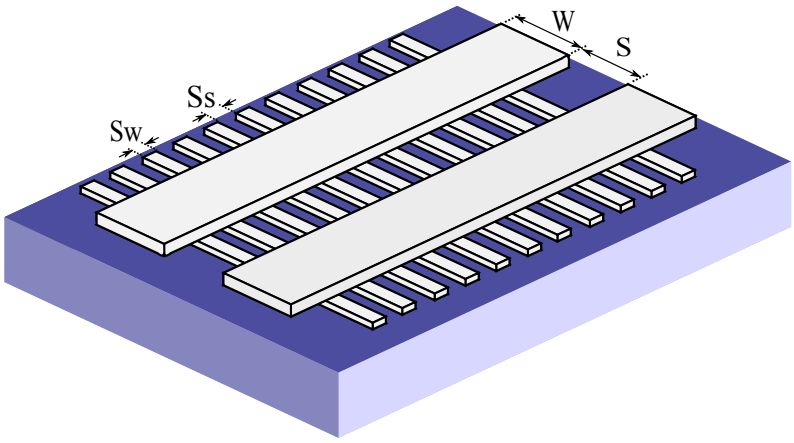

Figure 3.7. 3D view of a slow-wave CPS. Three-dimenesional view of a slow-wave CPS that is composed of a CPS and an array of the floating metallic strips, which are separated with a thin layer of dielectric. The floating metallic strips prevent the electric field from penetration into the lossy silicon substrate.

with effective relative permittivity that is much higher than the relative permittivity of the constitutive dielectrics, resulting in the reduced velocity of propagation of the guided electromagnetic waves in the medium.

From the equivalent circuit point of view, in a conventional CPS, inductance per unit length L and capacitance per unit length C of the TL are dependent on each other , thus, increasing one, decreases the other. For example increasing the spacing between signal and ground strips of a CPS increases the inductance per unit length, which results in a decrease in the capacitance per unit length of the line. As a result, reducing the electromagnetic wave velocity is only dependent on the effective dielectric constant of the surrounding media (Cheung and Long 2006). Slow-wave transmission line structures in contrast, are essentially structures with spatially separated electric and magnetic energy storage. Thus, in these structures it is possible to increase L and C simultaneously and as a result reduce the propagation velocity of the guided waves (Gorur 1994, Kaddour *et al.* 2008). For instance for the structure of Fig. 3.7, the line inductance is not affected by the floating strips. However the floating metallic strips add parasitic capacitances between the two traces of the transmission line and consequently reduces the velocity of propagation of electromagnetic waves.

It is worth mentioning that, considering the wavelength as the ratio between velocity and frequency, another important feature of the slow-wave TLs in MMIC design is revealed: The decrease of the propagation speed results in a shorter the guided wavelength (Cheung and Long 2006). Therefore, more compact components based on shorter TLs can be implemented on-chip, hence resulting in a reduction of the required silicon area (Kaddour *et al.* 2008, Lai and Fujishima 2007).

3.4 Design Guidelines for the Slow-Wave Coplanar Strips

The aim of this section is to design a high quality factor shorted $\lambda/4$ slow-wave CPS resonator for 60 GHz CMOS VCOs with minimal on-chip area. To this end, a comprehensive parametric study, based on 3D electromagnetic simulations, is conducted on the geometrical dimensions of a slow-wave CPS structure in a standard 90 nm CMOS process. On that basis guidelines are derived for the design of slow-wave CPS with high quality factor, small on-chip area and desired characteristic impedance. Then, using the extracted guidelines, a high quality factor slow-wave CPS resonator is designed.

3.4.1 CAD Tool Settings

All simulations for this work are conducted with Ansoft HFSS, 3D full-wave EM simulator. Since the physical dimensions of the structure varies from less than 1 μm for the width of the floating strips, to hundreds of micrometers for the length of the CPS conductors, the simulation requires an extremely large number of small tetrahedrons to discretize the structure with sufficient resolution. To reduce the number of tetrahedrons and consequently, reduce the simulation time and required memory, all simulations are conducted for a relatively short length of the TL. The minimum length of the TL necessary for accurate results depends on the floating strips width. Convergence study in this case shows that in order to have an accurate simulation result, a TL with at least 20 floating strips is required.

To extract the propagation properties of the TL in a usable form for cascading, the S-parameters are converted to ABCD parameters. Then, the following set of equations for characteristic impedance Z_c, propagation constant γ, guided wavelength λ_g, and quality factor Q are used to calculate the corresponding parameters:

$$Z_c = \sqrt{\frac{B}{C}} \ , \tag{3.9}$$

$$\gamma = \alpha + j\beta = \cosh^{-1}(A)/l \ , \tag{3.10}$$

$$\lambda = \frac{2\pi}{\beta} \ , \tag{3.11}$$

$$Q = \frac{\beta}{2\alpha} \ , \tag{3.12}$$

where l is the transmission line length and α and β are the attenuation coefficient and propagation constant, respectively.

3.4.2 Technology and Design Parameters

The design guidelines are derived in the following using parameters for a 90 nm CMOS process with nine metallic layers made of copper. For the full-wave electromagnetic simulations, typical parameters and dimensions of the CMOS process are as follows. Silicon substrate thickness, relative permittivity and resistivity are $t_{\mathrm{si}} = 700\,\mu$m, $\epsilon_r = 11.9$ and $\rho = 10\,\Omega \cdot$ cm, while the relative permittivity of the dielectric layer between the CPS and the floating strips is $\epsilon_r = 3.8$ and its thicknesses is $t_{\mathrm{ox}} = 1\,\mu$m. Metal layers thicknesses are 2.8 μm for the CPS and 0.64 μm for the array of floating strips. These parameters are used for modeling both conventional and slow-wave CPS transmission lines. However, the guidelines are generic and can be used for designing similar structures in other processes. Because the upper metallic layer is the thickest, it is used for the realization of the CPS in order to have minimum conductive losses as well as the maximum distance away from the lossy silicon substrate (Kleveland *et al.* 2001). All simulations are targeted for 60 GHz operation.

It is recommended that the passivation layer be kept to achieve a higher effective permittivity (Kaddour *et al.* 2008) and consequently, smaller guided wavelength and lower penetration of electromagnetic wave into the lossy substrate. The design parameters for the structure shown in Figure 3.7 are as follows: W is the width of the signal strips, S is the spacing between the strips, S_w is the width of the floating strips, and spacing between the floating strips is denoted by S_s. The period (or pitch) of the floating strips is defined as $p = S_w + S_s$ and the duty cycle as $d = S_w/S_s$.

In the following sections the influence of each of these parameters on the quality factor, characteristic impedance, and guided wavelength of the propagating electromagnetic wave is studied and design guidelines are extracted.

3.4.3 CPS Dimensions: S and W

This section covers the effect of the width and spacing of the strips on the TL quality factor, characteristic impedance, and guided wavelength at 60 GHz for a conventional CPS in 90 nm CMOS technology. Figures 3.8 and 3.9 show the simulated characteristics of the conventional CPS for different values of the CPS width and spacing from 1 μm to 15 μm.

As shown in Fig. 3.8(a), an increase in the spacing between the strips S results in an increase in the characteristic impedance of the line. This can be explained by the fact that as the spacing is increased, the capacitance per unit length of the line decreases and the inductance per unit length of the line increases. Thus, it can be inferred from the definition of $Z_c = \sqrt{L/C}$ that an increase in S leads to an increase in Z_c. Fig. 3.8(b) shows that an increase in S from 0.2 μm to 15 μm results in a slight increase in the guided wavelength from 2200 μm to 2550 μm. This can be explained from the definition of the guided wavelength as $\lambda_g = 2\pi/\sqrt{LC}$. The different curves in the figures also illustrates the variation of characteristic impedance and guided wavelength with W. Considering that an increase in W increases the capacitance per unit length and decreases the inductance per unit length of the line, it can be explained that an increase in W, results in a decrease in the characteristic impedance, whereas the guided wavelength does not change significantly.

Simulation results for the variations of the quality factor versus the spacing between the strips of the conventional CPS for different values of the strips width W are illustrated in Fig. 3.9(a). The figure shows that Q increases with an increase in S and has a maximum for a specific value of S. To explain the effect of the physical TL parameters on the quality factor it is useful to review the most commonly used definition for the quality factor, which can be expressed as

$$Q = \omega_0 . \frac{\text{average energy stored}}{\text{average power loss}} \approx \frac{\beta}{2\alpha}, \tag{3.13}$$

where

$$\alpha \approx \frac{R}{2Z_0} + \frac{GZ_0}{2}, \tag{3.14}$$

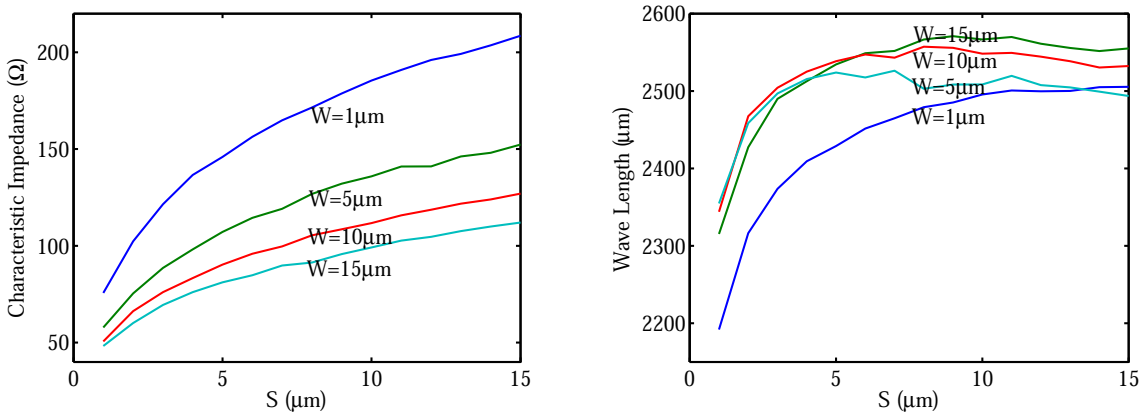

Figure 3.8. Characteristic impedance and guided wavelength of conventional CPS. Effect of width and spacing of transmission line tracks on (a) characteristic impedance and (b) wavelength. The parameteric study shows that an increase in the spacing between conductors results in an increase in both the characteristic impedance and the guided wavelength.

and

$$\beta = \omega_0 \sqrt{LC}\,, \tag{3.15}$$

R and G being the resistance and conductance per-unit-length of the TL. With this definition it can be explained that, the maximum quality factor is achieved for a specific value of spacing between the transmission line's strips that maximizes the propagation constant β. Whereas, very small or very large values of S correspond to small inductance or capacitance per unit length, resulting in a small quality factor.

In a similar manner, Fig. 3.9(b) shows that for small values of the strips width W, the quality factor is low. By increasing W, the quality factor increases, reaching its maximum value for $W \approx 6$ μm, and a further increase in the strips width results in a decrease in the TL's quality factor. This behavior can be explained with the different effects of W on resistance, conductance, capacitance and inductance of the line. Low values of W lead to higher values of inductance and lower values of conductance, but they also increase the resistive loss and decreases the capacitance of the line. On the other hand, although, a wide line has low resistive loss and higher capacitance per unit length, it suffers from high conductance and low inductance per unit length. Thus, as shown in Fig. 3.10, there is a specific point in the 2D space of W and S for which, a conventional CPS has the maximum quality factor. For the 90 nm CMOS

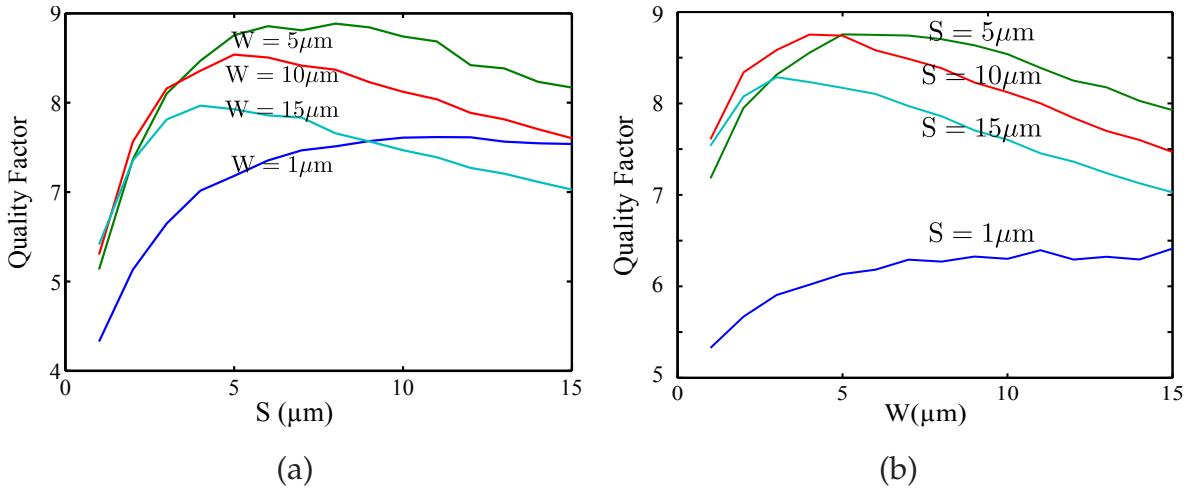

Figure 3.9. Qualtity factor of a conventional CPS. Effect of width and spacing of the transmission line tracks on the quality factor of a conventional CPS.

process parameters mentioned earlier in this section, the maximum quality factor of 8.8 is achieved for $W = 6\,\mu$m and $S = 6\,\mu$m.

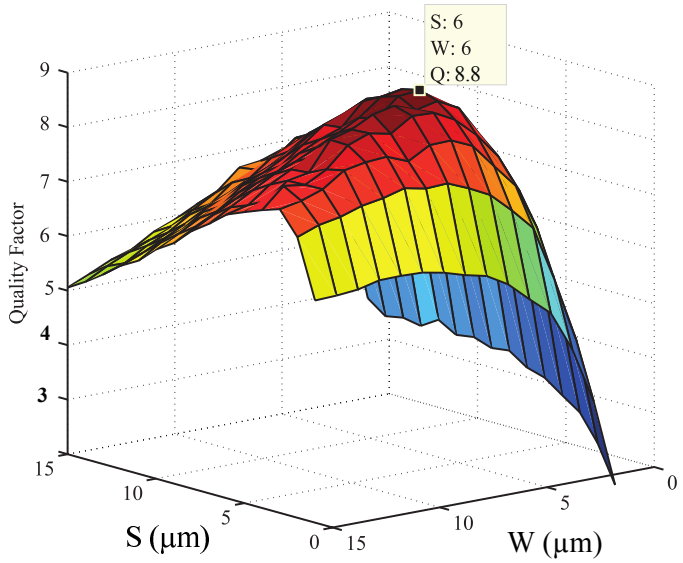

Figure 3.10. Two-dimensional parametric study on the qualtity factor of a conventional CPS. Effect of width and spacing of a conventional CPS tracks on quality factor. The two-dimentional parametric study shows that maximum quality factor of 8.8 is achieved for a $S = W = 6\mu$m.

3.4.4 Floating Strips Width: S_w

Let us now focus on the effect of the width S_w of the floating strips of the slow-wave CPS of Fig. 3.7 on different characteristics of the TL. In order to reduce the simulation time and required memory, slow-wave CPSs with different width W and spacing S, both varying from 5 μm to 65 μm, are simulated, first. A maximum quality factor is achieved for $W = 20\,\mu$m. Thus, to study the influence of the width of floating strips S_w on the quality factor, wavelength, and characteristic impedance of the slow-wave CPS, a slow-wave CPS with $W = 20\,\mu$m is simulated. Also, the period of the floating strips, i.e. $(p = S_w + S_s)$, is kept constant. In Fig. 3.11, the simulated quality factors of the slow-wave CPS for three different values of the width S_w of the floating strips are compared with that of a conventional CPS. The figure shows that the quality factor of the slow-wave CPS is increased when decreasing the width of the floating strips, and the maximum quality factor of 16 is obtained for S_w of 0.2 μm. This can be explained by considering that using wider floating strips results in higher eddy current loss in the shield (Cheung and Long 2006). Thus, in order to achieve the maximum quality factor, the narrowest floating strips available in the design rules for the considered process (0.2 μm in this specific case) should be used.

Figure 3.12(a) compares the guided wavelength of the conventional CPS to that of the slow-wave CPS for different values of S_w from 0.2 μm to 0.8 μm in steps of 0.2 μm. The simulation results clearly show that the guided wavelength is decreased from above 2200 μm for a conventional CPS to around 800 μm in the case of the slow-wave CPS. As mentioned in Section 3.3.1 this is one of the most important advantages of the slow-wave structure, which is especially useful for the miniaturization of microwave and millimeter-wave components. The figure also shows that an increase in S_w results in a slight decrease in the on-chip wavelength (increasing the S_w from 0.2 μm to 0.8 μm, results in only a 5% decrease in the guided wavelength). That is because, using wider floating strips increases the capacitance per unit length of the line, which results in a larger phase constant.

Figure 3.12(b) shows the simulated characteristic impedance of a slow-wave CPS with the strip width $W = 20\,\mu$m for different values of the strip spacing S, versus the floating strips width S_w. The figure shows that, as expected from the theory and TL circuit model, an increase in S_w results in an increase in the capacitance per unit length of the TL, and consequently a decrease in its characteristic impedance. For instance for a line with $W = 20\,\mu$m and $S = 25\,\mu$m, the characteristic impedance decreases from

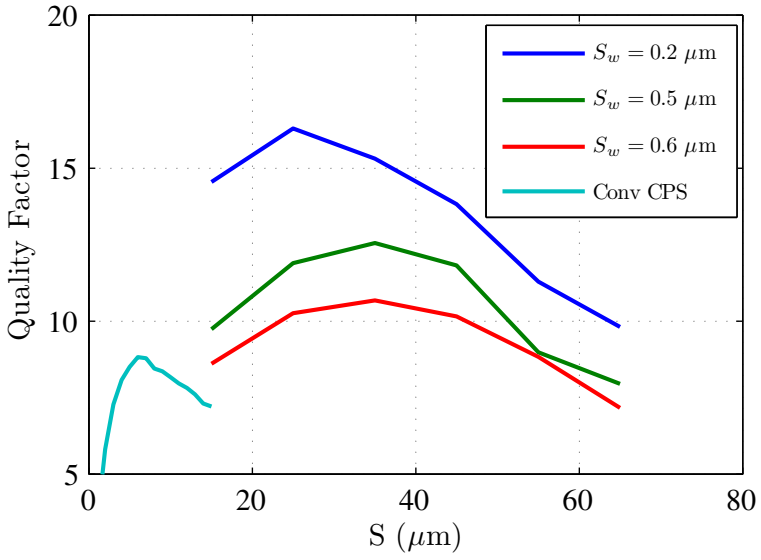

Figure 3.11. Comparison between the quality factor of a conventional and a slow-wave CPS. Simulation results for the quality factor of a slow-wave CPS with $W = 20\,\mu$m, for different values of S_w, as well as the simulated quality factor of an optimized conventional CPS with $W = 6\,\mu$m. The quality factor of the slow-wave CPS is increased with a decrease in the width of the floating strips, and the maximum quality factor of 16 is obtained for S_w of 0.2 μm.

$Zc = 41\ \Omega$ for $S_w = 0.2\,\mu$m to $Zc = 37\ \Omega$ for $S_w = 0.8\,\mu$m. Thus, the simulation results show that the floating strips width can be used as an extra degree of freedom to achieve a desired value of the characteristic impedance, if needed.

3.4.5 Floating Strips Duty Cycle: p

From the previous section we know that the best quality factor is achieved with the narrowest floating strips. Thus, in order to study the influence of the floating strips period ($p = S_w + S_s$) on the quality factor and wavelength of the slow-wave CPS, all simulations of this section are conducted with $S_w = 0.2\ \mu$m and only the spacing between strips S_s is changed. Note that, in order to save the computing time and memory, this study assumes that S_w and p are more or less independent. Otherwise, they need to be optimized concurrently. Figures 3.13(a) and (b) show the simulated quality factor and guided wavelength of a slow-wave CPS with $W = 20\,\mu$m and $S = 25\,\mu$m for different values of the floating strips period from 0.6 μm to 7.2 μm. Assume that the

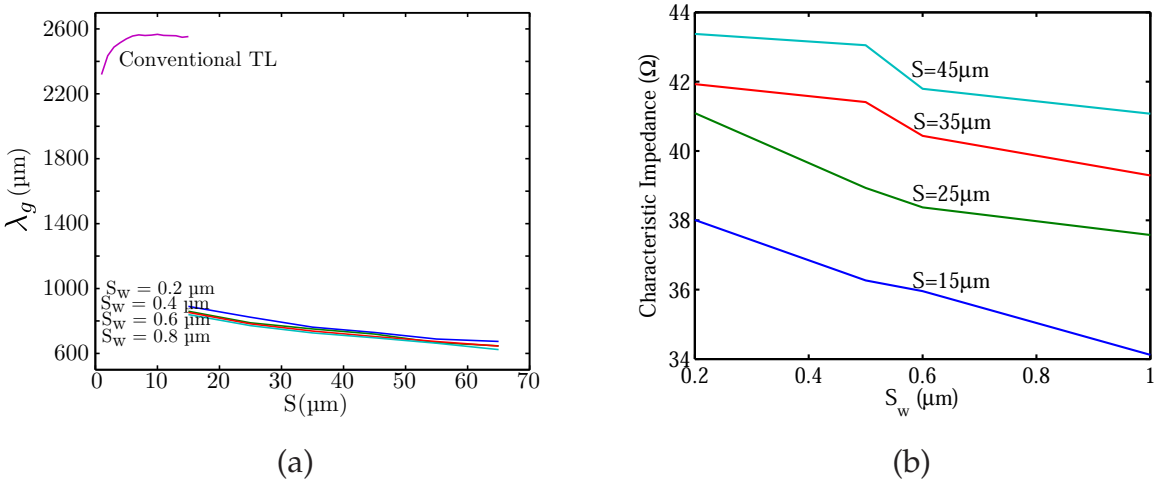

(a) (b)

Figure 3.12. Guided wavelength and characteristic impedance of a conventional and a slow-wave CPS. (a) Comparison between simulated guided wavelength of the optimized conventional CPS with with $W = 6\,\mu$m and that of a slow-wave CPS for different values of S_w. The comparison shows that the guided wavelength is decreased from above 2200 μm for the conventional CPS to around 800 μm in the case of the slow-wave CPS. (b) Characteristic impedance of slow-wave CPS with $W = 20\,\mu$m,

parameters are more or less independent, and that this assumption allows to save computing power. Figure 3.13(a) shows that a maximum quality factor of 16.2 is achieved for $p = 2.4\,\mu$m. This can be explained with the fact that an increase in the spacing between the floating strips S_s increases the inductance per unit length and reduces the capacitance per unit length of the slow-wave CPS. Thus, for small values of the S_s, the TL has low inductance and for large values of S_s it has low capacitance. Since the quality factor is directly proportional to the stored electromagnetic energy, the maximum quality factor can be achieved when the TL has large values for both equivalent inductance and equivalent capacitance. Figure 3.13(b) shows that decreasing the period of floating strips, reduces the guided wavelength of the structure. Thus, in order to achieve miniaturized components, a dense array of floating strips is required.

3.4.6 Discussion

By using the guidelines of the previous sections, a quarter-wavelength slow-wave CPS with at 60 GHz is simulated $S = 25\,\mu$m, $W = 20\,\mu$m, $S_w = 0.2\,\mu$m and $p = 2.4\,\mu$m.

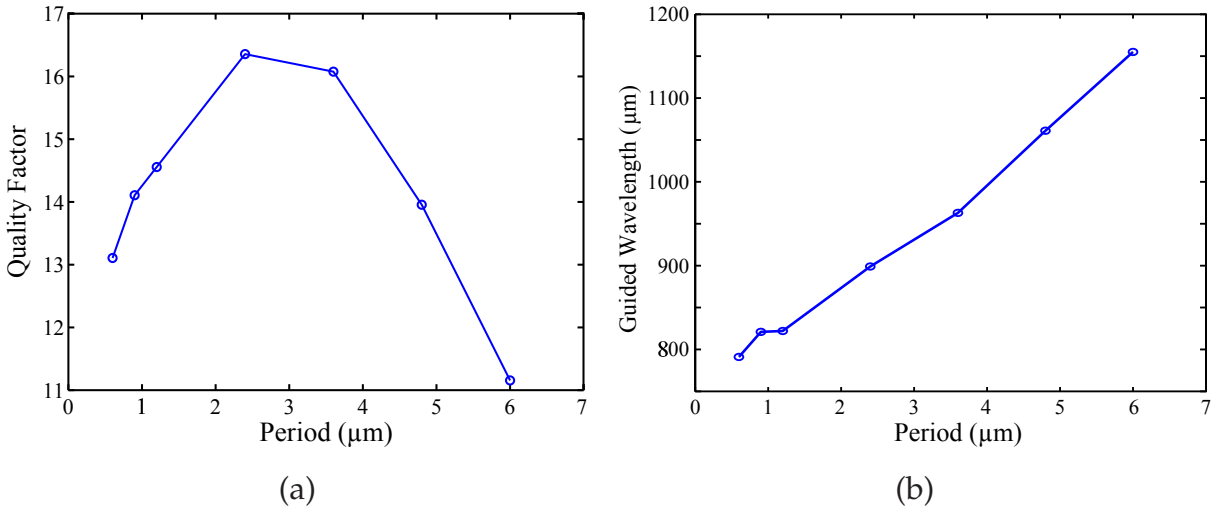

Figure 3.13. Quality factor and guided wavelength of a slow-wave CPS versus duty cycle of floating strips. Effect of duty cycle of the floating strips p on (a) quality factor and (b) guided wavelength of the slow-wave CPS. A maximum quality factor of 16 is achieved for $p = 2.4\,\mu$m, while in order to minimize the guided wavelength, a dense array of floating strips is required.

The properties of this device are compared with those of a corresponding quarter-wavelength conventional CPS with optimized performance obtained with $S = 6\,\mu$m and $W = 6\,\mu$m. Although the S and W of the slow-wave CPS are much larger than those of the conventional CPS the total on-chip area of both structures are almost equal (13000 μm^2 for slow-wave CPS and 11200 μm^2 for conventional CPS). That is because, the guided wavelength for slow-wave CPS at 60 GHz is 800 μm while the guided wavelength for a conventional CPS operating at same frequency is 2500 μm. However, the aspect ratio of the slow-wave CPS is significantly different from the conventional counterpart, leading to an efficient utilization of the chip area. As shown in Figure 3.14 the quality factor of the optimized slow-wave CPS is 16.2, which is 84% more than the maximum quality factor of the conventional CPS. Furthermore, when using S_w and S_s of the floating strips as two extra degrees of freedom for adjusting the properties of the transmission line, a characteristic impedance near 50 Ω is achieved for slow-wave CPS, while the characteristic impedance for the optimal conventional CPS is greater than 100 Ω.

It is worth mentioning that while the effective relative permittivity of the conventional CPS is about 4, the optimized slow-wave CPS behaves as a one-dimensional metamaterial medium with an effective relative permittivity of about 25. This, elegantly explains

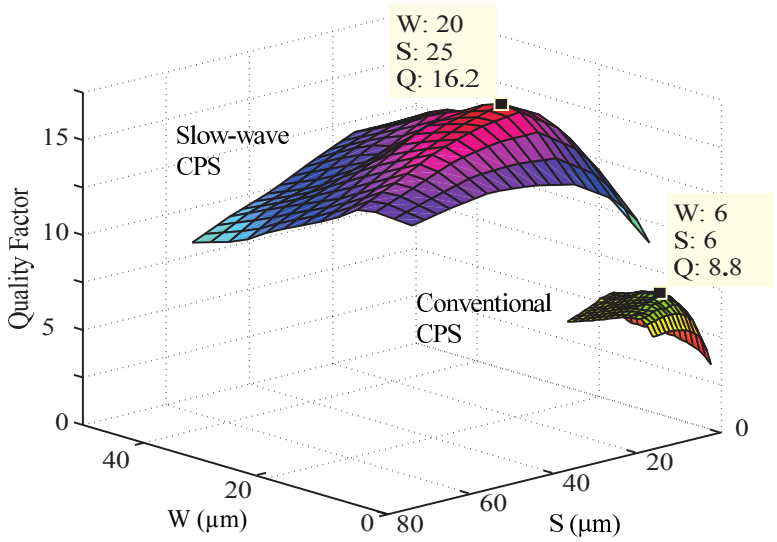

Figure 3.14. Comparison between the quality factor of a conventional and a slow-wave CPS. A comparison between the simulated quality factor of a conventional and a slow-wave CPS for different values of width W and spacing S of the CPS strips. The simulation results show that a maximum Q-factor of 16.2 is achieved for the slow-wave CPS with $W = 20\,\mu$m and $S = 25\,\mu$m, which is loaded with an array of floating strips with $S_w = 0.2\,\mu$m and $p = 2.4\,\mu$m.

the reduced guided wavelength that is defined as $\lambda_g = \lambda_0/\sqrt{\epsilon_{\text{eff}}}$. As mentioned in Section 3.3, this miniaturized high quality factor balanced resonator an be used for the realization of millimeter-wave low-phase noise VCOs in CMOS technology.

3.5 Characterization of the Complex Permittivity of Thin Films

Further to application as a balanced resonator for the realization of low phase noise VCOs, the optimized slow-wave CPS can be used for thin film characterization. Characterization of thin films of dielectrics for integrated circuit applications, where thin films of dielectrics are used as isolations between metallic layers, is of great importance in microelectronics (Baker-Jarvis *et al.* 1998). At microwave and millimeter-wave frequencies, characterization is usually based on transmission lines (TLs), in contrast to parallel plate capacitors used at low frequencies (Baker-Jarvis *et al.* 1990, Janezic and Jargon 1999). The main limitation of the TL method is that extremely thin film layers, as encountered in integrated circuit technologies, result in a too low characteristic

impedance in microstrip lines, and are not sufficient to provide mechanical support for coplanar structures. Recently, Franc *et al.* (2012) proposed adding a thick layer of an already known material underneath the unknown thin film to provide the required mechanical support for coplanar waveguide technology. However, since adding a thick layer reduces the sensitivity, a patterned shielded coplanar waveguide was used to confine the electric field to the unknown thin film, resulting in an increased sensitivity to the thin film electromagnetic properties.

In the previous section we derived the guidelines for the design of high quality factor slow-wave CPS. As an alternative application benefiting from a high quality factor, this section proposes the characterization of both relative permittivity and conductivity of an unknown thin film using a slow-wave CPS. The proposed concept is demonstrated through simulation by characterizing a thin silicon dioxide layer in a CMOS process.

3.5.1 Proposed Method and Simulation Results

Figure 3.15 depicts the structure of the proposed slow-wave CPS for the characterization of the thin SiO_2 layer, which is sandwiched between the CPS and the floating strips. If the far end of the CPS is short-circuited a balanced resonator is realized. It is shown that resonant frequency and quality factor of the resonator can be used for determination of the complex permittivity of the sandwiched layer. In order to maximize the sensitivity of the thin film characterization the balanced resonator needs to have a high quality factor. To this end, based on the guidelines proposed in the previous sections, as well as in (Horestani *et al.* 2010, Horestani *et al.* 2011a), in order to reduce the resistive loss, the thick top metal layer is used for the implementation of the CPS. Furthermore, an array of very narrow floating strips are placed in the underlying metal layer to confine the electric field to the thin film under test and reduce the substrate conductive loss. In this structure the floating strips also reduce the resonator length.

For full-wave electromagnetic simulations, typical parameters and dimensions of a standard CMOS process, mentioned in the caption of Fig. 3.15 are used. Metal layers thicknesses are 2.8 μm for the CPS and 0.64 μm for the array of floating strips. The short circuited CPS resonator has a length of 230 μm, width of $W = 25\,\mu$m and spacing $S = 30\,\mu$m and it is loaded with an array of floating strips with width $W_s = 0.6\,\mu$m and spacing $S_s = 1.8\,\mu$m to resonate at 59 GHz.

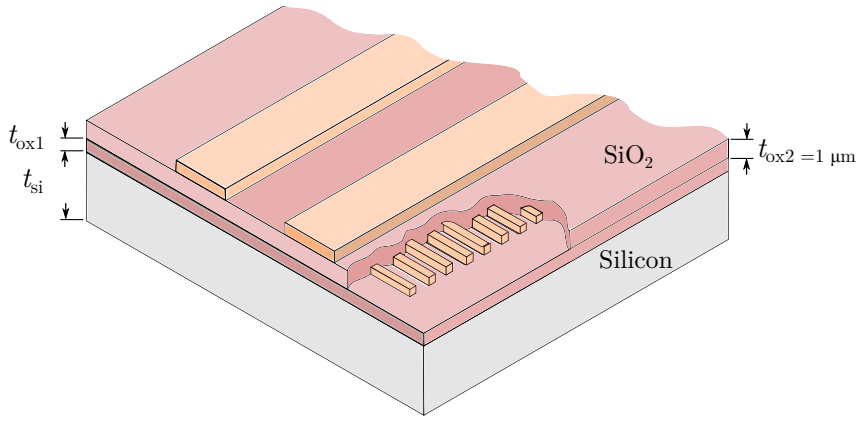

Figure 3.15. Slow-wave CPS structure for thin film characterization. Slow-wave CPS with underlying floating strips in a CMOS process. The top SiO_2 layer is the thin film under test. For the full-wave EM simulations following parameters and dimensions are used: silicon substrate thickness, relative permittivity and resistivity are $t_{si} = 700\,\mu$m, $\epsilon_r = 11.9$ and $\rho = 10\,\Omega\cdot$cm, while the dielectric layers, relative permittivity is $\epsilon_r = 3.8$ and their thicknesses are $t_{ox1} = 2.8\,\mu$m and $t_{ox2} = 1\,\mu$m.

Figure 3.16 shows the simulated normalized (relative to 1 Ω) input impedance of the resonator. Comparing the simulated resonant frequency and quality factor of the resonator for a lossless thin film with $\epsilon_r = 3.8$ (black dashed line) to those of a lossless dielectric with $\epsilon_r = 3.9$ (red solid line) shows that since the electric field is mostly confined to the thin film under test, the resonant frequency of the structure is highly dependent on the permittivity of the thin film. Furthermore, the simulation results for a lossy thin film with $\epsilon_r = 3.8$ and $\tan\delta = 0.02$ (blue dot line) shows that while any change in the loss tangent of the thin film does not have a considerable effect on the resonant frequency, it effectively changes the quality factor of the resonator.

Figure 3.17 depicts the resonant frequency (blue solid line) and the quality factor (red dashed line) of the resonator versus relative permittivity of the thin film under test. The figure clearly shows that while the change in the thin film relative permittivity from $\epsilon_r = 3.6$ to $\epsilon_r = 4$ changes the resonant frequency from $f_0 = 60.4\,$GHz to $f_0 = 57.5\,$GHz, the resonance quality factor is almost unchanged. Thus, the resonant frequency of the proposed slow-wave resonator can be used for the characterization of the relative permittivity of a thin film of an unknown dielectric.

In contrast to Fig. 3.17, effect of the thin film conductivity on the central frequency and quality factor of the proposed slow-wave resonator is depicted in Fig. 3.18. The figure clearly shows that while a change in the loss tangent of the thin dielectric layer has

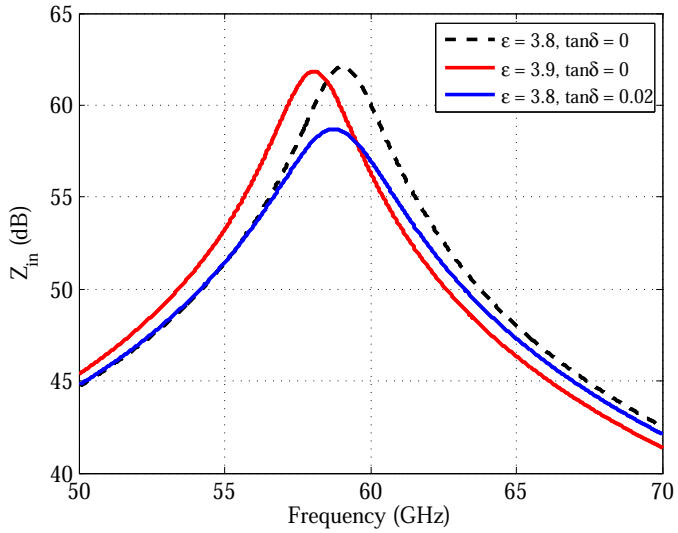

Figure 3.16. Normalized input impedance of a slow-wave CPS. Simulation results for normalized input impedance, demonstrating the variation of resonant frequency and quality factor of the resonator by small changes in the permittivity and conductivity of the thin film under test.

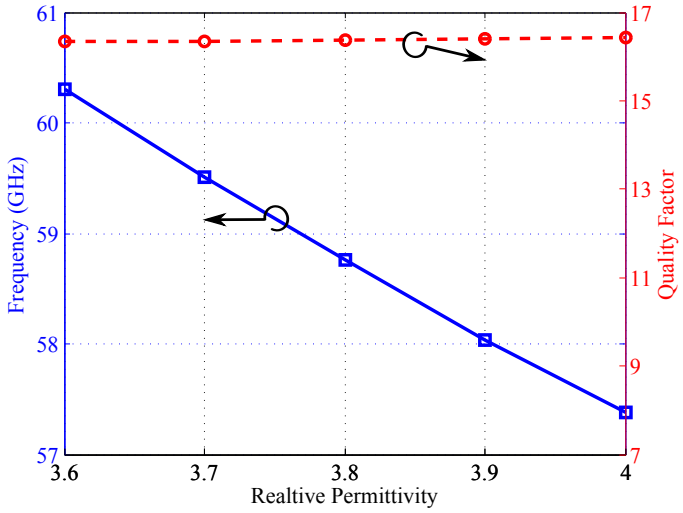

Figure 3.17. Affect of relative permittiviy on a slow-wave CPS resonator. Simulated resonant frequency and quality factor of the proposed slow-wave resonator versus relative permittivity of the thin film under test with $\tan\delta = 0.02$. Simulation results show that while an increase in the relative permittivity of the thin film under test effectively decreases the resonant frequency of the structure, it does not have a significant affect on the resonance quality factor.

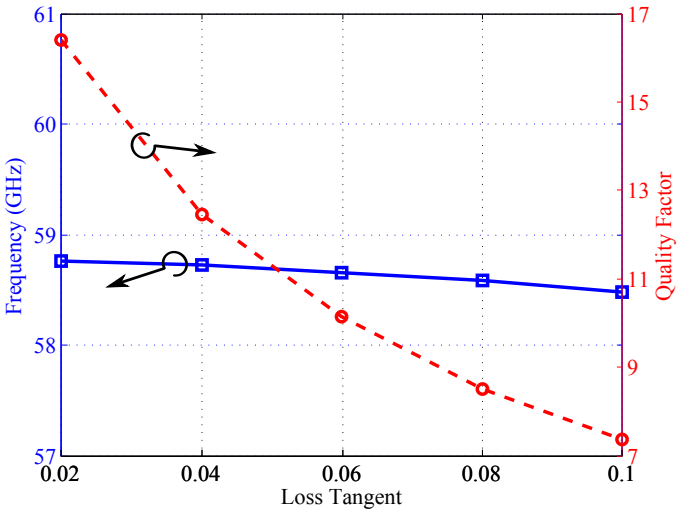

Figure 3.18. Affect of loss tangent. Simulated resonant frequency and quality factor of the resonator versus the loss tangent of a thin film with $\epsilon_r = 3.8$. Simulation results show that quality factor of the resonator can be used for determining the conductivity of the thin film under test.

very small affect on the resonance frequency of the structure, it effectively changes the quality factor of the resonance. Thus, the quality factor of the resonance can be used for the characterization of the thin film loss tangent $\tan\delta$.

3.6 Design of High Quality Factor SRR-Based Coplanar Strip Resonator

The resonance frequency of a conventional TL resonator is determined by its electrical length. In fact, a conventional short-ended TL acts as a quarter-wavelength resonator when $\Delta\phi = \beta l = \pi/2$, where $\Delta\phi$ is the traveling wave phase delay, β is propagation phase constant and l is the physical length of the line (Abielmona *et al.* 2006). Based on this criterion, the traveling wave phase shift along a quarter-wavelength resonator at the resonance frequency f_r is $\pi/2$ and for the waves at other nearby frequencies, i.e. $f_r + \Delta f$, the phase shift has some deviation from $\pi/2$. In other words, assuming a TL loaded with the load impedance Z_L the reflection coefficient at the input port is given by

$$\Gamma_{\text{in}} = S_{11} + \frac{S_{12}\Gamma_{\text{L}}S_{21}}{1 - S_{22}\Gamma_{\text{L}}}, \tag{3.16}$$

where $S_{i,j}$ are the TL S-parameters and Γ_L is the load reflection coefficient (Gonzalez 1997). For a reciprocal quarter-wavelength short-ended TL resonator, such as CPS resonator of this work, $S_{12} = S_{21}$, $S_{11} = S_{22}$, and $\Gamma_L = -1$. Thus, (3.16) can be simplified to

$$\Gamma_{in} = S_{11} - \frac{S_{21}^2}{1 + S_{11}}. \tag{3.17}$$

For a resonator at resonance frequency, Γ_{in} should be $1\angle 2k\pi$. One solution is the case of an ideal quarter-wavelength short-ended TL, where $|S_{11}| = 0$ and $S_{21} = 1\angle 90°$. Resonance occurs at a frequency where $\angle\Gamma_{in} = 0°$. For the frequencies either higher or lower than f_r, $\angle\Gamma_{in} \neq 0°$. The key point is that, since the resonator quality factor is determined by the rate of deviation of $\Gamma_{in}(f)$ from $\Gamma_{in}(f_r)$, the quality factor of a quarter-wavelength TL resonator in CMOS technology can be improved by increasing the deviation rate around the resonance frequency. Here we show that by loading a CPS resonator with split ring resonators (SRRs) an increased deviation rate in the reflection coefficient, and consequently an improved quality factor can be achieved.

Figure 3.19 depicts an illustration of the proposed structure, which is composed of a short-ended conventional CPS in the top metal layer of the CMOS process and a pair of SRRs which are located in a lower metal layer. The CPS resonator, without the SRRs, is designed to operate at 60 GHz, and the SRRs are symmetrically laid out below the slot between the CPS strips to obtain high inductive coupling at resonance (Martín *et al.* 2003b).

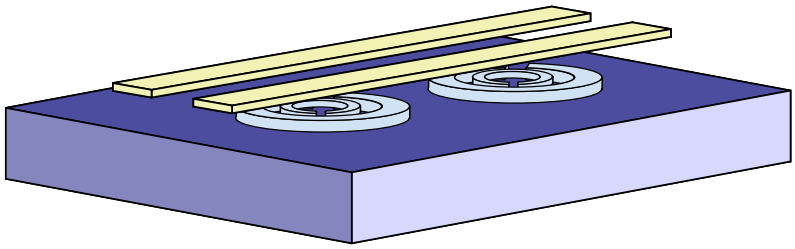

Figure 3.19. SRR-loaded high quality factor quarter-wavelength resonator. Three-dimentional illustration of an SRR-loaded high quality factor quarter-wavelength CPS resonator. The structure is composed of a short-ended conventional CPS in the top metal layer of the CMOS process and a pair of SRRs which are aligned with the symmetry plane of the CPS and located in the lower metal layer.

The introduced SRRs are tuned to resonate at 65 GHz. According to (3.17), the rejection band caused by SRRs leads to an increased phase and amplitude deviation rate of the Γ_{in} at frequencies above 60 GHz.

Figure 3.20 compares the normalized simulated input impedances for the proposed quarter-wavelength CPS resonator with and without the pairs of loading SRRs. The figure clearly shows that while the bare CPS resonator has a bandwidth of 6.1 GHz, loading the CPS with the SRRs that are tuned to resonate around 65 GHz decreases the bandwidth to about 3.4 GHz. In other words, as listed in Table 3.2, the proposed structure has a quality factor of 17.7 compared to the quality factor of 8.8 for the bare CPS resonator. In terms of the quality factor of the resonance, this shows a 100% improvement.

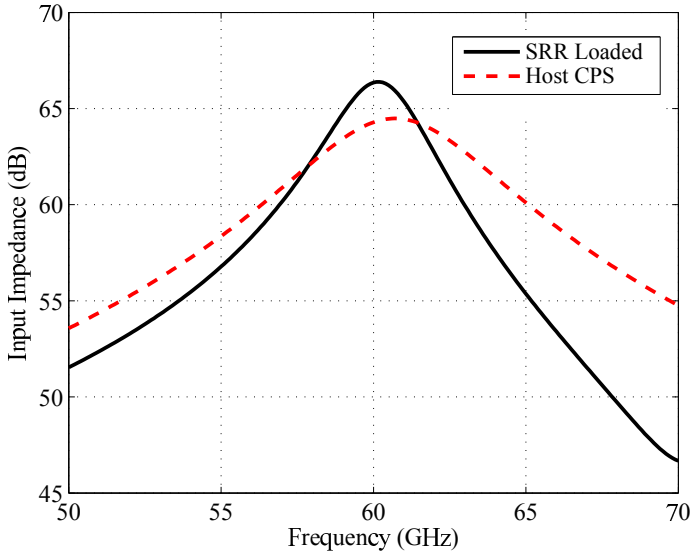

Figure 3.20. Input impedance of the SRR-loaded CPS. Comparison between the input impedance of a conventional CPS resonator and that of the SRR-based CPS resonator. Impedances are normalized to 1 Ω.

Table 3.2 also compares the length of the two resonators, that shows about 20% miniaturization in the case of the SRR-loaded CPS resonator. As shown in Fig. 3.20, the proposed resonator also benefits from a 2 dB higher normalized input impedance at resonance. This high input impedance results in lower bias current of the oscillator, which implies lower power consumption.

3.7 Tapered Transmission Line Resonator

As explained in the previous sections, using slow-wave TL-based resonator is an effective solution for reducing substrate losses in CMOS technologies and achieving a

Table 3.2. Conventional CPS versus SRR-loaded CPS. Comparison between the quality factor, resonance frequency and length of the quarter-wavelength CPS resonator with and without SRRs.

Resonator Type	Length (μm)	f_0 (GHz)	Q-factor	Q-factor Improvement
Host CPS without SRRs	600	60	8.8	-
SRR-loaded CPS	490	60	17.7	100%

high quality factor resonator. Furthermore, the standing wave behavior of the quarter-wavelength resonator can be exploited by varying the shape along the transmission line to reduce the effective wavelength and consequently achieve even higher quality factor (Marcu and Niknejad 2008b). A quarter-wavelength differential CPS, which is shorted at one end, exhibits a standing wave mode at its resonance frequency, as shown in Figure 3.21 (Marcu and Niknejad 2008b, Marcu and Niknejad 2008a). Keeping this in mind and considering the general TL model of Fig. 3.22, the quality factor of a TL is given by

$$Q = w\frac{E_{\text{stored}}}{P_{\text{diss}}} = \omega\frac{\int_0^l \frac{1}{4}(V^2(x)C(x) + I^2(x)L(x))\,dx}{\int_0^l \frac{1}{2}(V^2(x)G(x) + I^2(x)R(x))\,dx}. \tag{3.18}$$

From this equation, it can be concluded that to reach a higher quality factor, the TL resonator needs to be more capacitive at the beginning of the transmission line, where the voltage is maximum. Also it needs to be more inductive at the end of the transmission line, where the current is maximal. Furthermore, to minimize the dissipated power, the TL needs to have its minimum conductance at the beginning and its minimum resistance at the end of the line. With this explanation, it has been shown by Marcu and Niknejad (2008b) that a maximum quality factor can be achieved with a numerical optimization of the width and spacing of two strips of the CPS.

3.7.1 Transmission Line Equations

Considering the general RLGC model of Fig. 3.22, with all R, L, G and C, functions of position x, the well known telegrapher's equations can be written as (Pozar 2005).

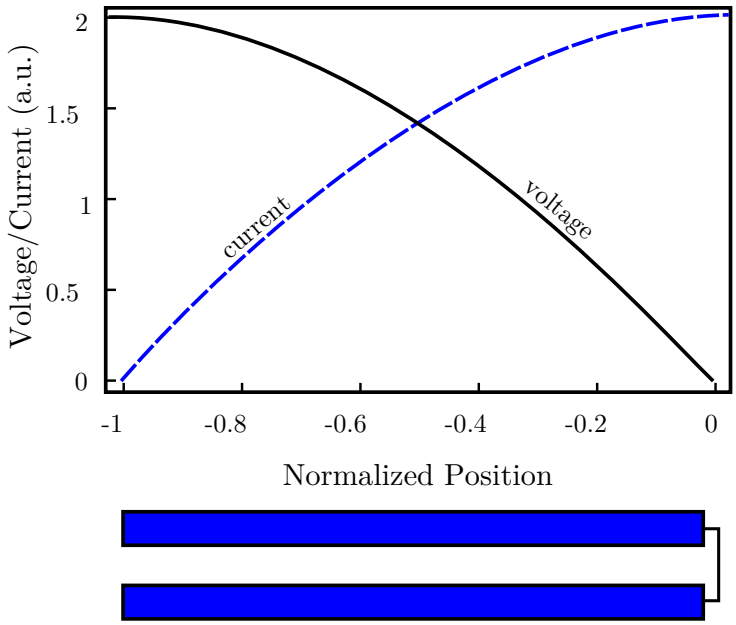

Figure 3.21. Standing wave behavior of the quarter-wavelength resonator. Standing wave voltage and current in a quarter-wavelength resonator. After Marcu and Niknejad (2008b).

$$\frac{dV(x)}{dx} = -(R(x) + j\omega L(x)) \cdot I(x) \tag{3.19}$$

$$\frac{dI(x)}{dx} = -(G(x) + j\omega C(x)) \cdot V(x). \tag{3.20}$$

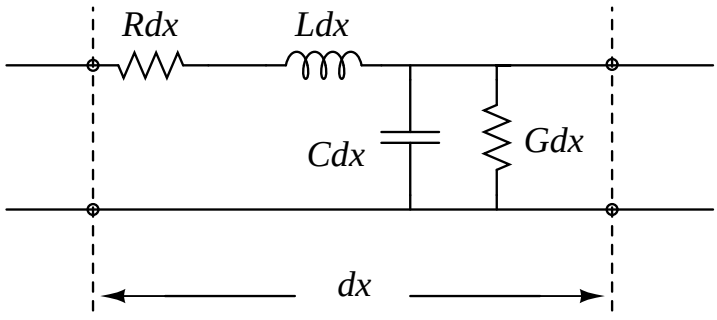

Figure 3.22. RLGC TL model. General RLGC model of transmission lines.

Assuming low-loss condition, i.e. $R = G = 0$, the above equations can be combined to from the following differential equations (Womack 1962, Youla 1964)

$$\frac{d^2V(x)}{dx^2} - \frac{1}{L(x)}\frac{dL(x)}{dx}\frac{dV(x)}{dx} - \omega^2 L(x)C(x)V(x) = 0 \tag{3.21}$$

$$I(x) = -\frac{1}{j\omega L(x)} \cdot \frac{dV(x)}{dx}. \tag{3.22}$$

The equations can be transformed from the physical domain to the phase domain by using (Andress and Ham 2005)

$$\theta(x) = \int_0^x \beta(x')dx', \tag{3.23}$$

$$L_\theta(\theta) = \frac{L(x)}{\beta(x)} = \frac{1}{\omega}\sqrt{\frac{L(x)}{C(x)}} = \frac{Z_0(x)}{\omega}, \tag{3.24}$$

$$C_\theta(\theta) = \frac{C(x)}{\beta(x)} = \frac{1}{\omega}\sqrt{\frac{C(x)}{L(x)}} = \frac{1}{\omega Z_0(x)}. \tag{3.25}$$

After transforming the variables of (3.21) from physical length into electrical length, the voltage distribution along the line can be described as

$$\frac{d^2V(\theta)}{d\theta^2} - \frac{1}{Z_0(\theta)}\frac{dZ_0(\theta)}{d\theta}\frac{dV(\theta)}{d\theta} - V(\theta) = 0. \tag{3.26}$$

Solution of this equation can be found analytically if the characteristic impedance profile is a well-behaved function, e.g. linear or exponential. However, for an *a priori* unknown arbitrary variation of the characteristic impedance along the line, as assumed in the present work, (3.26) cannot be solved analytically (Marcu and Niknejad 2008b).

3.7.2 Numerical Optimization

The optimization of the tapering is performed based on the data gathered from the parametric study of uniform slow-wave CPS segments in Section 3.4. For convenience, the illustration of the uniform slow-wave CPS is repeated here (Fig. 3.23). Based on the guidelines given in Section 3.4, the slow-wave floating strips have been chosen to be $S_W = 0.2\,\mu$m wide with a spacing $S_S = 2.4\,\mu$m between strips. Taking on-chip area limitation into account, the maximum of width W and spacing S of the CPS strips are set to $65\,\mu$m. Since the resonator is also used as DC bias line, the minimum width of the lines was set to $5\,\mu$m. The full wave 3D EM simulator, HFSS, was first used

for ABCD matrix extraction of uniform 100 μm long differential coplanar strips. The values of widths and spacings are varied between 5 μm and 65 μm and simulated at 60 GHz. The computed scattering matrices are saved in a file as a database for the optimization. Parameters of a standard 90 nm CMOS process are used for modeling the silicon substrate, dielectric and metal layers in HFSS. Top metal is used for CPS paths and metal 5 for the underneath floating strips. The S-parameters are converted to ABCD parameters using Matlab, which is also used in the subsequent optimization of the resonator tapering.

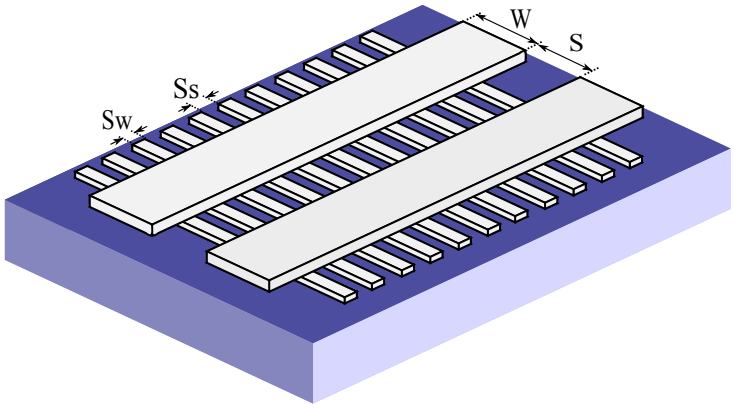

Figure 3.23. Uniform slow-wave CPS. Three-dimensional illustration of a uniform slow-wave coplanar strips structure.

The optimization is initiated from a uniform CPS resonator with $l = \lambda_{\text{eff},1}/4$, where $\lambda_{\text{eff},1}$ is the effective wavelength in the first iteration. Then the resonator is divided into 100 cascaded uniform sections of equal length of $l/100$. After assigning the S and W, as depicted in Figure 3.23, varying for each section along the resonator length as determined by the optimization algorithm, the resonator ABCD parameters are calculated from multiplication of ABCD matrices of all the small sections as shown in (3.27)

$$\begin{bmatrix} A & B \\ C & D \end{bmatrix}_{\text{Tot}} = \prod_{i=1}^{100} \begin{bmatrix} A & B \\ C & D \end{bmatrix}_{l/100\,(S_i,W_i)} . \tag{3.27}$$

The HFSS simulations of the uniform lines are performed for 100 μm long lines, therefore, the ABCD matrix of the corresponding sections with 1 μm length is

$$\begin{bmatrix} A & B \\ C & D \end{bmatrix}_{1\,\mu\text{m}(S_i,W_i)} = \sqrt[100]{\begin{bmatrix} A & B \\ C & D \end{bmatrix}_{100\,\mu\text{m}(S_i,W_i)}} . \tag{3.28}$$

From this equation, the ABCD matrix of the corresponding sections with length $l/100$ needs to be adapted by using appropriate exponentiation according to

$$\begin{bmatrix} A & B \\ C & D \end{bmatrix}_{l/100\,(S_i,W_i)} = \begin{bmatrix} A & B \\ C & D \end{bmatrix}_{1\,\mu\mathrm{m}(S_i,W_i)}^{l/100\,\mu\mathrm{m}}. \tag{3.29}$$

From the total ABCD matrix (3.27) of the tapered resonator, the characteristic impedance Z_c, the propagation constant γ, the effective wavelength λ_{eff} and the quality factor Q can be readily obtained as

$$Z_c = \sqrt{\frac{B}{C}}, \tag{3.30}$$

$$\gamma = \alpha + j\beta = \cosh^{-1}(A)/l, \tag{3.31}$$

$$\lambda_{\mathrm{eff}} = \frac{2\pi}{\beta}, \tag{3.32}$$

$$Q = \frac{\beta}{2\alpha}. \tag{3.33}$$

It must be mentioned that since the effective wavelength of the tapered transmission line is not constant along the line, the total length varies with the resonator shape. A scaling factor therefore needs to be introduced for the resonator length. The optimization procedure starts then from an initial effective wavelength, $\lambda_{\mathrm{eff},1}$, and after calculation of the more accurate effective wavelength $(\lambda_{\mathrm{eff},2})$ of the tapered transmission line from (3.32), the calculation of the total ABCD matrix is repeated with the new resonator length i.e. $\lambda_{\mathrm{eff},2}/4$. This process continues iteratively until the scaling factor $\lambda_{\mathrm{eff},n}/l$ in the n^{th} iteration converges satisfactorily to one. Then the optimizer starts the next set of W and S to form another tapered resonator and this process continues iteratively until the tapered CPS converges to the optimum resonator with a maximum quality factor.

In this work a Harmony Search (HS) optimization algorithm is used to optimize the geometric configuration of the slow-wave CPS to achieve the maximum quality factor. This method was developed based on the process of music improvisation (Geem 2009). The harmony of a piece is analogous to the quality of the solution in HS and the musicians improvisation is analogous to the global and local search schemes. Note that, HS has been successfully applied to various optimization problems including the traveling salesperson problem, water supply networks, hydrologic model parameter calibrations and thermal systems optimization (Fesanghary 2009).

3.7.3 Optimization Results

The optimum tapered shape of the slow-wave coplanar strips resonator derived in this work is shown in Figure 3.24. To confirm the results of the optimization, simulations of both the optimized tapered slow-wave CPS, and uniform slow-wave CPS resonators are performed using HFSS. Table 3.3 compares the resonance frequency, length and quality factor of four types of quarter-wavelength CPS resonators. The reference for the comparison is the measured characteristics of the conventional uniform CPS resonator which was simulated and fabricated by Marcu and Niknejad (2008b). This resonator has a length of 635 μm to resonate at 57.9 GHz and has a quality factor of 8.8. All other resonators are also designed to resonate at around 60 GHz. The second resonator in the table is a conventional tapered CPS resonator from (Marcu and Niknejad 2008b). It has a length of 498 μm and quality factor of 15, which shows 70.4% improvement in quality factor, compared to the uniform resonator.

Comparing the simulation and measurement, some variations in the resonance frequency are observed in both cases, however, there is a good match in quality factors of simulation and measurement results. The table also shows the slow-wave uniform and slow-wave tapered CPS resonators from Horestani *et al.* (2010) and the optimized variable width CPS of this section, respectively. The uniform slow-wave resonator has a length of 222 μm and quality factor of 16.2. The optimum tapered slow-wave resonator designed in this section has a length of 320 μm that is relatively short and reasonable for on-chip implementation. The quality factor can be calculated from the resonator input impedance curve which is shown in Figure 3.25. The optimum resonator has a quality factor of 28.4 which is a significant improvement in quality factor by 220% compared to the conventional uniform resonator, or 75% improvement, compared to the tapered resonator proposed by Marcu and Niknejad (2008b). Figure 3.25 also shows the resonator input impedance that is calculated from optimizer results. Since the optimization has been done just in one frequency, 60 GHz, the input impedance is shown just in that frequency. The figure shows a very good match between optimization results and HFSS simulation results.

3.8 Conclusion

In this chapter, the influence of the geometric dimensions of conventional and slow-wave CPS on their characteristic performance have been studied by using full wave

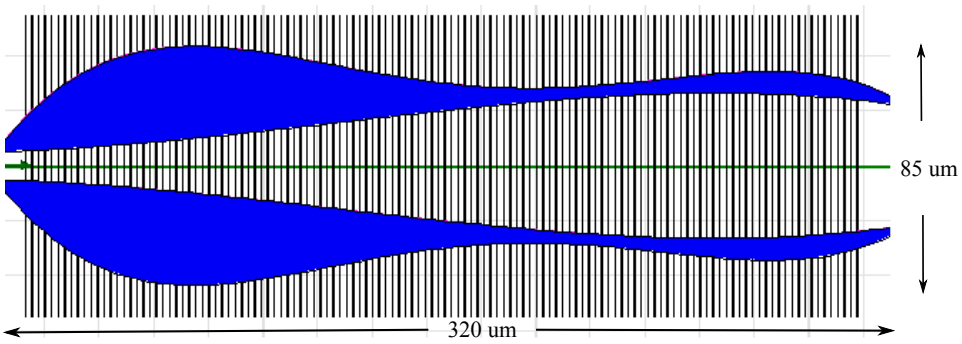

Figure 3.24. Optimum slow-wave tapered resonator. Top view of the optimum tapered slow-wave coplanar strips resonator. The resonator has a length of 320 μm that is relatively short and reasonable for on-chip implementation.

electromagnetic simulations. The quality factor, characteristic impedance and guided wavelength of the lines have been investigated and compared towards this aim. Design guidelines for high quality factor slow-wave CPS in a standard 90 nm CMOS MMICs technology have been extracted. For high quality factor slow-wave CPS, in a standard 90 nm CMOS MMICs technology, we have shown that exploiting the narrowest floating strips available in the process results in the maximum quality factor. Note that, although reducing the strips spacing results in smaller guided wavelength, it does not result in the maximum quality factor of the slow-wave CPS. It also has been concluded that starting from a conventional CPS optimized for maximum quality factor, adding the floating strips leads to a higher quality factor in a smaller on-chip area. However, further optimization on the CPS parameters allows an even higher quality factor of the slow-wave CPS. In other words, to achieve the maximum quality factor of the slow-wave CPS, a search using 3-dimensional space of S, W and S_s, while using smallest S_w allowed by the design rules, is required.

As a potential application, in addition to its use as a compact waveguide structure, resonance properties of an optimized slow-wave CPS resonator has been used for electromagnetic characterization of thin films of dielectrics. It has been shown through simulation that the resonant frequency of the structure is proportional to the relative permittivity of the thin film, while its quality factor is a function of conductivity of the thin film. Thus, it is demonstrated that the resonant frequency and the quality factor of the resonator can be used for accurate determination of the complex permittivity of

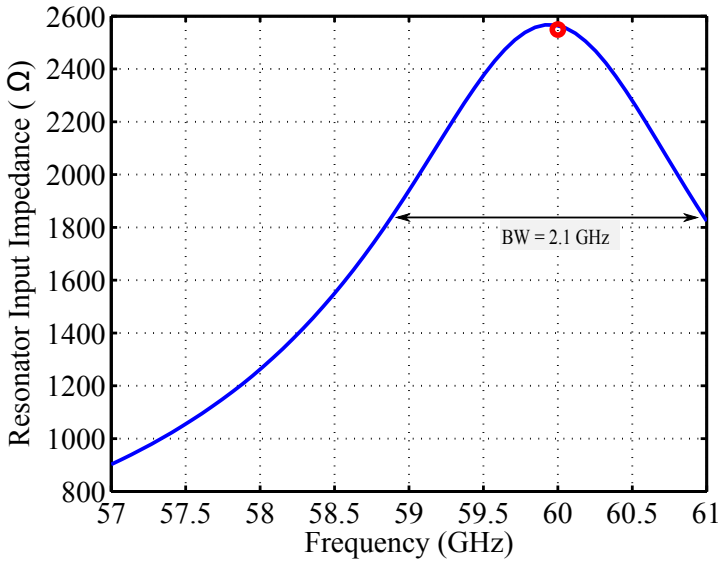

Figure 3.25. Input impedance of the optimum tapered slow-wave CPS resonator. HFSS simulation results for the input impedance the optimum slow-wave tapered CPS resonator. The single red point shows the calculated input impedance from the optimizer results.

Table 3.3. Comparison between the characteristics of different CPS resonators. Comparison of quality factor, resonance frequency and length of different types of quarter-wavelength CPS resonators.

Resonator Type	Length	f_0(GHz)	Q-factor	Q-factor Improvement
Uniform, Simulated (Marcu and Niknejad 2008b)	635 (μm)	62	8.8	reference
Uniform, Measured (Marcu and Niknejad 2008b)	635 (μm)	57.9	8.8	reference
Tapered, Simulated (Marcu and Niknejad 2008b)	498 (μm)	58	15	70.4%
Tapered, Measured (Marcu and Niknejad 2008b)	498 (μm)	54.4	15	70.4%
Slow-wave Uniform, Simulated (Horestani *et al.* 2010)	222 (μm)	60.5	16.2	84%
Slow-wave Tapered Simulated (this work)	320 (μm)	59.9	28.4	220%

the thin film. It is worth mentioning that, since the method exploits a balanced slow-wave CPS, the on-chip sensing structure is very compact and the measurement process benefits from higher immunity to environmental noise.

The results of the parametric study of this chapter show that slow-wave CPS resonators are promising structures for use as high quality factor resonators in CMOS VCOs at millimeter-wave frequencies. Thus, the chapter has proposed two other high quality factor quarter-wavelength resonators operating at 60 GHz. The quality factor of the first resonator is 17.7, which is a 100% improvement compared to the quality factor of an optimized conventional CPS resonator ($Q = 8.8$) operating at the same frequency, and a 10% improvement compared to the slow-wave CPS resonator of this chapter. It also shows a 2 dB improvement in the normalized input impedance at resonance, which results in lower bias current and consequently lower power consumption, when the resonator is used in an oscillator.

In the last section of the chapter, the optimization process for a quarter-wavelength slow-wave CPS resonator with an optimum quality factor at 60 GHz has been presented. Using the Harmony Search optimization method a slow-wave tapered resonator has been designed, demonstrating a significant quality factor improvement of 220% compared to the conventional uniform CPS resonator and 75% improvement compared to the uniform slow-wave resonator. Due to the limitations of certain geometrical and material parameters that we have applied in the optimization process, the on-chip area of the optimized resonator using a slow-wave structure remains reasonable. The minimum width of the signal paths is also limited to $5\,\mu$m, to guarantee a sufficient width for safe use as DC bias of the VCO core. Experimental validation has not been possible in the timeframe of this work, but the validation with published results (Marcu and Niknejad 2008b, Marcu and Niknejad 2008a) provides confidence in the validity.

Inspired from the promising results of the tapered slow-wave CPS, the next chapter is focused on miniaturized metamaterial-inspired resonators with enhanced functionality.

Chapter 4

Miniaturization of Metamaterial-Inspired Filters

MINIATURIZATION of microwave components is of great importance especially for the development of light-weight microwave circuits and antennas for portable wireless devices. In the previous chapter it was shown that metamaterial transmission lines have the potential to be applied as compact high quality factor resonators for cross-coupled CMOS VCOs in millimeter-wave frequency band. This chapter is focused on the miniaturization of microwave filters that is achieved either by miniaturizing metamaterial resonators or through creating resonators with dual-band functionality. To this end, the chapter proposes three compact resonators: In the first section of the chapter a compact double-resonance structure based on the combination of a pair of CSRRs and a defected ground structure (DGS) is proposed. The proposed structure can be used as the building block of dual-band or wideband filters. Next it is shown that complementary spiral resonators can be used for the design of compact bandpass filters with wide upper stopband. Finally, a modified edge-coupled SRR with tapered strip width is proposed in the third section of the chapter. It will be shown both theoretically and experimentally that the proposed shape modification results in a 33% reduction in the resonator's size, or 84% wider fractional bandwidth.

4.1 Introduction

During the last decades RF and microwave technology has had a dramatic impact on the ever-expanding world of information. This impact can be clearly seen from the way people access voice, video and data in virtually every corner of the world, using smart phones, computers and other electronic devices, from various wireless networked services such as WiFi, Bluetooth, Global Positioning Systems (GPS), satellites, and so on.

Miniaturization of the electronic devices is of great importance, especially in order to develop light-weight portable devices, or in the areas such as aerospace, where every gram sent into the outer space contributes to the costs. While during the last decades rapid scaling of microelectronic devices resulted in a high level of miniaturization of electronic devices, the progress was not evenly achieved in other areas. Thus, significant effort is focused on the miniaturization of devices and components in critical areas such as planar microwave circuits, where components generally exhibit large dimensions.

Utilizing metamaterial-inspired TLs, consisting of a host TL loaded with electrically small resonators proves to be an efficient approach towards the miniaturization of planar microwave circuits. Moreover, the electromagnetic properties of these lines can be engineered to achieve enhanced functionalities such as wideband or dual-band operation. Thus, by using metamaterial-inspired TLs, a size reduction can be achieved by miniaturizing each component and/or through providing components with enhanced functionalities.

Thus, arising from the need for compact microwave components, three different structures for the miniaturization of the metamaterial-inspired microwave filters are proposed throughout this chapter.

Section 4.2 proposes a double resonance defected ground resonator. The resonator is composed of complementary split ring resonators (CSRRs) embedded in a defected ground structure (DGS) with a dumbbell shape. Through a parametric study, it is demonstrated that the two resonance frequencies can be independently tuned. Therefore the structure can be used for different applications such as dual-band or wide bandstop filters. Furthermore, since the CSRRs are embedded inside the defection areas of the DGS the proposed structure is very compact.

In Section 4.3, complementary spiral resonators are used in the design of coupled resonator bandpass filters. It will be shown that compared to the bandpass filters based

on open-loop resonators, the proposed filter not only has a more compact size but also benefits from a wider upper stopband.

Finally, Section 4.4 presents a modified edge-coupled split ring resonator (SRR), composed of two concentric metallic rings with a nonuniform strip width. It will be shown that , the shape-modification, which is based on the current and voltage profile in the SRR structure, enables us to reduce the SRR electrical area. Furthermore, it is shown that compared to a uniform SRR, a tapered SRR with the same electrical size provides a stronger resonance as well as a wider bandwidth, as desired in wideband filter design. The theory and simulation results are validated through measurement.

4.2 Compact Filter Element Based on Complementary Split Ring Resonator and Defected Ground Structure

It is well known that periodic arrangements such as photonic bandgap (PBG) structures can be combined with planar transmission lines (TLs) in order to obtain different types of filters (Radisic *et al.* 1998, Yang *et al.* 1999, Kim *et al.* 2000, Yun and Chang 2001). Photonic bandgap structures, however have some drawbacks: Firstly, they consume a large layout area because usually a number of periodic patterns are required for satisfactory operation. Furthermore, it is difficult to define and extract an equivalent circuit model for a PBG unit element. Equivalent circuit models allow for direct application of well known circuit design theories, such as those commonly used in the theory of RF and microwave filters. Because of the lack of an equivalent circuit model for PBG structures, their applications in microwave and millimeter wave circuits are relatively limited (Lim *et al.* 2005).

Recently, defected ground structures (DGSs) have attracted an increasing interest due to their simple planar structure, ease of design, and fabrication with photolitographic techniques (Radisic *et al.* 1998, Yang *et al.* 1999, Kim *et al.* 2000, Lim *et al.* 2002a). Unlike PBGs, a unit element of DGS can be easily modeled and the parameters of the circuit model can be conveniently extracted from electromagnetic simulations or measured data. Furthermore, only a few unit elements of the DGS are required in order to achieve the same frequency response as that of a photonic bandgap structure using many unit cells. This property of the DGS, which results in miniaturized circuits, makes it very popular particularly in the microwave filter design.

In brief, the simplicity of modeling, ease of fabrication and compactness have resulted in vast applications of these structures in many microwave and millimeter wave circuits such as filters, power dividers, couplers or amplifiers (Lim *et al.* 2001, Lee *et al.* 2002, Lim *et al.* 2002b, Lim *et al.* 2002c, Lim *et al.* 2002d, Lee *et al.* 2003). It is worth mentioning that in addition to the intrinsic compactness, a DGS also adds a slow wave characteristic to the host TL. As a result, TLs loaded with DGS can also be applied to design miniaturized microwave structures and components (Yang *et al.* 1999, Yun and Chang 2001, Lim *et al.* 2002d).

On the other hand, as shown in Chapter 2 the complementary split ring resonator (CSRR) is a resonant element that is relatively small compared to the wavelength at the frequency of operation and can be excited by an external time varying magnetic field parallel to the ring axis. Due to negative effective permittivity near the resonance frequency, a CSRR element coupled to a TL is able to inhibit the propagation of electromagnetic waves in a narrow frequency range (Falcone *et al.* 2004a, Falcone *et al.* 2004b).

There are both advantages and disadvantages in using DGS and CSRR structures. A CSRR provides a sharp transition between the stopband and passbands. However, it provides a very narrow rejection band. By contrast, in spite of providing a relatively wide stopband, a DGS suffers from slow transitions between passbands and the stopband. Thus, in this section a novel structure based on the combination of DGS and CSRRs is proposed. The proposed structure is a double-resonance structure that provides a relatively wide rejection band with sharp transitions in the transmission spectrum of the loaded TL. Alternatively, since the two resonances can be controlled independently, the structure can be used to the design of dual-band filters. Furthermore, the structure benefits from a compact size.

4.2.1 Defected Ground Structure

Fig. 4.1 shows the three dimensional and top views of a microstrip line with a dumbbell-shaped defected ground (Kim *et al.* 2000). The defected structure is composed of two rectangular areas etched in the ground layer on both sides of the microstrip line. The two rectangular areas are connected through a narrow slot laid beneath and across the microstrip line.

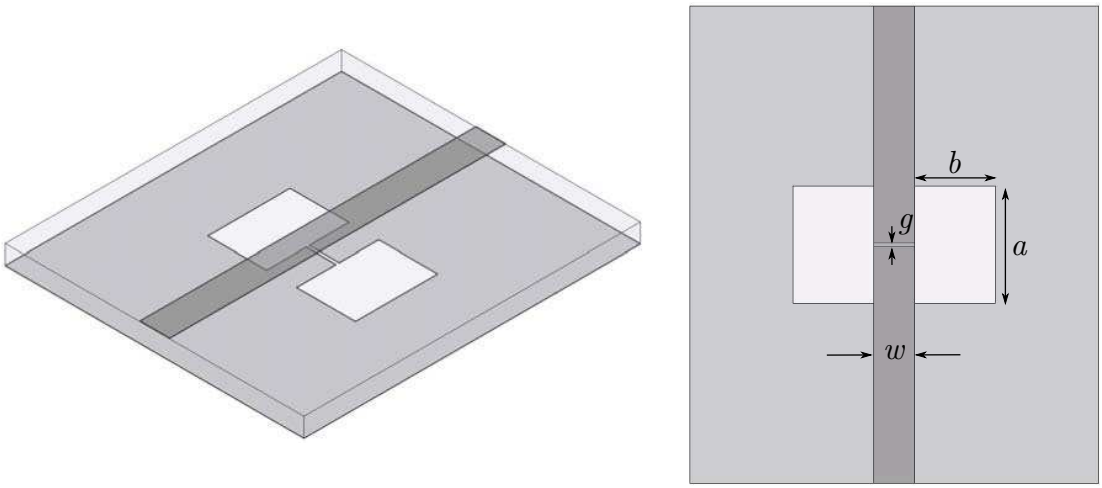

(a) (b)

Figure 4.1. Layout of a microstrip line with defected ground. 3D view (a) and top view (b) of a microstrip line loaded with a dumbbell-shape DGS.

The TL, shown in Fig. 4.1(a), has a width of $w = 1.34$ mm resulting in a characteristic impedance of 50 Ω at frequencies in the *C* band (4 to 8 GHz) on a substrate with a relative permittivity of 10 and a thickness of 1.65 mm. All the simulations are performed using the full-wave 3D electromagnetic field simulation tool HFSS. Fig. 4.2 depicts the simulated transmission coefficients of the structure for slot widths $g = 0.1$ mm, 0.3 mm and 0.5 mm, and rectangular defect lengths $a = 1.6$ mm, 2.2 mm and 2.8 mm. For simplicity, the rectangular defect width $b = 1.6$ mm is kept constant in all simulations. The figures clearly show that the TL loaded with DGS provides a stopband with slow transitions between stopband and passbands. The simulation results also show that in a TL with a dumbbell shape DGS, an increase in the dimensions of the rectangular defects results in a decrease in the resonance frequency. Narrowing the slot width decreases the resonance frequency as well. These effects can be explained by the current and charge distributions in the ground layer. In fact, charges are accumulated on both sides of the slot and therefore this adds some series capacitance to the TL, while the return current route becomes longer because of the rectangular defects, which results in an increase in the inductance of the TL (Guan *et al.* 2005). Therefore, a microstrip line loaded with a dumbbell shape DGS can be modeled with a parallel *LC* resonator connected in series with the transmission line model as shown in Fig. 4.3(a). In this model the capacitor represents the slot while the inductor represents the rectangular defects. Thus, the resonance occurs at $\omega_0 = 1/(LC)^{1/2}$, which shows that a TL with

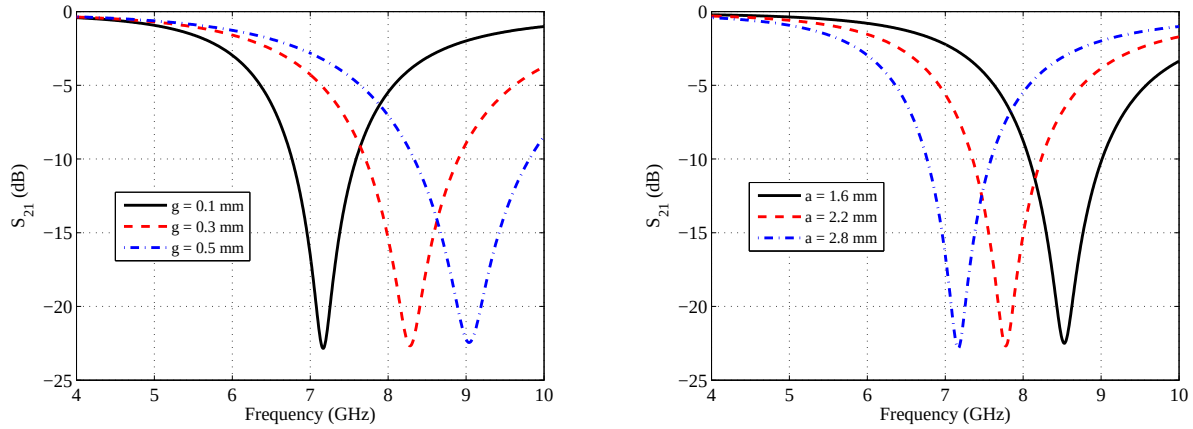

Figure 4.2. Transmission coefficient of a DGS. Variation of the resonance frequency in terms of (a) the rectangular defect slot width g, with $a = 2.8$ mm and (b) the width a, with $g = 0.1$ mm. The substrate thickness is 1.65 mm with a relative permittivity of 10 for all cases.

dumbbell shape DGSs has a bandstop property.

Two different approaches can be exploited to extract the parameters of the equivalent circuit model, i.e., the curve fitting approach and the analytical approach. In the curve fitting approach the S-parameters of the DGS-loaded TL are first simulated or measured. In a second step an optimization technique is used to fit the S-parameters of the circuit model to the simulated or measured S-parameters. In the analytical approach, the frequency response of the DGS is compared to the response of a standard prototype filter. Based on this comparison, the values of the circuit model components are extracted through appropriate analytical equations. Fig. 4.3 depicts the equivalent circuit of the DGS and the prototype of the one-pole Butterworth low-pass filter (Lim *et al.* 2002a). These two circuits must have an equivalent impedance and admittance at the cutoff frequency. Also, L and C must comply with $\omega_0 = 1/\sqrt{LC}$ to have a resonance at ω_0. Thus, L and C in the equivalent circuit model can be obtained from

$$C = \frac{\omega_c}{Z_0\, g_1} \cdot \frac{1}{\omega_0^2 - \omega_c^2}, \tag{4.1}$$

$$L = \frac{1}{\omega_0^2\, C}, \tag{4.2}$$

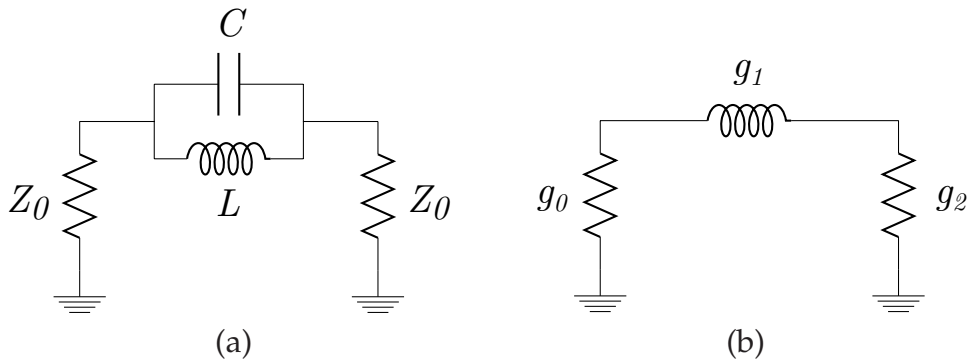

Figure 4.3. Equivalent circuit model of a DGS. (a) Equivalent circuit model of the microstrip line with dumbbell-shaped defected ground (Lim *et al.* 2002a), and (b) one-pole Butterworth lowpass filter prototype.

where ω_c is the 3-dB cutoff frequency, $g_1(=2)$ is the element value of the one-pole Butterworth LPF prototype and $Z_0 = 50\,\Omega$ is the port impedance of the filter.

4.2.2 Complementary Split Ring Resonators (CSRRs)

The top view of a microstrip line loaded with two CSRRs etched in the ground layer is depicted in Fig. 4.4(a). Note that in contrast to the conventional method of loading a TL with CSRRs, in this configuration a pair of CSRRs are etched on both sides of the line. For 3D electromagnetic simulation of the structure the substrate thickness of 1.65 mm and the relative permittivity of 10 are again used. The CSRR dimensions are chosen as $a = 2.8$ mm, $b = 1.6$ mm, $c_1 = c_2 = 0.2$ mm, $d = 0.1$ mm and the gap $g = 0.1$ mm. The simulated transmission coefficient of the structure, depicted in Fig. 4.4(b), shows that the CSRR-loaded microstrip line of Fig. 4.4(a) inhibits the transmission of electromagnetic waves in a narrow band of frequency in the vicinity of the CSRRs' resonance frequency. Compared to the stopband of the microstrip line loaded with a DGS, the rejection band of the CSRR-loaded TL is sharper and narrower.

As mentioned in Chapter 2 a unit cell of the CSRR-loaded TL can be modeled as a parallel *LC* resonator, which is capacitively coupled to the microstrip line as shown in Fig. 4.5. In this model C_{cpl} represents the electric coupling between the CSRR and the TL whereas the parallel *LC* represents the equivalent capacitance and inductance of the CSRR itself (Baena *et al.* 2005). The parameters of the equivalent circuit model can be extracted using either analytical method or curve fitting method (Bonache *et al.* 2006b). It is well known that the resonance frequency of a TL loaded with CSRRs can

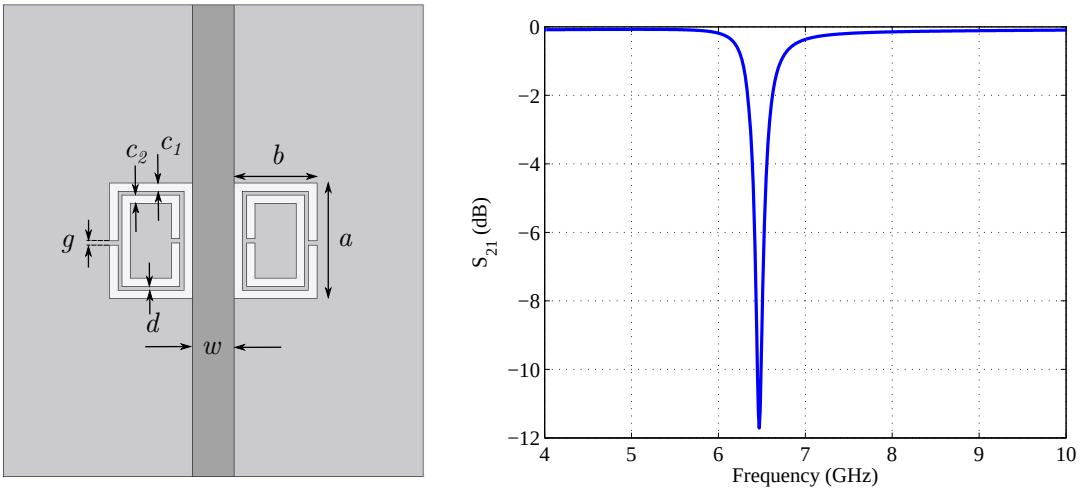

(a) (b)

Figure 4.4. CSRR-loaded microstrip line. Microstrip line loaded with a pair of CSRRs, (a) the top view and (b) the simulated transmission coefficient of the structure.

be changed by manipulating the physical dimensions of the CSRRs. For instance, an increase in c_1 or c_2 results in a decrease in C_c, which in turn results in an increase in the resonance frequency.

Again, it is worth emphasizing that the present circuit models provide a significant advantage for the DGS and CSRR, namely that a single element of the structure can be modeled and all the parameters of the model can be extracted. In contrast, periodic structures such as photonic bandgaps impose difficulties in the definition and modeling of the unit elements.

4.2.3 Compact Filter Element Based on CSRR and DGS

Fig. 4.6 shows the three dimensional and top view of a microstrip line loaded with a combined CSRR-DGS structure. The defected structure can be assumed either as two CSRRs connected to each other through a slot line, or as two CSRRs embedded inside a dumbbell-shape DGS. The latter consideration gives a better intuition about the behavior of the structure. Fig. 4.7 illustrates the effects of changing the different dimensions of the CSRRs on the transmission coefficient S_{21} of the CSRR-DGS loaded microstrip line. The same substrate and TL dimensions as in the two previous simulations are used for the simulations of the CSRR-DGS structure. For all the simulations shown in Fig. 4.7 $a = 2.8$ mm, $b = 1.6$ mm, and $g = 0.1$ mm to keep the DGS dimensions

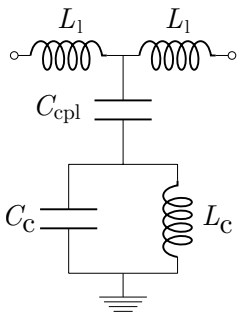

Figure 4.5. Equivalent circuit model of a CSRR-loaded microstrip line. Equivalent circuit model of a microstrip line loaded with a pair of CSRRs. In this model, C_{cpl} represents the electric coupling between the CSRR and the TL, whereas the parallel LC represents the equivalent capacitance and inductance of the CSRR itself.

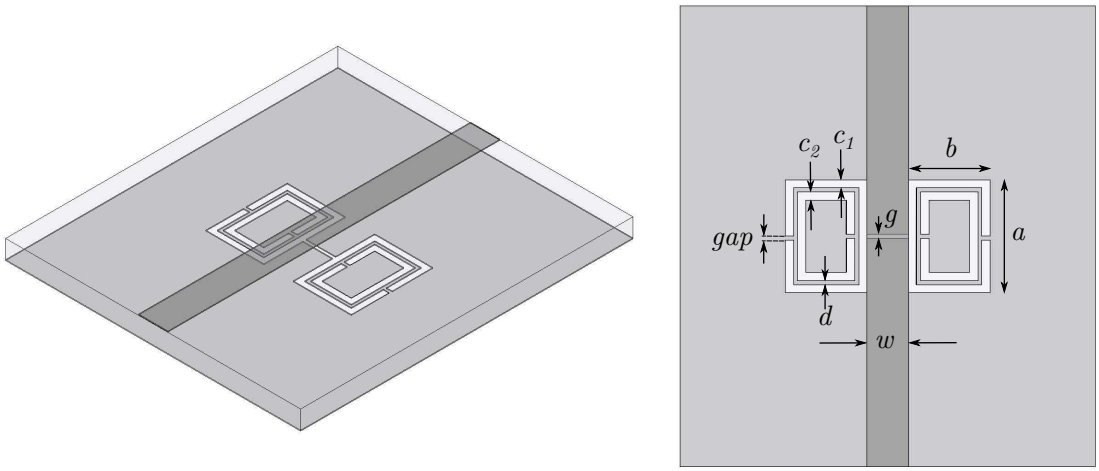

(a) (b)

Figure 4.6. Layout of the proposed CSRR-DGS. Three dimensional (a) and top view (b) of a microstrip line loaded with a CSRR-DGS. The structure can be either considered as a pair of complementary split ring resonators connected to each other through a slot or two CSRRs embedded inside the rectangular defect of a DGS.

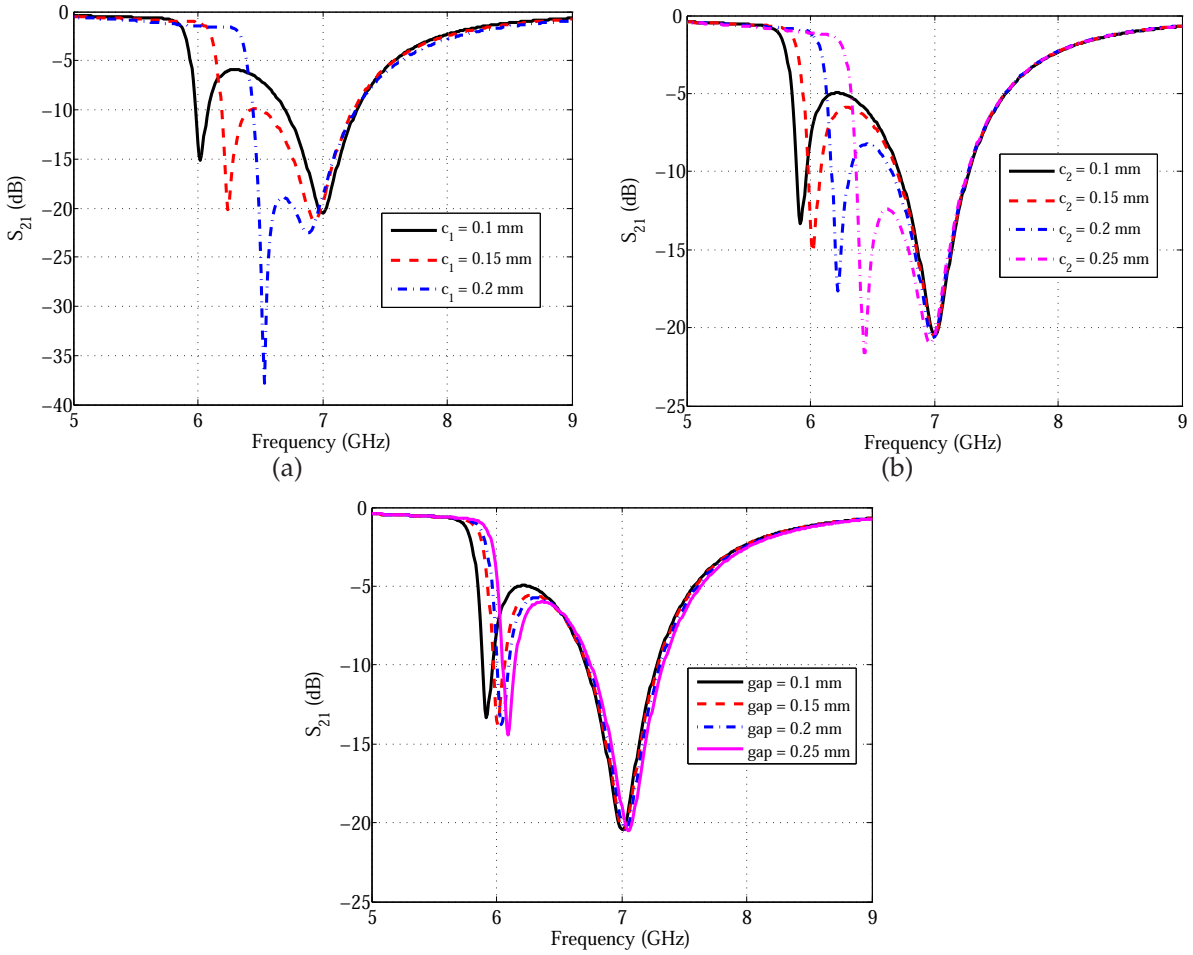

Figure 4.7. Simulated transmission coefficients of a CSRR-DGS-loaded microstrip line. Simulation results for the S_{21} of a microstrip line loaded with a CSRR-DGS. The results show that any change in c_1, c_2 and gap size only changes the resonance frequency of the CSRR and does not have a significant affect on the DGS resonance frequency.

constant. Fig. 4.7.(a) depicts the variation of the resonance frequencies in terms of c_1, which is the width of the outer slot of the CSRRs as shown in Fig.4.6(b). This parametric study shows that although a decrease in c_1 leads to an increase in the frequency of the lower resonance it has a very small effect on the higher resonance frequency. Thus, it can be deduced that one of the resonances (lower resonance in this case) is related to the CSRR, while the other resonance (higher resonance in this case) is due to the DGS. In a similar manner Figs. 4.7(b) and (c) show that varying c_2 and the gap size, does not have a significant effect on the frequency of the second resonance. As shown in

Section 4.2.1, the second resonance can be changed by adjusting the dimensions of the rectangular defect or the slot of the DGS.

Therefore, from these simulations it can be deduced that the resonance related to the CSRRs can be tuned independently from the resonance of the DGS. This is one of the most important advantages of the proposed structure compared to other dual resonance structures such as combined SRR-DGS, where there is a strong coupling between the two components (Safwat *et al.* 2007). This feature makes it much easier to design and realize different RF and microwave circuit components such as dual stopband filters or wide stopband filters. It is worth mentioning that since the CSRR is located inside the rectangular defect of the DGS the structure footprint is kept compact. This is another important characteristic of the proposed structure, which can lead to miniaturized circuits.

4.3 Miniaturized Complementary Spiral Resonator for use as Bandpass Filter with Wide Upper Stopband

This section is focused on the application of complementary spiral resonators to the design of compact planar bandpass filters with wide upper stopband. Based on an inductively loaded transmission line model for the complementary spiral resonator it is shown that the ratio of the spurious resonance frequency to the fundamental resonance frequency can be increased. Comparing two filters realized by conventional open-loop resonators and complementary spiral resonators it is shown that the utilization of complementary spiral resonators not only results in a more compact filter but also a wide upper stopband is achieved.

4.3.1 Introduction

Because of their planar structure and ease of fabrication, conventional microstrip bandpass filters such as end-coupled and parallel-coupled half-wavelength resonator filters are widely used in many microwave applications (Hong and Lancaster 2001). However, since the conventional bandpass filters are relatively large in size, large efforts were invested in the miniaturization of these types of filters, for example by using slow-wave or metamaterial inspired structures (Hong and Lancaster 1997, Bonache *et al.* 2004, García-García *et al.* 2006, Bonache *et al.* 2006a).

Furthermore, while bandpass filters with wide stopband are required in many applications, conventional bandpass filters suffer from unwanted harmonic passbands (Li *et al.* 2010). To overcome the spurious passband limitation, many approaches have been proposed. For instance, modification of the capacitance and inductance of the coupled line bandpass filters by wiggly-lines have been proposed by Lopetegi *et al.* (2004) and Lopetegi *et al.* (2001) to create a rejection band that suppresses the spurious passband. Utilizing dissimilar resonators such as half- and quarter-wavelength resonators is another approach for spurious passband suppression (Lin *et al.* 2006). Several dissimilar resonators with discriminating coupling can be used to obtain zero coupling coefficient at third harmonic that results in suppressing the third spurious passband and increases the rejection level in the filter's stopband (Li *et al.* 2010). However, these methods are rather complicated and since they are based on either half- or quarter-wavelength resonators the synthesized filters are relatively large in size. Other approaches such as adding metamaterial particles, e.g. SRRs or CSRRs to conventional bandpass filters have been used to eliminate the spurious passband (García-García and Martín 2004). Due to the slow-wave effect of these structures, utilizing these methods also results in more compact filters. Note that in these cases, metamaterial-inspired resonators are not the main building blocks of the filter, they are rather used as an extra part to eliminate the harmonic passband (Abdel-Rahman *et al.* 2005).

Thus, in this section an alternative approach is used in which complementary spiral resonators (CSRs) are utilized as the central building blocks of a coupled resonator bandpass filter. It is shown that by utilizing the CSRs, a coupled resonator bandpass filter can be designed that is not only compact in size but more importantly has a wide upper stopband.

4.3.2 Complementary Spiral Resonator and Analysis of Spurious Passband

One of the widely used methods for designing compact bandpass filters with wide stopband is based on capacitively loaded coupled microstrip open-loop resonators (Hong and Lancaster 1997). Here, the dual approach is proposed in which CSRs are used as the building blocks of a compact bandpass filter with suppressed spurious passband.

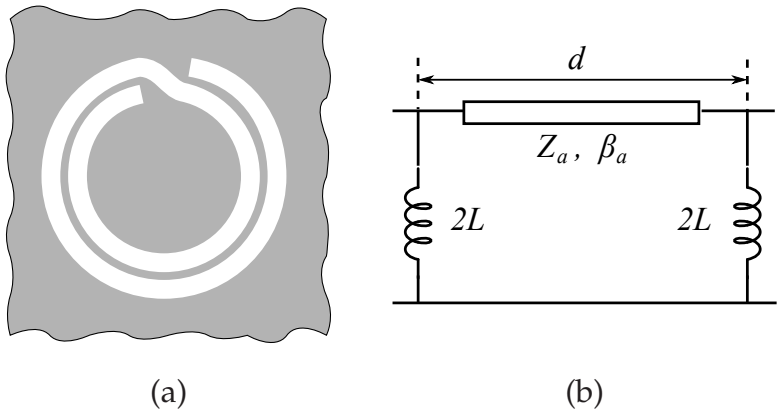

Figure 4.8. Layout and circuit model of a CSR. (a) Layout of a CSR. The gray shading shows the patterning of the ground plane. (b) The equivalent circuit model of the CSR. The model is composed of a TL with characteristic impedance Z_a, propagation constant β_a and length d, which is loaded with $2L$ inductors on each end.

Figure 4.8 illustrates the geometry and a circuit model of the CSR. The model is composed of a TL with characteristic impedance Z_a, propagation constant β_a and length d, which is loaded with $2L$ inductors at each end. Following the same approach as for the analysis of the capacitively loaded microstrip line resonators presented by Hong and Lancaster (1997) or using the duality theorem, it can be shown that loading the half-wavelength resonator with inductors not only reduces fundamental (f_0) and second harmonic (f_1) resonant frequencies but also results in a higher ratio of the second harmonic resonance frequency to the fundamental resonance frequency, i.e. f_1/f_0. Figure 4.9 demonstrates the simulated f_0 and f_1 calculated with a circuit model for of an ideal $\lambda/2$ resonator (at 2 GHz), which is loaded with different inductor values. As expected, when $L = 0$ the first and second resonant frequencies are at 2 GHz and 4 GHz, respectively. However, as the loading inductance is increased both f_0 and f_1 are shifted down, thus the resonator's electrical size is decreased. The figure also depicts the ratio of the second harmonic resonance frequency to the fundamental resonance frequency f_1/f_0 of the structure versus inductance value L. The graph clearly shows that even though both resonant frequencies are decreased, the ratio f_1/f_0 is increased. This property of the CSR can be used in the design of compact coupled resonator bandpass filters with a wide upper stopband.

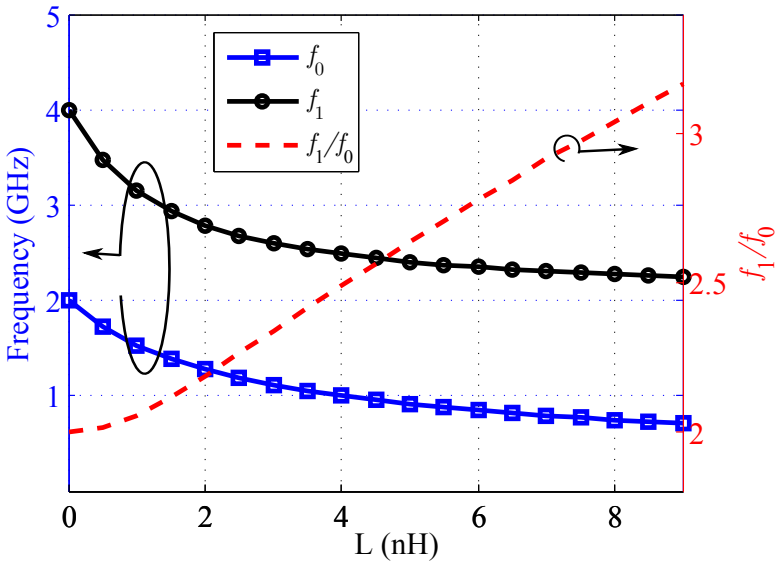

Figure 4.9. f_1/f_0 of an inductively loaded TL. Simulated fundamental resonance frequency f_0 and second harmonic resonance frequency f_1 of an inductively loaded TL resonator along with the ratio of f_1/f_0. The results are computed for the circuit model of Fig. 4.8(b)

4.3.3 Two-pole Bandpass Filter with Wide Upper Stopband

This section provides a comparison between the level of compactness and the bandwidth of the upper stopband in two narrow-band bandpass filters based on coupled complementary resonator. The first filter, shown in Fig. 4.10, is a two-pole filter in which conventional complementary open-loop resonators are used, while the second one, illustrated in Fig. 4.11, is a similar filter in which CSRs are used as the filter building blocks. The filters are designed to meet the following specifications

Center frequency	2.7 GHz
3-dB bandwidth	200 MHz
Passband loss	3 dB Max

Given the specifications of the filter, the coupling coefficient M_{12} and the external quality factor Q_e are obtained from (Hong and Lancaster 2001)

$$Q_e = \frac{g_0 g_1}{\text{FBW}} = 41 \tag{4.3}$$

$$M_{12} = \frac{\text{FBW}}{\sqrt{g_1 g_2}} = 0.058, \tag{4.4}$$

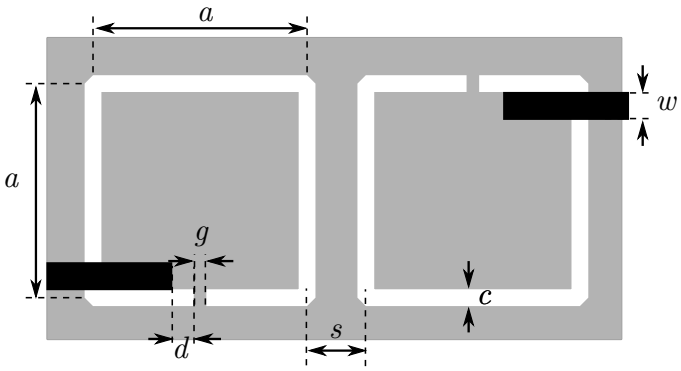

Figure 4.10. Second-order bandpass filter based on coupled open-loop resonators. Structure of a second-order bandpass filter based on coupled complementary open-loop resonators. The black lines indicate the 50 Ω feeding microstrip lines on the top of the substrate, whereas the gray shading shows the patterning of the ground plane on the bottom side of the substrate.

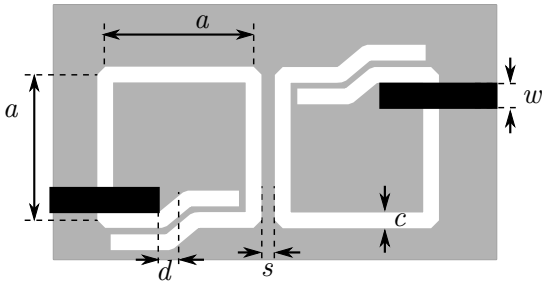

Figure 4.11. Second-order bandpass filter based on coupled CSRs. Structure of a second-order bandpass filter based on coupled CSRs. The black lines indicate the 50 Ω feeding microstrip lines on the top of the substrate, whereas the gray shading shows the patterning of the ground plane on the bottom side of the substrate.

where g_0, g_1 and g_2 are the lowpass prototype elements, and FBW denotes the fractional bandwidth of the filter. The structure of both bandpass filters and the variables describing the dimensions of the resonators are depicted in Figs. 4.10 and 4.11. The structure is realized on a substrate with a relative permittivity of 10.2 and a thickness of 0.78 mm. In the figure, the black lines indicate the 50 Ω feeding microstrip lines on the top of the substrate, whereas the gray shading shows the patterning of the ground plane on the bottom side of the substrate.

The next step of the filter design is the characterization of the coupling between the adjacent resonators as well as the external quality factors. The coupling coefficient of the adjacent resonators can be obtained from (Hong and Lancaster 2001)

$$M_{ij} = \frac{f_2^2 - f_1^2}{f_2^2 + f_1^2}, \tag{4.5}$$

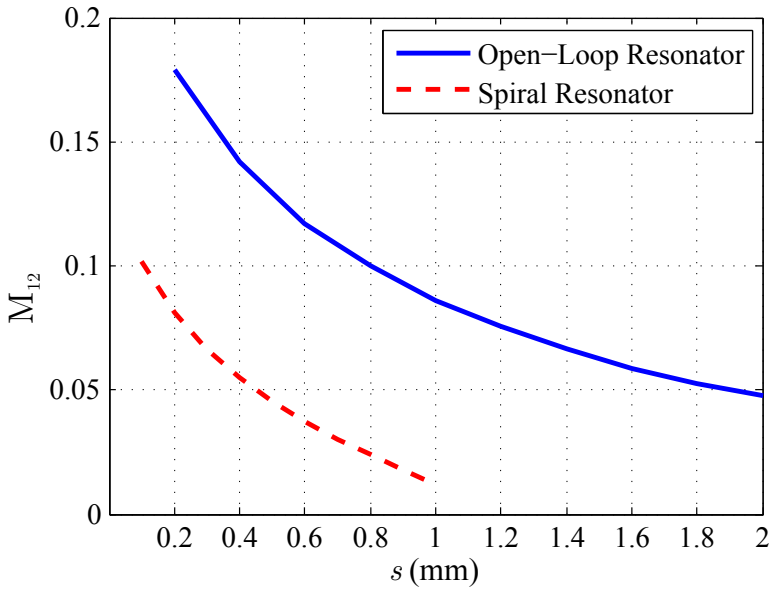

Figure 4.12. Coupling coefficients of open-loop and CSR resonators. Simulated coupling coefficient of pairs of complementary open-loop resonators (blue solid line) and that of pairs of CSRs (red dashed line) as a function of the distance between the paired resonators s.

where f_1 and f_2 are the two resonant frequencies of the pair of coupled resonators. The external quality factor Q_e can be characterized by (Hong and Lancaster 2001)

$$Q_e = \frac{2\pi f_0 \tau_{11}}{4}, \tag{4.6}$$

where f_0 is the resonance frequency and τ_{11} is the group delay of S_{11}.

The electromagnetic simulation tool Agilent Momentum is used for the characterization of the coupling coefficients and the external quality factors. Figure 4.12 depicts the simulated coupling coefficient of a pair of coupled complementary open-loop resonators (blue solid line) and that of a pair of coupled CSRs (red dashed line) versus the spacings between the resonators in each pair. The simulated quality factor of the external coupling between the complementary open-loop resonator as well as that of the CSR with 50 Ω microstrip line, are depicted in Fig. 4.13. On the basis of the graphs of the extracted coupling coefficients and the external quality factors, two bandpass filters with the given specifications are designed and simulated. Dimensions of the designed filters are given in Table. 4.1.

Figure 4.14 compares the simulated transmission coefficients of both bandpass filters, showing that both filters meet the specifications, however, the bandpass filter based

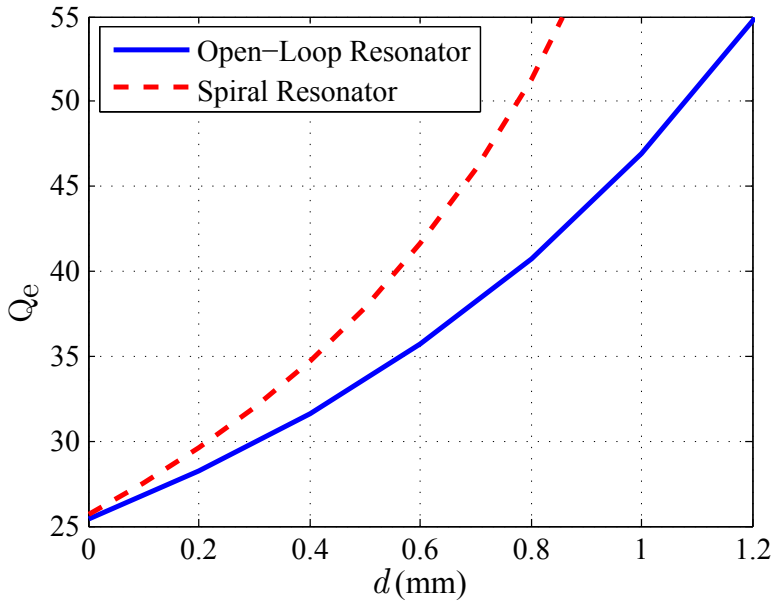

Figure 4.13. External quality factor of open-loop- and CSR-loaded microstrip lines. Simulated external quality factor of the coupling between complementary open-loop resonators (blue solid line) as well as CSRs (red dashed line) with their microstrip feed line as a function of the distance between feed line and symmetry line of the resonators d.

Table 4.1. Dimensions of the designed filters. Dimensions of complementary open-loop filter, shown in Fig. 4.10, as well as the CSR filter, shown in Fig.4.11.

Dimension	Complementary Open-loop Resonator	Complementary Spiral Resonator
a	6.8 mm	4.1 mm
c	0.4 mm	0.4 mm
g	0.1 mm	0.1 mm
d	0.8 mm	0.6 mm
s	1.6 mm	0.4 mm

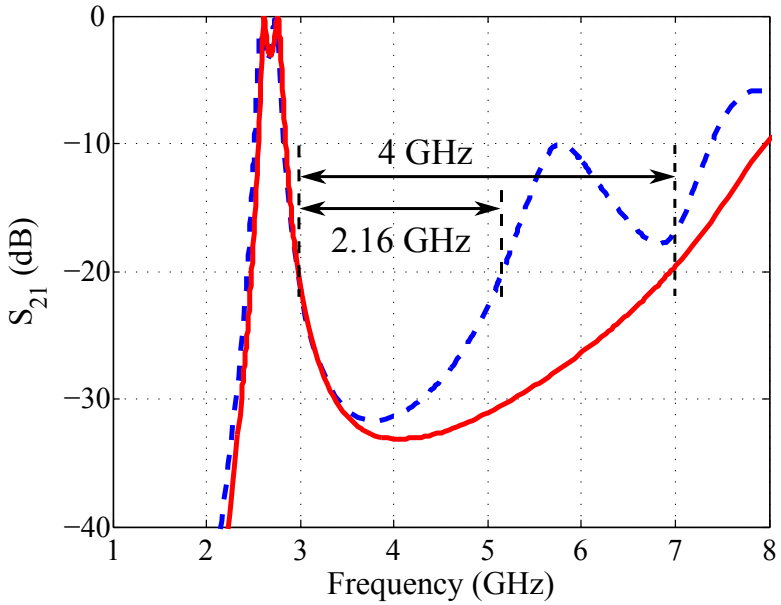

Figure 4.14. Comparison between the transmission coefficinets of filters based on open-loop- and CSR-loaded lines. Comparison between the simulated transmission coefficients of narrowband coupled resonator bandpass filter realized with complementary open-loop resonators (blue dashed line) and that of the same filter realized with CSRs (red solid line).

on CSRs benefits from an 85% wider upper stopband (defined at 20 dB rejection). Furthermore, the filter based on the CSR has a more compact size, i.e. a patterned area of 35 mm^2 compared to 103 mm^2 in the case of the filter based on complementary open-loop resonators.

These results demonstrate how geometrical modifications of the metamaterial-inspired resonators can enhance the performance of compact filters. A further example is shown in the next section.

4.4 Split Ring Resonators with Tapered Strip Width for Wider Bandwidth and Enhanced Resonance

This section presents a modified edge-coupled split ring resonator. The proposed SRR is composed of two concentric metallic rings with a nonuniform strip width, which is tapered based on the current and voltage profile in the SRR structure. In contrast to other SRR miniaturization methods, which are based on increasing the equivalent capacitance of the SRR, the proposed SRR benefits from both increased capacitance and

inductance to preserve the strength and bandwidth of the resonance. It is also shown that compared to a uniform SRR, a tapered SRR with the same electrical size provides a stronger resonance with 84% wider bandwidth, as desired in wideband filter design. The theory and simulation results are validated through measurement.

4.4.1 Introduction

Generally there are two main methods for the realization of planar metamaterials with negative permeability. In the first method a composite right/left-handed TL is achieved by periodically loading a conventional TL with series capacitors and shunt inductors (Lai *et al.* 2004). The second method is based on loading a conventional TL by sub-wavelength resonators, such as SRRs (Pendry *et al.* 1999, Smith *et al.* 2000). In spite of the advantages of the metamaterial structures based on the SRRs, such as easier fabrication and application in bulk metamaterial media, SRRs are more lossy and have a narrower bandwidth (Lin and Cui 2008).

Many investigations have aimed at achieving SRRs with small electrical size, wide bandwidth and strong resonance (Marqués *et al.* 2002, Baena *et al.* 2004, Hao *et al.* 2005). It has been shown using equivalent circuit models for SRRs that the fractional area occupied by the interior of the resonator's ring within the unit cell can be enlarged in order to achieve a relatively wider bandwidth resonance (Marqués *et al.* 2002, Baena *et al.* 2005). However, this is in conflict with the miniaturization of the structure, which is required for compact filters or to realize an effective medium. In order to create miniaturized left-handed media, other sub-wavelength resonators have been proposed. For instance, compared to the edge-coupled SRR proposed by Pendry *et al.* (1999), the broad-side coupled split ring resonator (BC-SRR) proposed by Marqués *et al.* (2002) benefits from smaller electrical size. However, due to the increased equivalent capacitance, the resonator has a narrower bandwidth. Furthermore, the fabrication of the structure is technologically more complex because of the need for a multilayer substrate. Other structures such as spiral resonators proposed by Baena *et al.* (2004) are compact and uniplanar, but compared to the edge-coupled SRRs, they are less efficient and provide weak resonances. Alternatively, methods, such as loading a single split ring resonator with a semi-lumped *LC* resonator suggested by Lin and Cui (2008) have been used for controlling the resonance bandwidth. However, this method results in narrower bandwidths with weaker resonances, and since it is based on single split ring, the structure has a relatively larger electrical size.

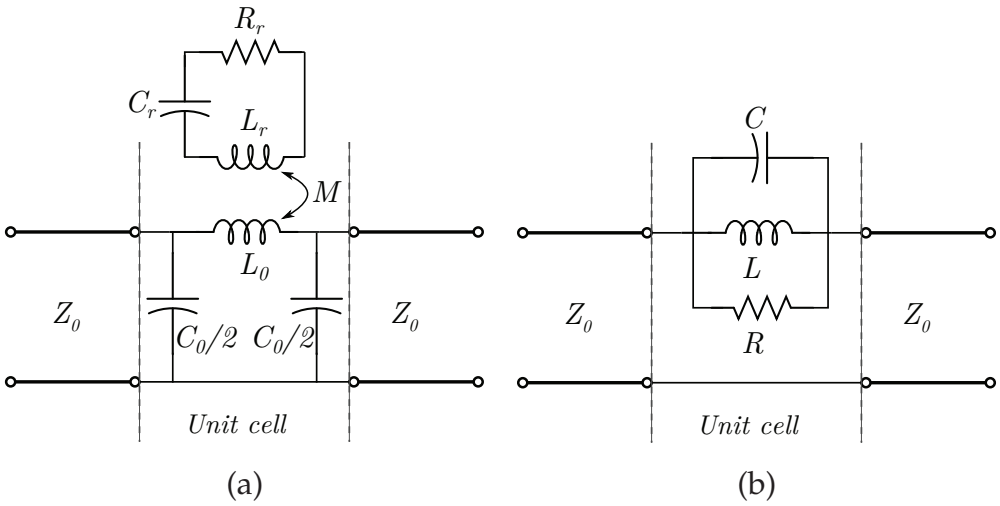

Figure 4.15. Equivalent circuit model of an SRR-loaded TL. Equivalent circuit model (Lin and Cui 2008) of an SRR loaded TL, including the SRR loss (a), and the simplified equivalent circuit model (b).

In this section a modified edge-coupled SRR with reduced electrical size is proposed. The proposed SRR has a strip width tapered in steps determined by considering the distribution of the current and voltage in the SRR structure. It is also shown that compared to the conventional SRRs, a tapered SRR with the same electrical size provides a wider bandwidth and a stronger resonance.

4.4.2 Resonance Characteristics of Split Ring Resonators Coupled to a Transmission Line

Fig. 4.15(a) depicts a simple circuit model for a unit cell of a TL loaded with an SRR, where L_r and C_r are equivalent inductance and capacitance of the SRR, respectively, and R_r models the SRR's losses. The magnetic coupling between the SRR and the loaded TL, M, can be approximated by $M = L_r \cdot \alpha F$ (Baena *et al.* 2005), where F is the fraction of the cell area occupied by the SRR and α is a fitting parameter. Near resonance, the model can be further simplified into the circuit model of Fig. 4.15(b) (Lin and Cui 2008), where $L = M^2/L_r$, $C = L_r/(\omega_0^2 M^2)$, $R = \omega_0 Q_0 M^2/L_r$. The resonance frequency can be obtained from

$$\omega_0 = \frac{1}{\sqrt{LC}} = \frac{1}{\sqrt{L_r C_r}}. \tag{4.7}$$

The coupling factor of the TL with a loading resonator is defined as the ratio of the resonator resistance at the resonance frequency to the sum of the external resistances which are observed from the resonator ports (Khanna and Garault 1983). Using the simplified model of the SRR-loaded TL, Fig 4.15(b), the coupling factor β can be expressed in terms of the circuit model parameters as

$$\beta = \frac{R}{R_{\text{ext}}} = \frac{R}{2Z_0} = \frac{1}{2Z_0 R_r}.\frac{L_r}{C_r}.(\alpha F)^2. \tag{4.8}$$

The coupling factor can also be obtained from simulated or measured scattering parameters as (Khanna and Garault 1983)

$$\beta = \frac{|S_{11_0}|}{|S_{21_0}|}, \tag{4.9}$$

where S_{11_0} and S_{21_0} are the reflection and the transmission coefficients of the structure at the resonance frequency f_0, respectively. It is worth emphasizing that based on (4.9) a high coupling factor translates into a high ratio of $|S_{11}|$ and $|S_{21}|$ at resonance, which means a stronger (i.e. higher Q) resonance. Thus, even though based on (4.7) the resonance frequency and electrical size of the SRR can be reduced by increasing either C_r or L_r, (4.8) and (4.9) show that decreasing the resonance frequency by increasing the SRR's equivalent capacitance results in a smaller coupling factor and consequently a weaker resonance. For instance, as shown by Withayachumnankul *et al.* (2010), a smaller electrical size, which is achieved by using interdigital capacitor, leads to a weak resonance. In contrast, (4.8) shows that increasing the SRR's equivalent inductance not only reduces the electrical size of the particle but also increases the coupling coefficient and results in a stronger resonance.

By using the following simplified equation of the loaded bandwidth for the structure (Lin and Cui 2008),

$$\text{BW}_\text{L} \approx \sqrt{\frac{L_r}{C_r}}.\frac{(\alpha F)^2}{2Z_0}, \tag{4.10}$$

it is also clear that while increasing the C_r reduces the resonance bandwidth, increasing the SRR's equivalent inductance L_r results in a resonance with a wider bandwidth, which is required in applications such as wideband filter design.

4.4.3 Tapered Split Ring Resonator

High level of miniaturization, while preserving the strength and bandwidth of the resonance, can be achieved by simultaneously increasing the equivalent capacitance and

inductance of the SRR. However, there is a conflict between increasing the inductance and capacitance of the SRR, i.e., increasing the equivalent inductance of the SRR by using widely spaced narrow rings results in a smaller equivalent capacitance, and vice versa.

In order to simultaneously increase the equivalent inductance and capacitance of an SRR structure, an SRR with tapered strips width is proposed here. A concept of tapering a TL based on the voltage and current distribution along the TL to improve the TL's quality factor has been used for different applications, especially for obtaining high quality factor resonators (Marcu and Niknejad 2008b, Horestani *et al.* 2011a), as also demonstrated in Chapter 3. Since there is a similar current distribution along the SRR rings (Baena *et al.* 2004), as schematically shown with arrows in Fig. 4.16 (a), a similar tapering strategy can be used to achieve an SRR with simultaneously increased equivalent inductance and capacitance. In fact, as shown in Fig. 4.16(b), an SRR with a lower resonance frequency can be realized by narrowing the SRR's rings where the current is maximal, i.e., in the middle of the rings, and widening the rings where voltage is maximal, i.e., close to the rings' splits.

To verify the theory, TLs loaded with two types of tapered SRRs are simulated and compared to a uniform SRR loaded TL. In all the cases, SRRs with outer edge length $a = 10$ mm are coupled to a $50\,\Omega$ microstrip line with width $w = 2.3$ mm on a 0.78 mm thick Duroid substrate with relative permittivity $\epsilon_r = 2.2$ and loss tangent $\tan(\delta) = 0.0009$. For the uniform SRRs, $c = 1$ mm, $g = 0.5$ mm, and d is set to be 0.2 mm. The tapered SRRs have the same dimensions as the uniform SRRs, however, the ring widths are narrowed in their middle segment to $c_l = 0.2$ mm and they are widened on each side of the split to $c_c = 1.5$ mm. Note that as shown in Fig. 4.16, for the sake of simplicity, square-shaped piecewise tapered SRRs are used.

Fig. 4.17 compares the simulated transmission coefficient of the structure based on the tapered SRRs (black line) to that of the structure based on the uniform SRRs (blue line). As predicted by the theory, the figure shows that by adapting the segment width of the SRRs, the resonance frequency is reduced by about 18% from 2.88 GHz for the uniform SRRs to 2.35 GHz in the case of tapered SRRs, which translates into 33% reduction in the SRRs' electrical area. Furthermore, the fractional bandwidth is increased slightly from 1.5% to 1.8%.

Fig. 4.17 also shows the simulated transmission coefficient of a tapered SRR with increased gap size $g = 3.6$ mm, and inter-ring spacing $d = 1$ mm (red line). Note that

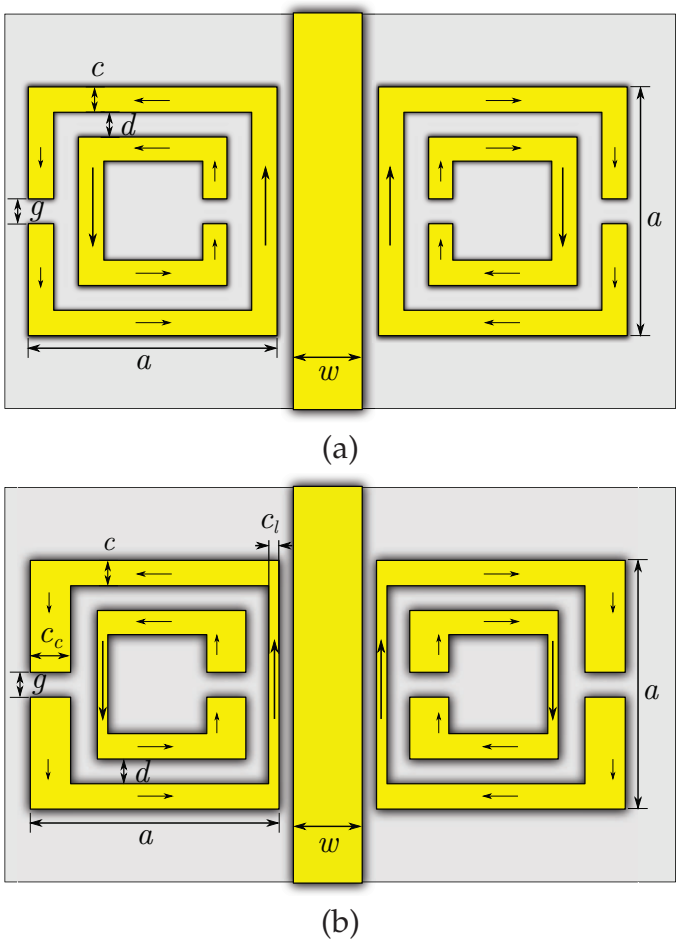

Figure 4.16. Layout of the microstrip lines loaded with uniform and tapered SRRs. Microstrip line loaded with a pair of uniform SRRs (a) and tapered SRRs (b). The arrows schematically depict the relative current distribution in different segments of the SRRs' rings

while tapering the SRR increases the equivalent inductance of the SRR, increasing the gap and inter-ring spacing decreases the equivalent capacitance of the SRR. Thus, the tapered SRR can be designed with the same resonance frequency as the uniform SRR. However, compared to the uniform SRR, the tapered SRR benefits from a higher L_r to C_r ratio. As predicted from (4.8), (4.9) and (4.10), the simulation results show that compared to the uniform SRR, the tapered SRR exhibits a stronger resonance and has a fractional bandwidth of 2.8%, i.e., 84% wider than the uniform one.

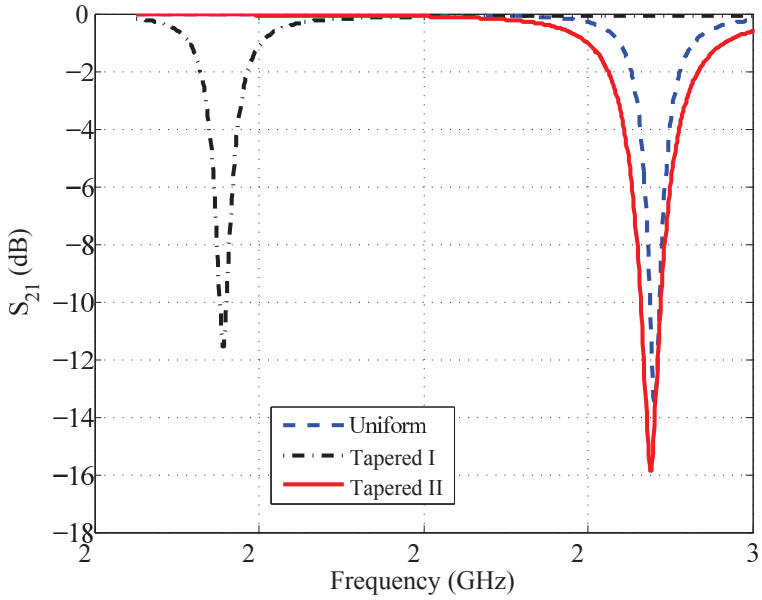

Figure 4.17. Comparison between the transmission coeffcients of TLs loaded with uniform and tapered SRRs. Simulated transmission coefficients of TLs loaded with uniform SRRs (blue dashed line) and two types of tapered SRRs (black dashed line and red continuous line).

4.4.4 Experimental Results

In order to validate the theory and simulation results, microstrip lines loaded with uniform and tapered SRRs have been fabricated and measured. Fig. 4.18 depicts the top view of one of the fabricated samples with tapered SRRs. The material used and the dimensions of the prototypes are same as the simulated structures given in Sec. 4.4.3.

Fig. 4.19 depicts the measured transmission coefficient of the TLs loaded with uniform SRRs and two types of the tapered SRRs with different resonant frequencies (corresponding to the simulated structures of the previous section). The graph shows good agreement between the measured and simulated results. This agreement validates the theoretical concept of tapering SRRs for miniaturization, while improving the strength, and widening the bandwidth of the resonance. It is worth mentioning that the same principle can be applied to SRR arrays for the realization of bulk metamaterials or frequency-selective surfaces.

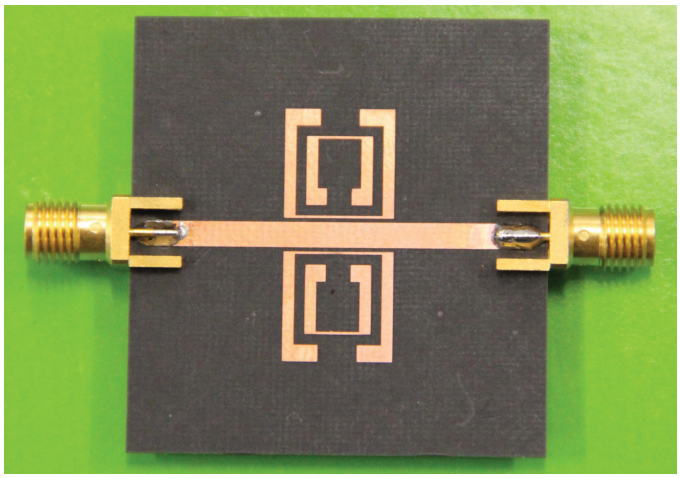

Figure 4.18. Fabricated prototype of the structure. Photograph of a fabricated sample of microstrip line loaded with a pair of tapered SRRs.

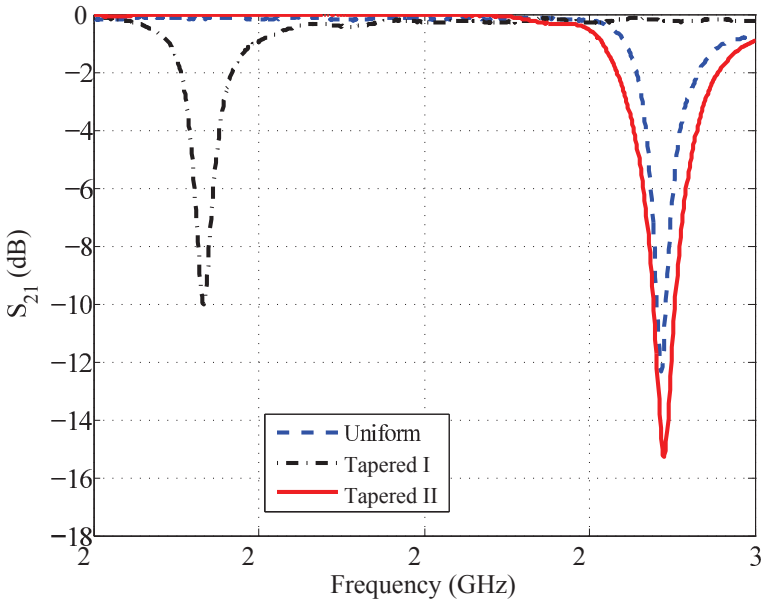

Figure 4.19. Measurement results for tapered SRRs. Measured transmission coefficients of TLs loaded with uniform SRRs and two types of tapered SRRs.

4.5 Conclusion

In this chapter, three different geometries of compact metamaterial-inspired structures have been proposed. The first structure was a novel defected structure based on CSRRs and a dumbbell-shaped DGS. Since the CSRRs are embedded inside the square-shape defection areas of the DGS the proposed structure is very compact. It has been demonstrated that the structure has two resonant frequencies that can be independently adjusted by manipulating the physical dimensions of the CSRRs and DGS. Having a small layout area and two independently adjustable resonances makes the structure a useful component for compact microwave circuits such as wideband filters or double stopband filters.

In the second section of the chapter, using an inductively loaded TL model, it has been shown that an increase in the equivalent inductance characteristic of a CSR results in an increase in the ratio of the second harmonic to the fundamental resonance frequency when compared to a complementary open-loop resonator with the same fundamental resonance frequency. This effect has been used for the design of a narrowband coupled resonators filter. Comparison of the CSR filter with an open-loop resonator filter shows that while the proposed filter is 65% more compact it provides 85% wider upper stopband.

Finally, a modified edge-coupled SRR with tapered strip width has been proposed in the last section of the chapter. The tapered shape, developed based on the current and voltage distribution in the SRR structure, has enabled us to reduce the SRR electrical area by 33%. More importantly, it has been shown that the proposed structure with the same electrical size as a uniform SRR has a stronger resonance with 84% wider fractional bandwidth. This strong and wideband resonance is required in many applications such as a wideband filter design.

The realization of high dynamic range displacement and rotation sensors based on similar shape modifications of metamaterial-inspired resonators will be presented in the next chapter.

Chapter 5

Metamaterial-Inspired Displacement and Rotation Sensors

BEYOND the initial goals of creating artificially engineered materials with electromagnetic constitutive parameters not available in nature, such as double-negative materials, metamaterials have opened new perspectives for other novel applications such as directive antennas and compact filters. Also, it has been shown that metamaterial-inspired resonators such as split ring resonators (SRRs) are ideal structures for the design of high sensitivity and high resolution sensors because of the high quality factor of their resonance, subwavelength dimensions, as well as their sensitivity to changes in surrounding materials and physical dimensions.

This chapter is focused on the application of metamaterial resonators in displacement and rotation sensing. To this end, the chapter presents three different metamaterial-inspired sensors. The first structure is a one-dimensional displacement sensor based on a diamond-shaped tapered SRR coupled to a coplanar waveguide (CPW). The second structure is a two-dimensional displacement sensor based on broadside-coupled SRRs in microstrip technology. Finally, a rotation sensor based on a horn-shaped SRR is presented and investigated, as a third structure.

5.1 Introduction

As mentioned in the previous chapters the concept of metamaterials was originally proposed for the realization of artificially engineered bulk materials with positive, near zero, or negative effective permittivity and/or permeability (Pendry *et al.* 1996, Pendry *et al.* 1999, Smith *et al.* 2000). However, due to their sub-wavelength dimensions, metamaterial fundamental elements such as SRRs, have also found applications in the design of compact one- and two-dimensional planar circuits such as filters (Martel *et al.* 2004, García-García *et al.* 2006, Bonache *et al.* 2006a, Gil *et al.* 2007, Velez *et al.* 2009, Horestani *et al.* 2011c, Horestani *et al.* 2012c), couplers (Caloz and Itoh 2004a, Lai *et al.* 2004, Jarauta *et al.* 2006, Liu *et al.* 2007a, Wang *et al.* 2007), and antennas (Herraiz-Martínez *et al.* 2011, Herraiz-Martínez *et al.* 2012, Paredes *et al.* 2012), or to improve the performance of these components (García-García *et al.* 2005b, Shi *et al.* 2012).

It has been also shown that resonators such as the SRR, inspired by metamaterials, can be used for the design of high sensitivity and high resolution sensors (Huang and Yang 2011, Huang *et al.* 2009, Yang *et al.* 2010). In fact, the high quality factor resonance, subwavelength dimensions, and the sensitivity of the resonance to the constituent materials and physical dimensions of the SRR make it an ideal structure for sensing applications (Withayachumnankul *et al.* 2012). Furthermore, it has been shown that the sensitivity of the conventional sensors can be dramatically enhanced by using metamaterial structures (Taya and Shabat 2011).

According to these unique properties, Zheludev (2010) pointed out that sensory devices open another promising area for the future application of metamaterials. This is evidenced by the increasing number of publications proposing the application of metamaterial particles in various types of sensors such as chemical sensing with enhanced sensitivity (Jakšić *et al.* 2007), biosensing (He *et al.* 2005), enhanced molecular detection techniques based on metamaterials (Cubukcu *et al.* 2009, Pattnaik *et al.* 2005), metamaterial-based wireless strain sensors (Melik *et al.* 2009), dielectric sensing (Alù *et al.* 2008) or structural defects detectors based on metamaterial lenses (Shreiber *et al.* 2011).

In this regard, this chapter presents three different metamaterial-inspired sensors: A displacement sensor based on a diamond-shaped SRR coupled to a CPW will be presented in Section 5.2. Section 5.3 proposes a metamaterial-inspired two-dimensional

displacement sensor based on broadside-coupled SRRs in microstrip technology. Finally, Section 5.4 is focused on the application of a horn-shaped SRR coupled to a CPW to the design of a rotation sensor.

5.2 Displacement Sensor Based on Diamond-Shaped Tapered Split Ring Resonator

This section presents a displacement sensor based on a modified SRR coupled to a CPW. The motivation for such a sensor over traditional methods (e.g. optical interferometry) is that it is low-cost, passive and hence not sensitive to environmental variations such as temperature, and easily integrable with , say, MEMS technology. The basic principle of displacement sensing based on SRRs is first briefly outlined in the next section. Two significant improvements over previous designs are then proposed in Section 5.2.2. Firstly, a diamond-shaped SRR is introduced to increase the sensor's linearity and dynamic range of displacement sensing. Secondly, compared to a previous design (Naqui *et al.* 2011), where the displacement changed both the resonant frequency and depth of the bandstop notch, a tapered shape SRR is introduced here to keep a fixed resonant frequency. This is an important improvement since the sensor does not require a frequency sweeping microwave source such as an expensive network analyzer, but can be operated at a single frequency. It is also demonstrated that, while retaining a compact size, the proposed sensor benefits from a lower operating frequency. A physical explanation involving the slot line mode is provided in Section 5.2.3. The design principle is validated through measurements in Section 5.2.4, followed by the concluding remarks.

5.2.1 Basic of SRR-based Displacement Sensor

Further to applications in extended array in metamaterial media, single SRRs can be used along with planar transmission lines (TLs) in filter applications (Martín *et al.* 2003b, García-García and Martín 2004). An SRR coupled to a TL can inhibit the propagation of the electromagnetic wave along the TL in the vicinity of the SRR resonant frequency. This introduces a notch in the transmission spectrum that can be interpreted as due to the negative effective permeability of the structure (Martín *et al.* 2003a). Metamaterial TLs and their sensitivity to slight environmental changes in

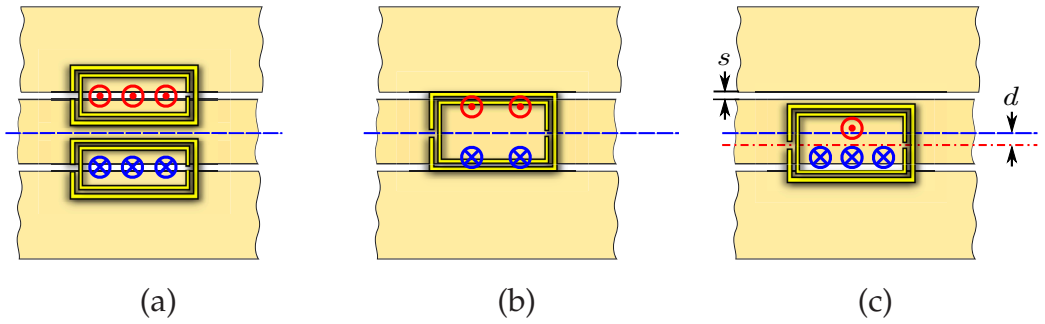

Figure 5.1. CPW loaded with SRRs. Bottom view of a CPW loaded with SRRs, (a) typical configuration in filter applications, which involves a pair of double ring SRRs under the CPW slots, (b) one double ring SRR aligned with CPW symmetry plane, (c) one double ring SRR displaced by d from the symmetry plane of the CPW. Adapted from Naqui *et al.* (2011).

their vicinity can be exploited in various types of sensors such as thin-film sensors (Withayachumnankul *et al.* 2012, He *et al.* 2010).

In order to implement SRR-based sensors, two main strategies have been used, both based on alteration of the resonance properties of SRRs caused by the variable to be sensed. Firstly, sensing can be based on changes of the resonance frequency of the SRR, and secondly, it can use the variation of the quality factor of the resonance (Withayachumnankul *et al.* 2012). Recently, displacement and rotation sensors based on the variation in the depth of notch in the transmission spectrum have been proposed by Naqui *et al.* (2011). The operation of these sensors relies on the loss of symmetry, which is caused by a displacement or rotation of an SRR coupled to a CPW.

A typical SRR-loaded CPW configuration consists of a pair of double ring SRRs etched on the back side of the CPW's substrate with the centre of double ring SRRs symmetrically located underneath the two slots of the CPW. The SRRs, which are magnetically coupled to the CPW, inhibit the electromagnetic wave propagation along the CPW in a narrow band in the vicinity of their resonant frequency (Martín *et al.* 2003a). As shown in Fig. 5.1.(a), in this case the magnetic fields passing through the surfaces of the two symmetrical SRRs are contra-directional.

In order to implement a displacement sensor, Naqui *et al.* (2011) used only a double ring rectangular SRR etched on the back side of the CPW substrate, and centred below the CPW line, instead of two SRRs aligned with the CPW's slots. In the initial position, shown in Fig. 5.1.(b), the SRR is therefore perfectly aligned with the symmetry

line of the CPW transmission line. Under these conditions, since the total magnetic flux passing through the surface of the SRR is the vector summation of the fluxes coming from both CPW's slots, the total magnetic flux passing through the SRR surface is zero. As a consequence, a symmetrically aligned SRR cannot be excited at resonance, and consequently there is no spectral notch in the structure's transmission coefficient. However, if the symmetry is broken by a lateral displacement d of the SRR, as shown in Fig. 5.1.(c), a net magnetic flux through the surface of the SRR appears. Thus, a transmission zero at the resonant frequency of the SRR is expected. Since the depth of the transmission notch depends on the deviation of the SRR from the symmetry plane, the amount of the displacement d can be sensed from the magnitude of such a transmission zero (Naqui *et al.* 2011).

5.2.2 Displacement Sensor Based on Diamond-Shaped SRR

In spite of the advantages of the displacement sensor proposed by Naqui *et al.* (2011) such as high sensitivity for small values of displacement, the sensor has some limitations, namely, a limited dynamic range and a displacement-dependent shift in the resonant frequency. The first part of this section proposes a diamond-shaped SRR, which increases the dynamic range and improves the linearity of the sensor, while the second subsection addresses the shift in the resonant frequency.

Dynamic Range and Linearity[1]

The limited dynamic range and non-linearity of the displacement sensor based on a rectangular SRR can be explained by the geometry. At first, for small values of the displacement of the rectangular-shaped SRR from the symmetry plane of the CPW, there is an increase in the amount of the net magnetic flux passing through the SRR surface. However, while further increasing the displacement, the net magnetic flux through the SRR surface reaches its maximum when the SRR's horizontal side passes the CPW slot. Beyond this point, as demonstrated by simulation and measurement results by Naqui *et al.* (2011), the displacement sensor goes into saturation, and only a minor increase in the notch magnitude can be observed. In fact, as will be shown later in this section, the linear dynamic range of the displacement sensor based on the rectangular-shaped SRR is approximately in the order of the CPW slot's width, s.

[1]Note that in this chapter "linearity" refers to the linearity of S_{21} in "dB" versus the displacement of the SRR.

In order to address the non-linearity and dynamic range limitations, a diamond-shaped SRR, shown in Fig. 5.2, is proposed. In this case, the magnetic flux through the SRR surface becomes maximal when the SRR horizontal diagonal is aligned with the CPW's slot. Thus, in contrast to the rectangular geometry, the angle between the sides of the diamond-shaped SRR and the slots of the CPW makes the spatial dynamic range of the diamond-shaped sensor dependent on the width of the CPW's signal strip (approximately half the width of the signal strip). Therefore, a diamond-shaped SRR coupled to a wide CPW can be used to increase the dynamic range and linearity of the displacement sensor. It is worth recalling that simultaneous increase of the width of the CPW's signal strip and its slots maintains the desired 50 Ω characteristic impedance.

Figure 5.2 depicts the bottom view of the proposed displacement sensor, which is composed of a diamond-shaped SRR coupled to a CPW with a relatively wide signal strip. For a specific design performed using 3D electromagnetic simulations, a 0.127 mm thick Rogers *RO3010* material with relative permittivity of 10.2 and copper thickness of 17 μm is used as the substrate. The CPW's signal trace width w is 3.1 mm and the width of slots is $s = 0.3$ mm, which correspond to a 50 Ω characteristic impedance. The horizontal and vertical diagonals of the diamond-shaped SRR are $a = 10$ mm and $b = 6$ mm, respectively. Finally, the width c of the metal strips of the SRR as well as the SRR's gap, g, are set to 0.2 mm.

Note that the sensitivity of the sensor not only depends on the geometry of the SRR, but is also affected by the coupling between the SRR and the CPW. Thus, in order to have maximum coupling between SRR and CPW, and consequently maximize the sensor's sensitivity, a thin substrate with 0.127 mm thickness and high relative permittivity ($\epsilon_r = 10.2$) is selected. However, using a thin substrate results in weak inter-coupling between the inner and outer rings of the SRR, and since there is a small difference between the length of the inner and outer rings, the second resonance is very close to the fundamental resonance of the SRR. In order to avoid the effect of the second resonance a single ring SRR, as shown in Fig. 5.2, is used instead of a double ring SRR as used by Naqui *et al.* (2011).

Figure 5.3 depicts the simulated transmission coefficient of the sensor based on the diamond-shaped SRR for the SRR displacement d varying between 0 mm and 1 mm in steps of 0.2 mm. As clearly observed from the figure, an increase in the displacement of the SRR leads to an increase in the notch magnitude, which can be used to sense the amount of the lateral displacement.

Figure 5.4 compares the notch magnitude versus the lateral displacement of the SRR in two different sensors, namely the displacement sensor based on the rectangular SRR (black dashed line) and the displacement sensor based on the diamond-shaped SRR (red solid line). It is clear from the simulation results that even though the sensor with the rectangular-shaped SRR has a high sensitivity for small values of the lateral displacement it suffers from limited dynamic range of about 0.6 mm. Furthermore, as mentioned earlier in this section, its linear behaviour is limited to a small range of displacement, approximately in the order of the CPW slot's width, $s = 0.2$ mm. In contrast, the sensor based on the diamond-shaped SRR benefits from a higher dynamic range of 1.2 mm and superior linearity within its dynamic range.

In short, the simulation results show that using a diamond-shaped SRR instead of rectangular-shaped SRR adds one degree of freedom to trade off sensitivity for dynamic range and linearity. In other words, the vertical diagonal of the diamond-shaped SRR b along with the width of the CPW's signal strip can be adjusted in order to achieve a linear displacement sensor with desired dynamic range or sensitivity.

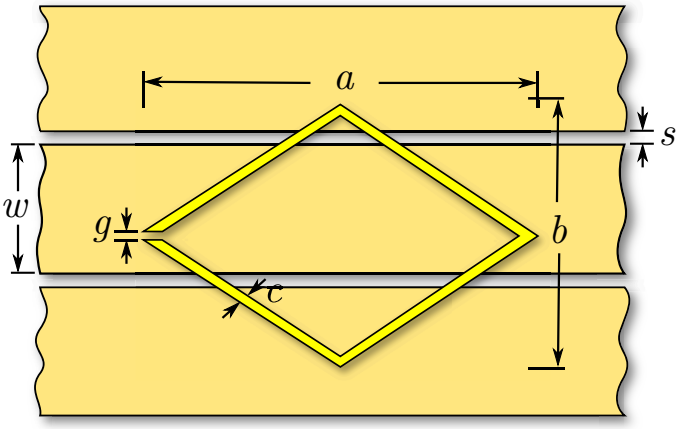

Figure 5.2. CPW loaded with a diamond-shaped SRR. CPW loaded with a diamond-shaped SRR (bottom view).

Shift in Resonant Frequency

The second limitation of the displacement sensor based on the rectangular SRR is that the displacement of the SRR not only changes the notch depth but also the resonant frequency. As can be seen in Fig. 5.3, this is also the limitation of the diamond-shaped sensor proposed in the previous subsection. In the following, the displacement sensor design is further improved so that the resonant frequency remains fixed allowing the

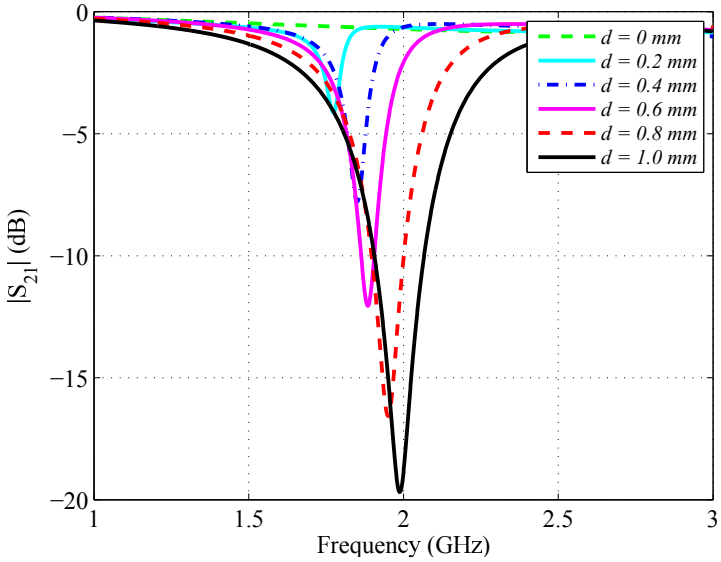

Figure 5.3. Simulation results. Simulated transmission coefficient of the displacement sensor based on the diamond-shaped SRR, shown in Fig. 5.2, for different values of displacement of the SRR from $d = 0$ mm to $d = 1.0$ mm in steps of 0.2 mm.

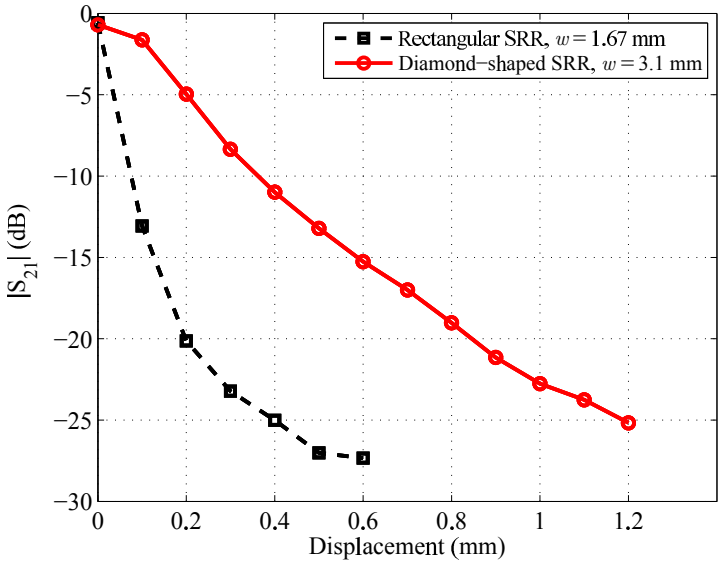

Figure 5.4. Comparison between the sensors based on rectangular-shaped and diamond-shaped SRRs. Comparison between the simulated linearity and dynamic range of displacement sensor based on rectangular-shaped double ring SRR and those of the displacement sensor based on the diamond-shaped SRR.

amount of displacement to be measured based on the notch magnitude in one fixed resonant frequency. This is an important improvement since the sensor can then be

operated at a single frequency, which allows to bypass the need for a sophisticated frequency sweeping microwave source and measurement system.

It is worth recalling that in the quasistatic limit the SRR's fundamental resonant frequency can be approximated from the SRR's circuit model, which is a parallel LC resonator (Marqués *et al.* 2002). In such circumstances, the equivalent inductance of the SRR can be calculated from the inductance of a single ring with the average dimensions of the SRR and the equivalent capacitance can be calculated from the capacitance of the split (Shamonin *et al.* 2005). However, in the case of the displacement sensor, the magnetic flux passing through the SRR surface is not uniform. As shown in Fig. 5.3, this results in a shift of the resonant frequency, which depends on the magnitude of displacement.

Since the resonant frequency is dependent on the equivalent inductance and capacitance of the SRR, it can be shown that a decrease in the horizontal diagonal b of the SRR can be used to reduce the equivalent inductance of the SRR. This will minimize the effect of the non-uniformity of the magnetic flux passing through the SRR surface, and consequently diminish the shift in the resonant frequency. However, as stated above, a decrease in the diagonals of the SRR degrades the dynamic range and linearity of the sensor. Furthermore, decreasing the equivalent inductance of the SRR by decreasing b pushes the operating frequency of the sensor to high frequencies, which is generally not desirable in sensory applications.

Alternatively, tapering and widening the SRR's metallic strip, as illustrated in Fig. 5.5, can be exploited to precisely compensate for the spatial non-uniformity of the magnetic flux passing through the SRR surface and consequently minimize the shift in the resonant frequency. Furthermore, as will be shown later in this section, this also reduces the operating frequency of the displacement sensor by increasing the SRR's equivalent capacitance.

Figure 5.5 depicts the bottom view of the proposed tapered diamond-shaped SRR. For 3D electromagnetic simulation the substrate properties ($\epsilon_r = 10.2$, thickness of 0.127 mm), the CPW dimensions ($w = 3.1$ mm, $s = 0.3$ mm) and the outer diamond shape ($a = 10$ mm, $b = 6$ mm, and $c = g = 0.2$ mm) remain unchanged. The only difference is in the width of the SRR's metallic strip on both sides of the SRR's split, which is optimized to be $c_c = 8$ mm to achieve a fixed resonant frequency.

Figure 5.6 depicts the simulated transmission coefficients versus frequency for the displacement sensor based on the proposed tapered diamond-shaped SRR for different

values of the lateral displacement of the SRR from $d = 0$ mm to $d = 1$ mm with steps of 0.2 mm. The figure, clearly illustrates that the shift in the resonant frequency can be minimized through optimization of the parameter c_c. In that cases, all resonances occur at 1.17 GHz independently of the displacement.

As mentioned earlier in this section, an increase in c_c also increases the SRR's equivalent capacitance. Thus, from the comparison between the resonant frequency in Fig. 5.6, at 1.17 GHz, and those in Fig. 5.3, which are higher than 1.75 GHz, it can be seen that the proposed tapered shape of the SRR pushes the resonant frequencies to lower frequencies without increasing the overall size of the SRR. That means that, in addition to having a fixed resonant frequency, the displacement sensor based on the tapered diamond-shaped SRR also benefits from a lower operating frequency.

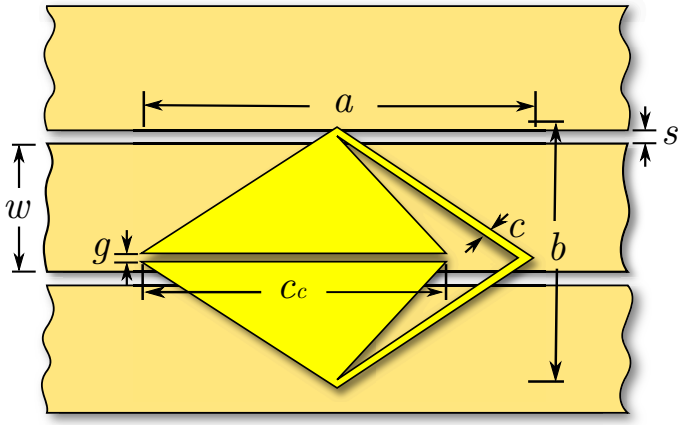

Figure 5.5. CPW loaded with a tapered diamond-shaped SRR. CPW loaded with a tapered diamond shaped SRR (bottom view).

Figure 5.7 depicts the simulated response of the tapered diamond-shaped sensor presented in Fig. 5.5 versus the lateral displacement of the SRR. The red line represents the notch magnitude in the transmission coefficient of the structure versus the lateral displacement of the SRR, and the blue line depicts the transmission coefficient of the structure at the fixed frequency $f = 1.17$ GHz. As clearly seen in the figure, for the SRR displacement less than 1.1 mm the blue line is aligned with the red line, indicating a dynamic range of 1.1 mm, when it is used at the fixed frequency of 1.17 GHz. Furthermore, the sensor can achieve wider dynamic range of 1.5 mm if it is not used at a fixed frequency, i.e along with a frequency sweeping measurement system such as a network analyzer.

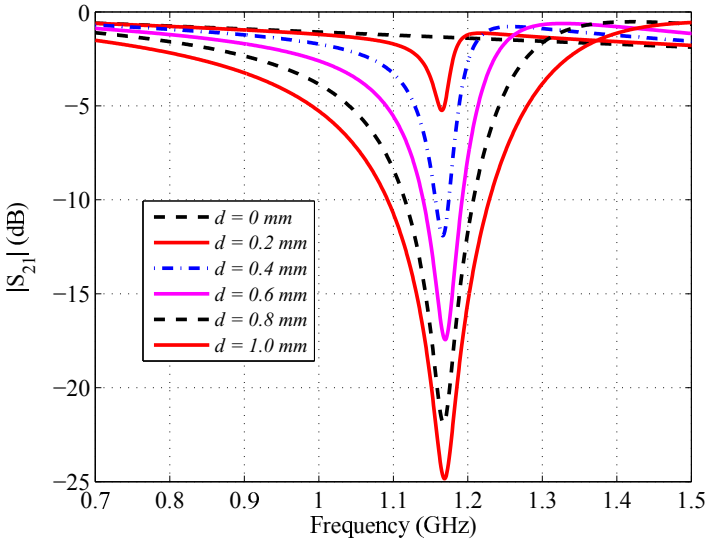

Figure 5.6. Simulated response of the displacement sensor based on the tapered diamond-shaped SRR. Simulated transmission coefficient of the displacement sensor based on the tapered diamond-shaped SRR, shown in Fig. 5.5, for different values of displacement of the SRR.

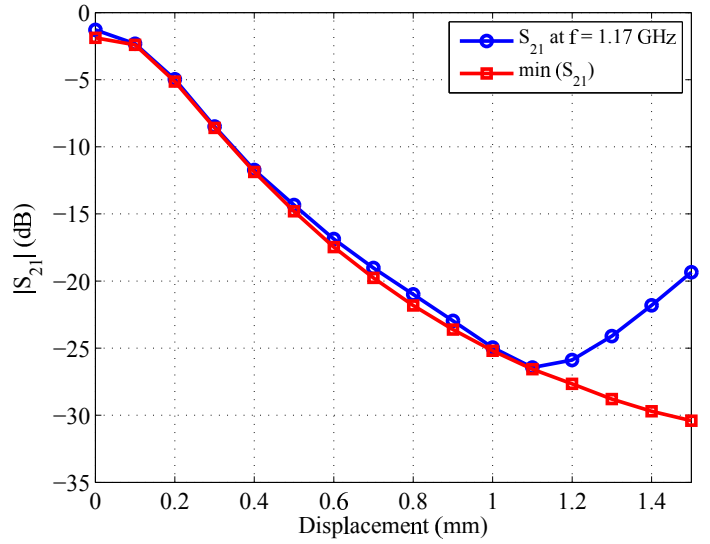

Figure 5.7. Simulated response of the sensor versus displacement. Simulated response of the displacement sensor based on the tapered diamond-shaped SRR corresponding to notch magnitude at its minimum (red dashed line), and at the fixed frequency $f = 1.17$ GHz (blue solid line)

5.2.3 Slotline mode

It is well known that any asymmetry and/or discontinuity in a CPW can excite the slotline mode (odd mode) in the line. For instance, the slotline mode is excited in a CPW at right-angle bends or T-junctions (Dib and Gupta 1993, Simons and Ponchak 1988). Note that, in all types of displacement sensors described in the previous sections, once the SRR is displaced from the symmetry plane of the CPW, the slotline mode is excited due to the asymmetry caused by the displaced SRR. As a result, the magnitude of the transmission notch becomes dependent on the length of the CPW. In all the presented simulations, the CPW's length is set to 30 mm and the CPW is directly connected to SMA coaxial connectors. In these cases, the length of the line becomes relevant as the slotline mode is suppressed by the coaxial connectors at both ends of the CPW. Nevertheless, in the case where a longer length of CPW would be required, the propagation of the slotline mode can be suppressed by adding air-bridges along the CPW structure on both sides of the SRR, as shown in Fig. 5.8, to connect the two lateral ground planes and consequently equalize the voltages on two ground planes of the CPW (Ponchak 2005).

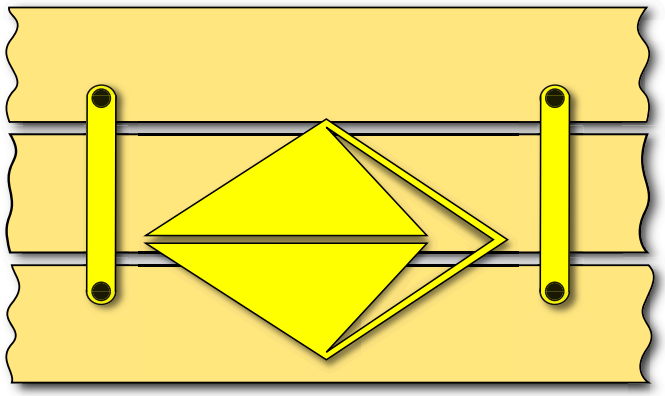

Figure 5.8. Slotline mode suppression. Slotline mode can be suppressed by adding air-bridges along the CPW structure on both sides of the SRR to connect two ground planes and consequently equalize the voltages on two ground planes.

5.2.4 Experimental Results

Experimental results are presented to validate the SRR shape variation concept and electromagnetic simulation results of the previous sections. Due to the high sensitivity of the proposed sensor to small values of the SRR lateral displacement it is technically

complex to perform an experimental validation by fabricating the structure with moving SRR. Thus, instead of a moveable SRR, several devices with different values of the SRR displacement are fabricated and measured as a proof-of-concept.

Figure 5.9 depicts the photograph of the top and bottom view of one of the fabricated samples with $d = 0.9$ mm displacement from the symmetry plane of CPW. The material used and the dimensions of the prototype corresponds to the simulation characteristic given in Section 5.2.2.B. Figure 5.10 depicts the measured transmission coefficients of

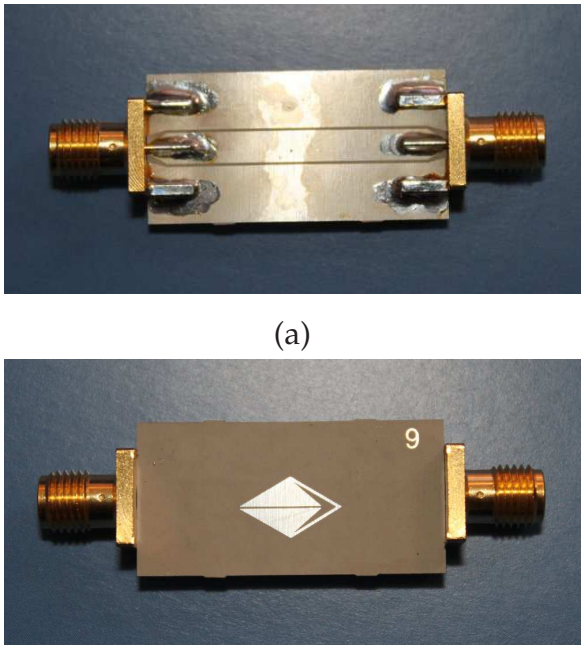

(a)

(b)

Figure 5.9. Fabricated prototypes. Photograph of a sample of the fabricated sensors; (a) top view of the CPW, and (b) the SRR on the back side substrate, which is displaced by 0.9 mm from the symmetry plane of the CPW.

the sensor based on the tapered SRR for several values of the SRR's displacement. The figure shows a fixed resonant frequency at $f = 1.13$ GHz, which is in reasonable agreement with the simulation results shown in Fig. 5.6. The small difference between the measured and simulated resonant frequency can be attributed to variations in the substrate relative permittivity.

These results demonstrate that unlike in the case of the sensor based on the uniform diamond-shaped SRR (and rectangular SRR), the resonance in the sensor based on the tapered SRR occurs as predicted at a fixed frequency $f = 1.13$ GHz. This also validates the prediction that in addition to having a fixed resonant frequency, while maintaining

a compact size, the displacement sensor based on the tapered diamond-shaped SRR also benefits from a lower operating frequency.

In Fig. 5.11, the measured transmission coefficient of the tapered diamond-shaped sensor versus the lateral displacement of the SRR at fixed frequency $f = 1.13$ GHz (blue solid line) is compared with that of the simulation results at fixed frequency $f = 1.17$ GHz (red dashed line). The graph shows good agreement between measured and simulated results.

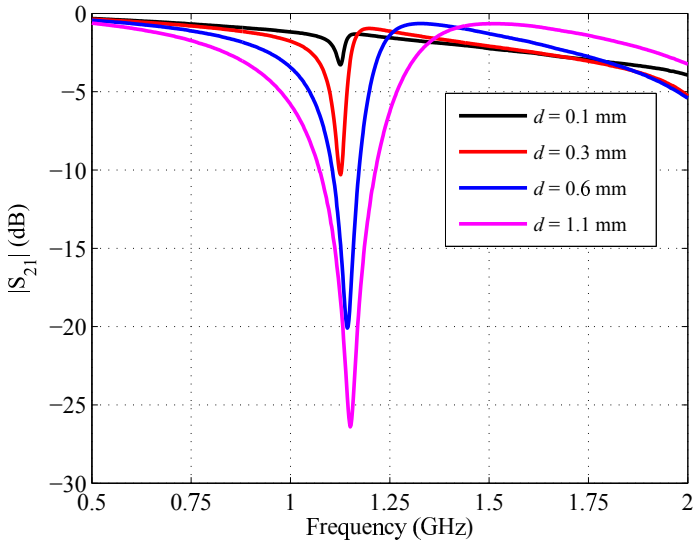

Figure 5.10. Measurement results. Measured transmission coefficients of the sensor based on the tapered diamond-shaped SRR for different values of the SRR displacement. The measurements are not as well aligned as the simulation in Fig. 5.6 due to the device-to-device variations. This is a consequence of each displacement requiring a separate device for this proof-of-concept. A movable SRR fabricated in MEMS technology will not exhibit this problem.

To investigate the effect of the thermal expansion of the substrate and metallic layers the transmission coefficient of a particular sample, specifically with 1.1 mm displacement, is measured at different temperatures from 20°C to 50°C. The measured results, depicted in Fig. 5.12, show that for a 30°C increase in the temperature, the measurement yields only a 1% increase in the resonant frequency of the structure and less than a 1 dB decrease in the depth of resonance. This demonstrates that the sensor has a good thermal stability.

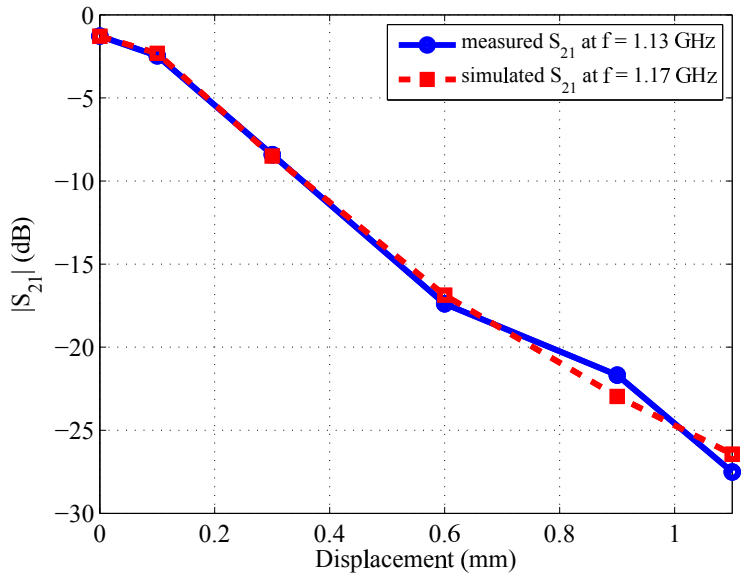

Figure 5.11. Comparison between simulated and measured results of the tapered diamond-shaped sensor. Comparison between the transmission coefficient of the tapered diamond-shaped sensor versus the lateral displacement of the SRR measured at fixed frequency $f = 1.13$ GHz (blue solid line) and those of the simulation results at fixed frequency $f = 1.17$ GHz (red dashed line).

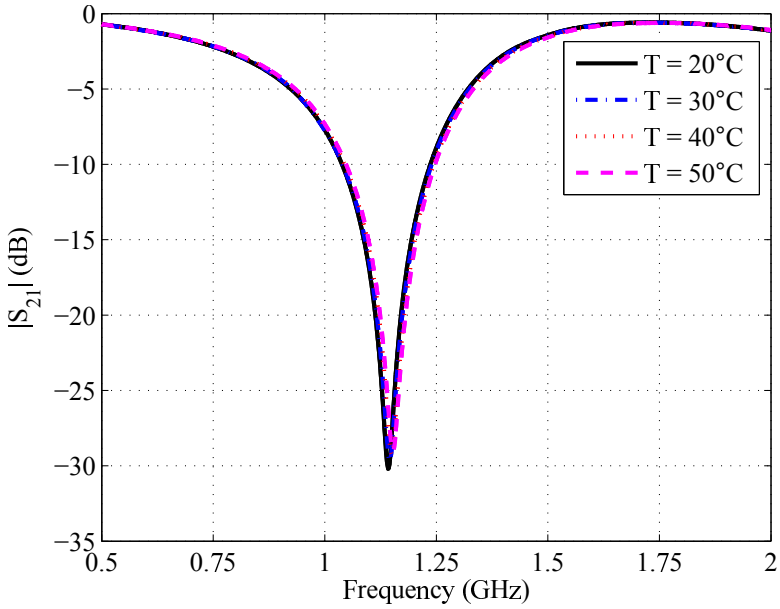

Figure 5.12. Effect of thermal expansions. Measured transmission coefficient of a 1.1 mm displaced tapered diamond-shaped sensor for different temperatures from 20°C to 50°C with steps of 10°C.

5.3 2-D Displacement Sensor with High Dynamic Range

The previous section presented a one-dimensional displacement sensor. Recently, a two-dimensional displacement sensor based on symmetry properties of SRR-loaded CPW has been proposed as well (Naqui *et al.* 2012a). In these sensors a displacement was characterized by measuring the depth of the notch in the transmission coefficient of the loaded CPW. Other displacement sensors based on the shift of resonance frequency are reported by Mandel and Kubina (2011) and Shaterian *et al.* (2013). The main advantage of the sensors based on symmetry properties over those based on the shift of resonance frequency is that external (ambient) conditions may affect the resonators' resonance frequency but not the transparency of the loaded lines with perfectly aligned resonators. Thus, the sensors based on symmetry properties of SRR-loaded CPW are more robust and specially suited for alignment purposes. However, they have a fundamental dynamic range limitation, set by the width of the CPW signal strip.

Thus, this section proposes a high dynamic range two-dimensional displacement sensor. As a basis for this sensor, a one-dimensional displacement sensor based on a microstrip line loaded with broadside-coupled split-ring resonators (BC-SRRs) is presented firstly. It is shown that in contrast to the above-mentioned displacement sensors (Naqui *et al.* 2011, Horestani *et al.* 2013b, Naqui *et al.* 2012a), in which a fundamental dynamic range limit was dictated by the CPW's lateral dimension, the proposed sensor has virtually no dynamic range limit. Secondly, it is shown that with modifications in the geometry of the BC-SRRs, the proposed one-dimensional sensor can be modified and extended by adding a second element to create a high-dynamic range two-dimensional displacement sensor. Since the proposed sensors operate based on the shift in the resonance frequency, rather than the resonance depth, they benefit from a high immunity to environmental noise, at a cost however of an increased system complexity because of the requirement of sweeping frequency operation. Furthermore, since the sensors' principle of operation is based on the deviation from symmetry, they are more robust to ambient conditions such as changes in the temperature, and thus they can be used as alignment sensors as well. A prototype of the proposed two-dimensional sensor is fabricated and the concept and simulation results are validated through experiment.

5.3.1 One-Dimensional Displacement Sensor Based on Broadside Coupled Split Ring Resonators

Figures 5.13(a) and (b) illustrate the side and top view of the one-dimensional displacement sensor (Shaterian *et al.* 2013), which is composed of a microstrip line loaded with a pair of BC-SRRs. Each BC-SRR is composed of two U-shaped split-rings printed on different layers, on top of each other and open in opposite directions. Note that in this structure one of the rings is printed on the same layer as the microstrip line, so it is fixed, while the second ring is on the top layer of a second substrate, which can be displaced along the direction of the microstrip line, as shown by the red arrows in the figure. The aim of the sensor is to measure this displacement.

The BC-SRR can be modeled as a parallel LC resonator (Marqués *et al.* 2003), in which the equivalent capacitance corresponds to the capacitance of the overlapping metallic area of the two U-shaped rings, and the equivalent inductance corresponds to the rectangular loop formed by the two U-shaped rings. The BC-SRR's resonance frequency is related to its equivalent capacitance and inductance by $f = \sqrt{LC}$. In the configuration shown in the figure, an increase in the displacement Δx of the upper ring results in a decrease in the equivalent capacitance and an increase in the equivalent inductance of the BC-SRR. However, as shown in the simulation results of Fig. 5.14, the change in the equivalent capacitance is dominant, which results in a shift of resonance frequency to higher frequencies. The shift in the resonance frequency can therefore be used to sense the amount of displacement in x direction. Note that the dynamic range of the sensor has virtually no intrinsic geometric limitation and can be increased by using longer BC-SRRs. Dimensions of the simulated structure are listed in the caption of Fig. 5.13.

Figures 5.15(a) and (b) illustrate the side and top views of a novel one-dimensional sensor, in which the BC-SRRs are rotated such that a lateral displacement increases the equivalent capacitance of one of the BC-SRRs, while it decreases the equivalent capacitance of the other BC-SRR. Also, the equivalent inductance of one of the resonators is decreased, while that of the other resonator is increased. Therefore, as shown with the blue solid line in Fig. 5.16, at the initial position, i.e. for $\Delta y = 0$ mm, when the symmetry plane of the top substrate is aligned with the symmetry plane of the microstrip line, both resonators are identical, and only one notch in the transmission coefficient of the loaded TL appears at f_{y0}. However, when the symmetry is broken by a lateral displacement of the upper substrate, one of the BC-SRRs becomes smaller than the other

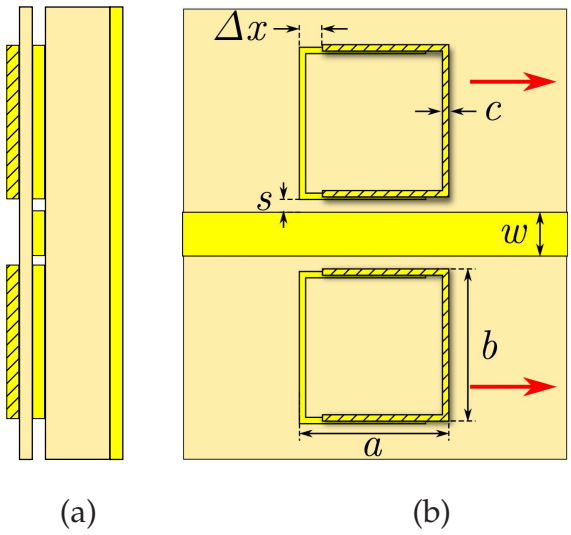

Figure 5.13. Layout of a 1-D displacement sensor based on BC-SRRs. (a) Side view and (b) top view of the displacement sensor based on BC-SRRs. Rogers *RO4003* substrates with relative permittivity of 3.38 and copper metalization with thickness of $35\,\mu$m are used. The thickness of the bottom and top substrates are 1.524 mm and 0.203 mm, respectively. The width of the microstrip line is $w = 3.3\,$mm which corresponds to a $50\,\Omega$ characteristic impedance. Other dimensions of the structure are $a = 10.2$ mm, $b = 12.4$ mm, $c = 0.4$ mm, and $s = 0.2$ mm.

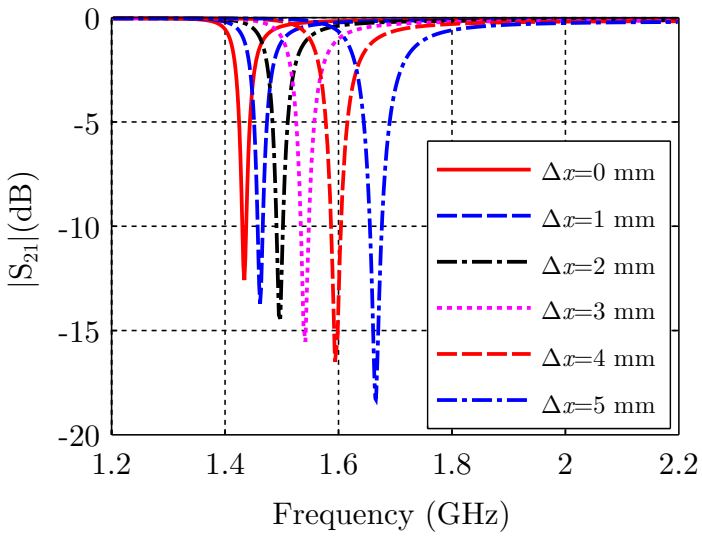

Figure 5.14. Simulated transmission coefficints of the 1-D displacement sensor. Simulated transmission coefficients of the structure of Fig.5.13 for different values of displacement from $\Delta x = 0$ mm to $\Delta x = 5$ mm in steps of 1 mm.

one, resulting in the splitting of the resonance in two notches f_{y0} and f_{y1} in the transmission spectrum of the TL. Thus, the frequency difference between the two notches $\Delta f_y \stackrel{\text{def}}{=} f_{y1} - f_{y0}$ can be used to sense the lateral displacement.

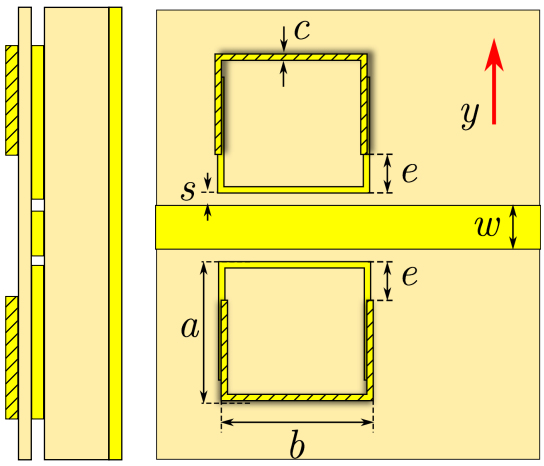

(a) (b)

Figure 5.15. Layout of the modified 1-D displacement sensor based on BC-SRRs. (a) Side view and (b) top view of the modified one-dimensional displacement sensor. Rogers *RO4003* substrates with relative permittivity of 3.38 and 35 μm thick copper metallization are used. The thickness of the bottom and top substrates are 1.524 mm and 0.203 mm, respectively. The width of the microstrip line is $w = 3.3\,\text{mm}$ which corresponds to a $50\,\Omega$ characteristic impedance. Dimensions of the BC-SRRs are as follows: $a = 13.2$ mm, $b = 12.4$ mm, $c = 0.4$ mm, $s = 0.2$ mm, and $e = 3$ mm.

Simulation results show that compared to the previously published displacement sensors (Naqui *et al.* 2012b, Horestani *et al.* 2013b) and the displacement sensor of the previous section, where an intrinsic dynamic range limitation of about 1 mm was dictated by the CPW's lateral dimensions, the proposed sensor has a much larger dynamic range of 3 mm, and its dynamic range can be further increased simply by using longer BC-SRRs. Also, since the proposed sensor operates based on the shift in the resonance frequency rather than the resonance depth, it benefits from a higher immunity to environmental noise (Naqui *et al.* 2012b). Furthermore, since the operation principle of the sensor is based on the break in symmetry arising from the displacement, the sensor is robust to variable ambient conditions such as changes in the temperature, and can be also used as alignment sensor (Naqui *et al.* 2012a, Horestani *et al.* 2013b).

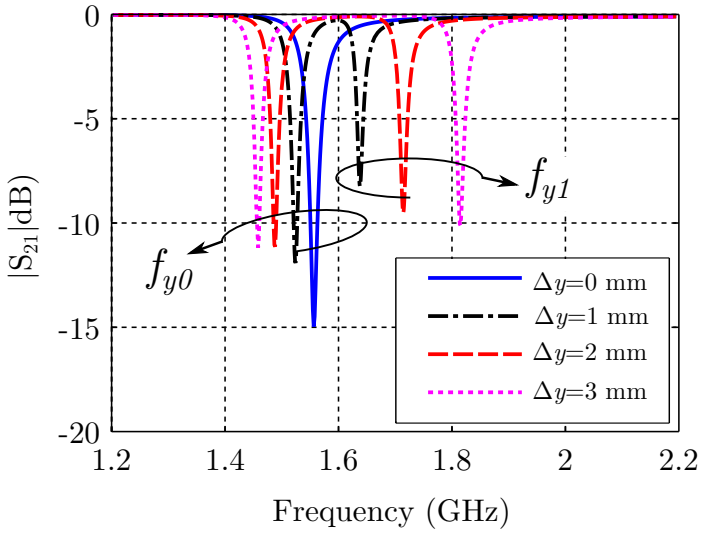

Figure 5.16. Simulated transmission coefficints of the modified 1D displacement sensor. Simulated transmission coefficients of the structure for different displacements $\Delta y = 0$ mm to $\Delta y = 5$ mm in steps of 1 mm.

5.3.2 Two-Dimensional Displacement Sensor

With some geometrical modifications, the proposed one-dimensional sensor can be extended to a dual-element configuration operating as a two-dimensional alignment and displacement sensor. To this end, as shown in Fig. 5.17, one possible strategy is to introduce a right angle bend in the microstrip line, and etch a pair of BC-SRRs with orthogonal orientation in each section. The pairs of BC-SRRs need to have different dimensions to resonate at sufficiently different frequencies such that a displacement in x direction can be distinguished from that in y direction. Furthermore, the geometry of the resonators needs to be modified so that the resonant frequency is altered by the displacement in one direction only. To this end, the upper rings are replaced with straight strips. In this configuration, provided the strips are long enough, the pair of the modified resonators that are coupled to the horizontal section of the microstrip line is only sensitive to a displacement in y direction, while the pair of the modified BC-SRRs coupled to the vertical section of the line is only responsive to a displacement in x direction. In a practical system, in order to avoid abrasion of metallic layers and substrates, metallic layers are printed face-to-face, and an air gap is added between the top and bottom substrates, as shown in the side view of Fig. 5.17(a). In order to increase the coupling between the modified BC-SRRs and the microstrip line,

based on the discussion in Section 4.4, the middle section of the U-shaped rings are narrowed (Horestani *et al.* 2012b).

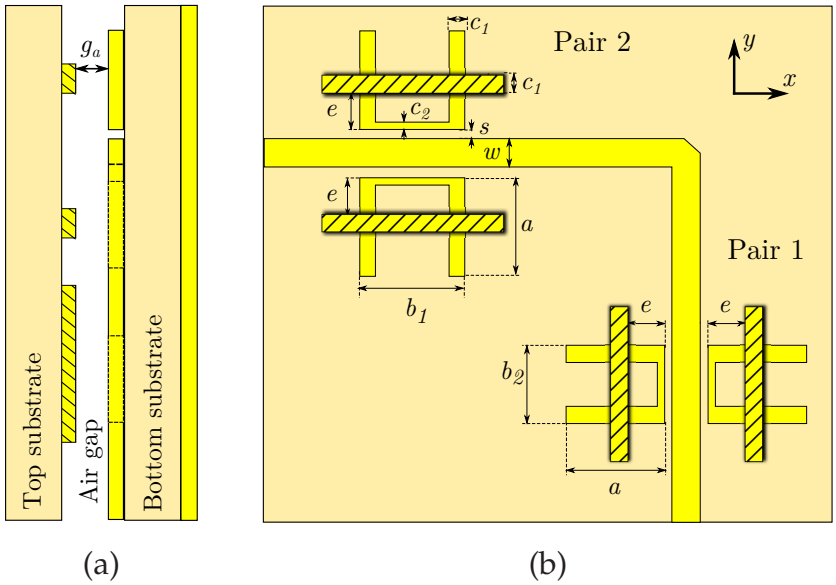

Figure 5.17. Layout of the proposed 2D sensor. (a) Side view and (b) top view of the proposed two-dimensional displacement sensor. Rogers *RO4003* material with relative permittivity $\epsilon_r = 3.38$ and thickness of 0.81 mm is used for the bottom and top substrates. The two substrates are separated with a air gap $g_a = 0.25$ mm. The microstrip line has a width $w = 1.85$ mm, which corresponds to a 50 Ω line. The dimensions of the resonators are as follows: $a = 12.2$ mm, $b_1 = 15.5$ mm, $b_2 = 10.5$ mm, $c_1 = 2.5$ mm, $c_2 = 1.2$ mm, $s = 0.2$ mm, and at initial position $e = 4.8$ mm.

Figure 5.18(a) and (b) depict the simulated response of the proposed two-dimensional sensor to displacements in x and y directions, respectively. Both sets of simulations are conducted by using parameters of Rogers *RO4003* material with relative permittivity $\epsilon_r = 3.38$ and thickness of 0.81 mm for the bottom and top substrates. The two substrates are separated with a 0.25 mm air gap. The structure's dimensions are listed in the caption of Fig. 5.17. Figure 5.18(a) depicts the simulated transmission coefficients of the proposed two-dimensional sensor for different values of displacement in x direction from 0 mm to 3 mm in steps of 1 mm when no displacement in y direction is applied, i.e. $\Delta y = 0$ mm. At initial position, when both pairs of the modified BC-SRRs are aligned with the symmetry plane of the corresponding sections of the microstrip line, only two notches at f_{x0} and f_{y0} appear in the transmission spectrum of the line (blue solid line). The resonance at frequencies f_{x0} and f_{y0} are associated with Pair 1

and Pair 2, respectively. However, as shown in the figure, a displacement in x direction results in the splitting of the resonance of the Pair 1 in two notches at f_{x0} and f_{x1}. The difference between the two frequencies, i.e. $\Delta f_x \stackrel{\text{def}}{=} f_{x1} - f_{x0}$, is increased with an increase in displacement in x direction, thus it can be used for sensing the value of Δx. Similarly, Fig. 5.18(b) shows the simulated transmission coefficients of the proposed sensor for variation of Δy from 0 mm to 3 mm in steps of 1 mm while the Pair 1 is aligned with the symmetry plane of the vertical section of the microstrip line, i.e. $\Delta x = 0$ mm. The figure clearly shows that $\Delta f_y \stackrel{\text{def}}{=} f_{y1} - f_{y0}$ increases with Δy, thus it can be used for sensing a displacement in y direction.

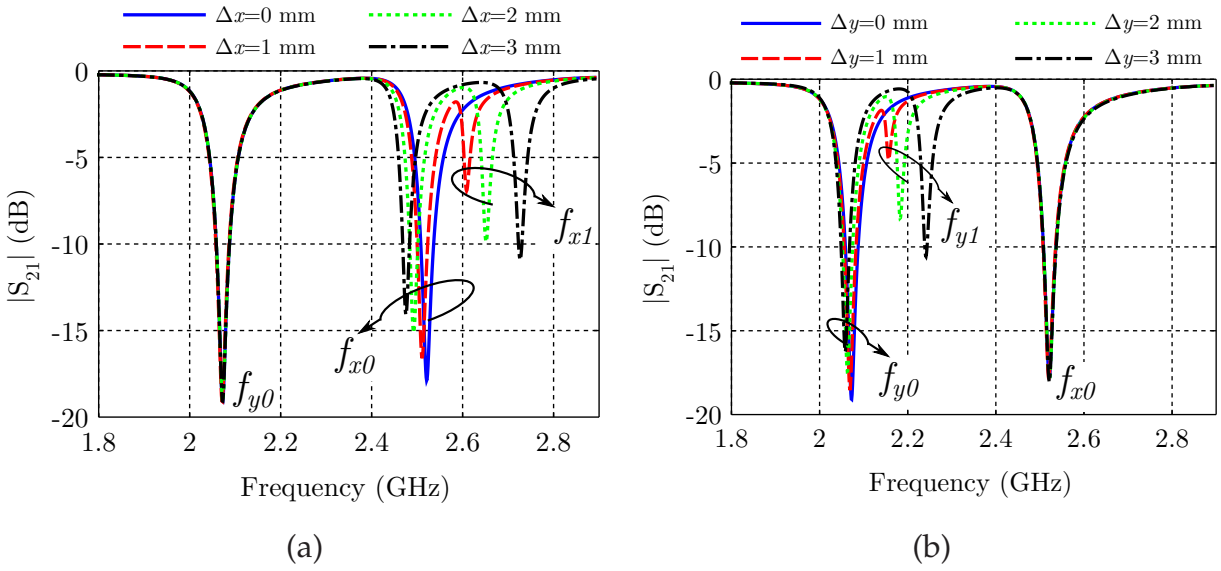

Figure 5.18. Simulated transmission coefficient of the proposed 2-D sensor. Simulated transmission coefficients of the proposed sensor (a) for different values of displacement in x direction from 0 mm to 3 mm in steps of 1 mm, while $\Delta y = 0$ mm, and (b) for different values of displacement in y direction from 0 mm to 3 mm in steps of 1 mm, while $\Delta x = 0$ mm.

5.3.3 Experimental Results

In order to validate the concept and the simulation results of the previous section, the designed two-dimensional sensor has been fabricated and measured. Dimensions of the prototype corresponds to the simulated structure of the previous section, as given in the caption of Fig. 5.17. Photographs of the top and bottom substrates of the fabricated prototype are depicted in Figs. 5.19(a) and (b). The measurements have

been performed at the Laboratory of GEMMA/CIMITEC, Departament d'Enginyeria Electronica, Universitat Autonoma de Barcelona, Spain. Fig. 5.20 shows a photograph of the measurement setup, which is composed of a pair of micrometer actuators for adjusting the air space between the two substrates, as well as two pairs of micrometer actuators for accurate displacement in x and y directions.

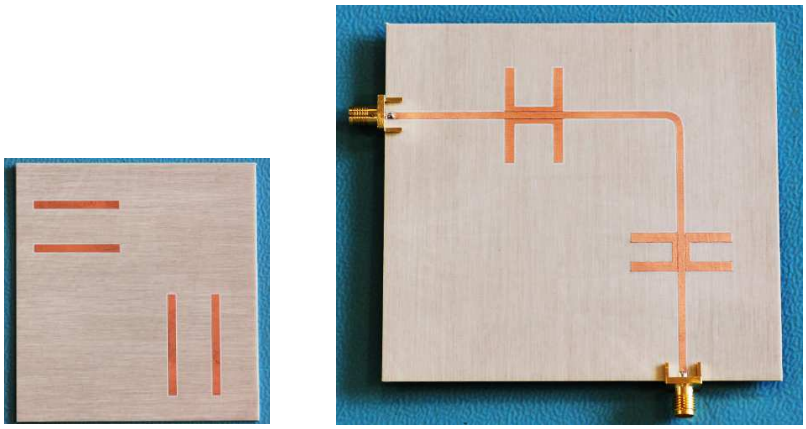

(a) (b)

Figure 5.19. Fabricated prototypes of the proposed 2D sensor. Photographs of the fabricated prototype of the proposed two-dimensional sensor (a) top and (b) bottom substrates.

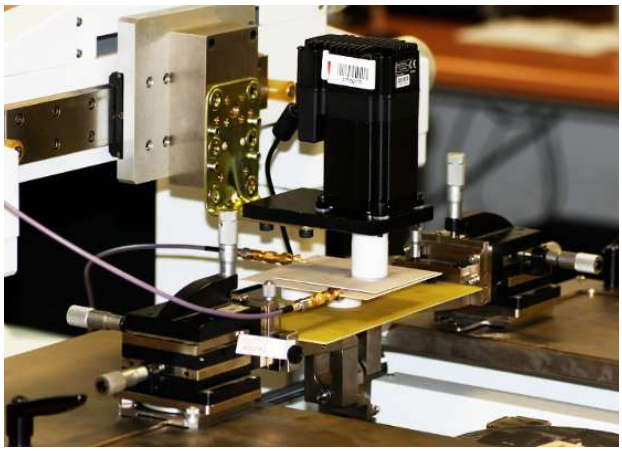

Figure 5.20. Measurement setup for the 2-D displacement sensor. Measurement setup, which is composed of three sets of micrometer actuators for accurate adjustment of the air gap between the substrates as well as displacement in x and y directions. The measurements have been performed at the Laboratory of GEMMA/CIMITEC, Departament d'Enginyeria Electronica, Universitat Autonoma de Barcelona, Spain.

Figure 5.21(a) depicts the measured transmission coefficients of the sensor for different values of $\Delta x = 1$ mm, 2 mm, and 3 mm, while the sensor has a fixed displacement of 2 mm in y direction. The figure shows that while the frequency difference Δf_x is increased from 105 MHz to 267 MHz, Δf_y does not change. Similarly, Fig. 5.21(b), shows the measured results for a fixed displacement of 0.5 mm in x direction, resulting in fixed notches at $f_{x0} = 2.5$ GHz and $f_{x1} = 2.6$ GHz, while Δy is changed from 1 mm to 3 mm in steps of 1 mm, which can be sensed from the increase in Δf_y from 95 MHz to 210 MHz. The experiment shows that each pair of the modified BC-SRRs are exclusively responsive to a displacement either in x or y direction. Thus, the proposed structure can be efficiently used as a two-dimensional alignment and displacement sensor. In Figs. 5.22(a) and (b) the measured Δf_x and Δf_y versus displacement in x and y directions, respectively, are compared with those of the simulation results. The satisfactory agreement between the results validates the concept and the simulations.

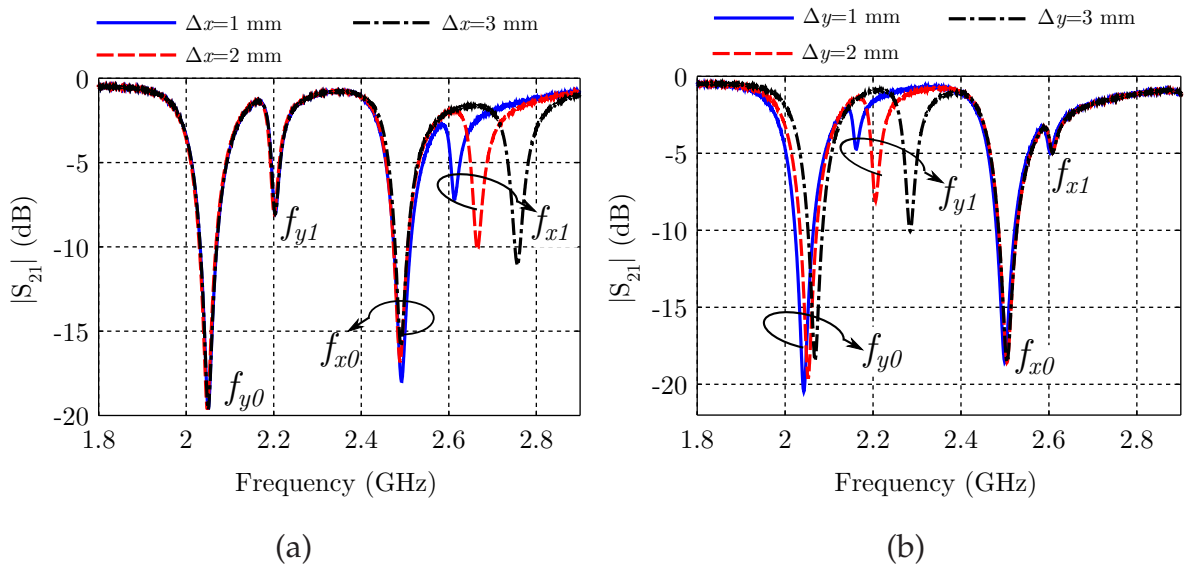

Figure 5.21. Measured transmission coefficients of the 2-D sensor. Measured transmission coefficients (a) for three different values of displacement in x direction, while $\Delta y = 2$ mm, and (b) for three different values of displacement in y direction, while $\Delta x = 0.5$ mm.

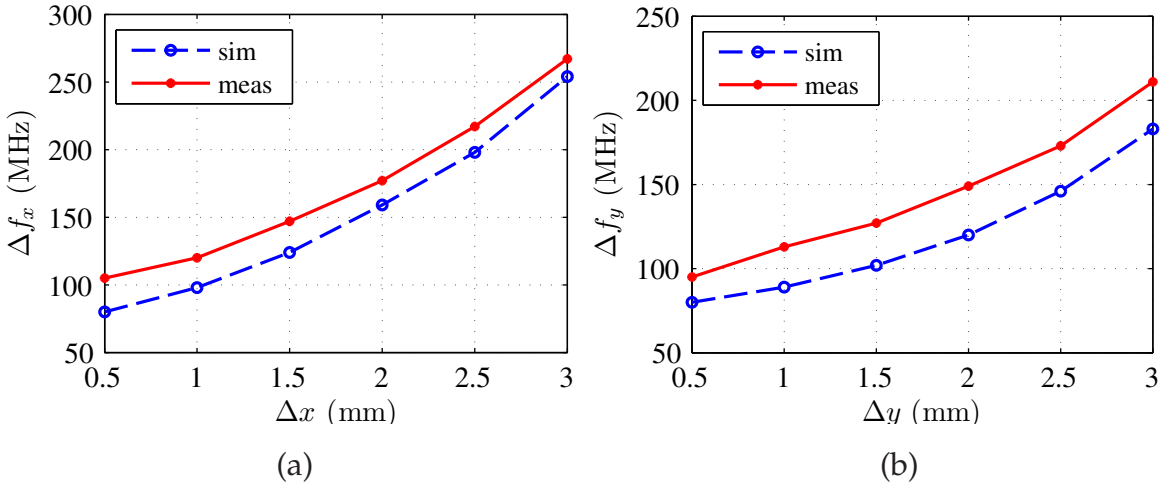

Figure 5.22. Measured transmission coefficients versus displacement of the 2-D sensor. Comparison between measured and simulated difference frequency versus displacement: (a) $f_{\Delta x}$ versus Δx, and (b) $f_{\Delta y}$ versus Δy.

5.4 Rotation Sensor Based on Horn-Shaped Split Ring Resonator

As shown in Section 5.2, the symmetry properties of an SRR-loaded CPW can be used for displacement sensing. It has been also shown by Naqui *et al.* (2011) that the same principle can be used to the design of SRR-based rotation sensors. As explained in detail by Naqui *et al.* (2011), a rotation of an SRR coupled to a CPW breaks the symmetry of the structure, resulting in a notch in the transmission coefficient of the structure. Since, the depth of the notch is dependent on the rotation of the SRR, this spectral feature can be used to sense the amount of the rotation. However, one limitation of the sensor is that a change in rotation not only changes the depth of resonance, but also causes a shift in the resonance frequency. Thus, the operation of the sensor requires a frequency sweeping microwave source such as an expensive network analyzer. In Section 5.2 it was shown that the shift in the resonance frequency in the displacement sensor based on uniform rectangular SRR is due to the non-uniformity of the magnetic flux passing through the SRR surface. Thus, the frequency shift can be suppressed by modifying the shape of the SRR to precisely adjust its equivalent capacitance and equivalent inductance. This allows the sensor to be operated as an inexpensive single frequency system.

In this section we show that a similar approach, based on the modification of the SRR shape, can be used to design a rotation sensor that not only operates at a single fixed frequency but also benefits from a higher dynamic range and superior linearity.

5.4.1 Rotation Sensor Based on Horn-shaped SRR

The proposed rotation sensor is composed of a CPW loaded with a horn-shaped SRR as illustrated in Fig. 5.23. The design starts by changing the rectangular SRR to a trapezoidal SRR, which increases the dynamic range. Next, the SRR sides are curved (as a 3-point spline) and the curvature is optimized to achieve a linear response. Finally, the length of the SRR's split is adjusted to achieve a fixed operating frequency. The geometric dimensions of the optimized structure are listed in the caption of Fig. 5.23.

Figure 5.24 compares the simulated transmission coefficients of the proposed sensor (solid lines) with those of a rectangular rotation sensor similar to the rotation sensor by Naqui *et al.* (2011) (dashed lines) for a rotation of the SRRs from $\theta = 0°$ to $6°$ in steps of $2°$. The figure clearly shows that while there is an angle-dependent shift in the resonance frequencies for the rectangular SRR, in the case of the optimized horn-shaped SRR all notches are at a fixed frequency $f = 1.38\,\mathrm{GHz}$.

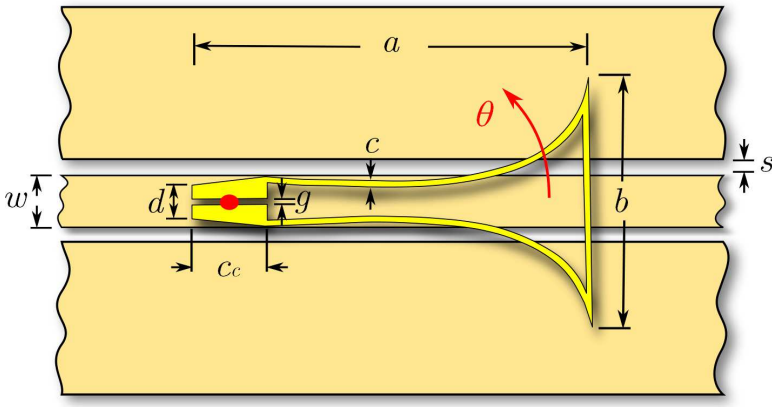

Figure 5.23. Layout of the proposed horn-shaped rotation sensor. Top view of the CPW loaded with a horn-shaped SRR. The angle and center of rotation are marked with a red arrow and a red dot, respectively. For electromagnetic simulation the parameters of a 0.127 mm thick RO3010 material with relative permittivity of 10.2 and copper metalization of $35\,\mu\mathrm{m}$ on both sides are used. The dimensions of the $50\,\Omega$ CPW and the horn-shaped SRR are as follows: $w = 1.67\,\mathrm{mm}$, $s = 0.2\,\mathrm{mm}$, $a = 12.6\,\mathrm{mm}$, $b = 7.8\,\mathrm{mm}$, $c = 0.2\,\mathrm{mm}$, $g = 0.2\,\mathrm{mm}$, $d = 1.1\,\mathrm{mm}$, and the optimized value of $c_c = 2.4\,\mathrm{mm}$.

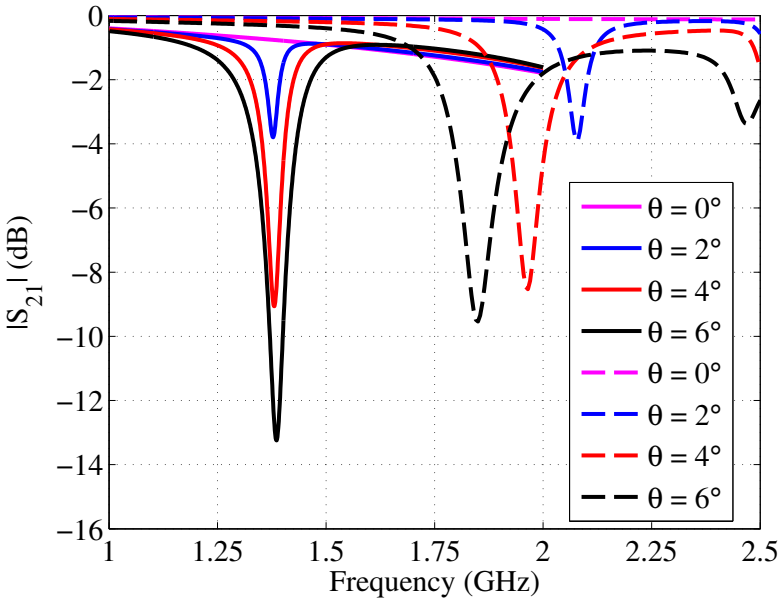

Figure 5.24. Simulated transmission coefficients of the horn-shaped rotation sensor. Simulated transmission coefficients of the horn-shaped rotation sensor (solid lines), and those of a rectangular-shaped rotation sensor (dashed lines) for the rotation of the SRRs from $\theta = 0°$ to $6°$ in steps of $2°$.

For proof-of-principle experimental validation of the concept, several versions of the rotation sensors were fabricated on a single substrate with different fixed angles of rotation ranging from $0°$ to $8°$. Fig. 5.25 shows the top and bottom view of one of the samples with $\theta = 5°$. The samples are fabricated on a 0.127 mm thick RO3010 material with relative permittivity of 10.2 and 35 μm thick copper metalization. The dimensions of the prototypes are as given in the caption of Fig. 5.23. Figure 5.26 depicts the measured transmission coefficients of the sensor for different values of rotation angle $\theta = 0°$, $2°$, $4°$, and $6°$. The figure shows a fixed resonance frequency at $f = 1.36$ GHz, which is in good agreement with the simulation results shown in Fig. 5.24.

Figure 5.27 compares the rotation angle dependence of the response for the rectangular and horn-shaped SRR sensors. For the rectangular sensor, the simulated depth of the notch, i.e. $\min(|S21|)$, is shown as a function of the angle. For the proposed horn-shaped sensor, the simulated transmission coefficients at a fixed frequency ($f = 1.38$ GHz) is plotted versus the rotation of the SRR. Additionally in the figure, the horn-shaped sensor simulations are successfully validated with the corresponding experimental data measured at $f = 1.36$ GHz. It is worth emphasizing that, for the rectangular sensor the center frequency of the notches varies with the angle of rotation. In contrast, the horn-shaped sensor operates at a fixed frequency, and thus does not

need a frequency sweeping system. The comparison also shows that, the proposed sensor benefits from a higher dynamic range which extends to about 7 degrees compared to 5 degrees for the rectangular sensor, and that it has a superior linearity in its dynamic range. Note that, while the dynamic range of the proposed rotation sensor has been significantly increased by using a horn-shaped SRR, the proposed rotation sensor suffers from a fundamental dynamic range limit. Thus, further investigation on the application of other types of metamaterial-inspired resonators for the design of rotation sensors with higher dynamic range (such as 0° to 360°) is required.

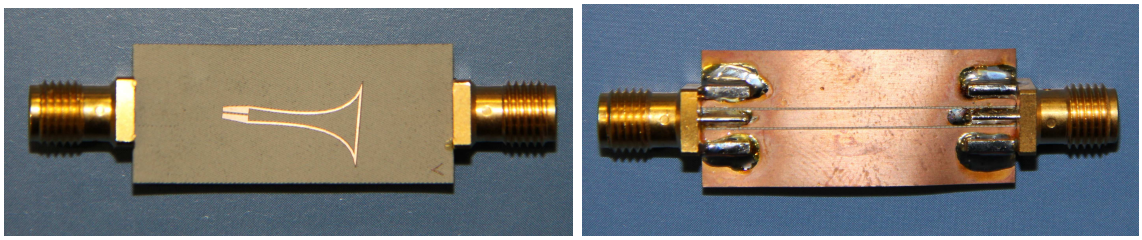

Figure 5.25. Fabricated prototype of the proposed rotation sensor. Top and bottom view of one of the fabricated samples of the proposed horn-shape rotation sensor with rotation of $\theta = 5°$.

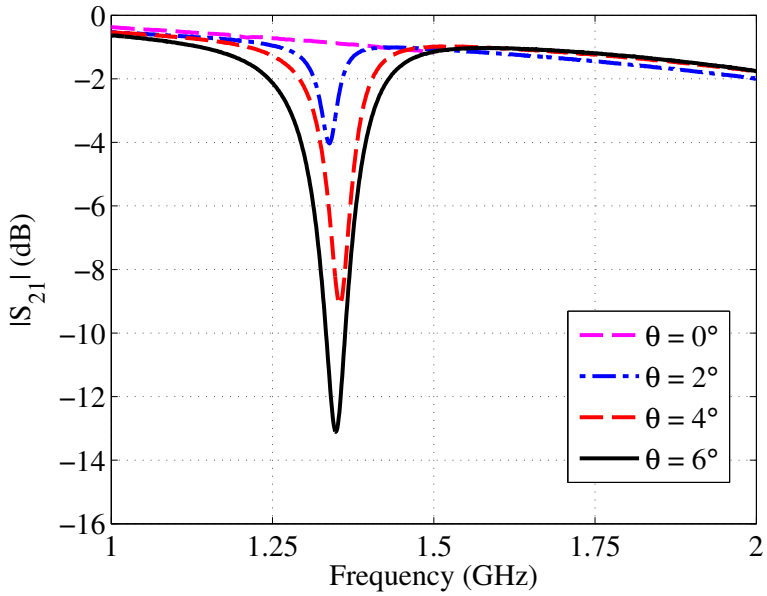

Figure 5.26. Measured transmission coefficients of the horn-shaped sensor. Measured transmission coefficients of the horn-shaped sensor for the rotation of the SRR from $\theta = 0°$ to 6° in steps of 2°.

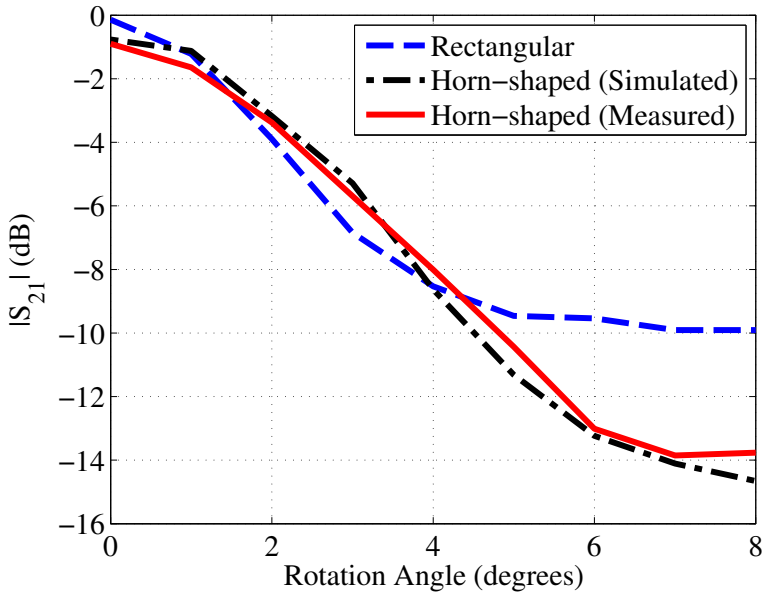

Figure 5.27. Measured transmission coefficients versus rotation angle of the horn-shaped sensor. Simulated depth of notch versus rotation angle for the sensor based on rectangular SRR (blue dashed line), and the simulated and measured transmission coefficients versus rotation angle for the horn-shaped sensor at a fixed frequency (black dash-dot line at 1.38 GHz and red solid line at 1.36 GHz, respectively).

5.5 Conclusions

This chapter has presented three different metamaterial-inspired sensors. The first sensor is a displacement sensor based on a diamond-shaped tapered SRR. The proposed shape modifications of the SRR improved the dynamic range of the sensor from 0.6 mm to 1.1 mm, which corresponds to an improvement of more than 80%. Also, compared to the displacement sensor based on a rectangular-shaped SRR, the proposed sensor has superior linearity. It is also shown that the undesirable shift in the resonant frequency in the characteristic of previous designs can be suppressed with an optimized tapered diamond-shaped SRR. This is a significant improvement since the sensor does not require a frequency sweeping microwave source, but can be operated as inexpensive single frequency system. Compared to the previously published displacement sensors, the proposed sensor also benefits from a lower operating frequency, which is generally desirable in sensing applications. Good agreement between simulation and measurement results validates the design principles.

The chapter also presented one- and two-dimensional displacement sensors based on microstrip lines loaded with broadside-coupled split-ring resonators. The principle of

operation of the proposed sensors is based on the splitting of the resonance frequencies caused by a displacement-induced break of symmetry. It has been shown that compared to the previously published metamaterial-inspired displacement sensors, the proposed sensors benefit from virtually unlimited dynamic range in displacement. Furthermore, since the operation principle of the sensors is based on the shift in the resonance frequency, rather than variation in the depth of notch, the sensors are generally immune to the environmental noise. Moreover, because the proposed sensors operate based on the breaking of symmetry, they are also robust to ambient conditions such as changes in the temperature, and can be also used as one- or two-dimensional alignment sensors. The concept and simulation results have been validated through good agreement between the simulated and the experimentally measured response of the manufactured two-dimensional sensor.

In the last section of the chapter, a rotation sensor based on a horn-shaped SRR has been presented. It has been shown that compared to previous SRR-based rotation sensors, the proposed sensor benefits from superior linearity and around 40% higher dynamic range. More importantly, it has been shown that the undesired frequency shift in the characteristic of a type of previously proposed metamaterial-inspired rotation sensor can be suppressed by precisely adjusting the length of the SRR's split. This is a significant improvement since the sensor does not require a frequency sweeping microwave source, but can be operated as an inexpensive single frequency system. The proposed sensor is possibly of greater interest in a scaled down structure using MEMS technology.

This chapter has been focused on the application of metamaterial-inspired resonators in the realization of high dynamic range displacement and rotation sensors. In the next chapter the focus will be placed on the miniaturization of metamaterial-inspired microwave filters.

Chapter 6

S-Shaped Split Ring Resonator and Complementary Split Ring Resonator

THE S-shaped split ring resonator (S-SRR) has been proposed as inclusion for synthesizing left-handed media. Despite its interesting features, the odd symmetry of the S-SRR precludes an axial magnetic field from exciting the fundamental resonance of the resonator. It is shown in this chapter that a high level of miniaturization can be achieved if the fundamental resonance of the particle is excited by contra-directional magnetic fluxes, which are readily available in CPW technology. This chapter also shows that the complementary counterpart of the particle, i.e., the S-shaped complementary split ring resonator (S-CSRR) acts as a compact resonator in differential microstrip technology. More importantly, it is shown that S-CSRRs can be used in the design of differential bandpass filters that inherently suppress the common-mode noise.

6.1 Introduction

As shown in the previous chapters, beside the application of the SRRs, CSRRs and other related particles in the synthesis of different types of bulk metamaterials with engineered electromagnetic properties, these resonators have been also used in the design of one- and two-dimensional planar circuits. In many cases effective media theory is not applicable, because the planar circuit is loaded with only a few resonators. Nevertheless, the key in the application of these resonators to the synthesis of metamaterial-inspired planar circuits is their small electrical size compared to the operating wavelength. As a consequence, these resonators can be considered as quasi-lumped elements that makes them especially interesting for the miniaturization of planar microwave structures and circuits such as filters (Martel *et al.* 2004, García-García *et al.* 2006, Bonache *et al.* 2006a, Gil *et al.* 2007, Velez *et al.* 2009, Horestani *et al.* 2012c), couplers (Jarauta *et al.* 2006), sensors (Naqui *et al.* 2011, Schueler *et al.* 2012, Naqui *et al.* 2012a, Withayachumnankul *et al.* 2012, Withayachumnankul *et al.* 2013, Horestani *et al.* 2013b), and antennas (Herraiz-Martínez *et al.* 2011, Herraiz-Martínez *et al.* 2012, Paredes *et al.* 2012) or to improve the performance of these components (García-García *et al.* 2005b, Shi *et al.* 2012).

In view of both the homogenized behavior of three-dimensional metamaterial, and quasi-lumped element in planar circuits, it is crucial for the unit resonator of the media to be much smaller than the operating wavelength at resonance. To this end, while maintaining the SRR physical size, the resonator's equivalent capacitance C or/and inductance L, which are related to the resonance frequency by $f_0 = 1/(2\pi\sqrt{LC})$, must be increased. The increase in the equivalent capacitance can be achieved either by narrowing the resonator's gap or decreasing inter-ring space, or by loading the resonator with lumped or semi-lumped capacitors, which for extreme values has limitations in terms of fabrication (Lin and Cui 2008, Withayachumnankul *et al.* 2010). Achieving a larger equivalent inductance by using narrower metallic rings has the same limitations, and additionally increases the resonator's Ohmic loss (Horestani *et al.* 2012b). A more efficient approach for the miniaturization of metamaterial resonators is to modify shape of the SRR to accommodate a higher equivalent capacitance and/or inductance. For instance, with a comparable dimension a higher equivalent capacitance can be obtained by using broadside-coupled SRRs, compared to edge-coupled SRRs (Marqués *et al.* 2002). The unit cell can be further miniaturized by modifying the SRR to spiral resonator (SR), multiple split ring resonator (MSRRs) or S-shaped

split ring resonator (S-SRR) (Chen *et al.* 2004, Falcone *et al.* 2004c, Chen *et al.* 2005a, Chen *et al.* 2005b, Chen *et al.* 2006b).

Despite the interesting feature of the bimetal S-SRR as inclusion for synthesizing left-handed media (Chen *et al.* 2004) , to the knowledge of the author, there has been no work on the application of single-layer S-SRR in planar circuits. The reason essentially arise from the odd symmetry of the S-SRR, which precludes an axial magnetic field from exciting the fundamental resonance of the resonator. It is shown in this chapter that a high level of miniaturization can be achieved in a single-layer S-SRR, if the loops of the S-SRR are excited by contra-directional magnetic fluxes, which makes the S-SRR very well suited for application in coplanar waveguide (CPW) technology. Furthermore, the proposed S-SRR is a single layer resonator that does not have the fabrication complexity of multi-layer S-SRRs (Chen *et al.* 2004). The combination of those two features makes the resonator ideally suited for the synthesis of different types of miniaturized filters in CPW technology.

The chapter also proposes the dual counterpart of the S-shaped split ring resonator, i.e., S-shaped complementary split ring resonator (S-CSRR) for application in the design of differential filters. It is shown that compared to the conventional configuration of CSRRs in differential microstrip technology, the proposed resonator benefits from a high level of miniaturization when excited by the contra-directional electric fields of a differential microstrip line. More importantly, it is shown that S-CSRRs can be used in the design of bandpass filters that suppress the common-mode noise inherently.

The chapter is organized as follows. The principle of even mode excitation of S-SRR in CPW technology is explained in Section 6.2, with demonstration of the achievable size reduction compared to edge-coupled SRRs. A corresponding circuit model and its parameter extraction method are introduced and validated through electromagnetic simulations. The methodology to design bandpass filters based on S-SRR loaded CPWs is presented in Section 6.3, firstly based on impedance inverters and secondly on coupled resonators theory. Prototypes of both S-SRR based filters have been fabricated and their performance has been measured. The satisfactory agreement between simulation and measurements experimentally validates the methodology.

Section 6.4 is focused on the S-shaped CSRR. The working principle of the resonator is explained and a circuit model is developed and validated through electromagnetic simulations. In Section 6.5 it is shown that an S-CSRR-loaded differential microstrip

line with series gaps can be used in the design of compact differential bandpass filters with common-mode suppression. The filter design procedure is explained and the theoretical concept is validated through fabrication and measurement of a compact ($0.09\lambda_g \times 0.25\lambda_g$) third-order differential bandpass filter with common-mode suppression. Finally, the main conclusions of the study are highlighted in Section 6.6.

6.2 S-Shaped Split Ring Resonator and its Application to Compact Bandpass Filter Design

The first part of this section focuses on the working principle of S-SRRs in CPW technology, and discusses the achieved level of miniaturization of the proposed S-SRR compared to conventional SRR. A circuit model and its parameter extraction method are presented in the second subsection.

6.2.1 S-SRR Operation Principle

Fig. 6.1(a) illustrates a layout of the typical configuration of SRR-loaded CPW for filter applications. It consists of a pair of double ring SRRs etched on the back side of the CPWs substrate, with the center of the rings symmetrically located underneath the two slots of the CPW. As shown in the figure, the CPW's magnetic field is induced in the inner region of the SRRs in this configuration, and electromagnetic wave propagation along the CPW is inhibited in a narrow band in the vicinity of the SRR resonance frequency (Martín *et al.* 2003b, Martín *et al.* 2003a). It is emphasized that, in this configuration the magnetic fields passing through the surfaces of the two symmetrical SRRs are contra-directional. Thus, as suggested in Fig. 6.1(b), if the CPW is loaded only with a double ring SRR etched on the back side of the substrate, and centered below the CPW line, the net magnetic flux passing through the surface of the SRR is zero. Hence, an SRR aligned with the symmetry plane of the CPW is not excited and does not create a spectral notch in the transmission coefficient of the CPW. Nevertheless, because of its sensitivity to the breaking of symmetry, the structure can be used as a rotation or displacement sensor or as a radio frequency bar code (Naqui *et al.* 2012a, Naqui *et al.* 2012a, Horestani *et al.* 2013b).

In contrast, the operation principle of the S-shaped SRR takes advantage of the contra-directional magnetic fields of the two slots of the CPW. To this end, the two SRRs in

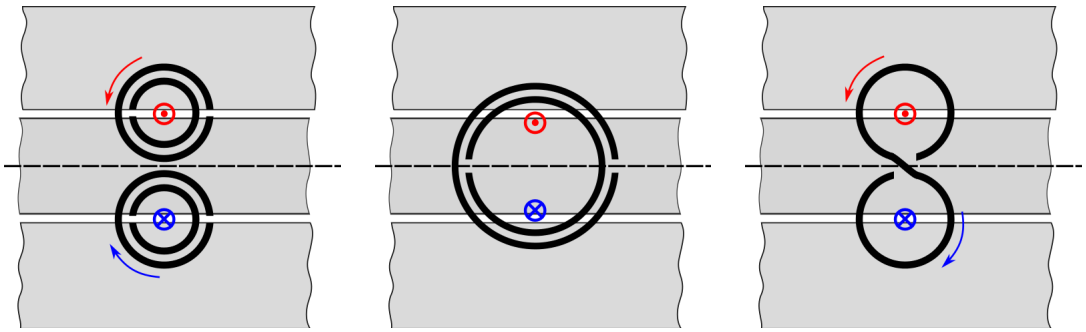

Figure 6.1. CPW loaded with SRRs or S-SRR. Bottom view of a coplanar waveguide loaded with various types of SRRs: (a) typical configuration in filter applications, which involves a pair of double ring SRRs under the CPW slots, (b) one double ring SRR aligned with CPW symmetry plane, (c) an S-shaped SRR.

the configuration of Fig. 6.1(a) are etched face-to-face so that they can be connected to form the S-shaped SRR, as shown in Fig. 6.1(c). In this configuration the currents induced by the contra-directional magnetic fields of the CPW's slots in both rings of the S-SRR are in same direction, and thus the structure can be excited by the CPW fields at resonance. Note that the equivalent inductance of the S-SRR is at least a factor of two larger than that of the pair of conventional SRRs with the same physical size, which allows attaining a lower resonance frequency, and thus effectively miniaturize the resonant element.

In order to investigate through simulation the achieved level of miniaturization, rectangular SRR and S-SRR are used as a test case for the sake of simplicity. The layout of the CPW loaded with the rectangular S-SRR is illustrated in Fig. 6.2. A 0.635 mm thick Rogers *RO3010* material with relative permittivity of 10.2 and 35 μm thick copper metalization is used as the substrate. The CPW's central strip width w is 4.8 mm and the slots' width is $s = 1$ mm, which correspond to a 50 Ω characteristic impedance. The dimensions of the S-SRR are $a = 6.2$ mm, $b = 5.7$ mm, $c = 0.2$ mm, $g = 1$ mm, and the space between the two connected rings is $d = 0.2$ mm. For comparison purposes, a CPW loaded with a pair of SRRs with the same dimensions (not shown in the figure) is simulated as well.

Fig. 6.3 compares the simulated transmission and reflection coefficients of the CPW loaded with the two different resonator configuration, i.e., a pair of SRRs and the S-SRR (dashed lines and solid lines, respectively). As clearly observed from the graph, the

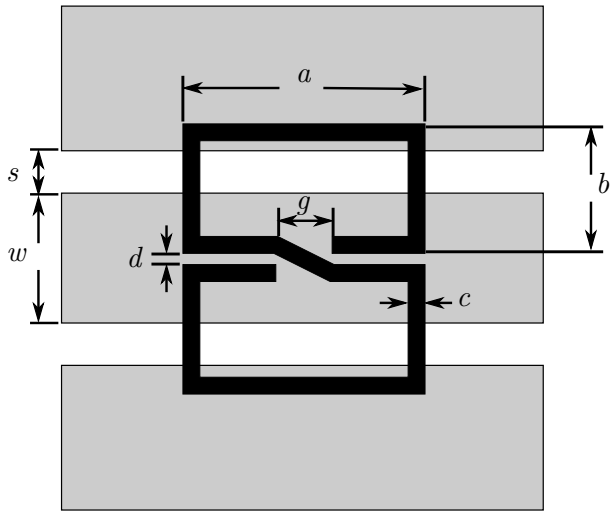

Figure 6.2. CPW loaded with a rectangular S-SRR. A coplanar waveguide loaded with a rectangular S-SRR. CPW is depicted in gray, whereas the S-SRR on the backside of the substrate is depicted in black.

resonance frequency of the S-SRR is at $f = 1.24$ GHz, while the pair of the SRRs with the same physical dimensions resonates at more than twice that frequency at 2.81 GHz.

6.2.2 Circuit Model and Parameter Extraction

Let us now focus on the equivalent circuit model for the structure of Fig. 6.2. The lumped element equivalent circuit model of the structure in CPW mode is depicted in Fig. 6.4(a). For clarity, the circuit model of a CPW loaded with an SRR which is symmetrically etched on the backside of the substrate, shown in Fig. 6.1(b), is also depicted in Fig. 6.5(a). Both models are drawn symmetrically with respect to the symmetry plane of the CPW. Note that, L and C are the per-section equivalent inductance and capacitance of the CPW, while the resonators are modeled by capacitance C_s and inductance L_s which are coupled to the CPW through the mutual inductance M. Note that in the circuit model of the CPW loaded with a symmetrically etched SRR, shown in Fig. 6.5(a), the currents induced by the CPW in the inductors of the SRR model are in opposite directions. Thus, for the CPW (even) mode, the current in the middle of the ring is zero, the ring can be considered as open circuit and the circuit model can be simplified to that depicted in Fig. 6.5(b). From the simplified circuit model it is clear

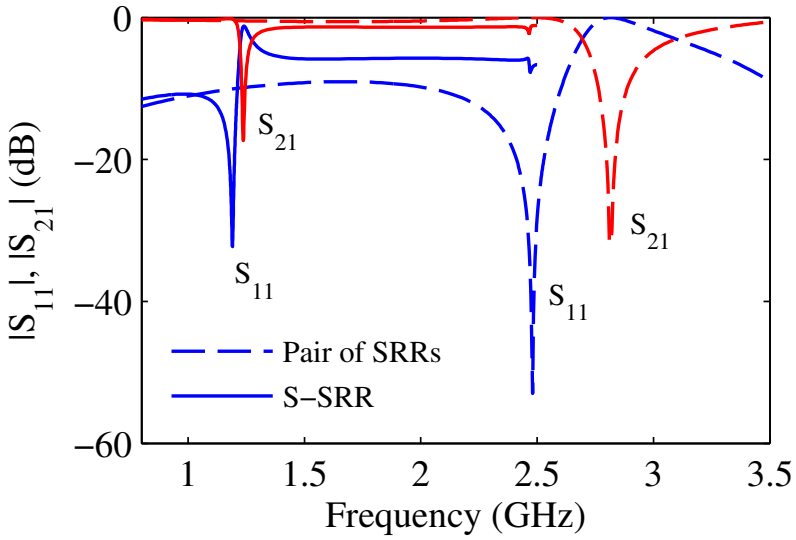

Figure 6.3. Comparison between the simulated S_{21} and S_{11} of the SRR-loaded CPW and those of the S-SRR-loaded CPW. Comparison between the simulated transmission and reflection coefficients of the CPW loaded with an S-SRR (solid lines) with those of a CPW loaded with a pair of SRRs with the same physical size (dashed lines). Simulation results clearly show that the resonance frequency of the S-SRR is less than half of the resonance frequency of the pair of SRRs.

that the structure is transparent to the propagation of electromagnetic waves. In contrast, it is clear from Fig. 6.4(a) that due to the twisted structure, induced currents in the inductors of the S-SRR model are in same direction. Thus, the S-SRR is excited at resonance and the circuit model can be simplified to the equivalent circuit of Fig. 6.4(b), where, $L'_s = \omega_0^2 M^2 C_s$, $C'_s = L_s/(\omega_0^2 M^2)$, $L' = L - L'_s$, and the resonance frequency is $\omega_0^2 = 1/(L_s C_s) = 1/(L'_s C'_s)$ (Martín *et al.* 2003a, Aznar *et al.* 2008b).

In order to validate the proposed model, the electromagnetic simulation results of Fig. 6.3, which corresponds to the S-SRR loaded CPW of Fig. 6.2 are considered, and the parameters of the simplified equivalent circuit model of Fig. 6.4(b) are extracted following the procedure explained by Aznar *et al.* (2008b). The extracted parameters are as follows: $C = 3.36$ pF, $L' = 1.94$ nH, $C'_s = 56.7$ pF , and $L'_s = 0.29$ nH. Fig. 6.6 shows a good agreement between the amplitude and phase of the transmission and reflection coefficients obtained from the circuit model and those from the electromagnetic simulations, validating the circuit model and the parameter extraction method.

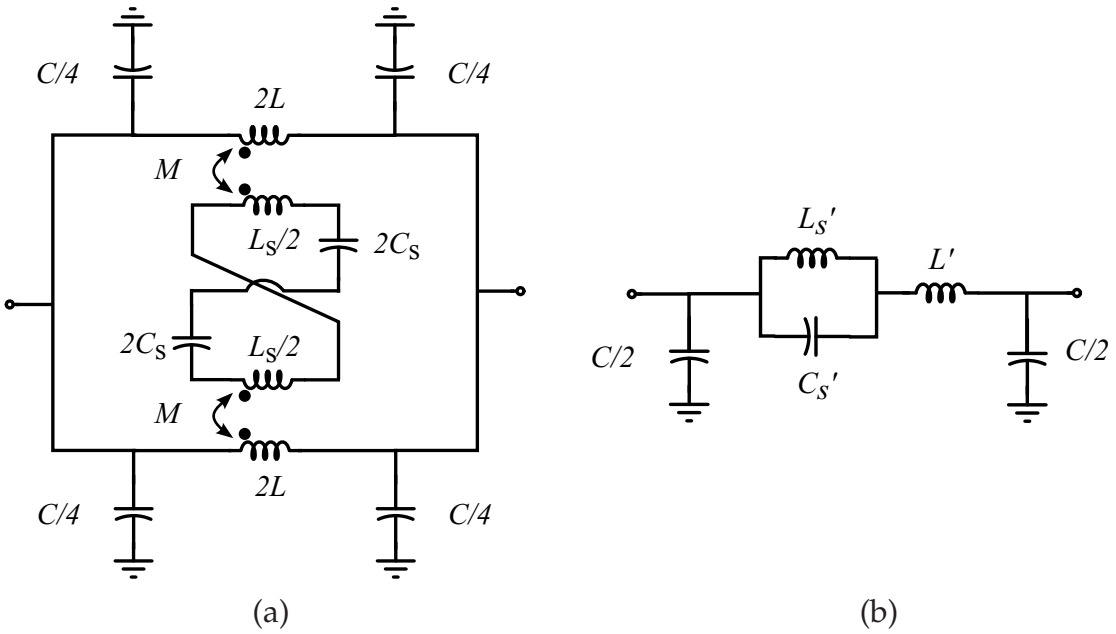

Figure 6.4. Equivalent circuit model of the S-SRR loaded CPW. (a) Lumped element equivalent circuit model of the S-SRR loaded CPW. Note that due to the twisted structure, induced currents in the inductors of the S-SRR model are in the same direction. Thus the resonator is excited. (b) The simplified circuit model of the structure.

6.2.3 CPWs Loaded with S-SRRs and Series Gaps

It is known that SRRs or CSRRs coupled to a transmission line can inhibit, in the vicinity of their resonance, the propagation of electromagnetic waves along the line. This bandstop can be interpreted as the spectrum where the SRR/CSRR loaded transmission line behaves as a single-negative one-dimensional media. It has been shown in (Martín *et al.* 2003a, Falcone *et al.* 2004c, Bonache *et al.* 2004) that this behavior can be switched to a bandpass behavior simply by introducing an extra element. Depending on the resonator type, which could be SRR or CSRR and the introduced element, which could be series capacitor or shunt inductor, the resulting bandpass structure can support either left-handed or right-handed waves. A typical layout is depicted in Fig. 6.7(a), where the extremes of the S-SRR are expanded to become rectangular patches, laying on top of the CPW central strip. These patches help to enhance the electric coupling, which is the dominant coupling mechanism between the line and the S-SRR since the line current is minimized due to the presence of the gap. In order to suppress the propagation of the slot mode, while avoiding the added complexity associated with the fabrication of air-bridges, the ground planes are connected by a

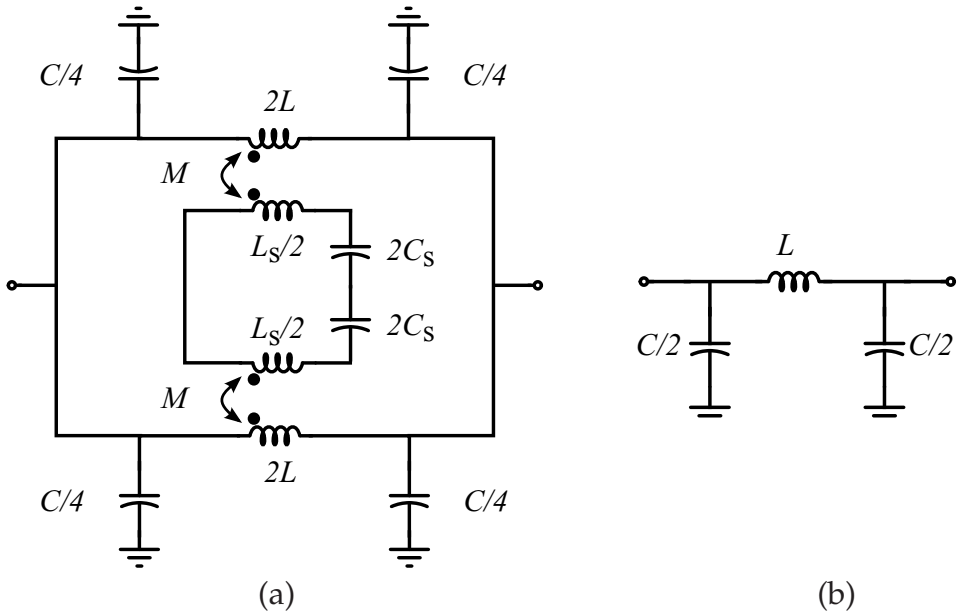

Figure 6.5. Equivalent circuit model of the SRR loaded CPW. (a) Lumped element equivalent circuit model of the CPW loaded with an SRR, which is aligned with the symmetry plane of the CPW. Note that in this case, induced currents in the inductors of the S-SRR model are in opposite directions. Thus the resonator is not excited. (b) The simplified circuit model of the structure at frequencies around the resonance frequency, identical to a section of transmission line.

narrow strip though the CPW's series gap. The proposed lumped element equivalent circuit model of the structure is depicted in Fig. 6.7(b). The physical interpretation of the different circuit parameters is as follows: L and C are the equivalent inductance and capacitance of the CPW section, while the CPW gap is modeled with C_g. The equivalent inductance of the S-SRR is represented by L_s. The capacitance between the S-SRR patches is modeled by C_{pat}, and the electric coupling between the S-SRR and CPW is modeled with C_s. To extract the six unknown parameters of the circuit model, we first extract L and C_g from EM simulation of the gap-loaded CPW without S-SRR. Then, the remaining four unknowns can be univocally extracted following the procedure in (Aznar *et al.* 2008b). This circuit can be simplified to that depicted in Fig. 6.7(c) by using transformation equations also given in the figure. To validate the equivalent circuit model, a comparison between circuit simulation with extracted parameters and full wave simulation of the structure of Fig. 6.7(a) is depicted in Fig. 6.8(b). The physical dimensions of the structure and the extracted circuit parameters are listed in the

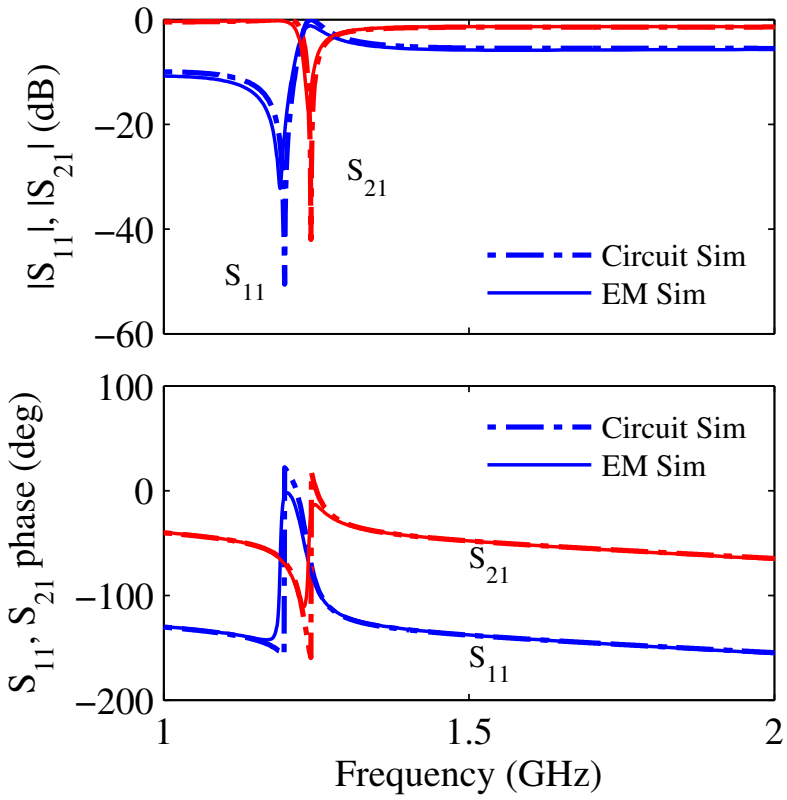

Figure 6.6. Comparison between circuit simulation and EM simulation results of the S-SRR loaded CPW structure. Comparison of the transmission and reflection coefficients from the proposed circuit model and those from electromagnetic simulation of the S-SRR loaded CPW structure. Top: amplitude, bottom: phase.

caption of Fig. 6.7. The very good agreement in the region of interest validates the proposed model.

6.3 Application to Miniaturized Band-pass Filters in CPW Technology

The main aim of this section is to demonstrate the potential of the S-SRR for the synthesis and design of miniaturized microwave bandpass filters in CPW technology. To this end, in the following subsections two types of bandpass filters based on S-SRRs are synthesized. In both cases the design and synthesis procedures are explained and validated through electromagnetic simulations and experiment.

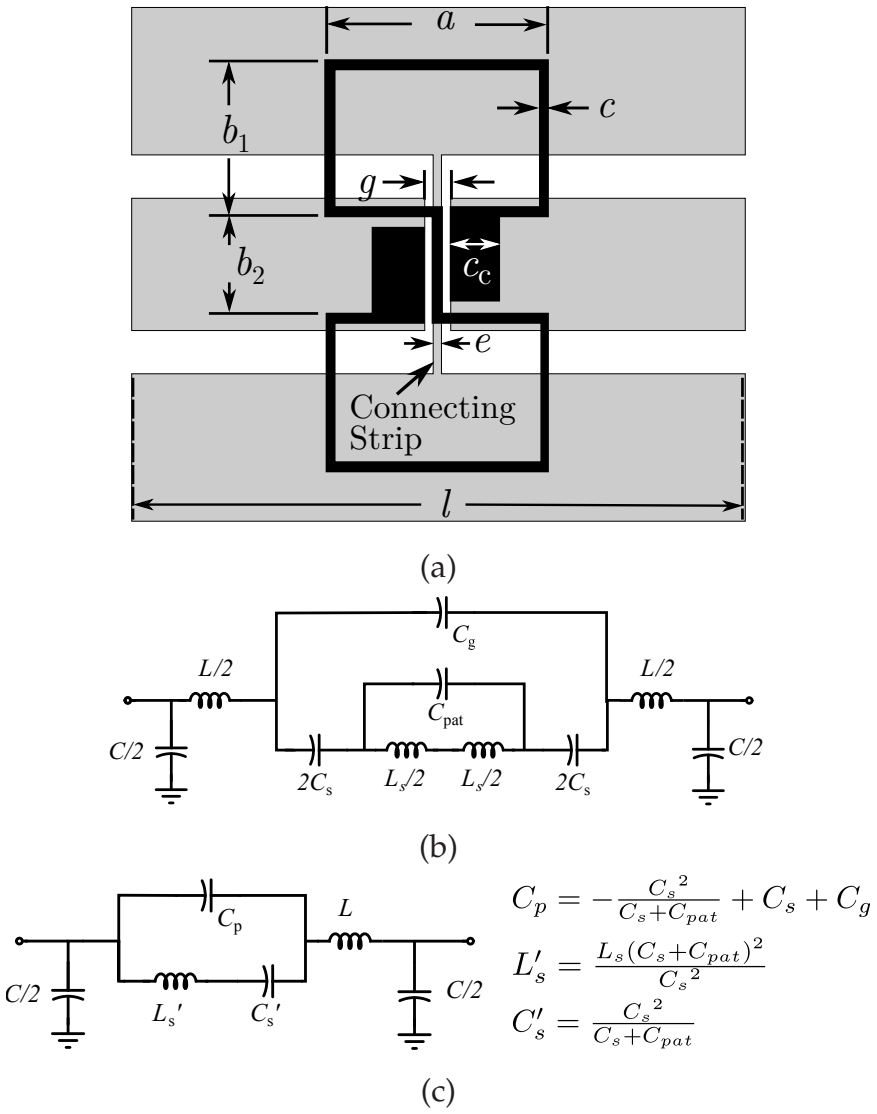

$$C_p = -\frac{{C_s}^2}{C_s+C_{pat}} + C_s + C_g$$
$$L'_s = \frac{L_s(C_s+C_{pat})^2}{{C_s}^2}$$
$$C'_s = \frac{{C_s}^2}{C_s+C_{pat}}$$

Figure 6.7. Layout and equivalent circuit models of the S-SRR/gap loaded CPW. (a) CPW loaded with a S-SRR and a series gap. A 0.635 mm thick Rogers *RO3010* material with relative permittivity of 10.2 is used for EM simulations. The dimensions (in mm) of the structure are $w = 4.8$, $s = 1$, $a = 6.2$, $b_1 = 4.2$, $b_2 = 3.2$, $c = 0.2$, $c_c = 1.4$, $e = 0.4$, and $g = 0.8$. (b) lumped element equivalent circuit model, and (c) simplified circuit model. The extracted parameters are as follows: $L = 1$ nH and $C = 4.15$ pF, $C_g = 0.1$ pF, $C_{pat} = 0.14$ pF, $L_s = 51$ nH, and $C_s = 0.29$ pF.

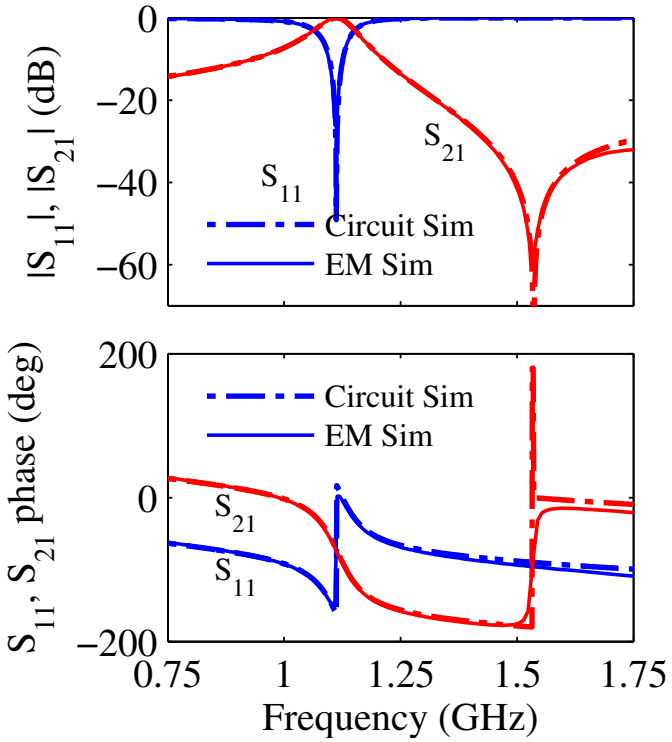

Figure 6.8. Comparison between circuit simulation and EM simulation results of the S-SRR/gap loaded CPW structure. Comparison of the transmission and reflection coefficients from the proposed circuit model and those from electromagnetic simulation of the S-SRR/gap loaded CPW structure. Top: amplitude, bottom: phase.

6.3.1 Band-pass Filter based on Impedance Inverters

As the first prototype device example for the application of the S-SRR, a bandpass filter based on impedance inverters is designed and synthesized. By coupling unit cells of Fig. 6.7(a) through impedance inverters, bandpass filters described by the network of Fig. 6.9 can be synthesized. In this configuration, the filter's unit cell is composed of the CPW section, which is loaded with series gap and S-SRR, whereas the feeding lines, in conjunction with the feeding lines of the adjacent cells, act as 90° impedance inverters with normalized impedance of $K = 1$. Note the filter cell also exhibits a transmission zero (see Fig. 6.8) that is interesting to enhance the filter selectivity above the passband.

The design procedure starts from optimization of the geometric dimensions of the unit cell to achieve the resonance at the central frequency of the filter. The filter's fractional

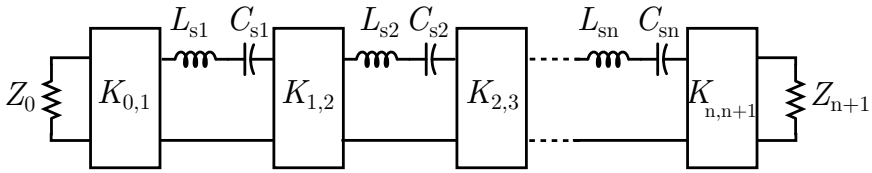

Figure 6.9. Generalized network of a bandpass filter. The generalized bandpass filter network using impedance inverters.

bandwidth (FBW) is controlled by the reactance slope of the resonators, while the feeding lines are de-embedded to the edges of the S-SRR (i.e. $l = a$), through [22]

$$\begin{aligned} K_{0,1} &= \sqrt{\frac{\mathrm{FBW}\, x_1}{g_0 g_1}}, \\ K_{n,n+1} &= \sqrt{\frac{\mathrm{FBW}\, x_n}{g_n g_{n+1}}}, \\ K_{i,i+1} &= \mathrm{FBW}\sqrt{\frac{x_i x_{i+1}}{g_i g_{i+1}}}, \end{aligned} \tag{6.1}$$

where g_i's are the elements of the lowpass filter prototype and the reactance slope of the resonator can be obtained from electromagnetic simulations by using

$$x_i = \frac{\omega_0}{2}\frac{dX_i(\omega)}{d\omega}|_{\omega=\omega_0}, \tag{6.2}$$

where $X_i(\omega)$ is the reactance of the unit cell. The optimization of the resonator's dimensions have been aided with the circuit model since simulations at the circuit level are faster and the effect of the geometry to the circuit parameters is known.

Once the dimensions of the resonators are optimized to satisfy the resonance frequency and the reactance slope, the length of the feeding lines should be optimized to achieve a 90° phase shift from port one to port two of the unit cell at resonance frequency. This procedure is repeated for all unit cells, and finally the filter can be simply realized by cascading the designed unit cells.

To demonstrate the validity of the proposed approach, a third-order periodic (although, this is not mandatory from the design point of view) bandpass filter with 6% FBW, ripple of 0.16 dB and central frequency of 1.1 GHz is designed. Since the filter is periodic, all resonators are identical with the same $g_i = g$ and consequently same reactance slope. The value of g is obtained to be 1.155 by forcing a third-order lowpass filter prototype with identical element values to exhibit a cutoff frequency at $\omega = 1$ rad/s while having 0.16 dB in-band ripple. The dimensions of the resonator are optimized to achieve the reactance slope that is calculated from substituting $g = 1.155$ in (6.1).

To this end, as shown in Fig. 6.7(a) the parameters a or b_1 can be used to adjust the equivalent inductance of the resonator while the parameter c_c controls its equivalent capacitance. A 0.635 mm thick Rogers *RO3010* material with relative permittivity of 10.2 is used as the substrate. The CPW's central strip width is $w = 4.8$ mm and the slots' width is $s = 1$ mm, which correspond to a 50 Ω characteristic impedance. The optimized dimensions of the resonator that meets the required resonance frequency and the reactance slope are $a = 6.2$ mm, $b_1 = 4.2$ mm, $b_2 = 3.2$ mm, $c = 0.2$ mm, $c_c = 1.4$ mm, and $g = 0.8$ mm.

The next step is to optimize the length of the feeding CPWs on both sides of the resonator to obtain a 90° phase shift between port one and port two of the structure. The filter layout, which is composed of three unit cells is depicted in Fig. 6.10. The longitudinal dimension of each unit cell is $l = 22.5$ mm. Similarly, the circuit model of the filter can be realized by alternatively cascading the circuit model of the three unit cells and impedance inverters. Fig. 6.11 compares the transmission and reflection coefficients of the filter's circuit model to those from the electromagnetic simulation of the device. The figure shows a very good agreement between the results in a sufficiently wide band around the filter's center frequency.

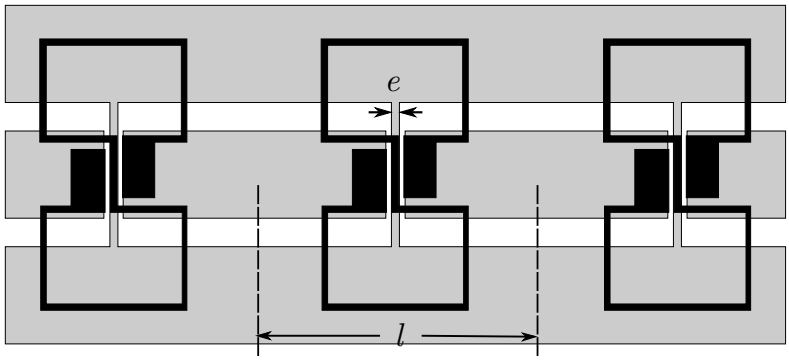

Figure 6.10. Layout of the third order periodic bandpass filter. Layout of the third order periodic bandpass filter using S-SRR loaded CPW and impedance inverters. Note that in order to suppress the propagation of the slotline mode, the ground planes are connected by a narrow strip though the CPW's series gaps.

It is worth mentioning that since the S-SRR is not a symmetric structure, the parasitic slotline mode may be excited in the CPW. The propagation of the slotline mode can

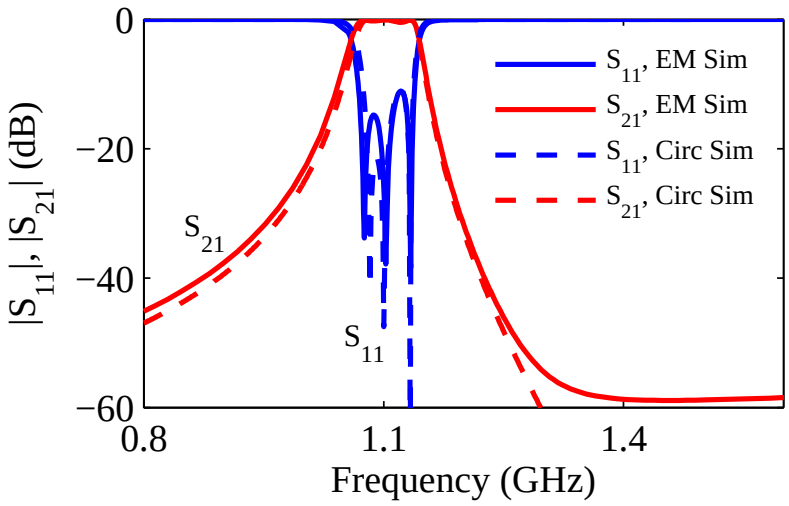

Figure 6.11. Comparison between circuit and EM simulation of the 3rd order filter. Comparison between transmission and reflection coefficients of circuit (dashed lines) and electromagnetic (solid lines) simulations of the third order periodic bandpass filter based on S-SRR-loaded CPW.

be suppressed by adding air-bridges along the CPW structure on both sides of each S-SRR to connect the ground planes and consequently equalize their voltages. However, specifically in this design, in order to avoid the added complexity associated with the fabrication of air-bridges, the ground planes are connected by a narrow strip though the CPW's series gaps, as shown in the filter layout of Fig. 6.10. The width of the strip is $e = 0.4$ mm.

Fig. 6.12 shows the top and bottom photographs of the fabricated filter. The lateral and longitudinal dimensions of the filter are 12 mm and 52 mm, respectively (i.e. $0.32\lambda_g \times 0.08\lambda_g$ where λ_g is the guided wavelength). The frequency responses obtained from electromagnetic simulation and measurement are depicted in Fig. 6.13. The figure shows a satisfactory agreement between the results. Note that the simulation results correspond to the case of a lossless device. By using the measured insertion loss at the center frequency of the filter in dB, i.e., $\Delta L_{A0} = 3.5$ dB, the S-SRR's unloaded quality factor $Q_{ul} = 80$ is calculated from Hong and Lancaster (2001)

$$\Delta L'_{A0} = 4.343 \sum_{i=1}^{n} \frac{1}{\mathrm{FBW} Q_{ul}} g_i \,\mathrm{dB}, \tag{6.3}$$

where Q_{ul} is the unloaded quality factor of the resonator, g_i's are the elements of the lowpass prototype and n is the order of filter.

Note that the electromagnetic simulation results correspond to the case of a lossless device. The simulated results, while excluding the conductor and substrate losses, confirm that radiation losses are not significant.

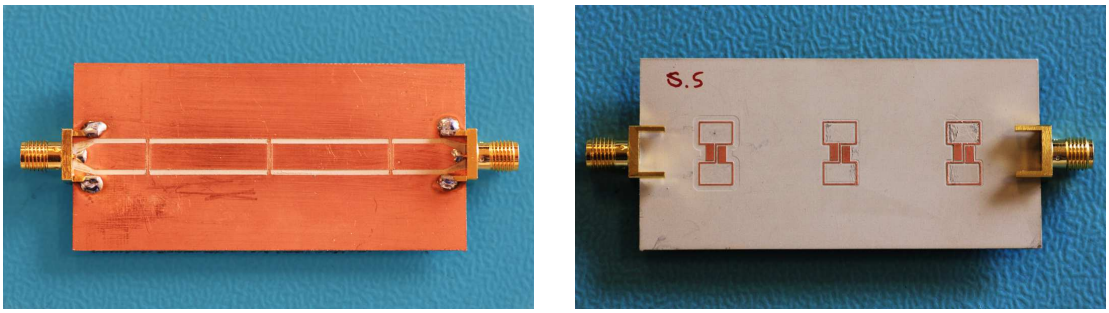

(a) (b)

Figure 6.12. Fabricated prototype of the 3rd order periodic fitler. Top (a) and bottom (b) photograph of the fabricated third order periodic bandpass filter.

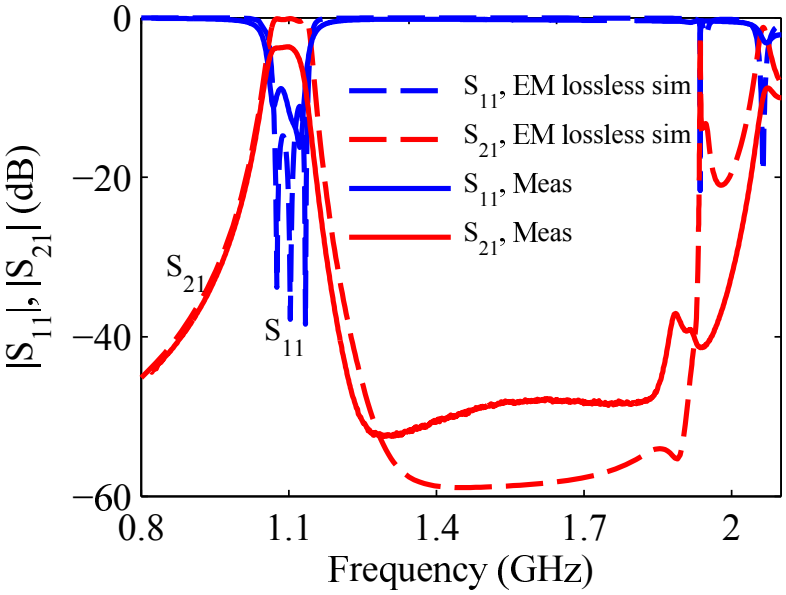

Figure 6.13. Simulated and Measured S_{21} and S_{11} of the 3rd order periodic filter. Simulated (dashed lines) and measured (solid lines) transmission and reflection coefficients of the third-order periodic filter of Fig. 6.12 based on S-SRR loaded CPW. Note that the simulated results correspond to the case of a lossless device.

6.3.2 Band-pass Filter Based on the Theory of Coupled Resonators

Despite the wide application of conventional bandpass structures based on end-coupled or parallel-coupled half-wavelength resonators, because of their relatively large size, great efforts have been devoted to the miniaturization of this type of filters, for instance by means of slow-wave or metamaterial-inspired structures (Hong and Lancaster 1997, García-García *et al.* 2006, Horestani *et al.* 2012c). Here it is shown that S-SRRs can be used as the miniaturized resonator elements in the design of bandpass filters based on the coupling theory.

To this end, a third order Chebyshev filter prototype is designed to meet the following specifications: center frequency $f_0 = 1.1$ GHz, bandwidth of 80 MHz, and a maximum passband ripple of 0.2 dB. Given the filter specifications, the coupling coefficients M_{12}, and M_{23} and the external quality factors Q_{e1} and Q_{e3} are obtained from Matthaei *et al.* (1963)

$$Q_{e1} = \frac{g_0 g_1}{\text{FBW}}, \qquad Q_{e3} = \frac{g_3 g_4}{\text{FBW}}, \tag{6.4}$$

$$M_{12} = \frac{\text{FBW}}{\sqrt{g_1 g_2}}, \qquad M_{23} = \frac{\text{FBW}}{\sqrt{g_2 g_3}}, \tag{6.5}$$

where g_i's are the Chebyshev lowpass prototype elements and FBW denotes the fractional bandwidth of the filter. Using these equations, the filter specifications are achieved using the external quality factors $Q_{e1} = Q_{e3} = 17$ and the coupling coefficients $M_{12} = M_{23} = 0.061$.

Fig. 6.14 illustrates the geometry of the filter, which is composed of two open ended CPWs (shown in gray shading) that are coupled through three S-SRRs etched on the backside of the substrate (shown in black color). In this configuration the coupling coefficients can be adjusted by changing the space between the S-SRRs, denoted as d in the figure, and the required external quality factor can be achieved by changing the area where the open-ended CPW and the S-SRRs are overlapped, i.e., by slightly displacing the full S-SRR either on the left or the right of the CPW open end. Note that since in this configuration open-ended CPWs are used, the dominant coupling mechanism between the CPW and the first and the last resonators is an electric coupling. Thus, alternatively the S-SRR is horizontally centered onto the open end of the CPW and the width of the capacitive parts of the S-SRR c_c can be adjusted to achieve the desired external quality factor.

The latter approach is applied in this example and the external quality factor and coupling coefficients are characterized through electromagnetic simulations from following equations (Matthaei *et al.* 1963)

$$Q_e = \frac{2\pi f_0 \tau_{11}(\omega_0)}{4}, \tag{6.6}$$

where f_0 is the resonant frequency and $\tau_{11}(\omega_0)$ is the group delay of S_{11} at resonance frequency, and

$$M_{ij} = \frac{f_2^2 - f_1^2}{f_2^2 + f_1^2}, \tag{6.7}$$

where, f_2 and f_1 are the two resonance frequencies of the pair of coupled resonators while they are weakly coupled to the open-ended CPWs.

The dimensions of the CPW are $w = 4.8$ mm and $s = 1$ mm, which corresponds to a characteristic impedance of 50 Ω on a 0.635 mm thick Rogers RO3010 material with relative permittivity of 10.2. Dimensions of the S-SRRs are as follows: $a = 6.2$ mm, $b_1 = 4.2$ mm, $b_2 = 3.2$ mm, $c = 0.2$ mm and $e = 0.8$ mm. The simulated external quality factor Q_e as a function of the S-SRR's dimension c_c and the coupling coefficient M_{ij} as a function of the distance between a pair of S-SRRs d are depicted in Fig. 6.15 (a) and (b), respectively. The figure shows that in order to meet the required external quality factor $Q_{e1} = Q_{e2} = 17$ and coupling coefficients $M_{12} = M_{23} = 0.061$, required by the filter specifications, c_c needs to be 1.4 mm, and the space between the resonators d needs to be set to 0.3 mm.

Fig. 6.16 depicts the photograph of the top and bottom view of the fabricated sample. The active area of the device has a longitudinal length of 19.2 mm and transverse length of 11.6 mm, i.e. $0.12\,\lambda_g$ by $0.08\,\lambda_g$, where λ_g is the guided wavelength. Fig. 6.17 compares the simulated and measured transmission and reflection coefficients of the filter. The figure shows a good agreement between the simulated and measured results, whereas the filter in-band measured insertion loss of 2.5 dB can accurately be predicted from (6.3).

In order to evaluate the performance of the proposed filters, Table 6.2 provides a comparison between the measured characteristics of the proposed filters to those of state-of-the-art narrow bandpass CPW filters. The table shows that in comparison to bandpass filters with similar order and fractional bandwidth, the filter based on S-shaped SRR/gap-loaded CPW (structure of Fig. 6.12) has a slightly high insertion loss. This

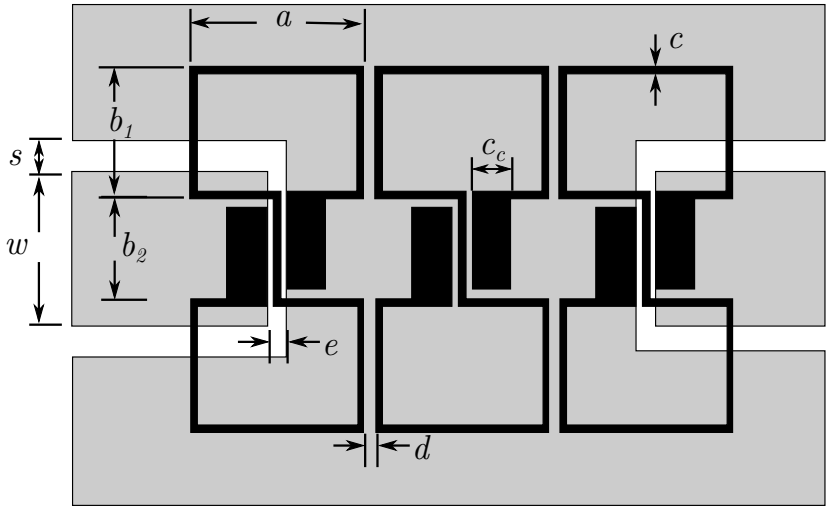

Figure 6.14. Layout of the third order coupled resonator bandpass filter. Layout of the third order coupled resonator bandpass filter based on S-SRRs.

can be attributed to the fabrication tolerance and inaccuracy of the substrate relative permittivity. However, in comparison to other filters listed in the table, the filter is more compact in size. Table 6.2 also shows that in comparison to the state-of-the-art narrow bandpass CPW filters, the proposed third-order filter based on coupled S-shaped SRRs (structure of Fig. 6.16) benefits from a good in-band insertion loss of 2.5 dB as well as a highly compact size. Overall, the comparison clearly shows that, while the proposed filters (especially the filter based on coupled SRRs) have very compact sizes, they have reasonably good in-band insertion losses for their order and FBW.

6.4 S-Shaped CSRR and its Application to Compact Differential Bandpass Filters

Transmission of high-speed digital and analog signals in differential mode is proven to be the most efficient method to increase the signal immunity to environmental noise, electromagnetic interference (EMI) and crosstalk. However, in practical differential systems, the presence of some level of common-mode noise is unavoidable (Wu *et al.* 2009). Thus, a differential-to-differential balanced filter that passes the desired frequency response of the differential signal, while suppressing the common-mode noise

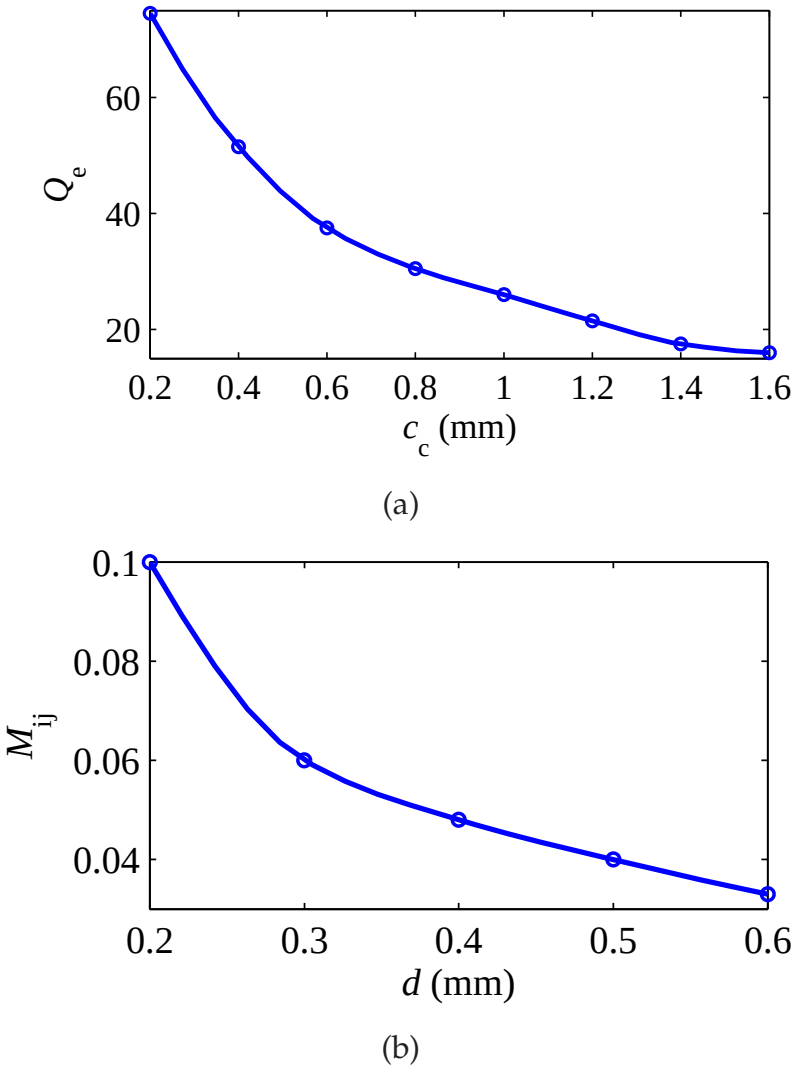

Figure 6.15. External quality factor and coupling coefficient parametric study. (a) The external quality factor of the S-SRR resonator coupled to an open-ended CPW for different values of c_c, and (b) the coupling coefficient of a pair of S-SRRs versus the space between the two resonators d for a 0.635 mm thick Rogers RO3010 material with relative permittivity of 10.2.

is one of the main building blocks in balanced circuits. A first category of realizations includes filters that are composed of a differential bandpass filter in combination with a dedicated structure for common-mode suppression (Wu *et al.* 2009, Tsai and Wu 2010, Naqui *et al.* 2012c). A second category includes structures that combine differential filtering and common-mode suppression, and are thus usually more compact (Lim and Zhu 2009, Lim and Zhu 2011, Shi *et al.* 2012, Velez *et al.* 2013). This section along with Section 6.5 are focused on the dual counterpart of S-shaped split

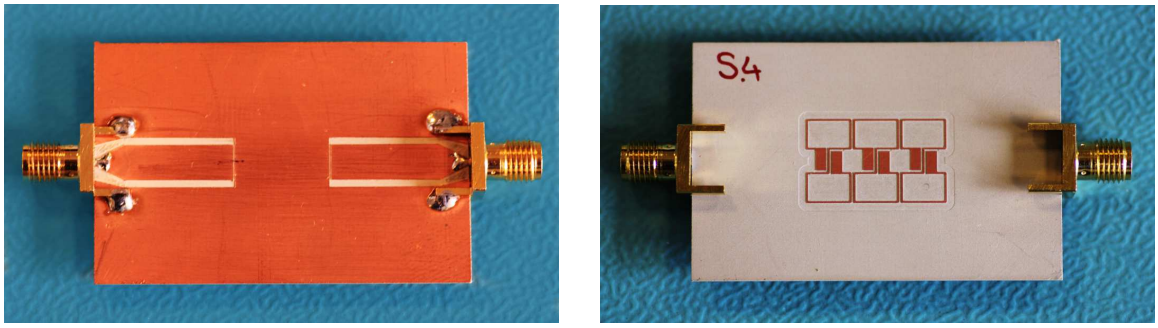

(a) (b)

Figure 6.16. Fabricated protoype of the 3rd order coupled resonator filter. (a) Top and (b) bottom photograph of the fabricated third order coupled S-SRR bandpass filter.

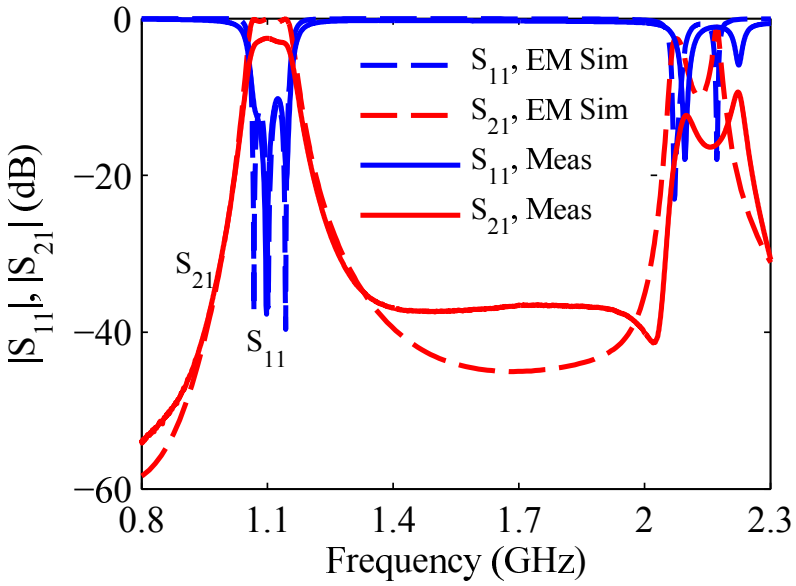

Figure 6.17. Comparison between the measurment and simulation results. Comparison between measured and lossless electromagnetic simulated transmission and reflection coefficients of the third-order coupled S-SRR filter of Fig.6.16.

ring resonator, i.e., S-shaped complementary split ring resonator (S-CSRR) for application in the design of differential filters. It is shown that compared to the conventional configuration of CSRRs in differential microstrip technology, the proposed resonator benefits from a high level of miniaturization when excited by the contra-directional electric fields of a differential microstrip line. More importantly, it is shown that S-CSRRs can be used in the design of bandpass filters that suppress the common-mode noise inherently.

Table 6.1. A Comparison of Various Narrow Bandpass CPW Filters.

Ref.	n	f_0 (GHz)	FBW (%)	IL (dB)	Electrical Size	Electrical area (λ_g^2)
(Borja *et al.* 2010)	3	4.5	3.5	2.8	$0.50\lambda_g \times 0.25\lambda_g$	0.125
(Zhou *et al.* 2004)	4	2.86	7	2.8	$0.84\lambda_g \times 0.46\lambda_g$	0.385
(Mao and Chueh 2007)	2	4.92	3.8	2.77	$0.46\lambda_g \times 0.20\lambda_g$	0.093
(Zhang and Chen 2006)∗	4	2.4	10	6	$0.25\lambda_g \times 0.25\lambda_g$	0.0625
(Mao *et al.* 2005)	2	5	5.4	2.7	$0.57\lambda_g \times 0.20\lambda_g$	0.115
(Wu and Wang 2007)	4	1.75	9.6	2.15	$0.37\lambda_g \times 0.33\lambda_g$	0.122
(Bonache *et al.* 2004)†	3	7	3.5	4	$0.41\lambda_g \times 0.30\lambda_g$	0.123
This work A	3	1.1	6	3.5	$0.32\lambda_g \times 0.08\lambda_g$	0.0256
This work B	3	1.1	7.2	2.5	$0.12\lambda_g \times 0.08\lambda_g$	0.0096

∗This filter was fabricated on FR4.

†This filter was based on SRRs.

6.4.1 Principle of Miniaturization

Fig. 6.18(a) shows the typical configuration of a CSRR-loaded differential microstrip line, with a pair of CSRRs etched in the ground plane under each strip of the differential line. In this configuration, regardless of the signal mode, the CSRRs are excited by the time-varying axial electric fields of the microstrip line. Thus, the propagation of electromagnetic waves is inhibited in a narrow band around the CSRR resonance. It was shown by Naqui *et al.* (2012c) that an array of single CSRRs aligned with the symmetry plane of the differential line can be used for common-mode suppression, while the differential signal is unaffected. The key to this application is that while the CSRRs are excited by the axial electric fields in common-mode, the electric field components of the differential signals, which are contra-directional, cancel each other and the CSRRs are not excited by this mode. In contrast, the fundamental resonance of the proposed S-shaped CSRR, shown in Fig. 6.18(b), is activated if the connected rings of the S-CSRR are excited by contra-directional axial electric fields of the loaded differential microstrip line. Thus, an S-CSRR can be used to efficiently inhibit the propagation of differential signals in a narrow frequency band near the resonance frequency of the resonator.

Fig. 6.19 shows the simulated transmission and reflection coefficients of the S-CSRR loaded structure in differential mode. For the electromagnetic simulations, a 0.635 mm thick Rogers *RO3010* substrate with relative permittivity of $\epsilon_r = 10.2$ is used. The

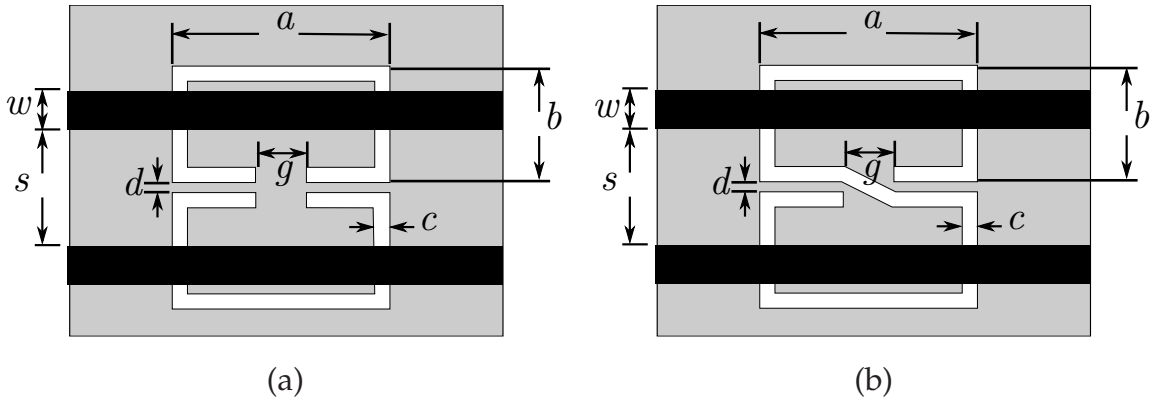

Figure 6.18. Differential microstrip line loaed with CSRRs and S-CSRR. A differential microstrip line loaded with (a) a pair of rectangular single ring CSRRs, and (b) an S-shaped CSRR.

width of the differential microstrip lines is $w = 0.5$ mm and the space between the strips is $s = 5.75$ mm, which correspond to a 50 Ω odd-mode characteristic impedance. The S-CSRR's dimensions are as follows: $a = 6.2$ mm, $b = 5.7$ mm, $c = 0.2$ mm, $d = 0.2$ mm, and $g = 1$ mm. For comparison, the simulated odd-mode frequency response of the differential microstrip line loaded with a pair of CSRRs with the same physical dimensions as the rings of S-CSRR is also depicted in the figure. The simulation results show that the resonance frequency of the structure with the pair of CSRRs is $f = 3.5$ GHz, while the S-CSRR resonates at a much lower frequency (1.43 GHz). The comparison shows that a high level of miniaturization is achieved by modifying the resonator shape to an S-shaped CSRR.

6.4.2 Modeling of S-CSRR/Gap-loaded Line

The bandstop behavior of an S-CSRR-loaded differential microstrip line can be interpreted as due to the negative permittivity of the structure in the vicinity of the S-CSRR's fundamental resonance. This bandstop behavior can be switched to a bandpass behavior simply by introducing series capacitive gaps in the strips of the differential line, as shown in Fig. 6.20(a) (Gil *et al.* 2006). Note that in this structure, inner split slot rings are added to the S-CSRR to achieve more compactness.

In order to study the behavior of the S-CSRR/gap-loaded differential microstrip line, we now focus on the circuit model and parameter extraction of the structure, in both differential and common modes. Fig. 6.20(b) depicts the proposed lumped element

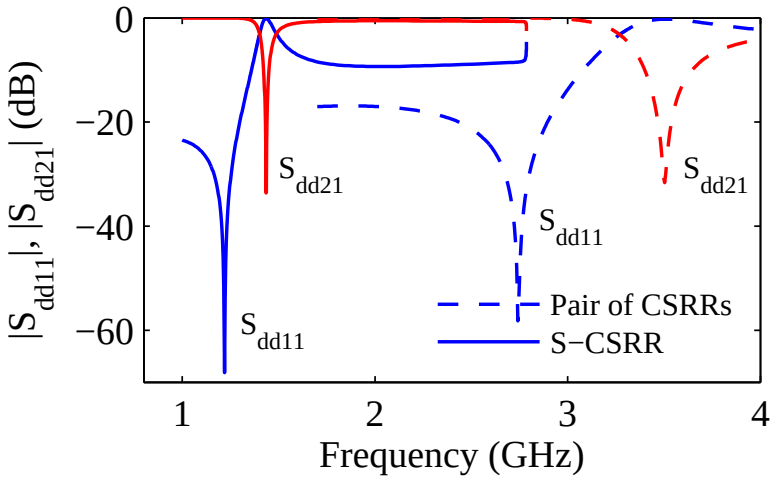

Figure 6.19. Frequency response of CSRR-loaded differential line and that of S-CSRR-loaed line. Comparison between the simulated transmission and reflection coefficients (differential mode) of the differential microstrip line loaded with an S-CSRR (solid lines) and a pair of CSRRs with the same physical size (dashed lines).

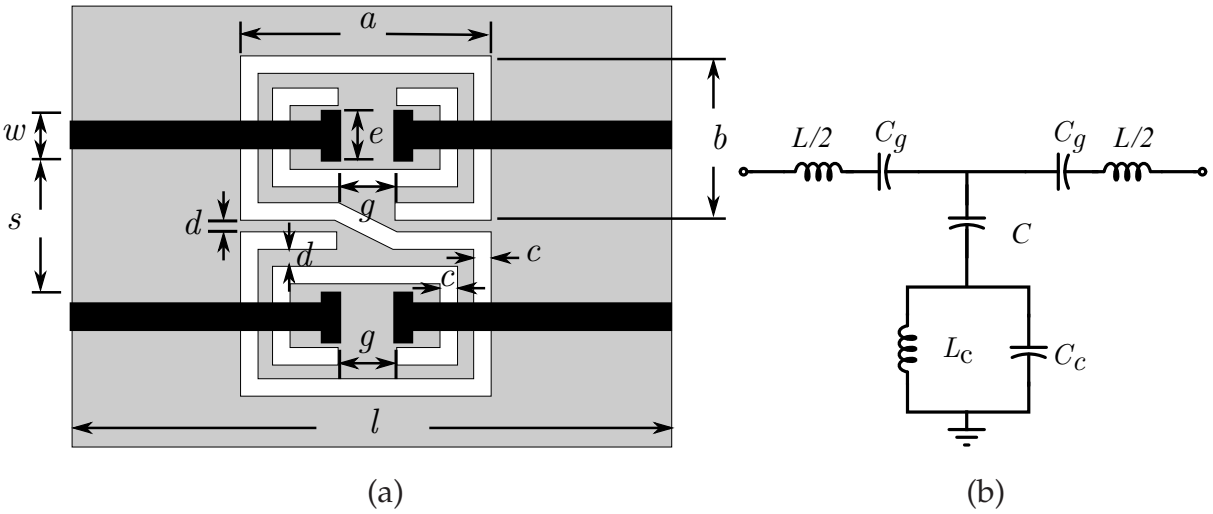

Figure 6.20. Layout and equivalent circit model of an S-CSRR-loaded differential line. (a) Layout of an S-CSRR/gap loaded differential line. The dimensions of the structure are as follows: $a = 9.8$ mm, $b = 7$ mm, $c = 0.8$ mm, $d = 0.2$ mm, $g = 0.6$ mm, $w = 0.5$ mm, $s = 5.75$ mm, $e = 2$ mm, and $l = 22$ mm. (b) Equivalent lumped element circuit model of the unit cell for both differential and common modes.

circuit model for the structure of Fig. 6.20(a), where L and C are the per-section equivalent inductance and capacitance of the differential line with the presence of the S-CSRR, and C_g models the line's capacitive gaps. The S-CSRR is modeled with an equivalent

capacitance C_c and an equivalent inductance L_c. This model is valid for both differential and common modes, however with different element values. Indeed, while the fundamental resonance of the S-CSRR is excited by differential mode (Fig. 6.21(a)), the common mode excites the S-CSRR's higher order resonance (Fig. 6.22(a)).

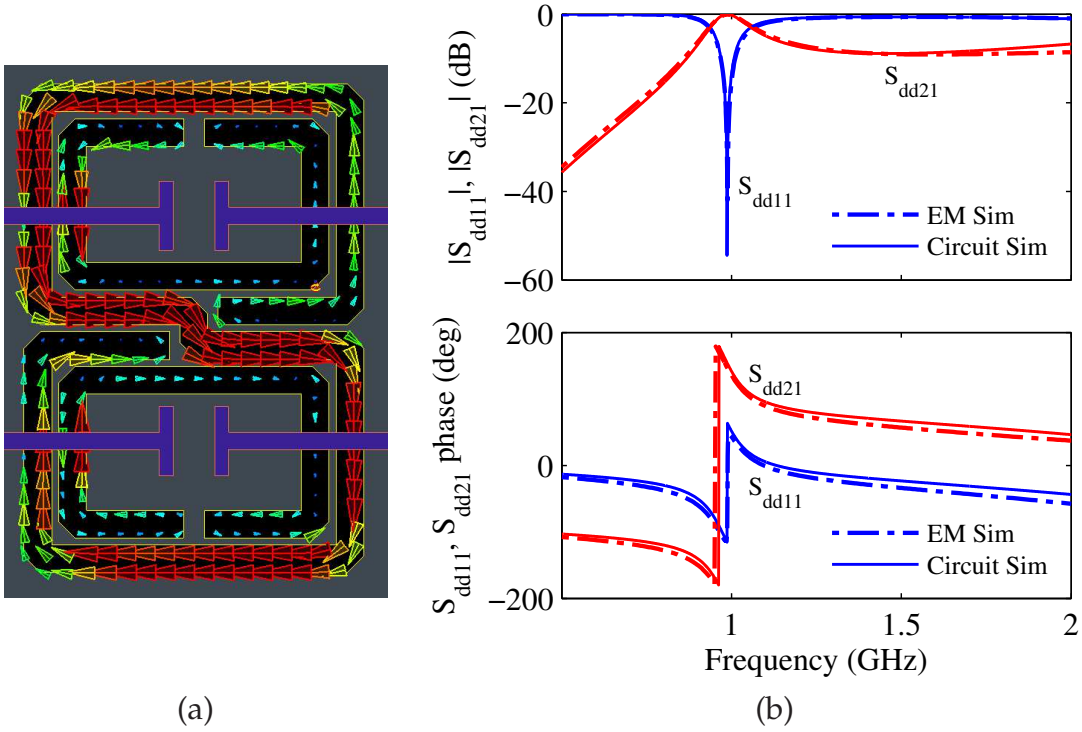

Figure 6.21. S-CSRR-loaded line in differential mode. (a) Magnetic current distribution in differential mode, and (b) comparison between the amplitude (top) and phase (bottom) of the differential-mode transmission and reflection coefficients from the electromagnetic simulation of the structure of Fig. 6.20 and those from the proposed circuit model.

Using the procedure explained by Bonache *et al.* (2006b) the parameters of the circuit model for differential and common modes are extracted from the electromagnetic simulations of the structure of Fig. 6.20(a). Dimensions of the structure are indicated in the caption of the figure, and the same substrate as in the Section 6.4.1 is used for electromagnetic simulations. The extracted parameters for differential mode are: $L = 8$ nH, $C = 70$ pF, $C_g = 0.33$ pF, $C_c = 1.2$ pF, and $L_c = 10$ nH, whereas the parameters for the common mode are: $L = 4$ nH, $C = 105$ pF, $C_g = 0.46$ pF, $C_c = 1.5$ pF, and $L_c = 4.2$ nH. Figs. 6.21(b) and 6.22(b) demonstrate a good agreement between the transmission and reflection coefficients of the circuit model and electromagnetic simulations for both modes, validating the proposed circuit model. Note that the structure's

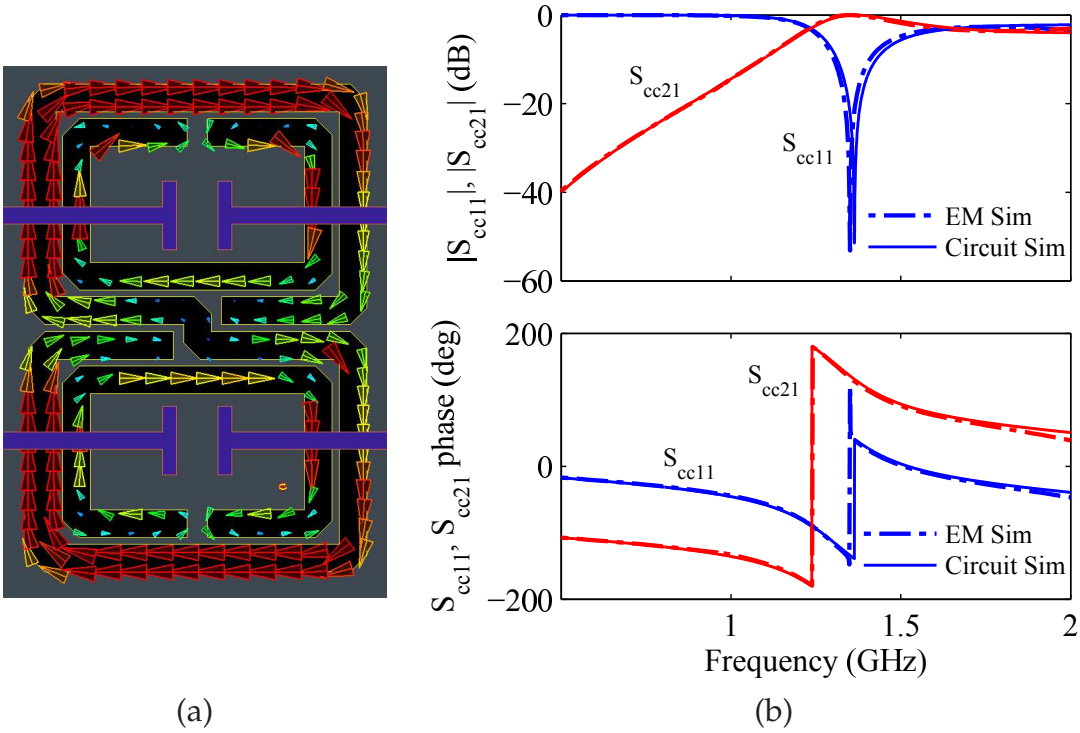

Figure 6.22. S-CSRR-loaded line in common mode. (a) Magnetic current distribution in common mode, and (b) comparison between the amplitude (top) and phase (bottom) of the common-mode transmission and reflection coefficients from the electromagnetic simulation of the structure of Fig. 6.20 and those from the proposed circuit model.

passband for differential mode is centered at $f = 1$ GHz, whereas the passband for the common mode is located at $f = 1.4$ GHz. This feature can be used in the design of differential bandpass filters with common-mode suppression.

6.5 Bandpass Filter with Common-mode Suppression

To illustrate the potential application of the S-CSRR in the design of a differential bandpass filter with common-mode suppression, a third-order periodic (although, periodicity is not mandatory from the design point of view) bandpass filter with fractional bandwidth of 10% and 0.16 dB in-band ripple is designed and synthesized for operation roughly centered around the frequency of 1 GHz. The focus of the design procedure is simply placed on the differential characteristics of the filter, while the common-mode is intrinsically suppressed by the proposed structure.

The structure of Fig. 6.20, which can be considered as a distributed resonator with two $\lambda/8$ feed lines, is used as the filter's unit cell. The feed lines of each unit cell in conjunction with those of the adjacent cells act as 90° impedance inverters with normalized impedance of $K = 1$. Based on the theory of impedance inverters, the fractional bandwidth of the filter can be controlled by the reactance slope of the unit cell, excluding the feed lines (Hong and Lancaster 2001), which is in turn controlled by gap dimensions (Gil *et al.* 2006). Thus, a parametric analysis has been applied in the design process in order to determine the optimum gap dimensions. The next step is to optimize the length of the feed lines to achieve a 90° phase shift from port one to port two of the unit cell at resonance frequency. Finally, the filter is realized by cascading the optimized unit cells.

The photograph of the fabricated filter, using the same substrate as in Sec. 6.4.1 and the dimensions in the caption of Fig. 6.20, is depicted in Fig. 6.23. The impedance inverters are meandered to achieve more compactness. The filter is as small as $0.09\lambda_g \times 0.25\lambda_g$, where λ_g is the guided wavelength at $f = 1$ GHz. A comparison between electromagnetic simulation and measured frequency response of the filter in differential and common modes is depicted in Fig. 6.24. The figure shows that the structure acts as a differential bandpass filter with 2.8 dB insertion loss at central frequency, common-mode suppression better than -25 dB, and common-to-differential mode conversion better than -16 dB. A comparison with other differential filters in terms of performance and size is provided in Table 6.2, where f_{1dd} and f_{2dd} are lower and upper -3dB cutoff frequencies in differential mode, and f_{1cc} and f_{2cc} are lower and upper -20 dB cutoff frequencies in common-mode stopband.

6.6 Conclusion

In summary, this chapter has proposed an S-shaped SRR and its complementary counterpart, i.e., an S-shaped CSRR. It has been demonstrated that in CPW technology, a high level of filter miniaturization can be achieved by using an S-SRR, compared to the typical configuration using a pair of SRRs aligned with the CPW's slot. The key to this level of miniaturization is that the fundamental resonance frequency of an S-SRR is excited when contra-directional axial magnetic fields are inducing currents in the two connected rings of the S-shaped resonator. Based on the explained working principle, an equivalent lumped element circuit model for an S-SRR-loaded CPW has been proposed, and the parameters of the model have been extracted. The proposed model has

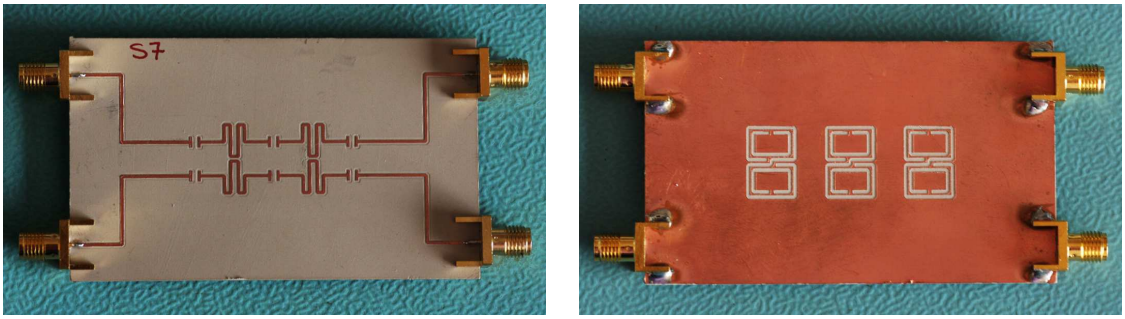

(a) (b)

Figure 6.23. Fabricated prototype of the differential filter with common-mode suppression. (a) Top and (b) bottom photograph of the fabricated third order differential bandpass filter with common-mode suppression.

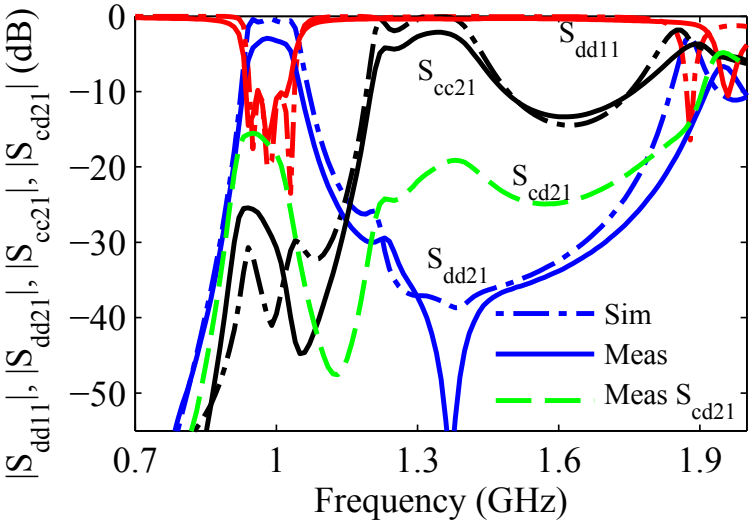

Figure 6.24. Comparison between simulated and measured response of the differential filter. Comparison between simulated (lossless) and measured transmission and reflection coefficients of the third-order differential filter with common-mode suppression.

been validated through the good agreement between the circuit and electromagnetic simulation. In order to demonstrate the potential application of the proposed structure in the design and synthesis of miniaturized microwave circuits, two types of bandpass filters based on S-SRR loaded CPW have been designed and synthesized. The first filter is a third-order periodic bandpass filter based on impedance inverters, demonstrating a good level of miniaturization with dimensions of $0.32\lambda_g \times 0.08\lambda_g$. The miniaturization is pushed further in the second filter, which exhibits dimensions of $0.12\lambda_g \times 0.08\lambda_g$

Table 6.2. A comparison of various differential bandpass filters. A comparison of various differential filters in terms of performance and size. Here, f_{1dd} and f_{2dd} are lower and upper -3dB cutoff frequencies in differential mode, and f_{1cc} and f_{2cc} are lower and upper -20 dB cutoff frequencies in common-mode stopband.

Ref.	n	CMRR in passband	$\frac{f_{1cc}}{f_{1dd}}$	$\frac{f_{2cc}}{f_{2dd}}$	Electrical Size
(Lim and Zhu 2009)	3	>24 dB	0.96	1.09	$0.5\lambda_g \times 0.5\lambda_g$
(Lim and Zhu 2011)	3	>18 dB	0.93	1.08	$0.5\lambda_g \times 0.5\lambda_g$
(Velez *et al.* 2013)	3	>25 dB	0	1.04	$0.15\lambda_g \times 0.3\lambda_g$
This work	3	>25 dB	0	1.15	$0.09\lambda_g \times 0.25\lambda_g$

when realized using coupled S-SRRs. In both cases, the design procedure has been explained and validated through electromagnetic simulations and measurements.

The chapter has also presented an S-shaped complementary split ring resonator for application in differential microstrip technology. Size reduction as compared to CSRRs has been achieved. More importantly, it has been shown that an S-CSRR-loaded microstrip line with series capacitive gaps can be used as a unit cell for differential bandpass filters with common-mode suppression. In-band common-mode rejection ratio better than -25 dB has been achieved.

The promising results of this chapter strongly support the application of metamaterial-inspired resonators in compact microwave filters. Application of split ring resonators for the realization of terahertz bandpass filters will be discussed in the next chapter.

Chapter 7

Metamaterial-Inspired Bandpass Filters for the Terahertz Planar Goubau Line

THIS chapter is focused on the application of split ring resonators (SRRs) to the design of compact bandpass filters for terahertz surface waves on single wire waveguides, the so-called planar Goubau lines (PGLs). Through equivalent circuit models, electromagnetic simulations, and experiments it is shown that while a pair of SRRs coupled to a PGL inhibits the propagation of surface waves along the line, introducing a capacitive gap to the PGL switches the bandstop behavior to a bandpass behavior. In order to highlight the potential application of the proposed structure to the design of practical higher-order terahertz bandpass filters, two types of compact bandpass filters are designed and fabricated: (i) third-order periodic bandpass filters based on SRR/gap-loaded PGL, and (ii) coupled-resonator bandpass filters. It is shown that while the frequency response of the both filter types can be controlled by altering the physical dimensions of the structure, a wider bandwidth can be achieved from the coupled resonator filters. The design concept and simulation results are validated through experiments.

7.1 Introduction

The terahertz band is loosely defined at the frequency range between 0.1 THz and 10 THz, as illustrated in Fig. 7.1. The band has been extensively investigated for numerous potential applications in imaging, medical diagnosis, security screening, chemical and biological sensing, and communications (Ferguson and Zhang 2002, Ferguson *et al.* 2002, Kawase *et al.* 2003, Withayachumnankul *et al.* 2003, Siegel 2004, Shen *et al.* 2005, Li and Li 2009, O'Hara *et al.* 2012). Despite the wide range of potential applications, numerous challenges have yet to be addressed for further development of passive and active devices operating in this spectral range.

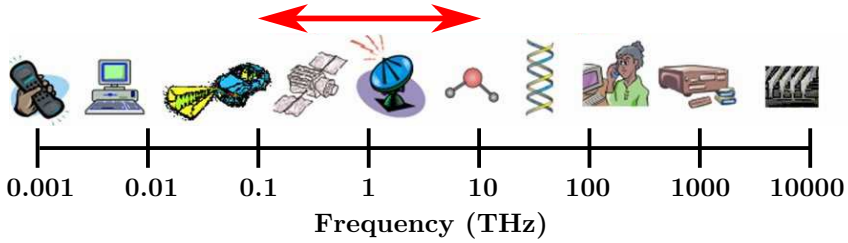

Figure 7.1. Tehrahertz band. The terahertz band is loosely defined at the frequency range between 0.1 THz and 10 THz.

Among many passive structures, low-loss and low-dispersion waveguides are crucial in the terahertz regime to enhance the efficiency of systems. Even though hollow waveguides and two-conductor transmission lines such as coaxial cables and microstrip lines are efficient for low to moderate radio-frequency operation, scaling these waveguides for terahertz applications is not an efficient solution because of the finite conductivity of metals at this higher frequency range (Ohashi *et al.* 2009). On the other hand, in spite of their high efficiency, conventional optical interconnects such as optical fibers are bulky and cannot be readily integrated into planar technologies (Ozbay 2006, Chen *et al.* 2011).

Surface electromagnetic waves that propagate along the interface of a dielectric and a conductor are one possible solution that has been proposed for realization of high-speed on-chip interconnects, where thin metal circuitry can be used for carrying both the optical signals and electrical currents (Ozbay 2006). In particular, it was demonstrated by Wang and Mittleman (2004) that a bare Goubau-like single metal wire carrying surface waves (Sommerfeld 1899, Brown 1953, Goubau 1956, King and Wiltse 1962) can be used as an efficient channel for terahertz waves with low attenuation and low dispersion. The planar version of such a waveguide, the so-called planar Goubau

line (PGL), has attracted increasing interest because of its compatibility with integrated circuit fabrication processes (Akalin *et al.* 2006a, Akalin *et al.* 2006b, Xu and Bosisio 2007, Si *et al.* 2008, Treizebré *et al.* 2010, Xu *et al.* 2011, Treizebré *et al.* 2012, Gacemi *et al.* 2012, Emond and Grzeskowiak 2012).

7.2 Research Objective and Framework

Fig. 7.2 depicts a block diagram of a exemplary multi-core system. In this system, electronic circuits inside the cores control the transport and storage of electrons, while communication between the different cores is enabled by inter-core interconnections. Generally, the performance of electronic interconnects is a bottleneck that can limit the data rates of inter-core communications. Among the terahertz transmission lines that have been proposed in the past, terahertz planar Goubau lines offer wide bandwidth and high data rate, low dispersion, low power consumption and low crosstalk and electromagnetic interference, thus can be an efficient solution for future broadband on-chip communication (Ohashi *et al.* 2009). As shown with black boxes in the figure, in order to exploit the propagation of surface waves on a single wire in real applications, particularly for future broadband terahertz communications, functional components such as various types of filters, multiplexers and demultiplexers are required.

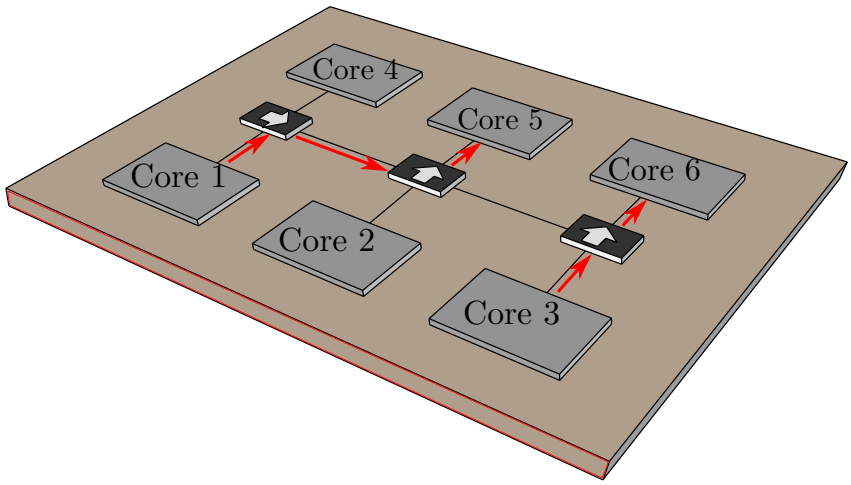

Figure 7.2. Plasmonic in multi-core systems. Block diagram of a multi-core system, in which electronic interconnections are used inside the cores, while terahertz surface waves on PGL interconnection are used for high-data-rate inter-core communication.

Throughout this chapter, the operation principle for the terahertz PGL bandpass filters is developed, and the effect of geometric parameters on the frequency response of the

proposed filters is studied. Two different types of bandpass filters are realized through parametric studies. The first type is based on a combination between SRRs and a gap-loaded PGL, and the second type involves coupled SRRs excited by open-ended PGLs. In both cases it is shown through simulations and experiments that the filter response, in particular the bandwidth, can be conveniently controlled by altering the geometrical dimensions of the structures.

This chapter is organized as follows. An introduction to the propagation of terahertz surface waves along the planar Goubau line as well as the excitation of the PGLs are presented in Section 7.3. The principle of first-order bandstop and bandpass filters based on SRR-loaded PGL is discussed in Section 7.4, accompanied by circuit models developed for both bandstop and bandpass filters. Based on the operation concept and circuit models, third-order periodic bandpass filters based on SRR/gap-loaded PGLs are presented in Section 7.5. Bandpass filters based on coupled SRRs are then discussed in Section 7.6. As a validation, prototypes for both types of the filters with geometrical variations have been fabricated and their performance have been evaluated. Satisfactory agreement between simulation and measurement results has been achieved. Finally, the main findings and principles of the study are summarized in Section 7.7.

7.3 Terahertz Surface Waves on the Planar Goubau Line

This section provides an introduction to the propagation of the terahertz surface wave along a planar Goubau line and its excitation method. The chapter also reviews two experiments that proves the structure is a non-radiating waveguide.

7.3.1 Excitation of the Planar Goubau Line

It can be shown that if the width of a signal strip of a microstrip line is tapered to a value much smaller than the substrate thickness, for instance to a width of about 1 μm on a 100 μm thick substrate, the electromagnetic energy is mostly confined to the spatial area around the strip, and the ground plane does not play a critical role (Akalin and Treizebré 2004, Akalin *et al.* 2006b). In fact, this can happen when a surface wave has been excited along the signal strip of the microstrip line. Since the surface wave is mostly confined to the immediate vicinity of the signal strip, the ground plane can

be removed from the structure to achieve a one-wire transmission line. Such a transmission line is called "Goubau line" or "G-line" for short, and the propagation mode is called "Goubau mode" (Sommerfeld 1899, Goubau 1956, King and Wiltse 1962). It is worth mentioning that the structure has found applications especially for the sensing, characterization and investigation of living entities rather than transmission of terahertz waves for long distances (Xu and Bosisio 2005, Xu *et al.* 2011).

The propagation of terahertz waves on a single metallic wire with very low attenuation (about 0.03 cm^{-1}) was demonstrated by Wang and Mittleman (2004). However, in this case the transition from free-space propagation to the metal wire propagation was not very efficient. In a more recent work, Akalin *et al.* (2006b) have presented a high-efficiency planar launching structure for surface waves on a PGL. The top view of such a CPW to G-line transition is illustrated in Fig. 7.3. The structure takes the form of a CPW with a tapered section and efficiently converts the CPW mode to the Goubau mode. Since Sec II of the structure is responsible for the conversion of the propagation mode from CPW mode to the Goubau mode, the efficiency of the G-line excitation is directly linked to the geometry of this section. In other words, the single wire transmission line can support both radiation and transmission modes; the radiation mode can be excited by a localized excitation, while a smooth transition from CPW to G-line is required for the transmission mode to be excited (Goubau 1956).

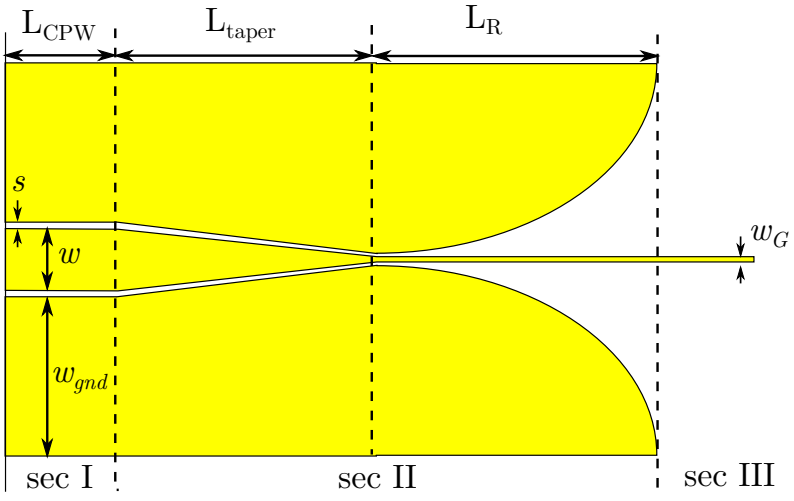

Figure 7.3. CPW to PGL transitions. Top view of the CPW-to-PGL transitions. sec II in the transition plays the most critical role in the excitation of Goubau mode. Adapted from Akalin *et al.* (2006b).

7.3.2 Is There Direct Coupling?

As suggested in Fig. 7.4 the CPW-to-PGL transition can be considered as a cross section of the classical excitation of Goubau mode on a wire with a horn antenna. By considering the CPW-to-PGL launching section as a planar cross section of a horn antenna, the question may arise whether the transmission is essentially due to the Goubau propagation mode or is it due to the direct coupling between the two launching sections?

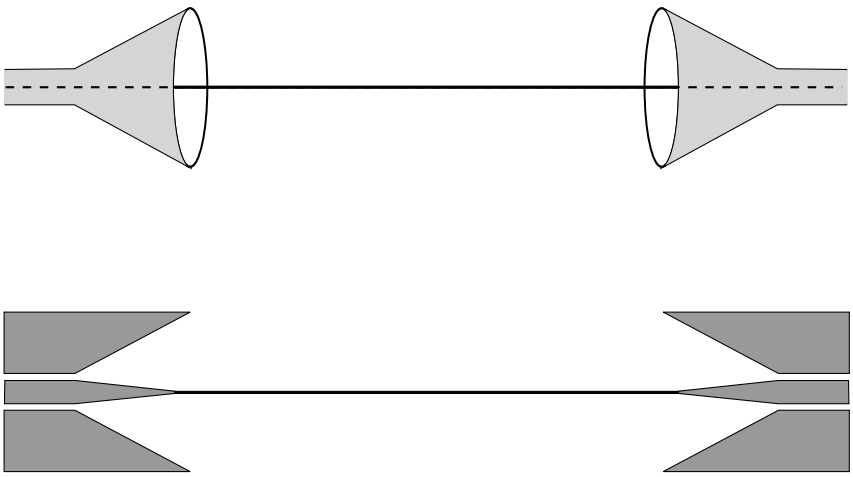

Figure 7.4. Horn antenna transition to G-line versus CPW to PGL transition. The CPW to PGL transition can be considered as a cross section of the classical excitation of Goubau mode with a horn antenna.

In order to demonstrate that the transmission is indeed through the surface wave on the excited PGL, and not due to the direct coupling between the two launching sections, two investigations were carried out by Akalin *et al.* (2006b). In the first investigation the structure of a 90° curved G-line section was used to minimize the possible direct coupling between the launching sections. High level of transmission verified that the transmission was due to the efficient excitation of the G-line, and not due to the direct coupling between the launching sections. In the second investigation the structure of two launching sections facing each other without being connected by a PGL was fabricated and measured. The measured transmission coefficient showed that there is no significant direct coupling between the launching sections. In a similar method Fig. 7.5 shows the simulated transmission coefficient of a PGL, which is excited by two launching structures (blue solid curve). The figure also depicts the transmission coefficient of the same structure when a 50 μm long gap is introduced in the middle of the PGL. The figure shows that while the normal PGL demonstrates a good transmission, introducing the gap in the PGL results in almost no energy transmission, proving that

the transmitted energy in the original structure is not due to the direct coupling of the launching sections.

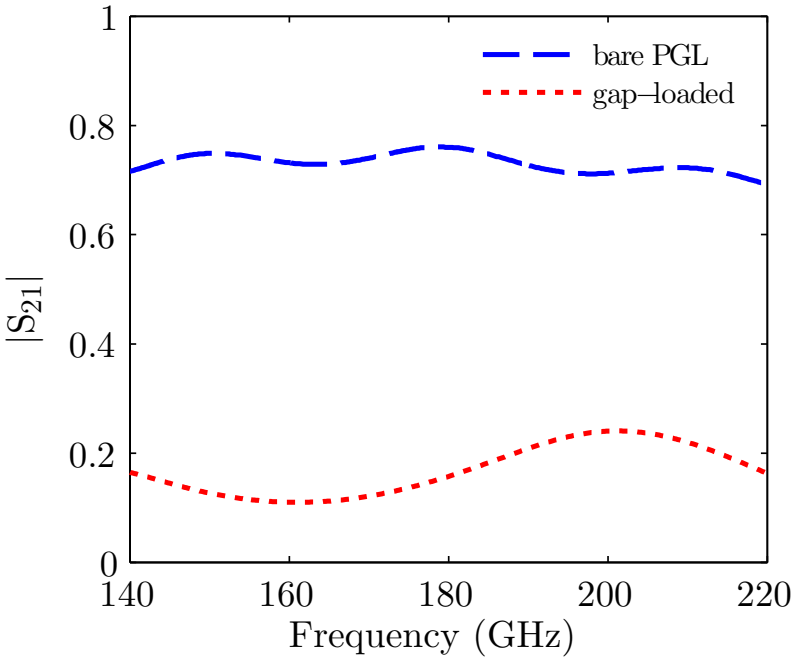

Figure 7.5. Bare PGL vs gap-loaded PGL. Simulated transmission coefficient of a bare PGL (blue dashed line) and that of a gap-loaded PGL (red dotted line). The simulation resutlts porves that the transmitted energy in the bare PGL is not due to the direct coupling of the launching sections.

7.4 Bandstop and Bandpass Filters for the Terahertz Goubau Line

Different types of terahertz filters based on frequency-selective surfaces, photonic crystals (Němec *et al.* 2004, Withayachumnankul *et al.* 2008, Li 2010), liquid crystals (Chen *et al.* 2006a), or metamaterials (Si *et al.* 2008, Withayachumnankul and Abbott 2009, Lu *et al.* 2011, Zhu *et al.* 2012, Liang *et al.* 2013) have been proposed. However, these filters are exclusively for free-space terahertz waves. In contrast, the filters proposed in this work are operating on guided waves.

A bandstop filter based on a corrugated PGL has been studied by Akalin *et al.* (2007). It was shown that the structure, which is essentially a stepped impedance filter, provides a stopband for surface wave propagation. A schematic of the PGL filter with a corrugated section is shown in Fig. 7.6 showing a period of 480 μm, and widths $w = 60\,\mu$m

and $w_c = 10\,\mu$m in the corrugated sections. The structure provides stopband characteristic for the surface surface waves propagation, and the length l can be used to control the bandwidth as well as the depth of notch (Akalin *et al.* 2007). However, from the above mentioned dimensions it is clear that the filter is large.

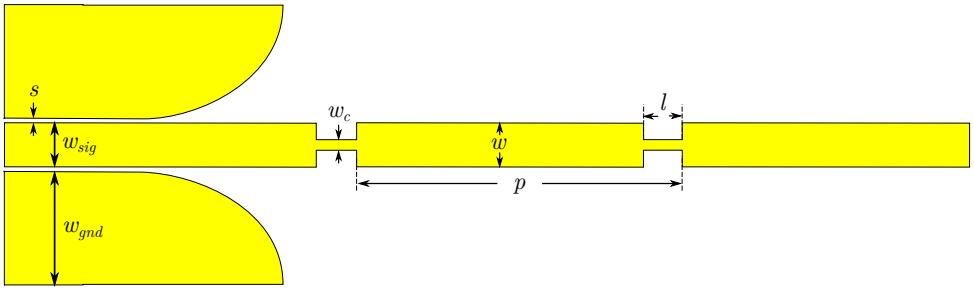

Figure 7.6. Corrugated planar Goubau line for application as a terahertz bandstop filter. Top view of a corrugated planar Goubau line. The corrugated section has a period of $p = 480\,\mu$m,and a width of $w = 60\,\mu$m in the not corrugated and $w_c = 10\,\mu$m in the corrugated sections. Adapted from Akalin *et al.* (2007).

7.4.1 Metamaterial-Inspired Bandstop Filters

More recently, an application of metamaterial resonators, more specifically electrical *LC* (ELC) resonators, has been investigated by Chen *et al.* (2011) for filtering. In this paper, a stopband in the transmission of guided surface waves on a PGL was demonstrated numerically and experimentally. Figure 7.7 shows the simulated electric and magnetic fields on the cross-section view of a planar Goubau line. The propagation mode is a quasi-TEM mode with the E field directed radially outward and the H field circulating around the single metallic strip. The red curve in the figure shows that, as characteristic for surface waves, both electric and magnetic fields exponentially decay radially in the transverse plane (Chen *et al.* 2011).

As shown in Fig. 7.8, in order to provide a notch band in the transmission spectrum of the PGL, a pair of electric-ring resonators (ERRs) was placed in both sides of the PGL and the PGL was excited by a CPW to PGL transition. Since, the electromagnetic wave along the PGL propagations in a quasi-TEM mode, which is strong close to the PGL and exponentially decays in the transverse plane, in order to have a strong interaction between the PGL and the resonators, the pair of ERRs need to be placed close to the PGL (Chen *et al.* 2011).

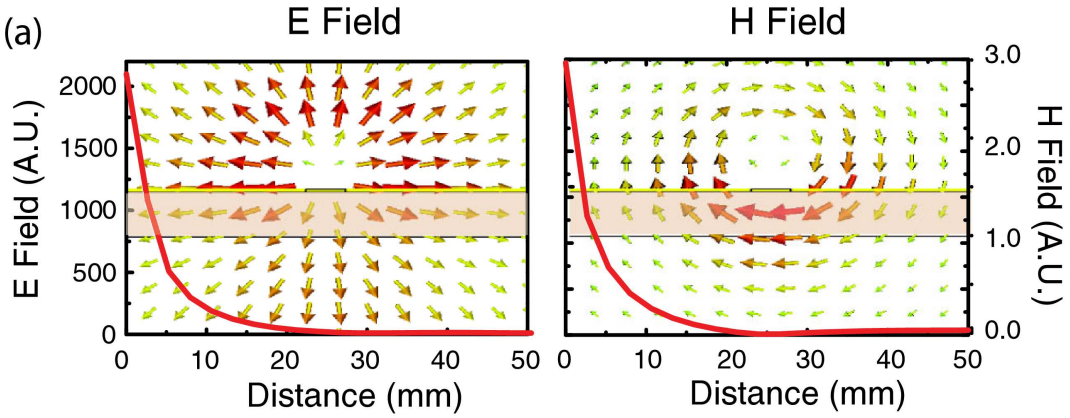

Figure 7.7. Electric and magnetic fields of PGL. Simulated electric and magnetic fields on the cross-section view of a planar Goubau line. The propagation mode is a quasi-TEM mode with the E field directed radially outward and the H field circularly around the single metallic strip. The red curve in the figure shows that, as it is the characteristic of the surface waves, both electric and magnetic fields exponentially decay in the transverse plane. Adapted from Chen *et al.* (2011).

7.4.2 Bandpass Filters

In a recent investigation (Horestani *et al.* 2013d), it was demonstrated through simulation that split-ring resonators (SRRs) can be used for realization of bandpass filters for terahertz PGLs. It is worth mentioning that SRRs and complementary SRRs have been extensively used in the microwave regime for designing bandpass or bandstop filters in microstrip lines and coplanar waveguides (CPWs) (Martín *et al.* 2003b, Gil *et al.* 2008, Horestani *et al.* 2011c, Horestani *et al.* 2012c). However, to the best of our knowledge, no study prior to Horestani *et al.* (2013d) has been conducted on bandpass structures for terahertz surface waves.

Here we first demonstrate through circuit modeling, EM simulation, and experiment that a pair of SRRs that are magnetically coupled to a continuous PGL also creates a notch in the transmission spectrum of the PGL. This transmission notch can be interpreted as the spectrum where the SRR-loaded PGL behaves as a one dimensional medium with negative effective permeability. As will be shortly explained by an equivalent circuit model, this bandstop behavior can be switched to a bandpass behavior by introducing a series capacitive gap to the SRR-loaded PGL.

The proposed bandpass structure, illustrated in Fig. 7.9, is composed of a PGL loaded with a pair of SRRs and a series capacitive gap. The PGL is excited through the CPW

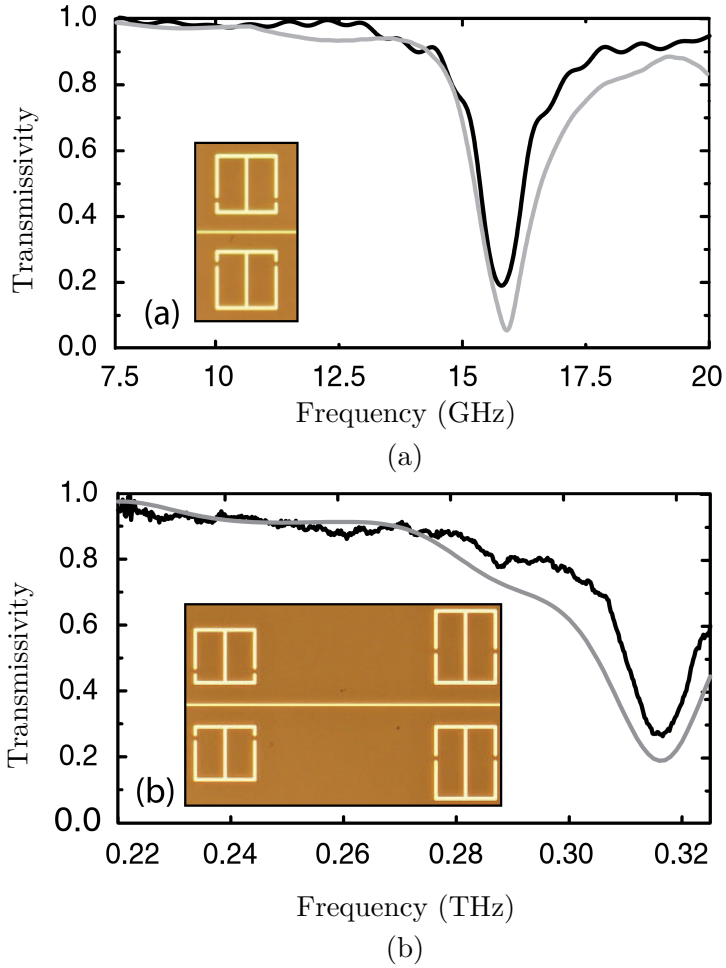

Figure 7.8. ERR-loaded PGL. Simulated (gray) and measured (black) transmission coefficients of (a) the GHz-range and (b) the THz-range metamaterial-inspired bandstop filters on the PGL. The two insets are photographs of single-pair (top) and dual-pair (bottom) ERR-loaded PGL. From Chen *et al.* (2011).

launching sections. As mentioned above the electromagnetic wave along the PGL propagates in a quasi-TEM mode, exhibiting field confinement around the line and exponential decay in the transverse plane. Therefore, the pair of single-ring SRRs must be placed in close proximity to the PGL in order to maximize the magnetic coupling with the PGL.

7.4.3 Equivalent Circuit Model

Equivalent circuit models for the SRR-loaded PGL with and without the series capacitive gap are depicted in Figs. 7.10(a) and 7.10(b), respectively. As a first order approximation, all losses are neglected in these models. In these equivalent circuits, C_s

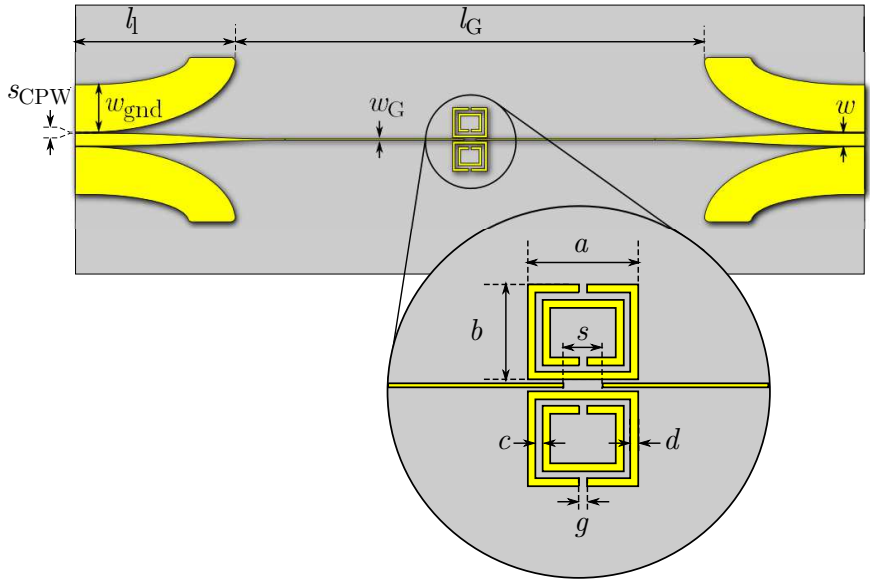

Figure 7.9. First-order bandpass fitler. Layout of the proposed metamaterial-inspired bandpass structure for terahertz surface wave on the PGL. Note that the PGL is a single wire structure with no ground plane or return current path.

represents the SRR's equivalent capacitance. The SRR's equivalent inductance is described with L_s, which is magnetically coupled to the PGL's equivalent inductance L through the mutual inductance M. The series capacitive gap on the PGL is modeled with C_g. The equivalent circuit models in Figs. 7.10(a) and 7.10(b) can be simplified to the circuit models shown in Figs. 7.10(c) and 7.10(d), respectively.

From the simplified circuit model in Fig. 7.10(c), a notch in the transmission response of the SRR-loaded PGL at the frequency that nullifies the series admittance, or $f_0 = 1/2\pi\sqrt{L_s C_s}$, is expected. In contrast, the equivalent circuit model for the SRR/gap-loaded PGL in Fig. 7.10(d) behaves as a bandpass circuit with a transmission band, right below the SRRs' resonance frequency, where the total series impedance nulls. The discussed design concept and circuit models are validated through full-wave 3D electromagnetic simulations and experimental investigations.

7.4.4 PGL Design

The design process begins with selecting a substrate with an appropriate thickness and relative permittivity to control the field confinement and prevent substrate modes. The

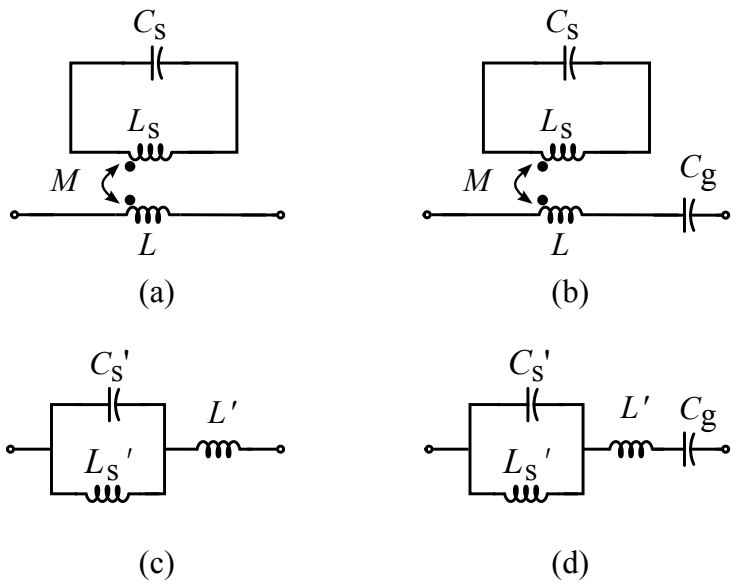

Figure 7.10. Equivalent circuit models. Equivalent circuit models for the SRR-loaded and SRR/gap-loaded PGL. (a) The model for the SRR-loaded PGL. (b) The model for the SRR/gap-loaded PGL. Their simplified versions are given in (c) and (d), respectively.

field confinement plays an important role since surface wave characteristics are determined by the extension of the electromagnetic field around the PGL. Excitation of substrate modes can be avoided by increasing their cut-off frequency through decreasing the substrate thickness and relative permittivity (Xu and Bosisio 2007). Thus, in this study a 250 μm thick quartz crystal with a relative permittivity $\epsilon_r = 3.78$ is chosen as a substrate. The next step involves determining an appropriate width w_G for the PGL. An increase in the width of this metallic strip w_G leads to a decrease in the modal confinement (Gacemi *et al.* 2013), which in turn results in a decrease in the conductor loss. In our present designs, however, a decrease in the confinement also weakens magnetic coupling between the PGL and the SRRs, owing to the lowered magnetic flux density around the PGL. Thus, as a trade-off between reducing the PGL conductive loss and achieving a strong coupling between the PGL and the SRRs, a width of $w_G = 5$ μm is used for the PGL in this study. To maximise the mode conversion between the CPW and PGL, the dimensions of the CPW launching structure are as follows: $w = 50$ μm, $w_{\text{gnd}} = 190$ μm, $s_{\text{CPW}} = 5$ μm, and $l_l = 650$ μm. The Goubau line has a total length $l_G = 2100$ μm including the $s = 50$ μm gap in its middle for the bandpass filter. These given dimensions and substrate specifications are common to all subsequent designs.

For the first-order filters presented in this Section, the PGL is loaded with a pair of SRRs with $a = 160\ \mu$m, $b = 130\ \mu$m, $g = 10\ \mu$m, $d = 10\ \mu$m, and $c = 10\ \mu$m, as depicted in Fig. 7.9 . Fig. 7.11 depicts the simulated transmission coefficients of the structure in four different configurations: a bare PGL, a PGL loaded only with the series capacitive gap, a PGL loaded only with the pair of SRRs, and a PGL loaded with both series capacitive gap and the pair of SRRs. Note that in order to exclude the losses of the launching sections, the transmission coefficients of the SRR- and SRR/gap-loaded structures are normalized to that of the bare PGL. It is clear that while the propagation of terahertz waves along the SRR-loaded line is inhibited at resonance around 180 GHz, the SRR/gap-loaded PGL exhibits a bandpass behavior at around 170 GHz, below the SRRs' resonance frequency. Once again, comparison between simulation results of the bare PGL and the broken PGL emphasizes that the high transmission level in the bare PGL is not caused by direct coupling between the CPW launchers.

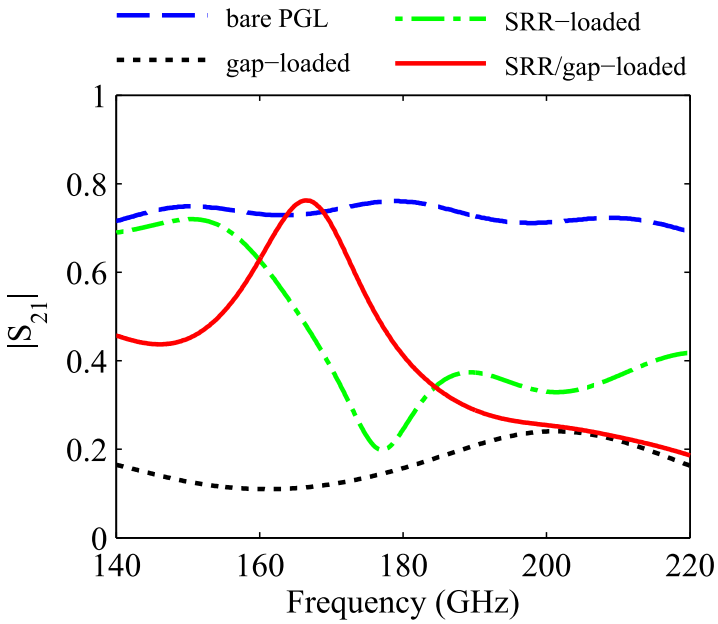

Figure 7.11. Simulation results. Simulated transmission coefficients of the PGL in four configurations: bare PGL (blue dashed line), PGL loaded only with the series capacitive gap (black dotted line), PGL loaded only with the pair of SRRs (green dash-dotted line), and PGL loaded with both series capacitive gap and the pair of SRRs (red solid line). The transmission coefficients of the SRR- and SRR/gap-loaded structures are normalized to that of the bare PGL.

In order to validate the simulation results, a prototype of the structure is fabricated and measured. Fig. 7.12 shows a microscopic image of the fabricated prototype, realized with the same materials, geometry, and dimensions as those used in the simulated structures. Fig. 7.13 shows a direct comparison between the measured and simulated transmission coefficients for the bare PGL as well as the SRR/gap-loaded PGL. The general concept and corresponding simulation results are validated through the satisfactory agreement between the simulation and measurement. Small discrepancies can be ascribed to fabrication tolerances.

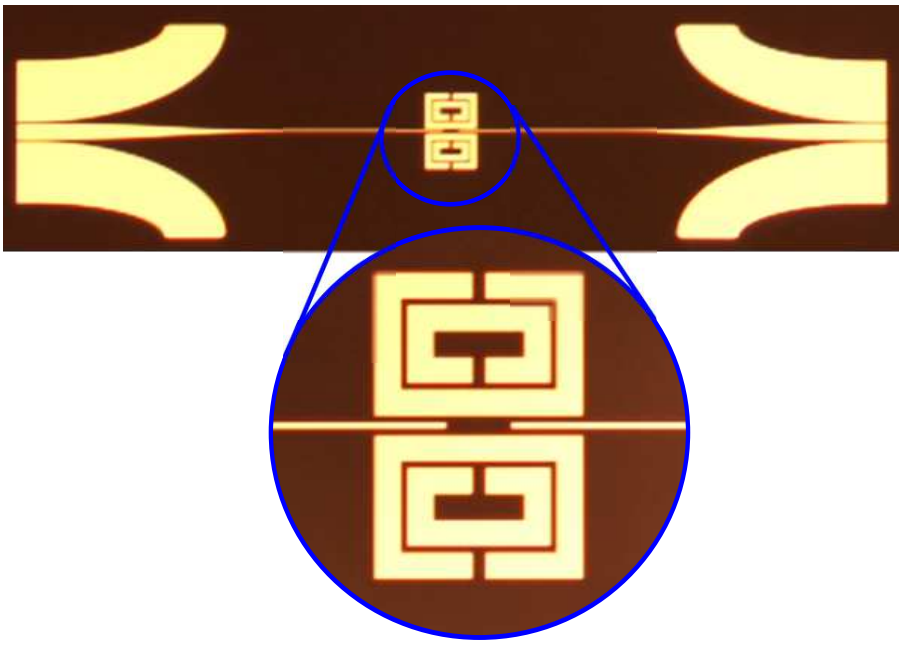

Figure 7.12. Fabricated prototypes. Image of the fabricated prototype of the SRR/gap-loaded PGL.

7.5 Higher-Order Bandpass Filters Based on SRR/Gap-loaded PGL

The main aim of this section is to highlight the potential of the proposed SRR/gap-loaded PGL in the design of practical terahertz bandpass filters with good in-band transmission and out-of-band rejection, as well as a controllable center frequency and bandwidth. To this end, a third-order periodic filter is designed, and the concept is validated through electromagnetic simulations and experiments.

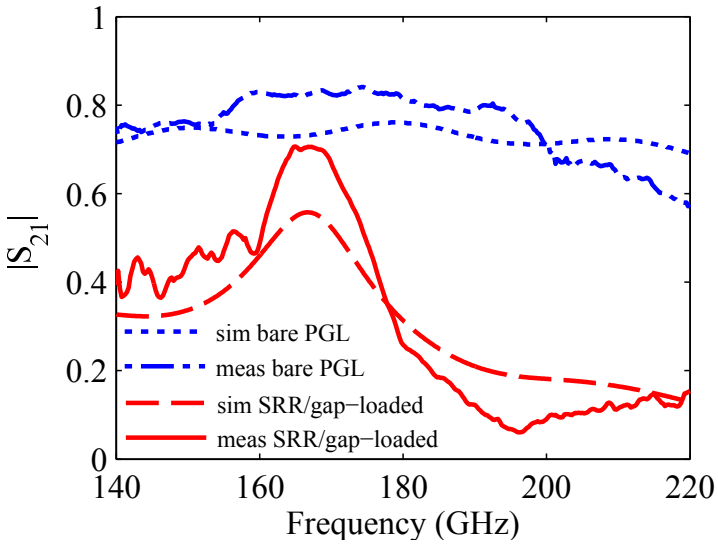

Figure 7.13. Comparison between simulation and measurement results. Comparison between the simulated and measured transmission coefficients for the bare PGL as well as those for the SRR/gap-loaded PGL.

Since controlling the center frequency of the filter can be simply achieved by scaling the SRRs, the study is focused on the impact of geometric parameters on the filter bandwidth. The layout of the proposed periodic bandpass filter, excluding the launching sections is illustrated in Fig. 7.14. The dimensions of the launching sections as well as the width of the PGL are the same as those of the structures of the previous section. Based on the equivalent circuit model for the first-order filter in Fig. 7.10, it can be shown that the bandwidth of the filter can be increased either by increasing the series gap capacitance C_g, or by decreasing the SRR's equivalent capacitance C_s and/or inductance L_s. Note that decreasing the SRR's equivalent inductance is not a viable option, as this can adversely affect the coupling between the SRRs and the PGL, which in turn significantly degrades the in-band transmission. On the other hand, controlling the bandwidth via the series capacitance C_g becomes complicated from the fabrication point of view, owing to required extreme gap sizes s. Thus, in the present design a series gap size is fixed at $s = 10\ \mu$m, and the filter bandwidth is controlled through variation of the SRRs' equivalent capacitance, which can be achieved by tuning the SRR's inter-ring space c. The other dimensions of the SRRs are as follows: $a = 130\ \mu$m, $b = 120\ \mu$m, $d = 10\ \mu$m, $g = 20\ \mu$m, and the space between SRRs is $m = 70\ \mu$m.

Fig. 7.15 depicts the simulated transmission coefficients of the filter for four different values of SRR's inter-ring space c from 15 μm to 30 μm in steps of 5 μm. The simulation

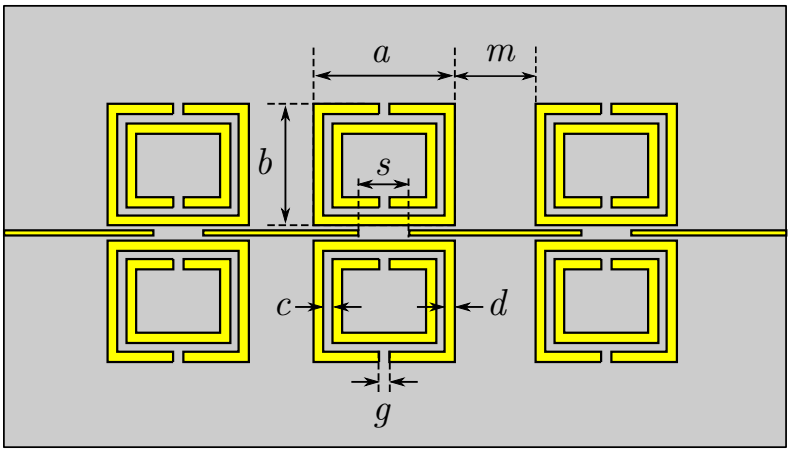

Figure 7.14. Third-order bandpass filter based on SRR/gap-loded PGL. Layout of the third-order periodic bandpass filter based on the SRR/gap-loaded PGL.

results clearly show that the designed third-order filter has a good level of in-band transmission as well as substantial out-of-band rejection. The figure also shows that, as predicted, the filter's bandwidth can be controlled by tuning the SRR's equivalent capacitance through tuning the SRR's inter-ring space c. The filter's 3 dB bandwidth is increased from 18.5 GHz for $c = 15$ μm to 26.4 GHz for $c = 30$ μm, which corresponds to a 42% wider bandwidth. These third-order bandpass filters are then fabricated and measured. Fig. 7.16 shows a good agreement between the simulated and measured transmission coefficients of the filter for different values of the SRR's inter-ring space c. The images of the filter prototypes are depicted in the insets. The filters are as compact as $0.55\lambda_g \times 0.23\lambda_g$, where λ_g is the guided wavelength at the filters' center frequency.

7.6 Bandpass Filters Based on Coupled SRRs

In this section the concept of coupled resonators (Hong and Lancaster 2001, Hong and Lancaster 1996, Aznar *et al.* 2008b) is demonstrated for the design of bandpass filters for terahertz surface waves on PGL. Different third-order coupled resonator filters are designed and experimentally validated. Importantly, it will be shown that compared with the filters based on the SRR/gap-loaded PGLs presented in the previous section, a much wider bandwidth can be achieved with the proposed coupled resonators bandpass filters.

Fig. 7.17 illustrates the layout of the proposed filter, excluding the CPW launching sections. The filter is composed of three pairs of coupled double-ring SRRs that are excited

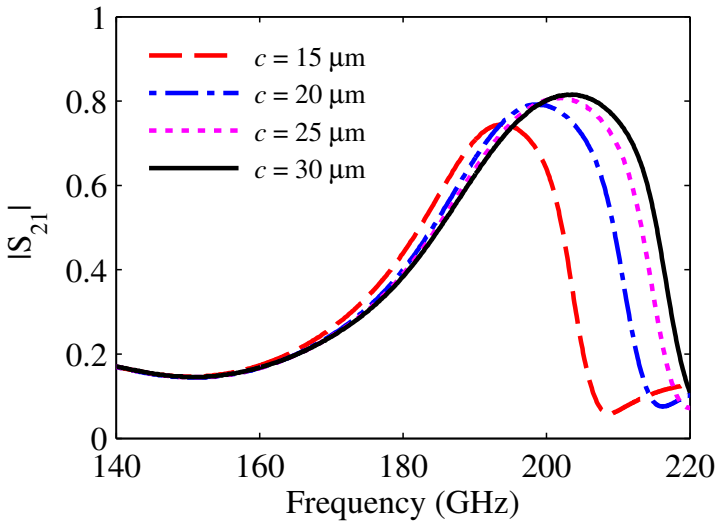

Figure 7.15. Transmission coefficient vs. frequency for third-order periodic filter. Simulated transmission coefficients of the third-order periodic filter for four different values of SRR's inter-ring space c from 15 μm to 30 μm in steps of 5 μm.

by open ends of the PGL. Thus, the terahertz surface waves on the PGL are transmitted across the gap through these coupled SRRs at resonance. In this configuration, the filter's in-band transmission level and bandwidth can be increased by increasing the PGL-to-SRR and SRR-to-SRR couplings. Based on the results of the previous section, the filter's bandwidth can be also increased by decreasing the equivalent capacitance of each SRR.

For comparison, two coupled-SRR filters with different dimensions are designed on the same quartz substrate as in previous sections, with the identical CPW launching sections and PGL width. The dimensions of the first filter are as follows: $a = 180$ μm, $b = 100$ μm, $d = 20$ μm, $c = 5$ μm, $g = 20$ μm, and the space between SRRs is $m = 15$ μm. In order to increase the in-band transmission and bandwidth, in the second filter the PGL-to-SRR coupling is increased by increasing the longitudinal dimension of the SRRs to $a = 190$ μm, while the SRR-to-SRR coupling is increased by decreasing the space between the SRRs to $m = 5$ μm. Furthermore, based on the results from the previous section, the bandwidth of the resonators is increased by increasing the SRRs' inter-ring space c to 10 μm.

Fig. 7.18 compares the simulated transmission coefficients of the two filters. The simulation results show that the maximum in-band transmission coefficient of the second filter is increased to 0.92, compared to 0.82 for the first filter. More importantly, the filter

bandwidth is increased from 25.3 GHz to 37.8 GHz. In order to validate the simulation results, prototypes of both filters have been fabricated and measured. Fig. 7.19 shows the measured transmission coefficients of the filters, which are in good agreement with the simulated ones. The images of the filters prototypes are depicted in the insets. The filters have the same compact dimensions as the SRR/gap-loaded filters presented in Section 7.5 ($0.55\lambda_g \times 0.23\lambda_g$).

7.7 Conclusion

In summary, it has been demonstrated that the bandstop behavior of an SRR-loaded PGL can be switched to a bandpass behavior by introducing a capacitive gap in the PGL. The concept has been interpreted through equivalent circuit models, and the simulation results have been validated through experiments. Furthermore, the effect of different geometrical dimensions of the structure on its frequency response, particularly the resonance bandwidth, has been discussed, and design guidelines have been developed. In order to highlight the potential application of the proposed structure to the design of compact filters for surface waves on PGL, two types of bandpass filters, one based on SRR/gap-loaded PGL, and the second one based on coupled SRRs, have been designed to operate in terahertz regime roughly at 200 GHz. It has been shown that, while the designed filters are compact ($0.55\lambda_g \times 0.23\lambda_g$ for the third-order realizations, λ_g being the guided wavelength at filters center frequency), they offer good in-band transmission and out-of-band rejection. More importantly, it has been shown that the filters bandwidth can be conveniently controlled over a large range, specifically in this design from 18.5 GHz to 37.8 GHz, by altering the geometrical dimensions of the resonators. The methodology and simulation results have been validated through measurement of the filters' fabricated prototypes. The results of this chapter, along with those of the previous chapters, support the concept of metamaterials and their application in the design of compact structures in different planar technologies, in a wide range of frequencies from microwave to millimeter waves to terahertz.

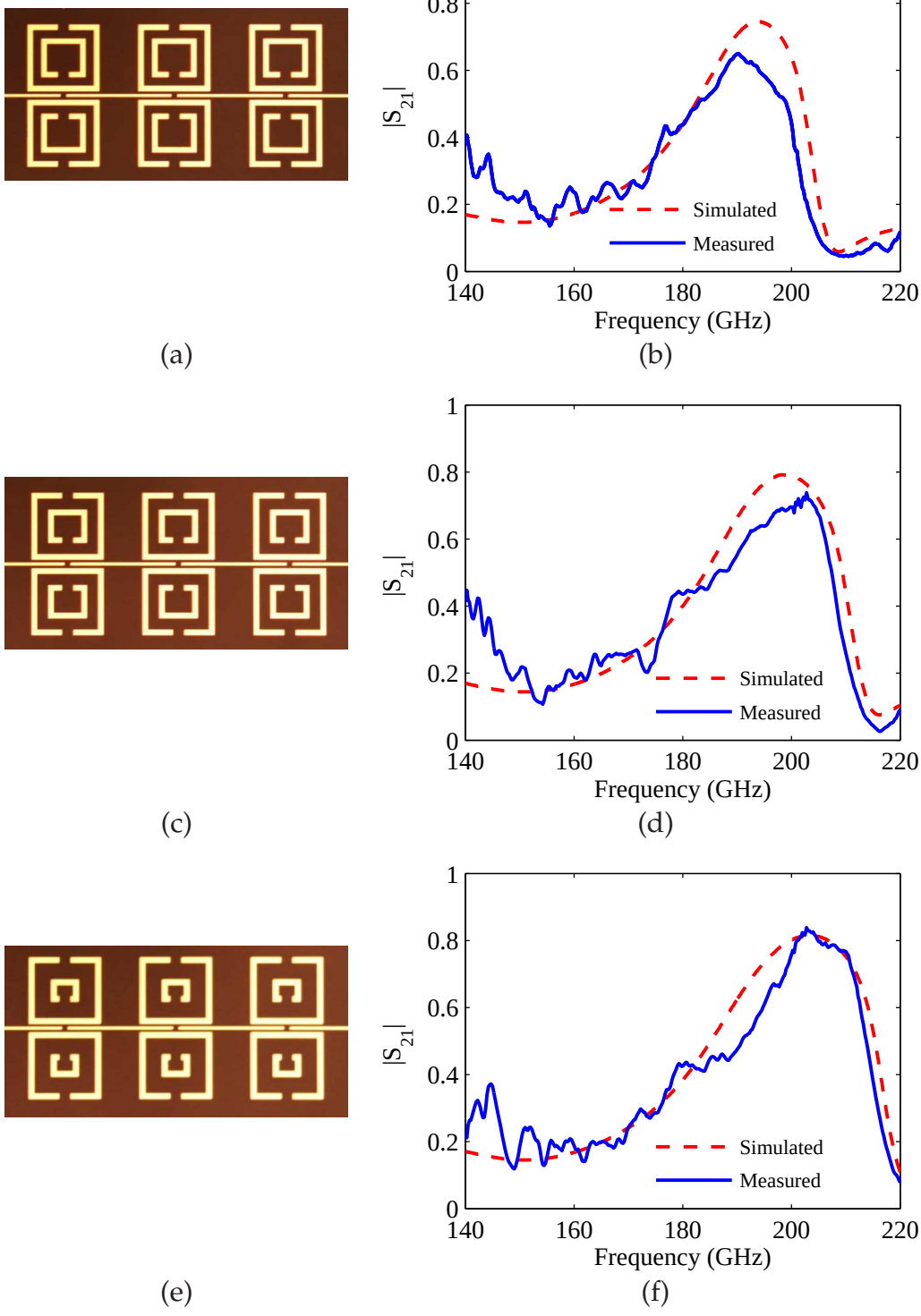

Figure 7.16. Comparison between simulation and measurement results. Photograph of the fabricated samples and comparison between the simulated and measured transmission coefficients of the third-order periodic filter for different values of SRR's inter-ring space (a), (b) $c = 15$ μm, (c), (d) to $c = 20$ μm, and (e), (f) $c = 30$ μm. Photographs of the fabricated prototypes are depicted in the insets.

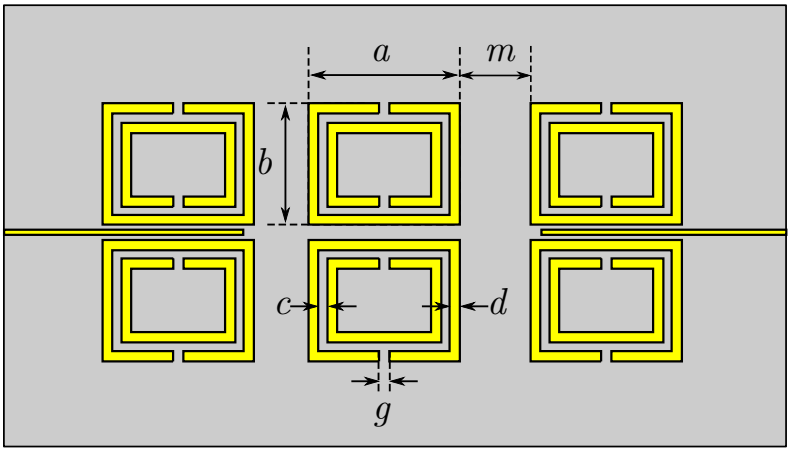

Figure 7.17. Third-order bandpass filter based on coupled SRRs. Layout of the third-order bandpass filter based on the coupled SRRs. Note that SRRs are coupled to open-ended PGLs.

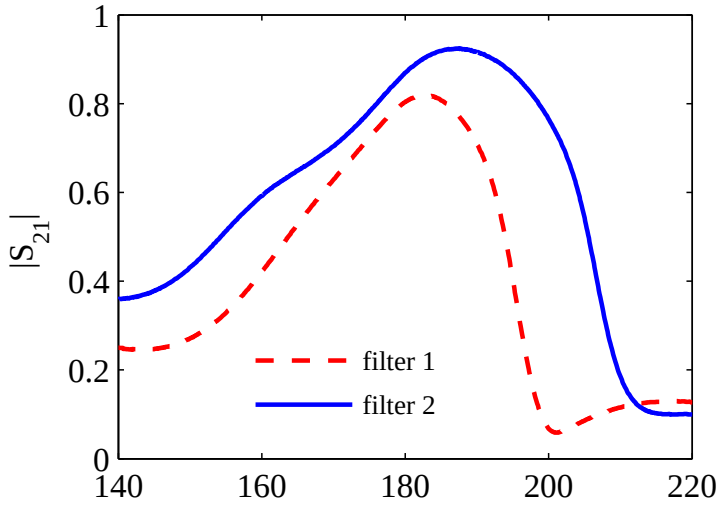

Figure 7.18. Simulated transmission coefficients of coupled-resonator bandpass filters with different geometric dimensions. Comparison between simulated transmission coefficients of two coupled-resonator bandpass filters with different geometric dimensions. The dimensions of the first filter (red dashed line) are $a = 180\ \mu\text{m}$, $b = 100\ \mu\text{m}$, $d = 20\ \mu\text{m}$, $c = 5\ \mu\text{m}$, $g = 20\ \mu\text{m}$, $m = 15\ \mu\text{m}$. A much wider bandwidth and higher in-band transmission level is achieved in the second filter (blue solid line) by changing the dimensions to $a = 190\ \mu\text{m}$, $m = 5\ \mu\text{m}$, and $c = 10\ \mu\text{m}$.

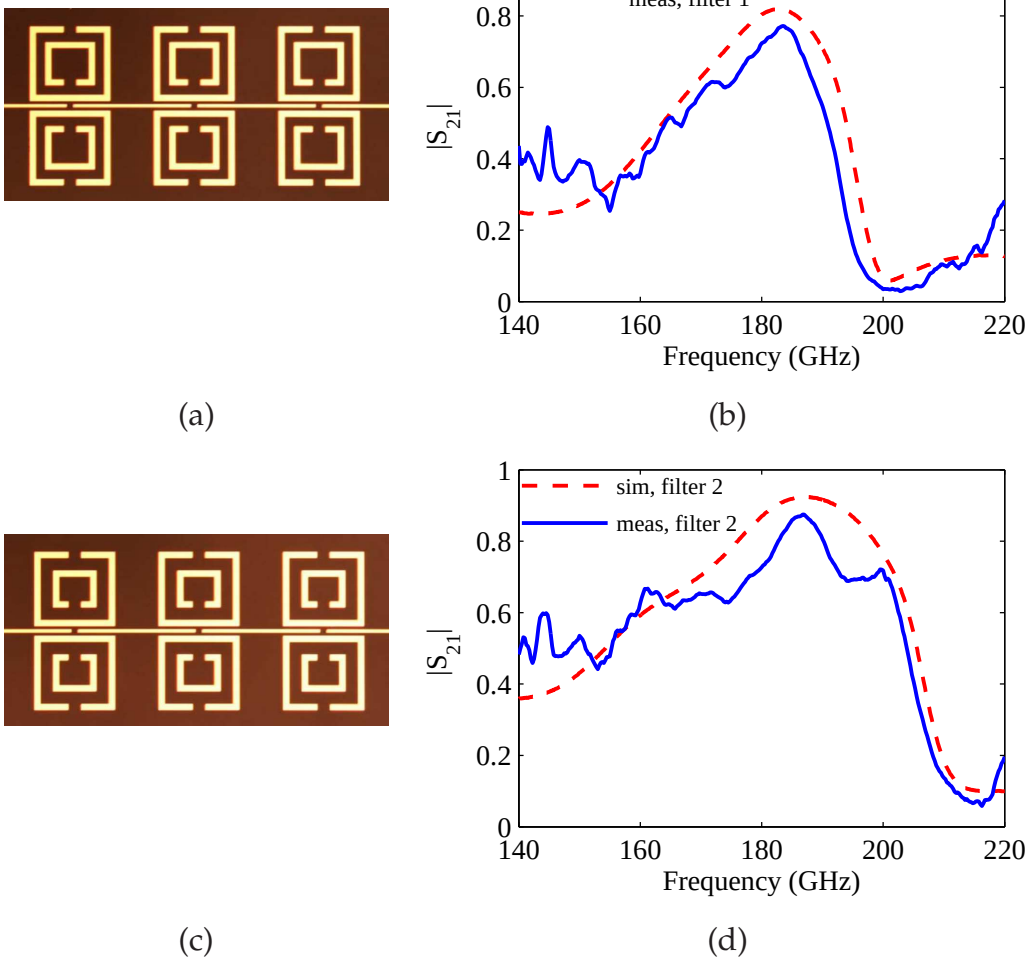

Figure 7.19. Comparison between simulation and measurement transmission coefficients of coupled-resonator bandpass filters. Photograph of the fabricated prototypes and comparison between the simulated and measured transmission coefficients of the fabricated coupled-resonator bandpass filters, (a), (b) prototype 1 with dimensions $a = 180\ \mu$m, $m = 15\ \mu$m, and $c = 5\ \mu$m, and (c), (d) prototype 2 with dimensions $a = 190\ \mu$m, $m = 5\ \mu$m, and $c = 10\ \mu$m.

Chapter 8

Conclusion and Future Work

THE research presented in this thesis has been described in three major parts related to various aspects of metamaterials: The first part of the thesis has placed the focus on the miniaturization of metamaterial components. The second part of the thesis has investigated the application of metamaterial-inspired resonators for the design of displacement and rotation sensors with improved dynamic range and linearity. And finally, the third part of the thesis was devoted to miniaturized metamaterial-inspired filters in microwave and terahertz planar circuits. This chapter concludes the thesis by summarizing the original contributions, results and findings of the thesis. The chapter also considers possible future research on metamaterial-inspired microwave, millimeter-wave and terahertz planar structures.

This chapter provides a summary of the original contributions and results of the three major parts of the thesis along with a number of research directions related to each part.

8.1 Part I: Miniaturization of Metamaterial Components

The first major part of the thesis encompasses Chapters 3 and 4 that focused on various types of metamaterial resonators and their miniaturization. This section gives a summary of the achieved results highlighting the original contributions described in this part of the thesis along with related possible future work.

8.1.1 Summary of Original Contributions

- A parametric study has been conducted on the effect of the geometrical dimensions of a slow-wave coplanar strips (CPS) structure on the guided wavelength, quality factor and characteristic impedance of the line in a standard 90 nm CMOS process. Based on this parametric study, guidelines for the design of high quality factor quarter-wavelength resonators have been extracted, and a high quality factor balanced resonator with small on-chip area has been designed for operation at 60 GHz. This resonator type can be used as a balanced resonator for the implementation of low phase noise VCOs in a standard 90 nm CMOS technology in the millimeter-wave range (Horestani *et al.* 2010, Mehdizadeh *et al.* 2011).

- As an alternative application, further to use as a balanced resonator for the implementation of low phase noise VCOs, a slow-wave quarter-wavelength CPS resonator has been used for the characterization of complex permittivity of thin films of dielectrics. It has been shown that the resonance frequency and the quality factor of the resonator can be exploited for the accurate determination of the permittivity and loss tangent of thin layers of dielectrics in the millimeter-wave band (Horestani *et al.* 2012a).

- Seeking to address the need for balanced resonators with higher quality factors, the chapter has proposed another metamaterial-inspired quarter-wavelength resonator for operation at 60 GHz where the improvement in the quality factor of the resonator has been achieved by loading a conventional CPS resonator with

pairs of SRRs. It has been shown that the proposed resonator can achieve a quality factor of 17.7 that shows a 100% improvement compared to the quality factor of a conventional CPS resonator ($Q = 8.8$) operating at the same frequency (Horestani *et al.* 2011b).

- Motivated by the promising quality factor and compactness of the designed quarter-wavelength CPS resonators, an optimization process for a quarter wavelength slow-wave CPS resonator with a maximum quality factor at 60 GHz has been presented in the last section of chapter. Using the Harmony Search optimization method a slow-wave tapered resonator has been designed, demonstrating a significant quality factor improvement of 220% compared to the conventional uniform CPS resonator and 75% improvement compared to the uniform slow-wave resonator proposed earlier in the chapter (Horestani *et al.* 2011a).

- A compact double-mode resonator based on a pair of CSRRs and defected ground structure (DGS) has been proposed. The proposed resonator benefits from a small electrical size because the pairs of CSRRs are embedded inside the dumbbell-shape DGS. More importantly, it has been shown that the two resonance frequencies of the structure can be independently adjusted by manipulating the physical dimensions of the CSRRs and the DGS. These features makes the proposed resonator an attractive component as a building block for compact microwave circuits such as wideband or dual-band filters (Horestani *et al.* 2011c).

- Based on a circuit model it has been shown that loading a quarter-wavelength resonator with inductive loads not only decreases the fundamental and second harmonic resonance frequencies, but also results in an increase in the ratio of the second harmonic to the fundamental resonance frequency. On this basis, it has been shown that a complementary spiral resonator (CSR) benefits from a higher ratio of the second harmonic to the fundamental resonance frequency when compared to a complementary open-loop resonator with the same fundamental resonance frequency. Exploiting this feature, a bandpass filter based on coupled CSRs has been designed. It has been shown through comparison to a filter based on coupled open-loop resonators that while the proposed CSR filter has a 65% smaller size it benefits from an 85% wider upper stopband (Horestani *et al.* 2012c).

- It has been shown theoretically that although the resonance frequency and electrical size of an SRR can be reduced by increasing either the equivalent capacitance

or equivalent inductance of the SRR, decreasing the resonance frequency by increasing the SRR's equivalent capacitance results in a smaller coupling factor and a narrower bandwidth. In contrast, a smaller electrical size as well as stronger resonance or a wider bandwidth can be achieved by increasing the equivalent inductance of the SRR. On this bases, a nonuniform edge-coupled SRR has been proposed. It has been shown that compared to a uniform SRR, the shape modification, which is based on the current and voltage profile in the SRR structure, enables us to reduce the SRR electrical area by 33%. Moreover, it has been shown that compared to a uniform SRR, a tapered SRR with the same electrical size provides a stronger resonance as well as a wider bandwidth, as desired as building block for wideband filter design. The theory and simulation results have been validated through measurement (Horestani *et al.* 2012b).

8.1.2 Future Work

- In order to address the increasing demand for low-cost high-speed wireless communication systems, Chapter 3 was focused on the design of high quality factor metamaterial-inspired resonators for millimeter-wave VCOs in standard CMOS technology. However, as the frequency of operation approaches the maximum oscillation frequency of transistors, f_{max}, achieving desired VCO specifications becomes more difficult. This limitation makes it necessary to pursue alternative approaches such as distributed oscillators that show great capability to operate at frequencies close to f_{max}. This type of oscillators originate from traveling-wave amplifiers, which have been widely used to achieve a higher gain-bandwidth. Correspondingly, a distributed oscillator, which is formed by feeding the output signal of a traveling-wave amplifier back to its input, can operate at frequencies close to f_{max} (Wu and Hajimiri 2000, Hajimiri and Wu 2000, Wu and Hajimiri 2001, Niknejad and Hashemi 2008). In this direction, the quarter-wavelength metamaterial-inspired resonators of Chapter 3 can be applied for the realization of distributed VCOs that are capable to operate close to the intrinsic cut off frequency of the active devices. Clearly, the proposed structures also can be used in the design of traveling-wave amplifiers to achieve a higher gain-bandwidth.

- Chapter 4 was focused on the miniaturization of metamaterial structures by proposing miniaturized metamaterial resonators with enhanced functionalities. Further

studies are required for applying these resonators in various planar or bulk metamaterial structures such as compact filters, couplers, antennas and frequency selective surfaces.

8.2 Part II: Metamaterial-Inspired Sensors

This section presents original contributions and possible future work related to the second part of the thesis, which focused on the applications of metamaterial-inspired resonators in displacement and rotation sensors.

8.2.1 Summary of Original Contributions

- A one-dimensional displacement sensor based on a diamond-shaped tapered SRR has been proposed. Using the proposed shape modification of the SRR, the dynamic range of the sensor has been increased from 0.6 mm to 1.1 mm, which corresponds to an improvement of more than 80%. Compared to a displacement sensor based on a rectangular-shaped SRR, the proposed diamond-shaped sensor also benefits from a smaller size and superior linearity. More importantly, it has been shown that the undesirable shift in the resonant frequency in the characteristic of previous designs can be suppressed with an optimized tapered diamond-shaped SRR. This is a significant improvement since the sensor does not require a frequency sweeping microwave source, but can be operated as inexpensive single frequency system. The concept and simulation results have been validated experimentally (Horestani *et al.* 2013b).

- In order to improve the dynamic range of previously published metamaterial-inspired displacement sensors, a one-dimensional displacement sensor based on a microstrip line loaded with broadside-coupled split-ring resonators (BC-SRRs) has been presented firstly. It has been shown that the proposed one-dimensional sensor benefits from virtually unlimited dynamic range in displacement. Secondly, with modifications in the geometry of the BC-SRRs, and adding a second element, the proposed one-dimensional sensor has been extended to a high-dynamic range two-dimensional displacement sensor. The proposed one- and two-dimensional sensors are robust to ambient conditions such as changes in the temperature, because the sensors' principle of operation is based on the deviation

from symmetry. This feature also makes them ideal structures as one- and two-dimensional alignment sensors. Furthermore, since the proposed sensors operate based on the shift in the resonance frequency, rather than the resonance depth, they benefit from a high immunity to environmental noise, at a cost however of an increased system complexity because of the requirement of sweeping frequency operation. A prototype of the proposed two-dimensional sensor has been fabricated and the concept and simulation results have been validated through experiment (Shaterian *et al.* 2013, Horestani *et al.* 2014).

- A rotation sensor based on horn-shaped SRR has been proposed. It has been shown that the proposed shape modification of the SRR results in superior linearity and around 40% improvement in the dynamic range of the sensor compared to previously published geometries. More importantly, it has been shown that the geometry of the SRR can be optimized to compensate for the non-uniformity of the magnetic flux through the SRR, in order to suppress the unwanted frequency shift in the resonance. This is a significant improvement because the sensor can be operated as an inexpensive single frequency system. The concept and simulation results are validated by experimental measurements (Horestani *et al.* 2013a).

8.2.2 Future Work

- In order to use the proposed displacement and rotation sensors, the value of the transmission coefficients of the structures must be read from the sensors' ports. However, in many applications such as in high-temperature or construction environments wireless sensors are required. Proposed sensors can be extended to form frequency-selective surfaces that are sensitive to small displacement or rotation, thus can be used as wireless sensors.

- While the dynamic range of the proposed diamond-shaped displacement sensor has been significantly increased by using BC-SRRs, the proposed rotation sensor suffers from a fundamental dynamic range limit. Further investigation on the application of other types of metamaterial-inspired resonator for the design of rotation sensors with higher dynamic range (such as 0° to 360°) are required.

- In several cases in the first and second parts of the thesis, shape modifications of the structures based on the profile of the standing voltage and current in the resonators have been used to achieve miniaturized resonators with high quality

factor or strong and wide resonance or to improve the dynamic range and linearity of the displacement and rotation sensors. This concept can be applied to other metamaterial-inspired resonators to achieved improved functionalities.

8.3 Part III: Metamaterial-Inspired Filters

This section presents original contributions and future studies related to the third major part of the thesis which focused on compact metamaterial-inspired microwave and terahertz filters.

8.3.1 Summary of Original Contributions

- The application of single layer S-shaped split ring resonators (S-SRRs) to the design of compact bandpass filters in coplanar waveguide (CPW) technology has been highlighted. It has been shown that in CPW technology, a high level of filter miniaturization can be achieved by using an S-SRR, compared to the typical configuration using a pair of SRRs aligned with the CPW's slot. It has been further shown that, rather than by a uniform time varying magnetic field, the resonant currents in the S-SRR are excited by contra-directional magnetic fields, axially applied to each loop of the resonator. Therefore, the S-SRR is a suitable particle for excitation by a CPW transmission line. A lumped element equivalent circuit model for the S-SRR-loaded CPW has been proposed, and it has been validated by comparing the circuit response with extracted parameters to full-wave electromagnetic simulations. To highlight the potential of S-SRR-loaded CPWs for compact filter design, two narrowband bandpass filters have been designed and fabricated: one of them based on S-SRR/gap-loaded CPW resonators coupled through admittance inverters; the other one based on coupled S-SRRs, externally driven by open-ended CPWs. Both filters have been designed following a systematic methodology, and standard (Chebyshev) filter responses in the region of interest have been obtained. The filters' performance has been found to be competitive, with sizes as small as $0.32\lambda_g \times 0.08\lambda_g$ and $0.12\lambda_g \times 0.08\lambda_g$ (λ_g being the guided wavelength at the central frequency) for the first and second prototype, respectively (Horestani *et al.* n.d.).

- An S-shaped complementary split ring resonator (S-CSRR) has been proposed for application in compact differential filters. The working principle of the proposed S-CSRR has been explained and a circuit model has been developed and validated through electromagnetic simulations. It has been shown that an S-CSRR-loaded differential microstrip line with series gaps can be used in the design of compact differential bandpass filters with common-mode suppression. The filter design procedure has been explained and the theoretical concept has been validated through fabrication and measurement of a compact ($0.09\lambda_g \times 0.25\lambda_g$) third-order differential bandpass filter with common-mode suppression (Horestani *et al.* 2014).

- The application of SRRs in the realization of bandpass filters for the planar Goubau line (PGL) at terahertz frequencies has been investigated. It has been shown that due to the exponentially decaying transverse electromagnetic field in the Goubau mode, a pair of SRRs in close proximity to a PGL inhibits the propagation of electromagnetic waves at resonance. Through equivalent circuit models, electromagnetic simulations, and experiments, it has been demonstrated that the band-stop behavior of the SRR-loaded PGL can be switched to a bandpass behavior by introducing a capacitive gap in the PGL. The effect of different geometrical dimensions of the structure on its frequency response, particularly the resonance bandwidth, has been studied, and design guidelines have been developed. In order to highlight the potential application of the proposed structure as the building block for compact filters for surface waves on PGL, two types of bandpass filters have been designed to operate in the lower terahertz regime, at around 200 GHz. The first filter is based on SRR/gap-loaded PGL, whereas the second filter is based on coupled SRRs. It has been shown that, while the designed filters are compact ($0.55\lambda_g \times 0.23\lambda_g$ for the third-order realizations, λ_g being the guided wavelength at the filters center frequency), they offer good in-band transmission and out-of-band rejection. More importantly, it has been shown that the filters bandwidth can be conveniently controlled over a large range by altering the geometrical dimensions of the resonators. The concept and simulation results have been validated through measurement of the filters' fabricated prototypes (Horestani *et al.* 2013c, Horestani *et al.* 2013d).

8.3.2 Future Work

- In Chapter 6, S-SRR and S-CSRR have been proposed for the design of miniaturized bandpass filters in CPW and differential microstrip technologies, respectively. Furthermore, it has been shown that S-CSRR inherently suppresses common-mode noise when used as the building block of differential bandpass filters. However, it can be shown that the odd symmetry of the resonators leads to some level of mode conversion. As shown in Chapter 6, mode conversion in an S-SRR loaded CPW can be suppressed by introducing air-bridges along the CPW. However, this approach increases the fabrication cost, and more importantly cannot be used for suppressing the common-to-differential mode conversion in the S-CSRR-loaded differential microstrip line. Therefore, addressing this issue by developing compact resonators with appropriate symmetry could be a future work.

- Propagation of terahertz surface waves on planar Goubau lines has attracted increasing interest in recent times especially as high-speed on-chip interconnections. Chapter 7 has proposed two different types of metamaterial-inspired bandpass filters for terahertz surface waves on PGL. However, in order to exploit the propagation of surface waves on a single wire in real applications, particularly for future broadband terahertz communications, research on the design of other functional components such as couplers, power dividers, multiplexers and demultiplexers are also required.

The results in this thesis emphasize the attractive features and versatility of metamaterial-inspired resonators for applications in various structures with divers functionalities in a wide range of frequencies.

And above all, the main conclusion of this thesis and any other research, can be Isaac Newton's quote stating that "What we know is a drop, what we don't know is an ocean."

Bibliography

ABDEL-RAHMAN-A., ALI-A., AMARI-S., AND OMAR-A. (2005). Compact bandpass filters using defected ground structure (DGS) coupled resonators, *IEEE MTT-S International Microwave Symposium Digest*, pp. 1479–1482.

ABIELMONA-S., NGUYEN-H. V., AND CALOZ-C. (2006). CRLH zeroth order resonator (ZOR): Experimental demonstration of insensitivity to losses and to size, *Proc. IEEE Asia-Pacific Microwave Conference*, IEEE, IEEE, pp. 657–662.

AKALIN-T., AND TREIZEBRÉ-A. (2004). THz microfluidic MEMS for cell membrane analysis, *12th International Conference on Infrared and Millimeter Waves*, pp. 3–4.

AKALIN-T., LAMPIN-J., DESPLANQUE-L., PEYTAVIT-E., AND TREIZEBRÉ-A. (2006a). Propagation of terahertz pulses along planar Goubau lines, *Proc. IEEE Joint 31st International Conference on Infrared Millimeter Waves and 14th International Conference on Teraherz Electronics*, pp. 568–568.

AKALIN-T., PEYTAVIT-E., AND LAMPIN-J. (2007). Bendings and filters with single strip THz plasmonic waveguides, *Joint 32nd International Conference on Infrared and Millimeter Waves and the 15th International Conference on Terahertz Electronics. IRMMW-THz*, pp. 75–76.

AKALIN-T., TREIZEBRÉ-A., AND BOCQUET-B. (2006b). Single-wire transmission lines at terahertz frequencies, *IEEE Transactions on Microwave Theory and Techniques*, **54**(6), pp. 2762–2767.

ALITALO-P., AND TRETYAKOV-S. (2009). Electromagnetic cloaking with metamaterials, *Materials Today*, **12**(3), pp. 22–29.

ALÙ-A., ENGHETA-N., AND ALÙ-A. (2008). Dielectric sensing in ϵ-near-zero narrow waveguide channels, *Physical Review B*, **78**(4), p. 045102.

ALÙ-A., SALANDRINO-A., AND ENGHETA-N. (2006). Negative effective permeability and left-handed materials at optical frequencies., *Optics Express*, **14**(4), pp. 1557–1567.

ANDRESS-W. W., AND HAM-D. (2005). Standing wave oscillators utilizing wave-adaptive tapered transmission lines, *IEEE Journal of Solid-State Circuits*, **40**(3), pp. 638–651.

ARIF-M. S., AND PEROULIS-D. (2009). Loss optimization of coplanar strips for CMOS RFICs, *IEEE Asia Pacific Microwave Conference*, pp. 2144–2147.

AZNAR-F., GIL-M., BONACHE-J., AND MARTÍN-F. (2008a). Modelling metamaterial transmission lines: a review and recent developments, *Opto-Electronics Review*, **16**(3), pp. 226–236.

AZNAR-F., GIL-M., BONACHE-J., JELINEK-L., BAENA-J. D., MARQUÉS-R., AND MARTÍN-F. (2008b). Characterization of miniaturized metamaterial resonators coupled to planar transmission lines through parameter extraction, *Journal of Applied Physics*, **104**(11), p. 114501.

BAENA-J., BONACHE-J., MARTÍN-F., SILLERO-R., FALCONE-F., LOPETEGI-T., LASO-M., GARCIA-GARCIA-J., GIL-I., PORTILLO-M., AND SOROLLA-M. (2005). Equivalent-circuit models for split-ring resonators and complementary split-ring resonators coupled to planar transmission lines, *IEEE Transactions on Microwave Theory and Techniques*, **53**(4), pp. 1451–1461.

BAENA-J. D., MARQUÉS-R., MEDINA-F., AND MARTEL-J. (2004). Artificial magnetic metamaterial design by using spiral resonators, *Physical review B*, **69**(1), p. 014402.

BAKER-JARVIS-J., GEYER-R. G., GROSVENOR JR.-J. H., JANEZIC-M. D., JONES-C. A., RIDDLE-B., WEIL-C. M., AND KRUPKA-J. (1998). Dielectric characterization of low-loss materials a comparison of techniques, *IEEE Transactions on Dielectrics and Electrical Insulation*, **5**(4), pp. 571–577.

BAKER-JARVIS-J., VANZURA-E. J., AND KISSICK-W. A. (1990). Improved technique for determining complex permittivity with the transmission/reflection method, *IEEE Transactions on Microwave Theory and Techniques*, **38**(8), pp. 1096–1103.

BONACHE-J., GIL-I., GARCÍA-GARCÍA-J., AND MARTÍN-F. (2006a). Novel microstrip bandpass filters based on complementary split-ring resonators, *IEEE Transactions on Microwave Theory and Techniques*, **54**(1), pp. 265–271.

BONACHE-J., GIL-M., GIL-I., GARCÍA-GARCÍA-J., AND MARTÍN-F. (2006b). On the electrical characteristics of complementary metamaterial resonators, *IEEE Microwave and Wireless Components Letters*, **16**(10), pp. 543–545.

BONACHE-J., MARTÍN-F., FALCONE-F., GARCÍA-J., GIL-I., LOPETEGI-T., LASO-M. A. G., MARQUÉS-R., MEDINA-F., AND SOROLLA-M. (2004). Super compact split ring resonators CPW band pass filters, *Proc. IEEE MTT-S International Microwave Symposium Digest*, Vol. 3, pp. 1483–1486.

BONACHE-J., SISÓ-G., AND GIL-M. (2008). of composite right/left handed (CRLH) transmission lines based on complementary split ring resonators (CSRRs) to the design of dual-band microwave components, *IEEE Microwave and Wireless Components Letters*, **18**(8), pp. 524–526.

BOOKER-H. (1946). Slot aerials and their relation to complementary wire aerials (Babinet's principle), *Journal of the Institution of Electrical Engineers-Part IIIA: Radiolocation*, **93**(4), pp. 620–626.

BORJA-A. L., CARBONELL-J., BORIA-V. E., CASCON-J., AND LIPPENS-D. (2010). A 2% bandwidth C-band filter using cascaded split ring resonators, *IEEE Antennas and Wireless Propagation Letters*, **9**, pp. 256–259.

BOSE-J. C. (1898). On the rotation of plane of polarisation of electric waves by a twisted structure, *Proceedings of the Royal Society of London (1854-1905)*, **63**(1), pp. 146–152.

BROWN-J. (1953). The types of wave which may exist near a guiding surface, *Proceedings of the IEE-Part III: Radio and Communication Engineering*, **100**(68), pp. 363–364.

CAI-W., CHETTIAR-U. K., KILDISHEV-A. V., AND SHALAEV-V. M. (2007). Optical cloaking with metamaterials, *Nature Photonics*, **1**(4), pp. 224–227.

CALOZ-C. (2006). Dual Composite Right/Left-Handed (D-CRLH) Transmission Line Metamaterial, *IEEE Microwave and Wireless Components Letters*, **16**(11), pp. 585–587.

CALOZ-C., AND ITOH-T. (2002). Application of the transmission line theory of left-handed (LH) materials to the realization of a microstrip, *International Symposium Antennas and Propagation Society*, **2**, pp. 412–415.

CALOZ-C., AND ITOH-T. (2004a). A novel mixed conventional microstrip and composite right/left-handed backward-wave directional coupler with broadband and tight coupling characteristics, *IEEE Microwave and Wireless Components Letters*, **14**(1), pp. 31–33.

CALOZ-C., AND ITOH-T. (2004b). Transmission line approach of left-handed (LH) materials and microstrip implementation of an artificial LH transmission line, *IEEE Transactions on Antennas and Propagation*, **52**(5), pp. 1159–1166.

CALOZ-C., AND ITOH-T. (2005). *Electromagnetic Metamaterials: Transmission Line Theory and Microwave Applications*, Wiley-Interscience.

CHEN-C.-Y., PAN-C.-L., HSIEH-C.-F., LIN-Y.-F., AND PAN-R.-P. (2006a). Liquid-crystal-based terahertz tunable Lyot filter, *Applied Physics Letters*, **88**(10), p. 101107.

CHEN-H., RAN-L., HUANGFU-J., ZHANG-X., CHEN-K., GRZEGORCZYK-T. M., AND AU KONG-J. (2004). Left-handed materials composed of only S-shaped resonators, *Physical Review E*, **70**(5), p. 057605.

CHEN-H., RAN-L., HUANGFU-J., ZHANG-X., CHEN-K., GRZEGORCZYK-T. M., AND KONG-J. A. (2005a). Negative refraction of a combined double S-shaped metamaterial, *Applied Physics Letters*, **86**(15), p. 151909.

CHEN-H., RAN-L.-X., JIANG TAO-H.-F., ZHANG-X.-M., CHENG-K.-S., GRZEGORCZYK-T. M., AND KONG-J. A. (2005b). Magnetic properties of S-shaped split-ring resonators, *Progress In Electromagnetics Research*, **51**, pp. 231–247.

CHEN-H., RAN-L.-X., WU-B.-I., KONG-J. A., AND GRZEGORCZYK-T. M. (2006b). Crankled S-ring resonator with small electrical size, *Progress In Electromagnetics Research*, **66**, pp. 179–190.

CHEN-W.-C., MOCK-J. J., SMITH-D. R., AKALIN-T., AND PADILLA-W. J. (2011). Controlling gigahertz and terahertz surface electromagnetic waves with metamaterial resonators, *Physical Review X*, **1**(2), p. 021016.

CHEUNG-T. S. D., AND LONG-J. R. (2006). Shielded passive devices for silicon-based monolithic microwave and millimeter-wave integrated circuits, *IEEE Journal of Solid-State Circuits*, **41**(5), pp. 1183–1200.

COLLIN-R. E. (2000). *Foundations for Microwave Engineering*, Wiley-IEEE Press.

CUBUKCU-E., ZHANG-S., PARK-Y.-S., BARTAL-G., AND ZHANG-X. (2009). Split ring resonator sensors for infrared detection of single molecular monolayers, *Applied Physics Letters*, **95**(4), p. 043113.

DAMM-C., FREESE-J., SCHUSSLER-M., AND JAKOBY-R. (2007). Electrically controllable artificial transmission line transformer for matching purposes, *IEEE Transactions on Microwave Theory and Techniques*, **55**(6), pp. 1348–1354.

DESCHAMPS-G. (1959). Impedance properties of complementary multiterminal planar structures, *IRE Transactions on Antennas and Propagation*, **7**(5), pp. 371–378.

DIB-N., AND GUPTA-M. (1993). Characterization of asymmetric coplanar waveguide discontinuities, *IEEE Transactions on Microwave Theory and Techniques*, **41**(9), pp. 1549–1558.

DOAN-C. H., EMAMI-S., NIKNEJAD-A. M., AND BRODERSEN-R. W. (2004). Design of CMOS for 60 GHz applications, *IEEE International Solid-State Circuits Conference*, pp. 440–449.

DOAN-C. H., EMAMI-S., NIKNEJAD-A. M., AND BRODERSEN-R. W. (2005). Millimeter-wave CMOS design, *IEEE Journal of Solid-State Circuits*, **40**(1), pp. 144–155.

DUBINOV-A. E., AND MYTAREVA-L. A. (2010). Invisible cloaking of material bodies using the wave flow method, *Physics-Uspekhi*, **53**(5), pp. 455–479.

DURAN-SINDREU-M., VELEZ-A., AZNAR-F., SISO-G., BONACHE-J., MARTÍN-F., DURÁN-SINDREU-M., AND VÉLEZ-A. (2009). Applications of open split ring resonators and open complementary split ring resonators to the synthesis of artificial transmission lines and microwave passive, *IEEE Transactions on Microwave Theory and Techniques*, **57**(12), pp. 3395–3403.

ELEFTHERIADES-G. (2002). Planar negative refractive index media using periodically LC loaded transmission lines, *IEEE Transactions on Microwave Theory and Techniques*, **50**(12), pp. 2702–2712.

ELEZZABI-A. Y., AND SEDERBERG-S. (2009). Optical activity in an artificial chiral media: a terahertz time-domain investigation of Karl F Lindmans 1920 pioneering experiment, *Optics Express*, **17**(8), pp. 6600–6612.

EMOND-J., AND GRZESKOWIAK-M. (2012). A low-loss planar Goubau line and a coplanar-PGL transition on high-resistivity silicon substrate in the 57-64 GHz band, *Microwave and Optical Technology Letters*, **54**(1), pp. 164–168.

FALCONE-F., LOPETEGI-T., BAENA-J., MARQUÉS-R., MARTÍN-F., AND SOROLLA-M. (2004a). Effective negative-ϵ stopband microstrip lines based on complementary split ring resonators, *IEEE Microwave and Wireless Components Letters*, **14**(6), pp. 280–282.

FALCONE-F., LOPETEGI-T., LASO-M. A. G., BAENA-J. D., BONACHE-J., BERUETE-M., MARQUÉS-R., MARTÍN-F., AND SOROLLA-M. (2004b). Babinet principle applied to the design of metasurfaces and metamaterials, *Physical Review Letters*, **93**(19), p. 197401.

FALCONE-F., MARTÍN-F., BONACHE-J., LASO-M. A. G., GARCÍA-GARCÍA-J., BAENA-J. D., MARQUÉS-R., AND SOROLLA-M. (2004c). Stop-band and band-pass characteristics in coplanar waveguides coupled to spiral resonators, *Microwave and Optical Technology Letters*, **42**(5), pp. 386–388.

FANG-N., LEE-H., SUN-C., AND ZHANG-X. (2005). Sub-diffraction-limited optical imaging with a silver superlens., *Science (New York, N.Y.)*, **308**(5721), pp. 534–537.

FERGUSON-B., AND ZHANG-X.-C. (2002). Materials for terahertz science and technology., *Nature Materials*, **1**(1), pp. 26–33.

FERGUSON-B., WANG-S., GRAY-D., ABBOTT-D., AND ZHANG-X.-C. (2002). T-ray computed tomography., *Optics Letters*, **27**(15), pp. 1312–1314.

FESANGHARY-M. (2009). Harmony search applications in mechanical, chemical and electrical engineering, *Music-Inspired Harmony Search Algorithm*, pp. 71–86.

FRANC-A.-N., PISTONO-E., AND FERRARI-P. (2012). Characterization of Thin Dielectric Films up to Mm-Wave Frequencies Using Patterned Shielded Coplanar Waveguides, *Microwave and Wireless Components Letters, IEEE*, **22**(2), pp. 100–102.

GACEMI-D., MANGENEY-J., COLOMBELLI-R., AND DEGIRON-A. (2013). Subwavelength metallic waveguides as a tool for extreme confinement of THz surface waves., *Scientific Reports*, **3**, p. 1369.

GACEMI-D., MANGENEY-J., LAURTENT-T., LAMPIN-J., AKALIN-T., BLARY-K., DEGIRON-A., CROZAT-P., AND MENG-F. (2012). THz surface plasmon modes on planar Goubau lines., *Optics Express*, **20**(8), pp. 8466–8471.

GARCÍA-GARCÍA-J., AND MARTÍN-F. (2004). Spurious passband suppression in microstrip coupled line band pass filters by means of split ring resonators, *IEEE Microwave and Wireless Components Letters*, **14**(9), pp. 416–418.

GARCÍA-GARCÍA-J., BONACHE-J., GIL-I., MARTÍN-F., MARQUÉS-R., FALCONE-F., LOPETEGI-T., LASO-M., AND SOROLLA-M. (2005a). Comparison of electromagnetic band gap and split-ring resonator microstrip lines as stop band structures, *Microwave and Optical Technology Letters*, **44**(4), pp. 376–379.

GARCÍA-GARCÍA-J., BONACHE-J., GIL-I., MARTÍN-F., VELAZQUEZ-AHUMADA-M. D. C., AND MARTEL-J. (2006). Miniaturized microstrip and CPW filters using coupled metamaterial resonators, *IEEE Transactions on Microwave Theory and Techniques*, **54**(6), pp. 2628–2635.

GARCÍA-GARCÍA-J., MARTÍN-F., FALCONE-F., BONACHE-J., BAENA-J. D., GIL-I., AMAT-E., LOPETEGI-T., LASO-M. A. G., ITURMENDI-J., SOROLLA-M., AND MARQUÉS-R. (2005b). Microwave filters with improved stopband based on sub-wavelength resonators, *IEEE Transactions on Microwave Theory and Techniques*, **53**(6), pp. 1997–2006.

GEEM-Z. (2009). *Music-Inspired Harmony Search Algorithm: Theory and Applications*, 1st edn, New York: Springer.

GETSINGER-W. (1983). Circuit Duals on Planar Transmission Media, *MTT-S International Microwave Symposium Digest*, Vol. 83, MTT005, pp. 154–156.

GIL-I., BONACHE-J., GARCIA-GARCIA-J., FALCONE-F., AND MARTÍN-F. (2005). Metamaterials in microstrip technology for filter applications, *Antennas and Propagation Society International Symposium*, Vol. 1, IEEE, pp. 668–671.

GIL-M., AND BONACHE-J. (2007). Broadband resonant-type metamaterial transmission lines, *IEEE Microwave and Wireless Components Letters*, **17**(2), pp. 97–99.

GIL-M., BONACHE-J., AND MARTÍN-F. (2008). Metamaterial filters: A review, *Metamaterials*, **2**(4), pp. 186–197.

GIL-M., BONACHE-J., GARCÍA-GARCÍA-J., MARTEL-J., AND MARTÍN-F. (2007). Composite right/left-handed metamaterial transmission lines based on complementary split-rings resonators and their applications to very wideband and compact filter design, *IEEE Transactions on Microwave Theory and Techniques*, **55**(6), pp. 1296–1304.

GIL-M., BONACHE-J., GIL-I., GARCÍA-GARCÍA-J., AND MARTÍN-F. (2006). On the transmission properties of left-handed microstrip lines implemented by complementary split rings resonators, *International Journal of Numerical Modelling: Electronic Networks, Devices and Fields*, **19**(2), pp. 87–103.

GONZALEZ-G. (1997). *Microwave Transistor Amplifiers: Analysis and Design*, Prentice hall New Jersey.

GORUR-A. (1994). A novel coplanar slow-wave structure, *IEEE Microwave and Guided Wave Letters*, **4**(3), pp. 86–88.

GOUBAU-G. (1956). Open wire lines, *IRE Transactions on Microwave Theory and Techniques*, **39**, pp. 6–9.

GRBIC-A., AND ELEFTHERIADES-G. V. (2002). Experimental verification of backward-wave radiation from a negative refractive index metamaterial, *Journal of Applied Physics*, **92**(10), pp. 5930–5935.

GUAN-X., LI-G., AND MA-Z. (2005). Optimized design of a low-pass filter using defected ground structures, *Proc. Asia-Pacific Microwave Conference (APMC)*, Vol. 1, p. DOI: 10.1109/APMC.2005.1606298.

GUPTA-K. C., GARG-R., BAHL-I., AND BHARTIA-P. (1996). *Microstrip lines and slotlines*, Artech House Boston.

HAJIMIRI-A., AND LEE-T. H. (1999). *The Design of Low Noise Oscillators*, Springer.

HAJIMIRI-A., AND WU-H. (2000). Analysis and design of silicon bipolar distributed oscillators, *IEEE VLSI Symposium Digest Technical Papers*, IEEE, pp. 102–105.

HAO-T., STEVENS-C., AND EDWARDS-D. (2005). Optimisation of metamaterials by Q factor, *Electronics Letters*, **41**(11), pp. 653–654.

HERRAIZ-MARTÍNEZ-F. J., PAREDES-F., ZAMORA-G., MARTÍN-F., AND BONACHE-J. (2012). Dual band printed dipole antenna loaded with open complementary split-ring resonators for wireless applications, *IEEE Microwave and Wireless Components Letters*, **54**(4), pp. 1014–1017.

HERRAIZ-MARTÍNEZ-F. J., ZAMORA-G., PAREDES-F., MARTÍN-F., AND BONACHE-J. (2011). Multiband printed monopole antennas loaded with OCSRRs for PANs and WLANs, *IEEE Antennas and Wireless Propagation Letters*, **10**, pp. 1528–1531.

HE-S., JIN-Y., RUAN-Z., AND KUANG-J. (2005). On subwavelength and open resonators involving metamaterials of negative refraction index, *New Journal of Physics*, **7**, pp. 210–210.

HE-X.-J., WANG-Y., WANG-J.-M., AND GUI-T.-L. (2010). Thin-film sensor based tip-shaped split ring resonator metamaterial for microwave application, *Microsystem Technologies*, **16**(10), pp. 1735–1739.

HONG-J. S., AND LANCASTER-M. J. (1996). Couplings of microstrip square open-loop resonators for cross-coupled planar microwave filters, *IEEE Transactions on Microwave Theory and Techniques*, **44**(12), pp. 2099–2109.

HONG-J. S., AND LANCASTER-M. J. (1997). Theory and experiment of novel microstrip slow-wave open-loop resonator filters, *IEEE Transactions on Microwave Theory and Techniques*, **45**(12), pp. 2358–2365.

HONG-J. S., AND LANCASTER-M. J. (2001). *Microstrip Filters for RF/Microwave Applications*, Wiley, New York.

HORESTANI-A. K., ABBOTT-D., AND FUMEAUX-C. (2013a). Rotation sensor based on horn-shaped split ring resonator, *IEEE Sensors Journal*, **13**(8), pp. 3014–3015.

HORESTANI-A. K., AL-SARAWI-S., AND ABBOTT-D. (2010). Designing of high-Q slow-wave coplanar strips for CMOS MMICs, *35th IEEE International Conference on Infrared, Millimeter, and Terahertz Waves*, p. DOI: 10.1109/ICIMW.2010.5612952.

HORESTANI-A. K., DURÁN-SINDREU-M., NAQUI-J., FUMEAUX-C., AND MARTÍN-F. (n.d.). Coplanar waveguides loaded with S-shaped split ring resonators (S-SRRs) and their application to compact bandpass filter design, *IEEE Trans. Microw. Theory Tech.*, submitted for publication.

HORESTANI-A. K., FUMEAUX-C., AL-SARAWI-S., AND ABBOTT-D. (2012a). Characterization of the complex permittivity of thin films using a slow-wave coplanar strips resonator, *37th IEEE International Conference on Infrared, Millimeter, and Terahertz Waves*, pp. DOI: 0.1109/IRMMW–THz.2012.6379510.

HORESTANI-A. K., FUMEAUX-C., AL-SARAWI-S., AND ABBOTT-D. (2012b). Split Ring Resonators With Tapered Strip Width for Wider Bandwidth and Enhanced Resonance, *IEEE Microwave and Wireless Components Letters*, **22**(9), pp. 450–452.

HORESTANI-A. K., FUMEAUX-C., AL-SARAWI-S., AND ABBOTT-D. (2013b). Displacement sensor based on diamond-shaped tapered split ring resonator, *IEEE Sensors Journal*, **13**(4), pp. 1153–1160.

HORESTANI-A. K., MEHDIZADEH-A., AL-SARAWI-S., FUMEAUX-C., AND ABBOTT-D. (2011a). Quality factor optimization process of a tapered slow-wave coplanar strips resonator in CMOS technology, *Proc. Asia-Pacific Microwave Conference (APMC)*, Melbourne, Victoria, Australia, pp. 45–48.

HORESTANI-A. K., NAQUI-J., SHATERIAN-Z., ABBOTT-D., FUMEAUX-C., AND MARTÍN-F. (2014). Two-dimensional alignment and displacement sensor based on movable broadside-coupled split ring resonators, *Sensors and Actuators A: Physical*, **210**, pp. 18–24.

HORESTANI-A. K., SHATERIAN-Z., AL-SARAWI-S., ABBOTT-D., AND FUMEAUX-C. (2012c). Miniaturized bandpass filter with wide stopband using complementary spiral resonator, *Proc. Asia-Pacific Microwave Conference (APMC)*, pp. 550–552.

HORESTANI-A. K., SHATERIAN-Z., AL-SARAWI-S., AND ABBOTT-D. (2011b). High quality factor mm-wave coplanar strip resonator based on split ring resonators, *Proc. 36th International Conference on Infrared, Millimeter and Terahertz Waves, (IRMMW-THz)*, IEEE, Houston, TX, pp. DOI: 10.1109/irmmw–THz.2011.6105225.

HORESTANI-A. K., SHATERIAN-Z., WITHAYACHUMNANKUL-W., FUMEAUX-C., AL-SARAWI-S., AND ABBOTT-D. (2011c). Compact wideband filter element based on complementary split-ring resonators, *Proc. SPIE Smart Nano-Micro Materials and Devices*, Melbourne, Australia, p. 820431.

HORESTANI-A. K., WITHAYACHUMNANKUL-W., CHAHADIH-A., GHADDAR-A., ZEHAR-M., ABBOTT-D., FUMEAUX-C., AND AKALIN-T. (2013c). Metamaterial-inspired bandpass filters for terahertz surface waves on Goubau lines, *IEEE Transactions on Terahertz Science and Technology*, **3**(6), pp. 851–858.

HORESTANI-A. K., WITHAYACHUMNANKUL-W., FUMEAUX-C., ABBOTT-D., AND AKALIN-T. (2013d). Metamaterial-inspired bandpass filter for the terahertz Goubau line, *Proc. 4th International Conference on Metamaterials, Photonic Crystals and Plasmonics, META'13*, Sharjah, United Arab Emirates, pp. 117–118.

HOWARTH-J., LAUTERBACH-A., BOERS-M., DAVIS-L., PARKER-A., HARRISON-J., RATHMELL-J., BATTY-M., COWLEY-W., BURNET-C., HALL-L., ABBOTT-D., AND WESTE-N. (2005). 60GHz Radios: Enabling Next-Generation Wireless Applications, *Proc. IEEE TENCON Conference*, IEEE, pp. 1–6.

HUANG-M., AND YANG-J. (2011). Microwave sensor using metamaterials, *in* Petrin A. (ed.), *Wave Propagation*, In-tech Press: Vienna, Austria, pp. 13–36.

HUANG-M., YANG-J., SUN-J., SHI-J., AND PENG-J. (2009). Modelling and analysis of Ω-shaped double negative material-assisted microwave sensor, *Journal of Infrared, Millimeter, and Terahertz Waves*, **30**(11), pp. 1131–1138.

IYER-A., AND ELEFTHERIADES-G. (2002). Negative refractive index metamaterials supporting 2-D waves, *2002 IEEE MTT-S International Microwave Symposium Digest (Cat. No.02CH37278)*, pp. 1067–1070.

JAKŠIĆ-Z., JAKŠIĆ-O., DJURIĆ-Z., AND KMENT-C. (2007). A consideration of the use of metamaterials for sensing applications: field fluctuations and ultimate performance, *Journal of Optics A: Pure and Applied Optics*, **9**(9), pp. S377–S384.

JANEZIC-M. D., AND JARGON-J. A. (1999). Complex permittivity determination from propagation constant measurements, *IEEE Microwave and Guided Wave Letters*, **9**(2), pp. 76–78.

JARAUTA-E., LASO-M. A. G., LOPETEGI-T., FALCONE-F., BERUETE-M., BAENA-J. D., MARCOTEGUI-A., BONACHE-J., GARCÍA-J., MARQUÉS-R., AND MARTÍN-F. (2006). Novel microstrip backward coupler with metamaterial cells for fully planar fabrication techniques, *Microwave and Optical Technology Letters*, **48**(6), pp. 1205–1209.

KADDOUR-D., ISSA-H., ABDELAZIZ-M., PODEVIN-F., PISTONO-E., DUCHAMP-J., AND FERRARI-P. (2008). Design guidelines for low-loss slow-wave coplanar transmission lines in RF-CMOS technology, *Microwave and Optical Technology Letters*, **50**(12), pp. 3029–3036.

KADDOUR-D., ISSA-H., FRANC-A. L., CORRAO-N., PISTONO-E., PODEVIN-F., FOURNIER-J. M., DUCHAMP-J. M., AND FERRARI-P. (2009). High-Q slow-wave coplanar transmission lines on 0.35 μm CMOS process, *IEEE Microwave and Wireless Components Letters*, **19**(9), pp. 542–544.

KAWASE-K., OGAWA-Y., WATANABE-Y., AND INOUE-H. (2003). Non-destructive terahertz imaging of illicit drugs using spectral fingerprints., *Optics Express*, **11**(20), pp. 2549–2554.

KHANNA-A., AND GARAULT-Y. (1983). Determination of Loaded, unloaded, and external quality factors of a dielectric resonator coupled to a microstrip line, *IEEE Transactions on Microwave Theory and Techniques*, **31**(3), pp. 261–264.

KIM-C., PARK-J., AHN-D., AND LIM-J. (2000). A novel 1-D periodic defected ground structure for planar circuits, *IEEE Microwave and Guided Wave Letters*, **10**(4), pp. 131–133.

KINGET-P. (1999). Integrated GHz voltage controlled oscillators, *Analog Circuit Design*, Springer, pp. 353–381.

KING-M., AND WILTSE-J. (1962). Surface-wave propagation on coated or uncoated metal wires at millimeter wavelengths, *IRE Transactions on Antennas and Propagation*, **10**(3), pp. 246–254.

KLEVELAND-B., DIAZ-C. H., VOOK-D., MADDEN-L., LEE-T. H., AND WONG-S. S. (2001). Exploiting CMOS reverse interconnect scaling in multigigahertz amplifier and oscillator design, *IEEE Journal of Solid-State Circuits*, **36**(10), pp. 1480–1488.

LAI-A., CALOZ-C., AND ITOH-T. (2004). Composite right/left-handed transmission line metamaterials, *IEEE Microwave Magazine*, **5**(3), pp. 34–50.

LAI-I. C. H., AND FUJISHIMA-M. (2007). High-Q slow-wave transmission line for chip area reduction on advanced CMOS processes, *IEEE International Conference on Microelectronic Test Structures, 2007. ICMTS '07.*, pp. 192–195.

LAI-I. C. H., TANIMOTO-H., AND FUJISHIMA-M. (2006). Characterization of high Q transmission line structure for advanced CMOS processes, *IEICE Transactions on Electronics*, **89**(12), pp. 1872–1879.

LEESON-D. (1966). A simple model of feedback oscillator noise spectrum, *Proceedings of the IEEE*, **54**(2), pp. 329–330.

LEE-Y. T., LIM-J. S., KIM-S., LEE-J., NAM-S., AND SEO-K. S. (2003). Application of CPW based spiral-shaped defected ground structure to the reduction of phase noise in V-band MMIC oscillator, *IEEE MTT-S International Microwave Symposium Digest*, Vol. 3, IEEE, pp. 2253–2256.

LEE-Y. T., LIM-J. S., PARK-J. S., AHN-D., AND NAM-S. (2002). A novel phase noise reduction technique in oscillators using defected ground structure, *IEEE Microwave and Wireless Component Letters*, **12**(2), pp. 39–41.

LIANG-L., JIN-B., WU-J., HUANG-Y., YE-Z., HUANG-X., ZHOU-D., WANG-G., JIA-X., LU-H., KANG-L., XU-W., CHEN-J., AND WU-P. (2013). A flexible wideband bandpass terahertz filter using multi-layer metamaterials, *Applied Physics B*, pp. DOI: 10.1007/s00340–013–5470–x.

LI-J. (2010). Terahertz wave narrow bandpass filter based on photonic crystal, *Optics Communications*, **283**(13), pp. 2647–2650.

LI-J.-S., AND LI-X.-J. (2009). Determination principal component content of seed oils by THz-TDS, *Chemical Physics Letters*, **476**(1), pp. 92–96.

LIM-J., KIM-C., AND AHN-D. (2005). Design of low-pass filters using defected ground structure, *IEEE Transactions on Microwave Theory and Techniques*, **53**(8), pp. 2539–2545.

LIM-J. S., KIM-C. S., LEE-Y. T., AHN-D., AND NAM-S. (2002a). A new type of low pass filter with defected ground structure, *Proc. of the 32nd European Microwave Conference*, pp. 1–4.

LIM-J. S., KIM-C. S., LEE-Y. T., AND NAM-S. (2002b). Design of lowpass filters using defected ground structure and compensated microstrip line, *Electronics Letters*, **38**(22), pp. 1357–1358.

LIM-J.-S., KIM-C.-S., LEE-Y.-T., MEMBER-S., JONG-SIK LIM., JUN-SEOK PARK., YOUNG-TAEK LEE., DAL AHN., SANGWOOK NAM., AND CHUL-SOO KIM. (2002c). A spiral-shaped defected ground structure for coplanar waveguide, *IEEE Microwave and Wireless Components Letters*, **12**(7), pp. 261–263.

LIM-J.-S., LEE-S.-W., V-C.-S., PARK-J.-S., AHN-D., AND NAM-S. (2001). A 4.1 unequal Wilkinson power divider, *IEEE Microwave and Wireless Components Letters*, **11**(3), pp. 124–126.

LIM-J.-S., PARK-J.-S., MEMBER-A., LEE-Y.-T., AND MEMBER-S. (2002d). Application of defected ground structure in reducing the size of amplifiers, *IEEE Microwave and Wireless Components Letters*, **12**(7), pp. 261–263.

LIM-T. B., AND ZHU-L. (2009). A differential-mode wideband bandpass filter on microstrip line for UWB application, *IEEE Microwave and Wireless Components Letters*, **19**(10), pp. 632–634.

LIM-T. B., AND ZHU-L. (2011). Highly selective differential-mode wideband bandpass filter for UWB application, *IEEE Microwave and Wireless Components Letters*, **21**(3), pp. 133–135.

LINDMAN-K. F. (1920). Über eine durch ein isotropes System von spiralförmigen Resonatoren erzeugte Rotationspolarisation der elektromagnetischen Wellen, *Annalen der Physik*, **368**(23), pp. 621–644.

LIN-S.-C., LIN-Y.-S., AND CHEN-C. H. (2006). Extended-stopband bandpass filter using both half- and quarter-wavelength resonators, *IEEE Microwave and Wireless Components Letters*, **16**(1), pp. 43–45.

LIN-X. Q., AND CUI-T. J. (2008). Controlling the bandwidth of split ring resonators, *IEEE Microwave and Wireless Components Letters*, **18**(4), pp. 245–247.

LIU-K.-Y., LI-C., AND LI-F. (2007a). A new type of microstrip coupler with complementary split-ring resonator, *Microwave and Optical Technology Letters*, **49**(7), pp. 1613–1616.

LIU-Z., DURANT-S., LEE-H., PIKUS-Y., FANG-N., XIONG-Y., SUN-C., AND ZHANG-X. (2007b). Far-field optical superlens., *Nano Letters*, **7**(2), pp. 403–8.

LI-Y., ZHANG-X., AND XUE-Q. (2010). Bandpass filter using discriminating coupling for extended out-of-band suppression, *IEEE Microwave and Wireless Components Letters*, **20**(7), pp. 369–371.

LOPETEGI-T., LASO-M. A. G., AND FALCONE-F. (2004). Microstrip wiggly-line bandpass filters with multispurious rejection, *IEEE Microwave and Wireless Components Letters*, **14**(11), pp. 531–533.

LOPETEGI-T., LASO-M., HERNANDEZ-J., BACAICOA-M., BENITO-D., GARDE-M., SOROLLA-M., AND GUGLIELMI-M. (2001). New microstrip "Wiggly-Line" filters with spurious passband suppression, *IEEE Transactions on Microwave Theory and Techniques*, **49**(9), pp. 1593–1598.

LU-M., LI-W., AND BROWN-E. (2011). Second-order bandpass terahertz filter achieved by multilayer complementary metamaterial structures, *Optics Letters*, **36**(7), pp. 1071–1073.

MANDEL-C., AND KUBINA-B. (2011). Passive chipless wireless sensor for two-dimensional displacement measurement, *41st European Microwave Conference (EuMC)*, pp. 79–82.

MAO-S., AND CHUEH-Y. (2007). Coplanar waveguide bandpass filters with compact size and wide spurious-free stopband using electromagnetic bandgap resonators, *IEEE Microwave and Wireless Components Letters*, **17**(3), pp. 181—-183.

MAO-S.-G., WU-M.-S., CHUEH-Y.-Z., AND CHEN-C. H. (2005). Modeling of symmetric composite right/left-handed coplanar waveguides with applications to compact bandpass filters, *IEEE Transactions on Microwave Theory and Techniques*, **53**(11), pp. 3460–3466.

MARCU-C., AND NIKNEJAD-A. M. (2008a). 60 GHz Tapered Transmission Line Resonators, *Technical Report UCB/EECS-2008-117*, EECS Department, University of California, Berkeley.

MARCU-C., AND NIKNEJAD-A. M. (2008b). A 60 GHz high-Q tapered transmission line resonator in 90nm CMOS, *IEEE MTT-S International Microwave Symposium Digest*, pp. 775–778.

MARQUÉS-R., MARTÍN-F., AND SOROLLA-M. (2008). *Metamaterials with Negative Parameters: Theory, Design, and Microwave Applications*, Wiley-Interscience.

MARQUÉS-R., MEDINA-F., AND RAFII-EL-IDRISSI-R. (2002). Role of bianisotropy in negative permeability and left-handed metamaterials, *Physical Review B*, **65**(14), p. 144440.

MARQUÉS-R., MESA-F., AND MEDINA-F. (2005). Near-field enhanced imaging by a magnetized ferrite slab, *Applied Physics Letters*, **86**(2), p. 023505.

MARQUÉS-R., MESA-F., MARTEL-J., AND MEDINA-F. (2003). Comparative analysis of edge- and broadside-coupled split ring resonators for metamaterial design–theory and experiments, *IEEE Transactions on Antennas and Propagation*, **51**(10), pp. 2572–2581.

MARTEL-J., MARQUÉS-R., FALCONE-F., BAENA-J. D., MEDINA-F., MARTÍN-F., AND SOROLLA-M. (2004). A new LC series element for compact bandpass filter design, *IEEE Microwave and Wireless Components Letters*, **14**(5), pp. 210–212.

MARTÍN-F., BONACHE-J., FALCONE-F., SOROLLA-M., AND MARQUÉS-R. (2003a). Split ring resonator-based left-handed coplanar waveguide, *Applied Physics Letters*, **83**(22), pp. 4652–4654.

MARTÍN-F., FALCONE-F., BONACHE-J., MARQUÉS-R., AND SOROLLA-M. (2003b). Miniaturized coplanar waveguide stop band filters based on multiple tuned split ring resonators, *IEEE Microwave and Wireless Components Letters*, **13**(12), pp. 511–513.

MATTHAEI-G. L., SCHIFFMAN-B., CRISTAL-E., AND ROBINSON-L. (1963). *Microwave Filters and Coupling Structures*, Artech House.

MEHDIZADEH-A., HORESTANI-A. K., AL-SARAWI-S., AND ABBOTT-D. (2011). An efficient 60 GHz resonator using Harmony Search, *2011 IEEE Recent Advances in Intelligent Computational Systems*, Ieee, pp. 369–372.

MELIK-R., UNAL-E., PERKGOZ-N. K., PUTTLITZ-C., AND DEMIR-H. V. (2009). Metamaterial-based wireless strain sensors, *Applied Physics Letters*, **95**(1), p. 011106.

MONTI-A., BILOTTI-F., AND TOSCANO-A. (2011). Optical cloaking of cylindrical objects by using covers made of core-shell nanoparticles., *Optics letters*, **36**(23), pp. 4479–81.

NAQUI-J., DURÁN-SINDREU-M., AND MARTÍN-F. (2011). Novel sensors based on the symmetry properties of split ring resonators (SRRs)., *Sensors*, **11**(8), pp. 7545–53.

NAQUI-J., DURÁN-SINDREU-M., AND MARTÍN-F. (2012a). Alignment and position sensors based on split ring resonators, *Sensors*, **12**(9), pp. 11790—-11797.

NAQUI-J., DURÁN-SINDREU-M., AND MARTÍN-F. (2012b). On the symmetry properties of coplanar waveguides loaded with symmetric resonators: Analysis and potential applications, *MTT-S International Microwave Symposium Digest*, IEEE, pp. 1–3.

NAQUI-J., FERNANDEZ-PRIETO-A., DURÁN-SINDREU-M., MESA-F., MARTEL-J., MEDINA-F., AND MARTÍN-F. (2012c). Common-mode suppression in microstrip differential lines by means of complementary split ring resonators: theory and applications, *IEEE Transactions on Microwave Theory and Techniques*, **60**(10), pp. 3023–3034.

NĚMEC-H., DUVILLARET-L., GARET-F., KUŽEL-P., XAVIER-P., RICHARD-J., AND RAULY-D. (2004). Thermally tunable filter for terahertz range based on a one-dimensional photonic crystal with a defect, *Journal of Applied Physics*, **96**(8), pp. 4072–4075.

NIKNEJAD-A., AND MEYER-R. (1998). Analysis, design, and optimization of spiral inductors and transformers for Si RF ICs, *IEEE Journal of Solid-State Circuits*, **33**(10), pp. 1470–1481.

NIKNEJAD-A. M., AND HASHEMI-H. (2008). *mm-Wave Silicon Technology:* 60 GHz *and Beyond*, Springer Verlag.

NIKNEJAD-A. M., AND MEYER-R. (2000). *Design, Simulation and Applications of Inductors and Transformers for Si RF ICs*, Springer.

O'HARA-J. F., WITHAYACHUMNANKUL-W., AND AL-NAIB-I. (2012). A review on thin-film sensing with terahertz waves, *Journal of Infrared, Millimeter, and Terahertz Waves*, **33**(3), pp. 245–291.

OHASHI-K., NISHI-K., SHIMIZU-T., NAKADA-M., FUJIKATA-J., USHIDA-J., TORII-S., NOSE-K., MIZUNO-M., YUKAWA-H., KINOSHITA-M., SUZUKI-N., GOMYO-A., ISHI-T., OKAMOTO-D., FURUE-K., UENO-T., TSUCHIZAWA-T., WATANABE-T., YAMADA-K., ITABASHI-S.-I., AND AKEDO-J. (2009). On-chip optical interconnect, *Proceedings of the IEEE*, **97**(7), pp. 1186–1198.

OLINER-A. (2003). A planar negative-refractive-index medium without resonant elements, *IEEE MTT-S International Microwave Symposium Digest, 2003*, Vol. 1, pp. 191–194.

OZBAY-E. (2006). Plasmonics: merging photonics and electronics at nanoscale dimensions., *Science*, **311**(5758), pp. 189–193.

PAREDES-F., ZAMORA-G., ZUFANELLI-S., HERRAIZ-MARTÍNEZ-F. J., BONACHE-J., AND MARTÍN-F. (2012). Recent advances in multiband printed antennas based on metamaterial loading, *Advances in OptoElectronics*, **2012**, pp. 1–12.

PATTNAIK-P., VIJAYAADITYA-B., SRINIVAS-T., AND SELVARAJAN-A. (2005). Optical MEMS pressure sensor using ring resonator on a circular diaphragm, *International Conference on MEMS, NANO and Smart Systems*, pp. 277–280.

PENDRY-J. B. (2000). Negative refraction makes a perfect lens, *Physical Review Letters*, **85**(18), pp. 3966–3969.

PENDRY-J. B., AND SMITH-D. R. (2004). Reversing light eith negative refraction, *Physics Today*, **57**(6), p. 37.

PENDRY-J. B., HOLDEN-A. J., ROBBINS-D. J., AND STEWART-W. J. (1999). Magnetism from conductors and enhanced nonlinear phenomena, *IEEE Transactions on Microwave Theory and Techniques*, **47**(11), pp. 2075–2084.

PENDRY-J. B., HOLDEN-A., STEWART-W., AND YOUNGS-I. (1996). Extremely low frequency plasmons in metallic mesostructures, *Physical Review Letters*, **76**(25), pp. 4773–4776.

PENDRY-J. B., SCHURIG-D., AND SMITH-D. R. (2006). Controlling electromagnetic fields., *Science*, **312**(5781), pp. 1780–1782.

PONCHAK-G. (2005). Excitation of coupled slotline mode in finite-ground CPW with unequal ground-plane widths, *IEEE Transactions on Microwave Theory and Techniques*, **53**(2), pp. 713–717.

POZAR-D. (2009). *Microwave Engineering*, 4 edn, John Wiley & Sons, Hoboken, NJ, USA.

POZAR-D. M. (2005). *Microwave Engineering, 3rd*, John Wiley & Sons, Hoboken, NJ, USA.

RADISIC-V., QIAN-Y., COCCIOLI-R., AND ITOH-T. (1998). Novel 2-D photonic bandgap structure for microstrip lines, *IEEE Microwave and Guided Wave Letters*, **8**(2), pp. 69–71.

RAZAVI-B. (1997). Challenges in the design of frequency synthesizers for wireless applications, *Proceedings of the IEEE Custom Integrated Circuits Conference*, pp. 395–402.

RAZAVI-B. (1998). *RF microelectronics*, Prentice-Hall, Inc. Upper Saddle River, NJ, USA.

REYES-A., EL-GHAZALY-S., DORN-S., DYDYK-M., AND SCHRODER-D. (1994). Silicon as a microwave substrate, *IEEE MTT-S International Microwave Symposium Digest*, pp. 1759–1762.

SAFWAT-A. M. E., TRETYAKOV-S., AND RÄISÄNEN-A. (2007). Dual bandstop resonator using combined split ring resonator and defected ground structure, *Microwave and Optical Technology Letters*, **49**(6), pp. 1249–1253.

SCHUELER-M., MANDEL-C., PUENTES-M., AND JAKOBY-R. (2012). Metamaterial inspired microwave sensors, *IEEE Microwave Magazine*, **13**(2), pp. 57–68.

SCHURIG-D., MOCK-J. J., JUSTICE-B. J., CUMMER-S. A., PENDRY-J. B., STARR-A. F., AND SMITH-D. R. (2006). Metamaterial electromagnetic cloak at microwave frequencies., *Science (New York, N.Y.)*, **314**(5801), pp. 977–980.

SHAMONIN-M., SHAMONINA-E., KALININ-V., AND SOLYMAR-L. (2005). Resonant frequencies of a split-ring resonator: Analytical solutions and numerical simulations, *Microwave and Optical Technology Letters*, **44**(2), pp. 133–136.

SHANNON-C. E. (1949). Communication in the Presence of Noise, *Proceedings of the IRE*, **37**(1), pp. 10–21.

SHATERIAN-Z., HORESTANI-A. K., AND FUMEAUX-C. (2013). Metamaterial-Inspired Displacement Sensor with High Dynamic Range, *Proc. 4th International Conference on Metamaterials, Photonic Crystals and Plasmonics, META'13*, Vol. 1, Sharjah, United Arab Emirates, pp. 9–11.

SHEN-Y. C., LO-T., TADAY-P. F., COLE-B. E., TRIBE-W. R., AND KEMP-M. C. (2005). Detection and identification of explosives using terahertz pulsed spectroscopic imaging, *Applied Physics Letters*, **86**(24), p. 241116.

SHI-S., CHOI-W.-W., CHE-W., TAM-K.-W., AND XUE-Q. (2012). Ultra-wideband differential bandpass filter with narrow notched band and improved common-mode suppression by DGS, *IEEE Microwave and Wireless Components Letters*, **22**(4), pp. 185–187.

SHREIBER-D., GUPTA-M., AND CRAVEY-R. (2011). Comparative study of 1-D and 2-D metamaterial lens for microwave nondestructive evaluation of dielectric materials, *Sensors and Actuators A: Physical*, **165**(2), pp. 256–260.

SIEGEL-P. (2004). Terahertz technology in biology and medicine, *IEEE Transactions on Microwave Theory and Techniques*, **52**(10), pp. 2438–2447.

SI-L., YUAN-Y., SUN-H., AND LV-X. (2008). Characterization and application of planar terahertz narrow bandpass filter with metamaterial resonators, *2008 International Workshop on Metamaterials*, pp. 351–354.

SIMONS-R., AND PONCHAK-G. (1988). Modeling of some coplanar waveguide discontinuities, *IEEE Transactions on Microwave Theory and Techniques*, **36**(12), pp. 1796–1803.

SMITH-D. R., PADILLA-W., VIER-D., NEMAT-NASSER-S., AND SCHULTZ-S. (2000). Composite medium with simultaneously negative permeability and permittivity, *Physical Review Letters*, **84**(18), pp. 4184–4187.

SMITH-D. R., PENDRY-J. B., AND WILTSHIRE-M. C. K. (2004). Metamaterials and negative refractive index., *Science*, **305**(5685), pp. 788–792.

SMOLYANINOV-I. I., HUNG-Y.-J., AND DAVIS-C. C. (2007). Magnifying superlens in the visible frequency range., *Science (New York, N.Y.)*, **315**(5819), pp. 1699–1701.

SMULDERS-P. (2003). 60 GHz radio: prospects and future directions, *Proceedings Symposium IEEE Benelux Chapter on Communications and Vehicular Technology*, pp. 1–8.

SOMMERFELD-A. (1899). Ueber die Fortpflanzung elektrodynamischer Wellen längs eines Drahtes, *Annalen der Physik*.

TAYA-S. A., AND SHABAT-M. M. (2011). Sensitivity enhancement in optical waveguide sensors using metamaterials, *Applied Physics A*, **103**(3), pp. 611–614.

TIEBOUT-M., ITOH-K., LEE-T., SAKURAI-T., SANSEN-W. M., AND SCHMITT-LANDSIEDEL-D. (2006). *Low Power VCO Design in CMOS*, Springer Verlag.

TIEBOUT-M., WOHLMUTH-H.-D., AND SIMBURGER-W. (2002). A 1 V 51GHz fully-integrated VCO in 0.12 μm CMOS, *Proc. IEEE International Solid-State Circuits Conference*, **1**, pp. 300–468.

TREIZEBRÉ-A., HOFMAN-M., AND BOCQUET-B. (2010). Terahertz spiral planar Goubau line rejectors for biological characterization, *Progress In Electromagnetics Research*, **14**, pp. 163–176.

TREIZEBRÉ-A., LAURETTE-S., AND XU-Y. (2012). THz power divider circuits on planar Goubau lines (PGLS), *Progress In Electromagnetics Research*, **26**, pp. 219–228.

TSAI-C.-H., AND WU-T. (2010). A broadband and miniaturized common-mode filter for gigahertz differential signals based on negative-permittivity metamaterials, *IEEE Transactions on Microwave Theory and Techniques*, **58**(1), pp. 195–202.

VALENTINE-J., ZHANG-S., ZENTGRAF-T., ULIN-AVILA-E., GENOV-D. A., BARTAL-G., AND ZHANG-X. (2008). Three-dimensional optical metamaterial with a negative refractive index., *Nature*, **455**(7211), pp. 376–379.

VAN TUYL-R. (1996). Unlicensed millimeter wave communications. A new opportunity for MMIC technology at 60 GHz, *GaAs IC Symposium IEEE Gallium Arsenide Integrated Circuit Symposium. 18th Annual Technical Digest 1996*, pp. 3–5.

VELEZ-A., AZNAR-F., BONACHE-J., VELAZQUEZ-AHUMADA-M. D. C. M., MARTEL-J., MARTÍN-F., AND VÉLEZ-A. (2009). Open complementary split ring resonators (OCSRRs) and their application to wideband CPW band pass filters, *IEEE Microwave and Wireless Components Letters*, **19**(4), pp. 197–199.

VELEZ-P., NAQUI-J., FERNANDEZ-PRIETO-A., DURÁN-SINDREU-M., BONACHE-J., MARTEL-J., MEDINA-F., AND MARTÍN-F. (2013). Differential bandpass filter with common-mode suppression based on open split ring resonators and open complementary split ring resonators, *IEEE Microwave and Wireless Components Letters*, **23**(1), pp. 22–24.

VESELAGO-V. G. (1968). The electrodynamics of substances with simultaneously negative values of ϵ and μ, *Physics-Uspekhi*, **10**(4), pp. 509–514.

WANG-K., AND MITTLEMAN-D. (2004). Metal wires for terahertz wave guiding, *Nature*, **432**(7015), pp. 376–379.

WANG-Y., ZHANG-Y., LIU-F., HE-L., LI-H., CHEN-H., AND CALOZ-C. (2007). Simplified description of asymmetric right-handed composite right/left-handed coupler in microstrip chip technology, *Microwave and Optical Technology Letters*, **49**(9), pp. 2063–2068.

WITHAYACHUMNANKUL-W., AND ABBOTT-D. (2009). Metamaterials in the terahertz regime, *IEEE Photonics Journal*, **1**(2), pp. 99–118.

WITHAYACHUMNANKUL-W., FISCHER-B. M., AND ABBOTT-D. (2008). Quarter-wavelength multilayer interference filter for terahertz waves, *Optics Communications*, **281**(9), pp. 2374–2379.

WITHAYACHUMNANKUL-W., FUMEAUX-C., AND ABBOTT-D. (2010). Compact electric-LC resonators for metamaterials, *Optics Express*, **18**(25), p. 25912.

WITHAYACHUMNANKUL-W., JARUWONGRUNGSEE-K., FUMEAUX-C., AND ABBOTT-D. (2012). Metamaterial-inspired multichannel thin-film sensor, *IEEE Sensors Journal*, **12**(5), pp. 1455–1458.

WITHAYACHUMNANKUL-W., JARUWONGRUNGSEE-K., TUANTRANONT-A., FUMEAUX-C., AND ABBOTT-D. (2013). Metamaterial-based microfluidic sensor for dielectric characterization, *Sensors and Actuators A: Physical*, **189**, pp. 233–237.

WITHAYACHUMNANKUL-W., PNG-G. M., YIN-X., ATAKARAMIANS-S., JONES-I., LIN-H., UNG-B. S. Y., BALAKRISHNAN-J., NG-B. W.-H., FERGUSON-B., MICKAN-S. P., FISCHER-B. M., AND ABBOTT-D. (2003). T-ray sensing and imaging, *Proceedings of the IEEE*, **95**(8), pp. 1528–1558.

WOMACK-C. (1962). The use of exponential transmission lines in microwave components, *IEEE Transactions on Microwave Theory and Techniques*, **10**(2), pp. 124–132.

WU-C.-H., AND WANG-C.-H. (2007). Parallel-coupled coplanar-waveguide bandpass filter with multiple transmission zeros, *IEEE Microwave and Wireless Component Letters*, **17**(2), pp. 118–120.

WU-H., AND HAJIMIRI-A. (2000). A 10 GHz CMOS distributed voltage controlled oscillator, *Proc. of the IEEE Custom Integrated Circuits Conference (CICC)*, pp. 581–584.

WU-H., AND HAJIMIRI-A. (2001). Silicon-Based Distributed Voltage-Controlled, *IEEE Journal of Solid-State Circuits*, **36**(3), pp. 493–502.

WU-S., TSAI-C.-H., WU-T., AND ITOH-T. (2009). A novel wideband common-mode suppression filter for gigahertz differential signals using coupled patterned ground structure, *IEEE Transactions on Microwave Theory and Techniques*, **57**(4), pp. 848–855.

XU-Y., AND BOSISIO-R. (2007). A comprehensive study on the planar type of Goubau line for millimetre and submillimetre wave integrated circuits, *IET Microwaves, Antennas & Propagation*, **1**(3), pp. 681–687.

XU-Y., NERGUIZIAN-C., AND BOSISIO-R. (2011). Wideband planar Goubau line integrated circuit components at millimetre waves, *IET Microwaves, Antennas & Propagation*, **5**(8), p. 882.

XU-Y.-S., AND BOSISIO-R. (2005). Application of Goubau lines for millimetre and submillimetre wave gas sensors, *IEE Proceedings - Microwaves, Antennas and Propagation*, **152**(5), p. 400.

YANG-F. R., MA-K. P., QIAN-Y., AND ITOH-T. (1999). Uniplanar compact photonic-bandgap (UC-PBG) structure and its applications for microwave circuit, *IEEE Transactions on Microwave Theory and Techniques*, **47**(8), pp. 1509–1514.

YANG-J. J., HUANG-M., XIAO-Z., AND PENG-J. (2010). Simulation and Analysis of Asymmetric Metamaterial Resonator-Assisted Microwave Sensor, *Modern Physics Letters B*, **24**(12), pp. 1207–1215.

YANG-N., CALOZ-C., AND WU-K. (2009). Lowpass filter with slow-wave rail coplanar stripline (R-CPS), *Electronics Letters*, **45**(17), pp. 895–897.

YOULA-D. (1964). Analysis and synthesis of arbitrarily terminated lossless nonuniform lines, *IEEE Transactions on Circuit Theory*, **11**(3), pp. 363–371.

YUN-T. Y., AND CHANG-K. (2001). Uniplanar one-dimensional photonic-bandgap structures and resonators, *IEEE Transactions on Microwave Theory and Techniques*, **49**(3), pp. 549–553.

ZHANG-H., AND CHEN-K. (2006). Miniaturized coplanar waveguide bandpass filters using multi-section stepped-impedance resonators, *IEEE Transactions on Microwave Theory and Techniques*, **54**(3), pp. 1090–1095.

ZHANG-X., AND LIU-Z. (2008). Superlenses to overcome the diffraction limit., *Nature Materials*, **7**(6), pp. 435–41.

ZHELUDEV-N. (2010). The road ahead for metamaterials, *Science*, **328**(5978), pp. 582–583.

ZHENG-H. H., XIAO-J. J., LAI-Y., AND CHAN-C. T. (2010). Exterior optical cloaking and illusions by using active sources: A boundary element perspective, *Physical Review B*, **81**(19), p. 195116.

ZHOU-J., LANCASTER-M., AND HUANG-F. (2004). Coplanar quarter-wavelength quasi-elliptic filters without bond-wire bridges, *IEEE Transactions on Microwave Theory and Techniques*, **52**(4), pp. 1150–1156.

ZHU-Y., VEGESNA-S., KURYATKOV-V., HOLTZ-M., SAED-M., AND BERNUSSI-A. A. (2012). Terahertz bandpass filters using double-stacked metamaterial layers., *Optics Letters*, **37**(3), pp. 296–298.

ZIOLKOWSKI-R., AND ENGHETA-N. (2003). Metamaterial special issue introduction, *IEEE Transactions on Antennas and Propagation*, **51**(10), pp. 2546–2549.

Acronyms

BC-SRR	Broad-Side Coupled Split Ring Resonator
CPS	Coplanar Strips
CPW	Coplanar Waveguide
CRLH	Composite Right/Left-Handed
CSRR	Complementary Split Ring Resonator
CSRS	Complementary Spiral Resonators
DGS	Defected Ground Structure
DNG	Double Negative
DPS	Double Positive
Dual-CRLH	Dual Composite Right/Left-Handed
EBG	Electromagnetic Bandgaps
ELC	Electrical LC
EMI	Electromagnetic Interference
ENG	Epsilon-Negative
ERR	Electric-Ring Resonators
FBW	Fractional Bandwidth
FCC	Federal Communication Commission
FOM	Figure Of Merit
GPS	Global Positioning Systems
HS	Harmony Search
LH	Left-Handed
MEMS	Micro-Electro-Mechanical Systems
MMIC	Monolithic Microwave Integrated Circuits
MNG	Mu-Negative
MSRR	Multiple Split Ring Resonator
OCSRR	Open Complementary Split Ring Resonators
OSRR	Open Split Ring Resonator
PBG	Photonic Bandgap
PGL	Planar Goubau Lines
RH	Right-Handed
S-CSRR	S-Shaped Complementary Split Ring Resonator

S-SRR	S-Shaped Split Ring Resonators
SNG	Single Negative
SRR	Split Ring Resonator
SR	Spiral Resonator
TL	Transmission Line
VCO	Voltage Controlled Oscillators

Index

Biography

Ali Karami Horestani was born in Isfahan, Iran in 1978. He received his B.Eng. and M.Eng. degrees in Electrical and Electronics Engineering from The University of Shiraz and The University of Shahid Beheshti, Iran, in 2003 and 2006, respectively. In 2009, he joined the School of Electrical and Electronic Engineering at The University of Adelaide to study towards his PhD in the area of microwave and millimeter-wave circuit design under the supervision of Prof Derek Abbott, Dr Said Al-Sarawi, and Prof Christophe Fumeaux.

During his candidature, he received an IEEE SA Section Student Travel Award in 2012 to attend the IEEE Asia-Pacific Microwave Conference (APMC) in Taiwan. He has been also the recipient of the 2012 Simon Rockliff Award for outstanding postgraduate mentorship from the School of Electrical and Electronic Engineering and DSTO. He was a Visiting Scholar at GEMMA/CIMITEC, Departament d'Enginyeria Electronica, Universitat Autonoma de Barcelona, Bellaterra, Spain, hosted by Prof Ferran Martín.

He has served as a reviewer for a number of journals including IEEE TRANSACTIONS ON MICROWAVE THEORY AND TECHNIQUES, IEEE TRANSACTIONS ON CIRCUITS AND SYSTEMS I, IEEE MICROWAVE AND WIRELESS COMPONENTS LETTERS, and IEEE SENSORS JOURNAL.

Ali Karami Horestani is a student member of the IEEE (Institute of Electrical and Electronics Engineers).

Ali Karami Horestani
alikaramih@gmail.com

Scientifc Genealogy of
Ali Karami Horestani

Formalised supervisor relationship
Mentoring relationship
Nobel prize

"If I have seen further it is by standing on the shoulders of Giants."
Isaac Newton